Using computational methods to rationalize organogel formation

Manuel Reche Tamayo

To cite this version:

Manuel Reche Tamayo. Using computational methods to rationalize organogel formation. Soft Condensed Matter [cond-mat.soft]. Sorbonne Université; Université de Mons, 2021. English. NNT : 2021SORUS464 . tel-03850753

HAL Id: tel-03850753

https://theses.hal.science/tel-03850753

Submitted on 14 Nov 2022

École doctorale 397 : Physique et chimie des matériaux (Paris)

THESE DE DOCTORAT
DE SORBONNE UNIVERSITE
en cotutelle avec l'Université de MONS
(Belgique)

Présentée par :
Manuel RECHE TAMAYO

Pour l'obtention du grade de : **Docteur de SORBONNE UNIVERSITE**
Spécialité : Chimie

Using computational methods to rationalize organogel formation

Thèse dirigée par Laurent Bouteiller et Patrick Brocorens

Soutenue le 12 **juillet 2021**

Devant un jury composé de :

President
Prof. Pascal Gerbaux, Université de Mons

Referees
Prof. Yves Geerts, Université Libre de Bruxelles
Prof. Luca Muccioli, Università di Bologna
Prof. Mònica Calatayud Antonino, Sorbonne Université

Thesis promoters
Dr. Patrick Brocorens, Université de Mons
Prof. Laurent Bouteiller, Sorbonne Université

University of Mons
Faculty of Sciences

Using computational methods to rationalize organogel formation

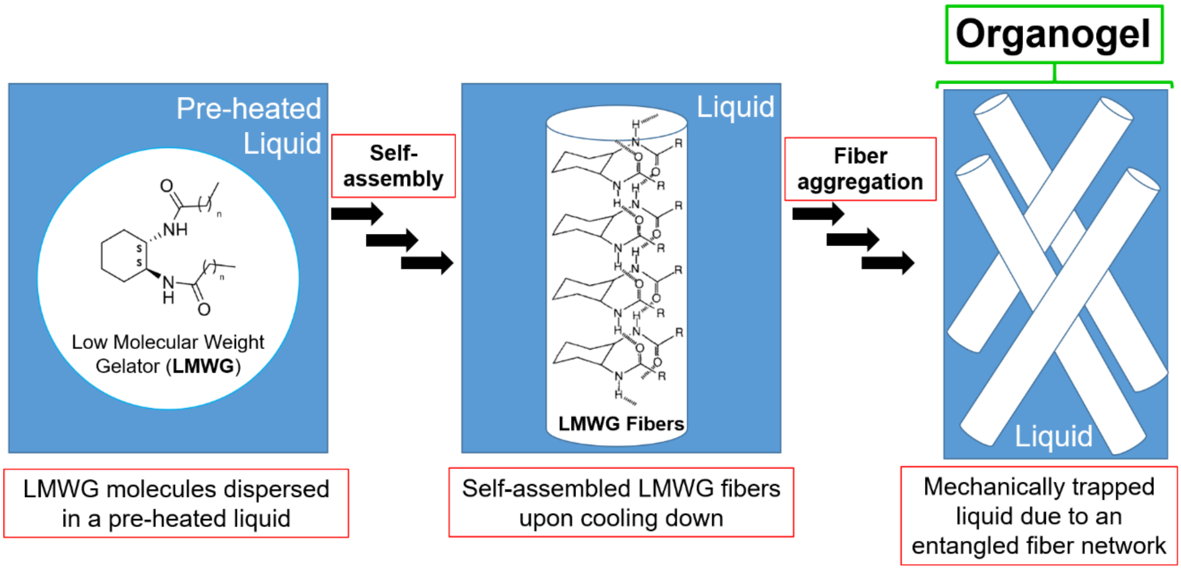

by

Manuel Reche Tamayo

Thesis defended on July 12th 2021, for the obtention of the diploma of
Doctor in Chemical Sciences

« Chaque homme doit inventer son chemin »

Jean-Paul Sartre

Voici j'invente le mien

University of Mons
Faculty of Sciences

Using computational methods to rationalize organogel formation

by

Manuel Reche Tamayo

Thesis defended on July 12th 2021, for the obtention of the diploma of Doctor in Chemical Sciences

Jury composition

President	Prof. Pascal Gerbaux	Université de Mons
Referees	Prof. Yves Geerts	Université Libre de Bruxelles
	Prof. Luca Muccioli	Università di Bologna
	Prof. Mònica Calatayud Antonino	Sorbonne Université
Thesis promoters	Dr. Patrick Brocorens	Université de Mons
	Prof. Laurent Bouteiller	Sorbonne Université

Abstract

This work deals with supramolecular organogels. These gels are obtained by dispersing in the organic solvent low molecular weight molecules (Low Molecular Weight Gelators, LMWGs), which are not soluble at room temperature and form a suspension. This suspension is heated, achieving solution, and cooled down back to room temperature where LMWG molecules self-assemble in non-covalently bonded Self-Assembled Fibrillar Networks (SAFiNs), e.g., by hydrogen-bonding, π-stacking, Van der Waals interactions, etc. This entangled network traps mechanically the liquid, principally by surface tension, triggering a gel state.

A precise description of the phenomena remains partially unknown, leaving open questions that still impede to predict beforehand whether a given LMWG candidate will be able to gelate a certain liquid of interest. If design rules could be established between the chemical structure of a LMWG and its gelation properties, it could be possible to design LMWGs for specific liquids of interest while providing insight about organogel formation. Thus, this work investigates sets of chemically diverse LMWG families, with the aim of correlating their chemical structure with their corresponding gelation behavior.

The approach followed in this thesis consists in modelling the self-assembly of different series of LMWGs, bisamide-cyclohexane compounds and thiazole compounds with alkyl chains of different lengths, with the aim of understanding the formation of the gel fibers and determining their structure. Most of the LMWGs that we have studied crystallize to form gels, and for such crystalline systems, our methodology starts with a Crystal Structure Prediction (CSP) of the gel fibers, combining crystal cell generation and powder X-ray diffraction simulations. Then, we determine their crystal morphology using growth kinetics principles, to finally characterize the gelation ability of the gel fibers using surface energy parameters. Our modelling activities have been carried out in very close interaction with corresponding experimental efforts undertaken in the groups of Prof. Laurent Bouteiller (Sorbonne Université) and Prof. Pierre-Antoine Albouy (Université Paris-Sud). Their results of gelation experiments, powder X-ray diffraction and SEM characterization were compared with our modelling data.

Résumé

Ce travail consiste en une étude théorique de la formation et de la structure d'organogels supramoléculaires. Ces gels sont obtenus par dispersion dans un solvant organique de molécules de bas poids moléculaire (Low Molecular Weight Gelators, LMWGs). Ces molécules LMWG s'auto-assemblent de manière non covalente, par exemple par liaison hydrogène, empilement π, interactions de Van der Waals, etc. et forment finalement des réseaux fibrillaires. Ces réseaux enchevêtrés piègent mécaniquement le liquide, principalement par tension superficielle, générant un gel.

La description précise des phénomènes de gélation de solvants organiques reste encore partielle, laissant des questions ouvertes qui empêchent de prédire si un candidat LMWG donné sera capable de gélifier un certain liquide d'intérêt. Si, par la modélisation, des règles de conception pouvaient être établies entre la structure chimique d'un LMWG et ses propriétés de gélification, il serait possible de concevoir des LMWG pour des liquides spécifiques, tout en améliorant la compréhension de la formation des organogels. Pour répondre à ces objectifs, ce travail étudie des familles de LMWG chimiquement différentes, dans le but de corréler leur structure chimique avec leur comportement de gélification.

L'approche suivie dans cette thèse consiste à modéliser l'auto-assemblage de différentes séries de LMWG (d'une part des composés bisamide-cyclohexane, d'autre part des composés de thiazole, tous porteurs de chaînes alkyles de différentes longueurs), dans le but de comprendre la formation des fibres de gel et de déterminer leur structure. La plupart des LMWG que nous avons étudiés cristallisent pour former des gels, et pour de tels systèmes cristallins, notre méthodologie de modélisation débute par la prédiction de la structure cristalline des fibres de gel, en combinant la génération de cellules cristallines et des simulations des diagrammes de diffraction des rayons X sur poudres. Ensuite, nous déterminons la morphologie des cristaux en utilisant les principes de cinétique de croissance. Enfin, nous caractérisons la capacité de gélification des fibres cristallines en utilisant des paramètres d'énergie de surface. Il est important de souligner que nos activités de modélisation ont été menées en interaction très étroite avec les efforts expérimentaux correspondants entrepris dans les groupes du Prof. Laurent Bouteiller (Sorbonne Université) et du Prof. Pierre-Antoine Albouy (Université Paris-Sud). Leurs résultats d'expériences de gélification, de diffraction des rayons X sur poudres et de caractérisation SEM ont été comparés à nos données de modélisation.

Contents

List of Figures

Acknowledgements

Three years and a half of doctoral studies have culminated in the writing of this thesis manuscript. I have met wonderful people during this time, and I have plenty of memories and gratitude that cannot be fitted in these pages. I will try my best to sum it up.

To my supervisors: Dr. Patrick Brocorens, Prof. Laurent Bouteiller and Prof. Roberto Lazzaroni. Thank you for making me a more mature scientist in the academic and personal sense. Thank you for your constant support and resilience that encouraged me to always do my best, un très grand merci.

To the CMN laboratory, where I had a warm stay from beginning to end. From scientific discussions to thematic barbecue parties, I really felt as a member of this laboratory and I am grateful to have done my doctoral studies here.

To my group of friends in the laboratory. In no specific order: Giacomo, Cuong, Suryoday, Quynh, Andrea, Sandra, Imane, Manoj, David, Marco and Edoardo, thank you so much for the incredible moments that we have shared together and your support, it has been a pleasure to be with you. Claudio, grazie mille per il tuo instancabile supporto, sei un vero amico per me e... lavora cane! Valentín, eres mi referente de constancia e integridad, me alegro mucho de haber compartido esta experiencia contigo y espero que tu futuro vaya sobre ruedas. Nemo, tu es cet enfant extraterrestre qui a atterri sur mon cœur, merci pour les chansons qui m'ont toujours remonté le moral.

To my family and my girlfriend Irina, I love you so much, you are the pillars of my life.

Thank you to all the people that has helped me to achieve the incredible milestone that is a PhD degree because, if I have seen further, it is by standing on your shoulders, thank you.

Chapter 1. **Introduction**

Since the introduction of the concept of a gel in 1861 by Thomas Graham [1], its definition has been changing through the years due to the broad physicochemical nature of gels [2]–[4]. In 2007, the International Union of Pure and Applied Chemistry (IUPAC) defined a gel as a "non-fluid colloidal network or polymer network that is expanded throughout its whole volume by a fluid"[5].

Because of this diverse nature, many applications have been developed designing gels with specific characteristics for specific needs. The presence of gels in today's society is quite remarkable as many applications are visible, from everyday life (such as gelatin or jelly-like food products in the food industry, hair/body gels or moisturizers for body care, paint or coatings formulations), to more technological applications (drug delivery in the pharmaceutical industry, pollutant removal, separation and analysis of macromolecules by gel electrophoresis in forensic science and many more).

Jointly with the broad applications of gels, the corresponding physicochemical nature of gels is very diverse too. In 1974 Paul Flory categorized gels considering the wide physicochemical characteristics that must be considered. Up to this day, the following classification still holds and is recommended by the IUPAC association [6]:

i. *a covalent polymer network, e.g., a network formed by crosslinking polymer chains or by nonlinear polymerization;*
ii. *a polymer network formed through the physical aggregation of polymer chains, caused by hydrogen bonds, crystallization, helix formation, complexation, etc., that results in regions of local order acting as the network junction points. The resulting swollen network may be termed a thermoreversible gel if the regions of local order are thermally reversible;*
iii. *a polymer network formed through glassy junction points, e.g., one based on block polymers. If the junction points are thermally reversible glassy domains, the resulting swollen network may also be termed a thermoreversible gel;*

iv. *lamellar structures including mesophases, e.g., soap gels, phospholipids, and clays;*

v. *particulate disordered structures, e.g., a flocculent precipitate usually consisting of particles with large geometrical anisotropy, such as in* V_2O_5 *gels and globular or fibrillar protein gels.*

Additionally, a popular complementary classification for gels is based on the liquid gelled. When the liquid is water, it is named hydrogel; if it is an organic solvent, it is named organogel.

This work deals with supramolecular organogels. These gels are obtained by dispersing in the organic solvent low molecular weight molecules (Low Molecular Weight Gelators, LMWGs), which are not soluble at room temperature and form a suspension. This suspension is heated, achieving solution, and cooled down back to room temperature where LMWG molecules self-assemble in non-covalently bonded Self-Assembled Fibrillar Networks (SAFiNs), e.g. by hydrogen-bonding, π -stacking, van der Waals interactions, etc. This entangled network traps mechanically the liquid, principally by surface tension, triggering a gel state (see Figure 1.1). Let us just mention that supramolecular organogelation would be classified in the second and perhaps fifth of Flory's categories [7].

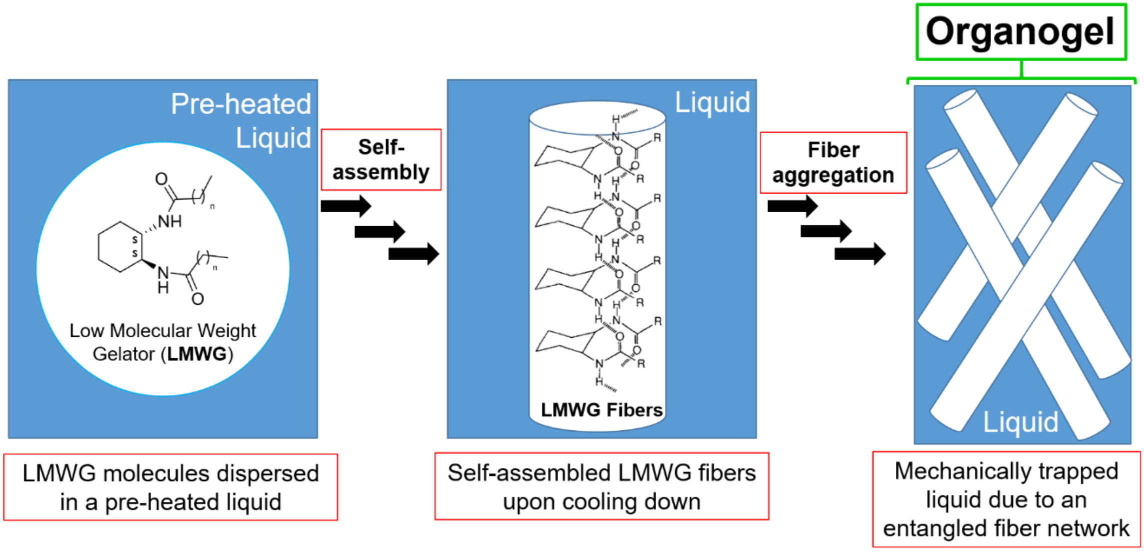

Figure 1.1: Sketch of organogel formation.

Supramolecular organogels, commonly referred as organogels in literature and from here on in this manuscript, mainly differ from the traditional gels, synthesized by polymerization reactions, in the non-covalently bonded nature of their cross-linking, whereas the traditional ones are covalent. This feature offers unique properties such as reversibility upon e.g. heating, irradiating or sonicating [8], and they can be used for many applications in the fields of organic electronics, nanotechnology, biomedicine, mechanochemistry, etc [9]–[11]. Consequently, this type of materials has spurred increasing attention over the years.

However, despite important advances in the field aiming to rationalize organogel formation [12]–[15], a precise description of the phenomena remains partially unknown, leaving open questions that still impede efficient prediction of organogelation. Those open questions are: (i) the interplay between LMWG and solvent, (ii) the relation between the chemical structure of the LMWG and its gelation properties, (iii) the organogelation mechanism, and (iv) the relationship between the molecular packing of gelator molecules in the gels and in their neat crystalline phases [16], [17].

Those open questions make it greatly difficult to predict beforehand whether a given LMWG candidate will be able to gelate a certain liquid of interest. If design rules could be established between the chemical structure of a LMWG and its gelation properties, it could be possible to design LMWGs for specific liquids of interest while providing insight about organogel formation. Thus, this work investigates sets of chemically diverse LMWG families, with the aim of correlating their chemical structure with their corresponding gelation behavior.

The approach followed in this thesis consists in modelling the self-assembly of different series of LMWGs, with the aim of understanding the formation of the gel fibers and determining their structure. It is important to mention that our modelling activities have been carried out in very close interaction with corresponding experimental efforts undertaken in the groups of Prof. Laurent Bouteiller (*Sorbonne Université*) and Prof. Pierre-Antoine Albouy (*Université Paris-Sud*). The results of gelation experiments, spectroscopic and structural studies were compared with our modelling data throughout this work.

In Chapter 2, the state of the art for describing organogel formation is detailed, including the different types of parameters that have been used to rationalize organogelation up to the present day [7], [18]–[21].

Chapter 3 details our modeling approach, which has been established and validated. Many LMWGs crystallize to form gels, and for such crystalline systems the methodology starts with a Crystal Structure Prediction (CSP) of the gel fibers, combining crystal cell generation and powder X-ray diffraction simulations. Then, we determine their crystal morphology using growth kinetics principles, to finally characterize the gelation ability of the gel fibers using surface energy parameters [22], [23].

Chapter 4 describes the crystal prediction and crystal morphology analysis for a series of bisamide-decorated cyclohexane compounds [24], combining modelling and powder X-ray diffraction and SEM characterization.

Chapter 5 describes the full procedure of predicting the gelation trend for a series of alkyl chain-decorated thiazole compounds [25], [26], in relation to their chemical structure.

Finally, Chapter 6 presents the major conclusions of the thesis and the research perspectives opened by this work.

Chapter 2. Gelation: basic principles and prediction

In the first part of the chapter, we introduce gelation from a rheological perspective and the models developed to characterize gel formation, solvent effects that trigger gelation and the specific case of organogelation. In the second part, we describe several approaches that aim at correlating the chemical structure and the solvent parameters of organogelators, to gain insight and predictability about organogelation.

2.1 Basic principles of gelation

2.1.1 Colloid aggregation

Colloids are microscopic dispersions of a substrate into another one, for instance, when solid, microscopic objects are dispersed in a liquid, forming a “sol”. In water, the surface of colloidal particles is often charged or polar, which provokes the diffusion of counterions from the liquid to the surface and the formation of an electric double layer at the interface [27]. Figure 2.1 shows schematically the historical three models characterizing the double layer: the Helmholtz [28], Gouy-Chapman [29], [30] and Stern [31] models.

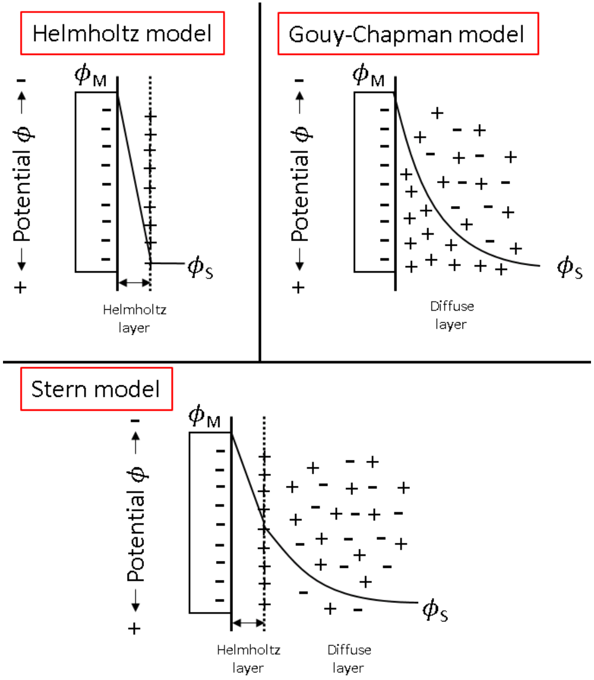

Figure 2.1: Historical models for characterizing the electrical double layer of colloidal particles. Top left panel: Helmholtz, top right: Gouy-Chapman and bottom:

Stern models. The solid black line represents the decay of the electric potential from the surface ($\boldsymbol{\phi}_{\mathbf{M}}$) to the solution ($\boldsymbol{\phi}_{\mathbf{S}}$).
The Helmholtz model considers that charges are fixed in a plane parallel to the surface (Helmholtz layer), leading to an interface between two rigid planes (the double layer) and no other interactions are further extended in the solution. The Gouy-Chapman model considers that charges are free to diffuse up to the bulk of the solution, forming a diffuse layer, and thus the thickness of the double layer depends on the electrolyte concentration. The Stern model combines the Helmholtz model and Gouy-Chapman model considering that there is a first compact layer of charges at the interface (at the Helmholtz layer) and then charges diffuse up to reaching the bulk of the solution (the diffuse layer).

In the Derjaguin-Landau-Verwey-Overbeek (DLVO) theory [32], [33], colloids tend to aggregate because of long-range attractive van-der-Waals forces between them. However, the shorter-range electrostatic repulsion between the double layers of the colloids prevents them from aggregating (Figure 2.2). Changes that affect the surface charge of colloids (e.g. in the ionic environment or adding surfactants) can reduce the electrostatic repulsion between colloids, triggering coalescence.

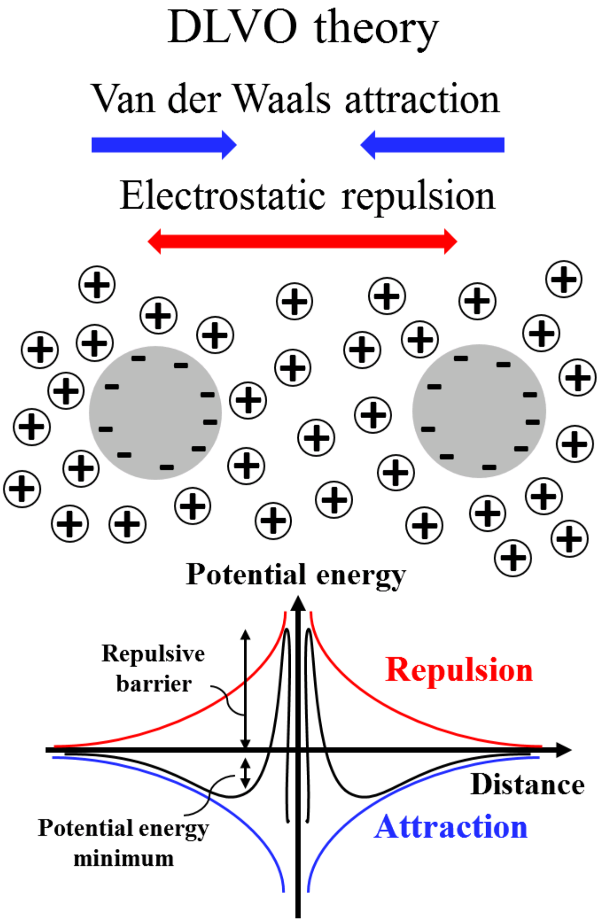

Figure 2.2: Sketch of the DLVO theory for colloidal aggregation.

When solids are dispersed in a liquid, the thermodynamic result of the coalescence of colloids is a precipitate. However, depending on the liquid, a kinetic aggregation state can be formed, consisting in a supramolecular cross-linked network that traps mechanically the liquid where it is embedded, increasing the viscosity abruptly. That aggregation state, which can now be considered as the dispersion of a liquid in a solid, is known as a gel.

2.1.2 Gel fundamentals

2.1.2.1 Gel rheology

We can picture the gelation process as the aggregation of clusters forming a single increasingly bigger connected cluster. During aggregation, there is a critical point where the cluster is big enough to limit the fluidity of the surrounding liquid, thus leading to an abrupt rise of the viscosity and to the apparition of an elastic resistance to stress. The gelation process can be studied by following the evolution of those two properties over time, and the gelation point corresponds to the observation of a sudden increase of the viscosity or the elasticity. This critical point can be defined from the time of gelation (t_{gel}) [34]. Note, however, that it can be different depending on the property that is measured. See for instance Figure 2.3, where the t_{gel} onset for the elasticity is retarded with respect to the viscosity one, as the aggregation of clusters into bigger connected cluster limits the fluidity and therefore triggers an abrupt change in viscosity, while the t_{gel} onset for the elasticity is triggered when a continuous solid network is formed. It is conceived that the main factor reducing the flow rate is the surface tension of the liquid in the gel network. Therefore, gel network geometries with a large, exposed surface area with respect to the volume favour gelation (e.g. a fibrillar geometry).

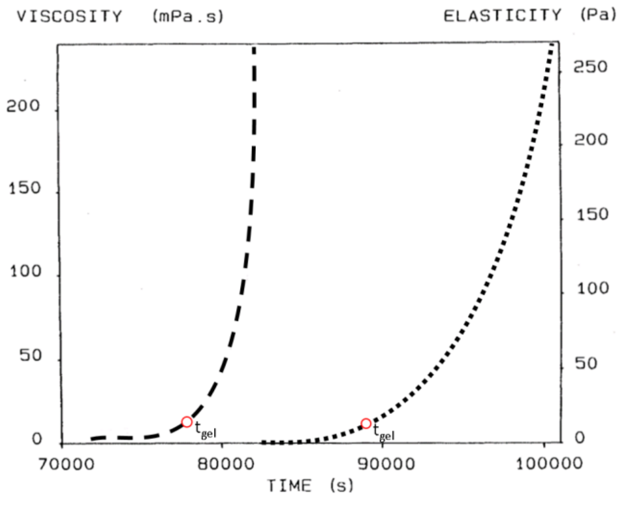

Figure 2.3: Abrupt change of viscosity and elasticity with time during formation of a silica gel. Dashes correspond to viscosity and square dots to elasticity. Reproduced from reference **[35]**.

2.1.2.2 Historical gelation models

In this section, we present three historical models considering polymer growth to explain gelation.

Classical theory

The "classical" theory of gelation corresponds to the polymer growth model developed by Flory and Stockmayer [36], which aims to rationalize gelation mathematically, considering the self-condensation of a monomer. In this model, an infinitely large polymer represents the single large cluster that triggers gelation. Therefore, considering the self-condensation polymerization reaction, this model aims to find the fraction of functional groups (p_c) that have reacted, at which an infinitely large polymer is formed, from a monomer with z functional groups. Considering that all bond formation events are equally probable, and the probability does not change with the polymerization degree, this condition is reached when:

$$p_c = \frac{1}{(z-1)} \qquad (2.1)$$

For example, when z=2, there is no cross-linking, the resulting polymer is a linear chain, and p_c=1, i.e. all bonds must be formed to obtain the infinite structure. As cross-linking is mandatory to form an infinite network leading to gelation, the minimum z-value is 3 and, in that case, gelation is expected when half the functional groups have reacted (p_c=1/2). Figure 2.4 shows one possible network resulting from the z=3 condition.

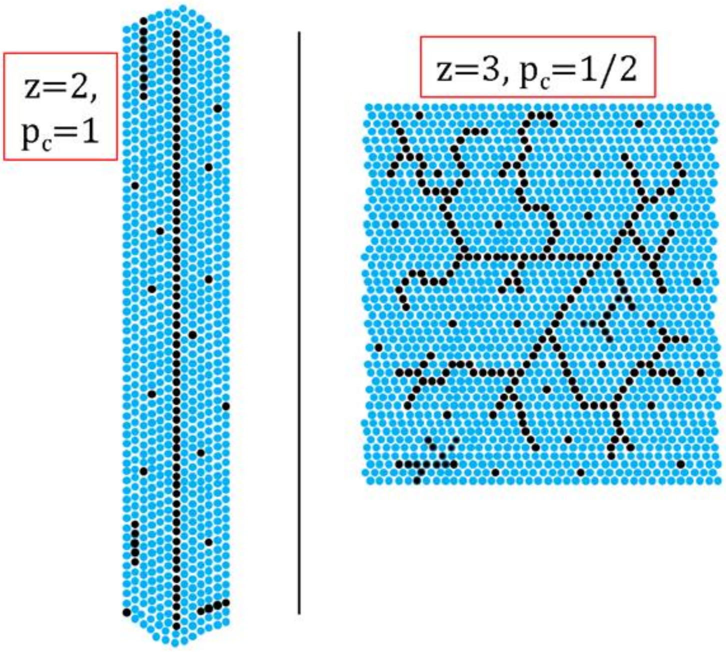

Figure 2.4: Possible polymer network resulting with the (left) z=2 or (right) z=3 condition. Blue and black dots represent the solvent and monomer molecules, respectively.

This theory has been useful for determining the critical degree of reaction at the gel point and the distribution of molecular weights in the sol. However, it also predicts a dependency of the volumetric mass of the polymer with the radius of the polymer [37], [38]. Hence, an infinitely growing density is unphysical, and the model does not provide a realistic description of the process.

Percolation theory

Percolation theory [39]–[41] is a mathematical model that aims to characterize gelation. A lattice composed of grid lines is defined. Intersections are called sites and the segment connecting two sites is called a bond (Figure 2.5). There are two approaches for filling the sites and bonds. The first one is called site percolation, which fills sites randomly when increasing progressively the fraction of filled sites (p) and considers that a bond is formed when two adjacent sites are occupied. The size of a cluster (s) is defined as the number of sites connected by bonds. The average cluster size (s_{av}) increases with p until p reaches the critical point (p_c) where there is at least one cluster that reaches across the entire grid, and it is considered of infinite size (s_∞), which corresponds to the formation of the gel. The second approach, called bond percolation, is similar to the previous one, except that it fills all sites initially and the bonds are formed randomly. This description can be used to represent gelation, considering that the sites are occupied by the colloidal particles and the space between the sites is filled by the liquid.

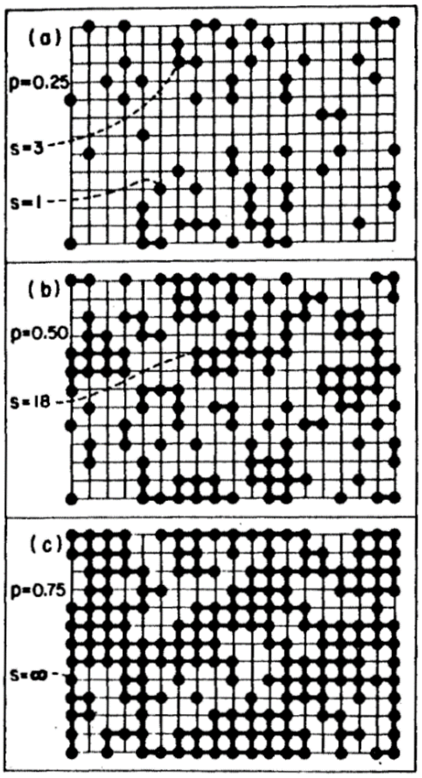

Figure 2.5: Site percolation at different fractions of filled sites p. Reference **[40]**.

As site/bond percolation characterizes the structure of gels numerically, gelation is characterized by computer simulations. This approach proves useful for giving p_c values and size distributions of clusters accurately [40]. On the other hand, there is no inclusion of effects such as the correlation of bond formation or the non-uniform distribution of bond formation over the lattice.

Smoluchowski's kinetic model

This approach uses a population balance equation to model how the number of clusters (n_s) of size s evolves in time (t) [42]–[44]:

$$\frac{dn_s}{dt} = \frac{1}{2}\sum_{i+j=s} k(i,j)n_i n_j - n_s \sum_{j=1}^{\infty} k(s,j)n_j \tag{2.2}$$

Assuming that cluster collisions are between two clusters, which is reasonable in dilute solutions, the first term represents the generation of clusters of size s by the coalescence of two clusters, one of size i and the other of size j, via the kinetic constant k(i,j). The second term represents the disappearance of clusters of size s due to further coalescence.

For large clusters where j>>i, the coalescence coefficients k(i,j) can be approximated as $k(i,j)=i^{\mu}j^{\nu}$, where μ and ν describe the dependence of k(i,j) to cluster size i and j, respectively. $\nu \leq 1$, and for μ, there are three possible situations [45]: (i) when $\mu>0$ the coalescence of large clusters is favored, (ii) when $\mu<0$ the coalescence between large and small clusters is favored, (iii) when $\mu=0$ none of the two previous cases are favored. When $\mu+\nu>1$ a gel occurs, whereas $\mu+\nu<1$ corresponds to non-gelling systems.

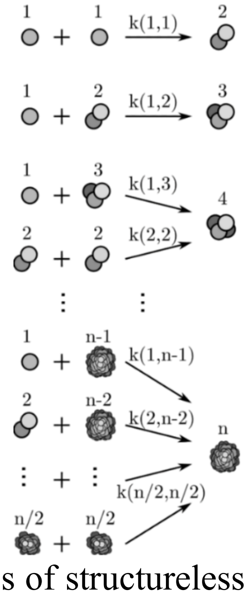

Figure 2.6: Aggregation kinetics of structureless spherical clusters via the kinetic constant k(i,j), following the Smoluchowski's equation.

2.1.3 Effect of the solvent in gelation

In order to understand the relation between solvent and gelation, we must address the concept of solubility. Solubility "quantifies the maximum amount of substance that will hold in homogeneous solution at a given temperature" [46]. Temperature and the chemical nature of solute and solvent affect all chemical solutions. Temperature enhances the diffusion of the substances into one another, often increasing solubility. On the other hand, how the chemical nature of solvent and solute correlates with solubility is more complex. Next, we introduce the Flory-Huggins parameter to rationalize this effect.

2.1.3.1 The Flory-Huggins parameter

The Flory-Huggins theory extends the ideal Gibbs free energy of mixing a polymer (A) with a solvent (B): $\Delta G_m = RT[n_A Ln\phi_A + n_B Ln\phi_B]$, by adding an additional parameter (χ_{AB}), named the Flory-Huggins parameter, that accounts for the energetic interactions between polymer and solvent [47]–[49].

$$\Delta G_m = \Delta H_m - T\Delta S_m \qquad (2.3)$$

$$\Delta G_m = \frac{RT}{V_r}\left[\frac{\phi_A Ln\phi_A}{V_A/V_r} + \frac{\phi_B Ln\phi_B}{V_B/V_r} + \chi_{AB}\phi_A\phi_B\right] \qquad (2.4)$$

where V_A and V_B are the molar volume and ϕ_A and ϕ_B are the molar fractions of A and B, respectively. V_r is the molar volume of the unit cell or the repetitive unit of the polymer, commonly referred as the reference volume [50]. In general terms, the closer the chemical nature of the solvent and solute, the more energetically favorable is their interaction (e.g. an apolar solvent with an apolar solute), thus lowering χ_{AB}; consequently, ΔG_m lowers, favoring the solvent-solute mixture and solvation as well. Oppositely, when the solute-solvent interaction is less favorable, χ_{AB} increases and instead of a mixture, a phase separation or a precipitation is more likely to occur. In solubility terms, gelation is an intermediate point between a solution and a precipitate where the difference in the solute-solvent interactions is small [19]. However, gelation is a kinetic aggregation state and therefore solubility is just a contributing effect.

2.1.4 Organogelation

Organogelation is a specific case of gelation where the gelator is a low molecular weight organic molecule (LMWG) that self-assembles non-covalently to form a fibrillar network (SAFiN). The anisotropy of the fibers allows percolation for a low volume fraction of fibers. Moreover, the high surface-area-to-volume ratio of the fibers allows a large exposure of the fiber facets, and the surface tension reduces the fluidity of the liquid embedded in, thus triggering gelation. Therefore, the main strategies to form organogels have focused on designing LMWGs with functional groups capable of triggering one-dimensional growth to form fibers (e.g. amide groups to form a one-dimensional hydrogen-bonding pattern [20], [24], [51]).

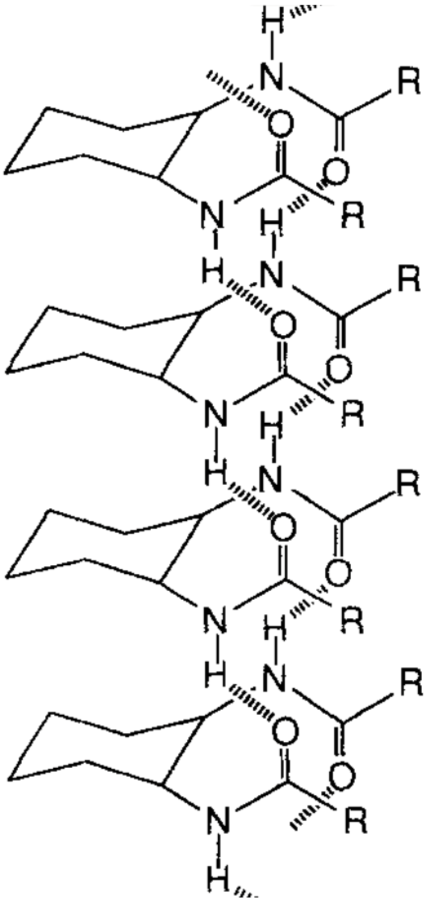

Figure 2.7: A schematic one-dimensional stack of LMWGs via hydrogen bonding. In this example, the fiber grows in the direction of the hydrogen bonding pattern. Reference **[52]**.

Organogels are prepared by heating the LMWG in a solvent until achieving solution, then cooling it down; the solubility of the LMWG then drops and molecules assemble to form SAFiNs. A small amount of LMWG (e.g. 2% wt) dispersed in the liquid can be sufficient to form a gel. Figure 2.8 shows a sequence of time transient AFM images [53], showing organogel formation stages. The authors describe the process as follows: (i) Figure 2.8a shows a solution homogeneously dispersed on a graphene substrate, (ii) in Figure 2.8b, solution starts dewetting from the surface, (iii) Figure 2.8c shows a one-dimensional growth of gel fibers, attributed to the stacking of gelator molecules, and (iv) in Figure 2.8d-f the fibers further aggregate in fiber bundles, which are likely to trap the solvent.

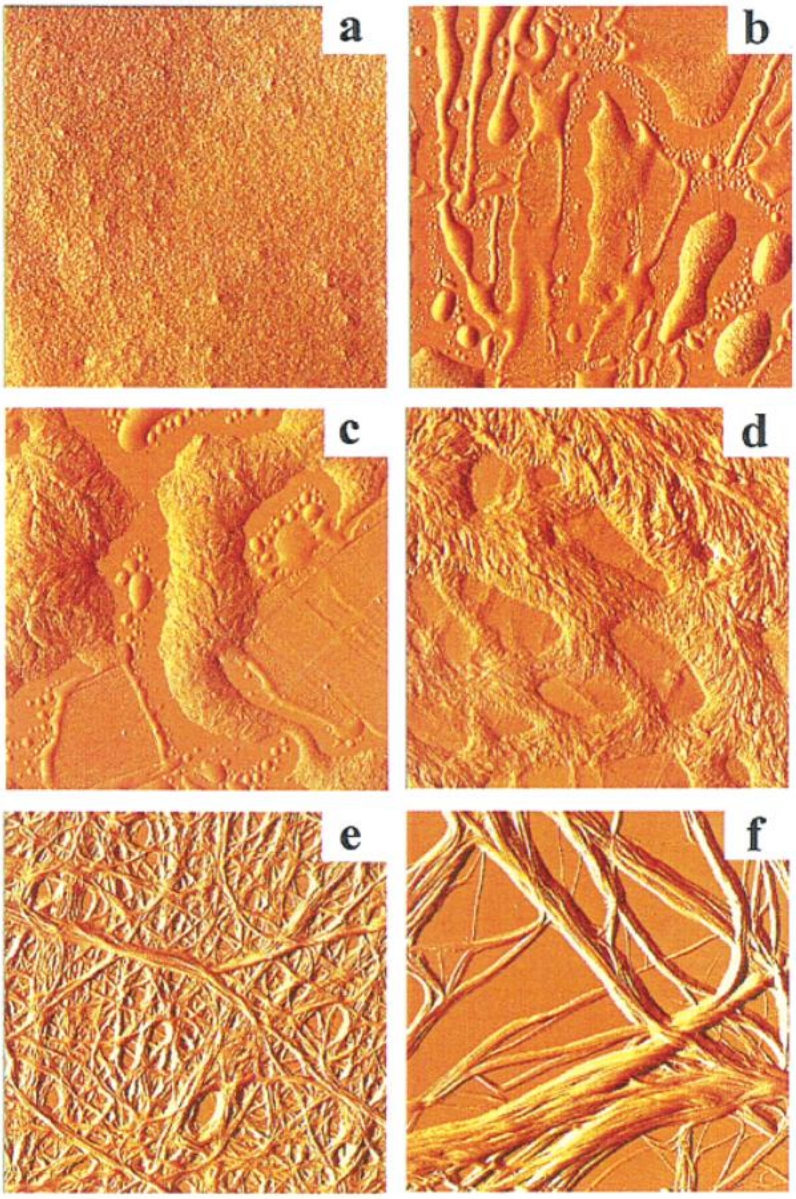

Figure 2.8: Time transient AFM images of the organogel formation of a cholesterol derivative at different times: (a) 0, (b) 10, (c) 15, (d) 18, (e) 21, and (f) 31 min. The scale of all the images is 12x12µm. Reference **[53]**.

The non-covalent aggregation of the gelator molecules makes this type of gels very interesting for industrial applications and basic science knowledge. One of the main challenges for organogelation is that, as for conventional gelation, the solute can form a different aggregation state depending on the solvent [16], [50]–[53]. Knowing beforehand which solvents are going to form a gel for a given LMWG would be highly relevant for designing new LMWGs for specific applications. Therefore, in the next section, we introduce the solvent characterization schemes developed so far to rationalize organogelation.

2.2 Organogelation prediction

As solute-solvent interaction is key for describing gelation, strategies developed over the years have focused on defining solvent-specific parameters in order to establish solvent-LMWG chemical composition gelation trends [7]. Solvent-defining parameters vary depending on the characterization scheme and in this section, we describe a handful of experimental approaches based on physical, thermodynamical or solvatochromic properties. The overall goal is to correlate the chemical structure of the corresponding LMWGs with the parameters of the solvents that form a gel.

2.2.1 Dielectric constant

This solvent characterization scheme represents solvents by their dielectric constant (ε) and aims to correlating the gelation properties of LMWGs with ε. Here we exemplify this strategy with the work of Zinic et. al. [57], who studied gelation of bis(amino acid) oxalylamide gelators (Figure 2.9) with alcohols as solvents.

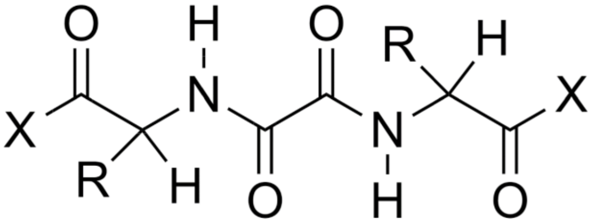

Figure 2.9: Structural formula of bis (amino acid) oxalylamide gelators, where X is a functional group and R and alkyl chain.

In **Figure 2.10**, the authors found an inverse linear relationship between the gel melting temperatures ($\mathbf{T_{gel}}$) and the dielectric constant of (C_1-C_6) n-alcohols and some cyclic and branched (C_3-C_6) alcohols, i.e. the higher ε, the lower $\mathbf{T_{gel}}$. The authors attribute this dependency to the polarity of the alcohol molecule, which governs the thermal stability of the gels: the higher ε, the better the solubility, thus a less stable gel network, corresponding to a smaller melting temperature. Therefore, when alcohol-related interactions dominate the gel stability, we can expect that this correlation applies.

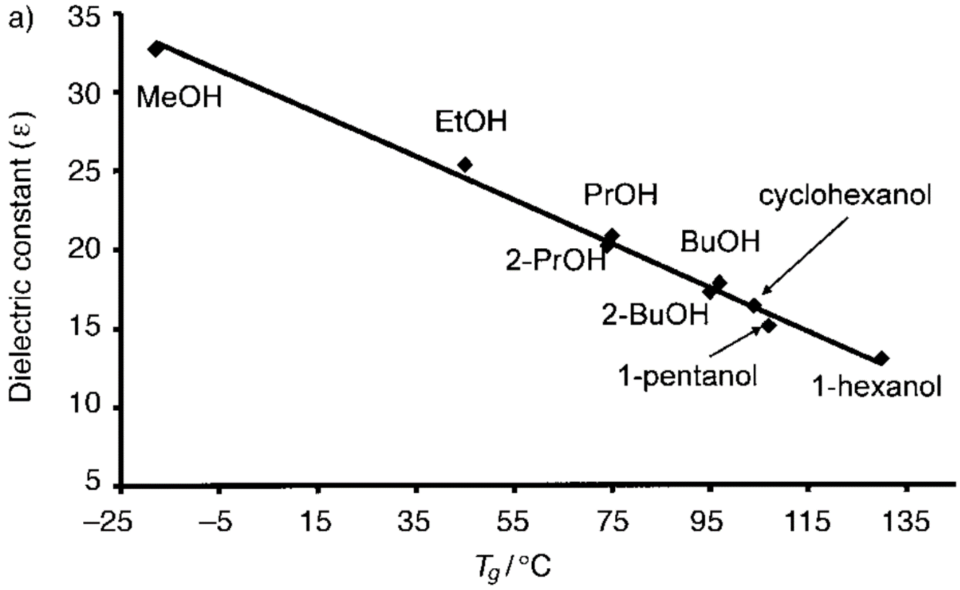

Figure 2.10: Alcohol dielectric constant (ε) vs $\mathbf{T_{gel}}$ linear dependency of the bis(amino acid) oxalylamide gelator with (C_1-C_6) n-alcohols and some cyclic and branched (C3-C6) alcohols. Reference **[57]**.

However, for alcohols with longer alkyl chains, from 1-heptanol to 1-dodecanol, no such correlation is observed. The authors hypothesize that a larger dispersive contribution, due to the longer alkyl chain, also influences the gel stability. Therefore, the dielectric constant scheme could be useful for rationalizing gelation when only polarity dominates gel stability. In other terms, any significant additional effect distorts the correlations and results in poorer predictions.

2.2.2 Reichardt's E_T solvent parameter

This scheme is based on characterizing the solvents polarity spectroscopically using the Dimroth-Reichardt betaine dye [58]:

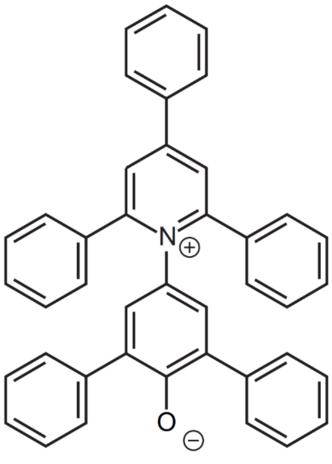

Figure 2.11: Chemical structure of the Dimroth-Reichardt betaine dye. Reference **[58]**.

The wavenumber of the maximum of the longest absorption band of this dye shifts depending on the solvent polarity where this dye is dissolved. The wavenumber of the maximum ($\tilde{\nu}_{max}$) can be converted to an E_T energy value [59]:

$$E_T = hcN_A\tilde{\nu}_{max}; \qquad (2.5)$$

where h is the Planck's constant, c is the speed of light and N_A is the Avogadro number. This solvent-dependent phenomenon is known as the solvatochromic effect and it is due to changes in the solvent-solute interactions, which provoke absorption band wavelength shifts [60], [61]. Smith et. al. correlated E_T values with T_{gel} for a gelator composed of diaminododecane hydrogen-bonded to two dendritic L-lysine-based peptides (see Figure 2.12) [18].

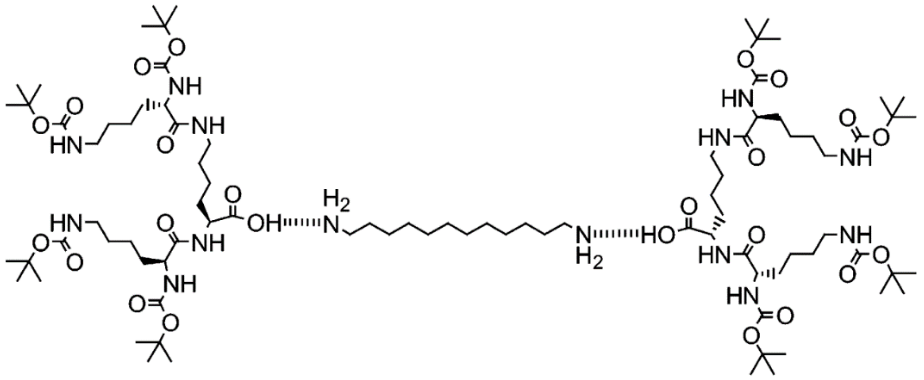

Figure 2.12: Chemical structure of a dendritic gelator unit **[18]**.

An inverse linear relationship was found between T_{gel} and E_T for dipolar and apolar non-hydrogen bond donor solvents, while protic solvents produced no gel, only solutions. This can be understood by the fact that protic solvents disrupt the interaction between diaminododecane and the lysine dendrimer. This description surpasses the dielectric constant characterization of solvents. However, for solvents such as chloroform and 1,2-dichloroethane, the experimental observations contradict the prediction from the model. Therefore, the E_T parameter identifies the solvent-solute interactions as a relevant factor for gelation, but it is far from giving a complete and fully reliable description of the phenomenon.

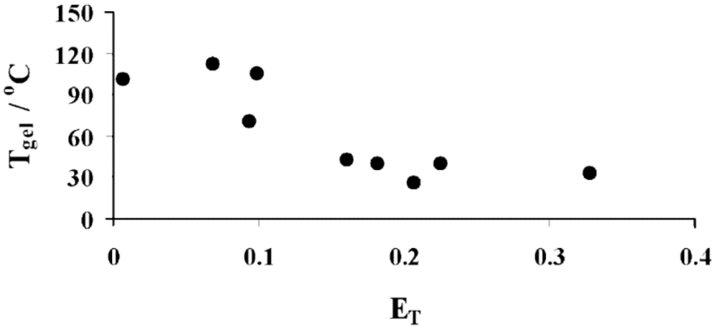

Figure 2.13: Effect of forming the dendritic gels with solvents of different E_T values on their respective gel-sol transition temperature $\mathbf{T_{gel}}$. Reference **[18]**.

2.2.3 Hildebrand solubility parameters

The Hildebrand solubility parameter (δ_t) is a thermodynamic quantity that represents a compound by the square root of its cohesive energy density $\left(\frac{E_t}{V}\right)$:

$$\delta_t = \left(\frac{E_t}{V}\right)^{1/2}, \qquad (2.6)$$

where E_t is the vaporization energy and V is the molar volume [62]. Fräßdorf et. al. used the Hildebrand parameters to rationalize the gel formation temperature T_{gel} for dibenzylidene sorbitol (DBS) in polymeric matrices [19].

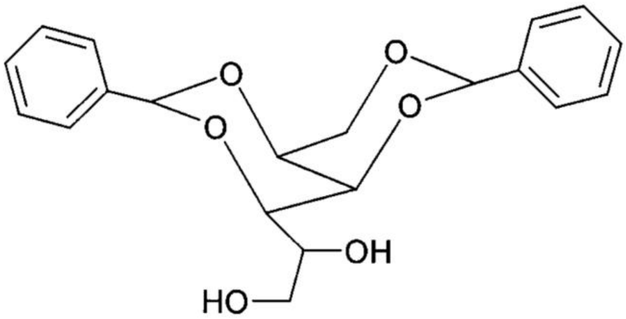

Figure 2.14: Chemical structure of dibenzylidene sorbitol (DBS). Reference **[19]**.

More specifically, the authors derived an equation relating T_{gel} with the difference between the Hildebrand parameter of the polymer matrix (δ_M) and that of DBS (δ_{DBS}):

$$\frac{T_{gel}}{\tilde{T}_{DBS}} = 1 + \frac{(\delta_{DBS} - \delta_M)^2}{\delta_C^2}, \qquad (2.7)$$

where $\tilde{T}_{DBS}$ and δ_C are related to matrix and DBS properties (melting temperature, melting enthalpy and molar volume). Figure 2.15 aims to verify the previous equation by plotting $\frac{T_{gel}}{\tilde{T}_{DBS}}$ against $\frac{(\delta_{DBS}-\delta_M)^2}{\delta_C^2}$, which should show a linear dependency.

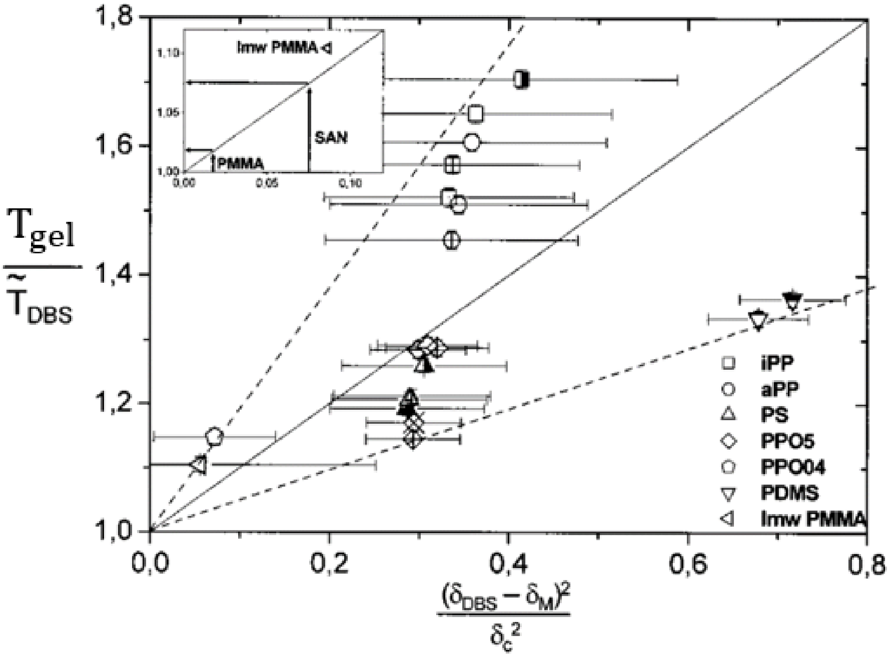

Figure 2.15: Evolution of the gel formation reduced temperature $\left(\frac{T_{gel}}{\tilde{T}_{DBS}}\right)$ against $\left(\frac{(\delta_{DBS}-\delta_M)^2}{\delta_C^2}\right)$ according to Equation (2.7), for dibenzylidene sorbitol (DBS) in polymeric matrices. Reference **[19]**.

The linear correlation between the two terms is weak. In the authors' words, the correlation is weak mainly because of the limited accuracy of the Hildebrand solubility parameter. However, the authors argue that the difference between the Hildebrand solubility parameter of the gelator and that of the polymer matrix is key, i.e., it must be different enough so there is a phase separation enabling the formation of the gel, otherwise it would be a dissolved state; oppositely, if they differ considerably it would trigger a precipitate or a phase separation. Thus, they propose that a small difference in the nature of the cohesive interactions of solvent and solute can trigger the partially dissolved state, that is a gel.

This conclusion can be further extended with the relation between the Flory-Huggins parameter (χ_{AB}) and the Hildebrand solubility parameter [63]–[65]:

$$\chi_{AB} = \frac{v_0}{kT}\left(\delta_{t,A} - \delta_{t,B}\right)^2, \tag{2.8}$$

where v_0 is the molecular volume of the solvent, k the Boltzmann constant, T is the temperature, $\delta_{t,A}$ and $\delta_{t,B}$ are the Hildebrand parameters of the solute and the solvent, respectively. In this scheme, a solute and solvent with very close Hildebrand parameters have a low χ_{AB}, favouring solvation and triggering a dissolved state. Oppositely, the larger the difference between solute and solvent Hildebrand parameters the larger χ_{AB} and the worse the solvation, reaching an insoluble state on the extreme. Thus, as in the authors conclusions, one factor that favours gelation is that solute and solvent have a slight difference in the Hildebrand parameters.

2.2.4 Kamlet-Taft parameters

This method characterizes solvents spectroscopically measuring the wavenumber of the maximum of absorbance of three dyes when dispersed in the solvent: the Dimroth-Reichardt betaine dye ($\tilde{v}_1$), p-nitroaniline ($\tilde{v}_2$) and N,N-dimethyl-p-nitroaniline (NNDN) ($\tilde{v}_3$) [66]–[69].

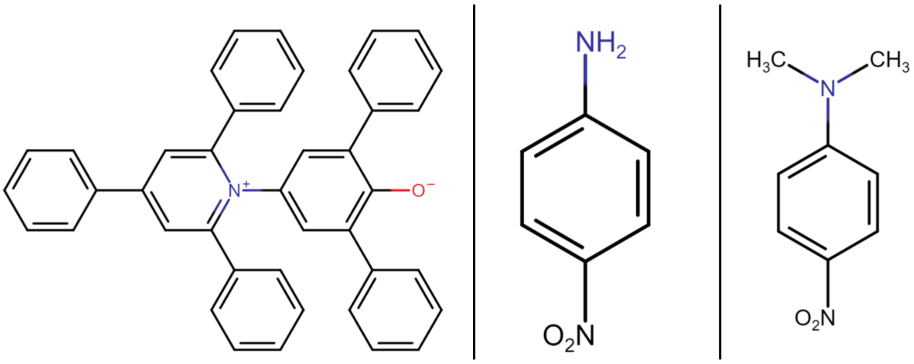

Figure 2.16: Chemical structure of the dyes employed for characterizing a solvent: (left) the Dimroth-Reichardt betaine dye, (center) p-nitroaniline and (right) N,N-dimethyl-p-nitroaniline (NNDN).

Three parameters are defined using the previously measured wavenumbers: a hydrogen bond donor (α), a hydrogen bond acceptor (β), and a polarizability (π*) parameter. These parameters are calculated as [66]:

$$\pi^* = \frac{\tilde{v}_3 - 28.18}{-3.52}; \alpha = \frac{1.318\tilde{v}_3 - 47.7 + \tilde{v}_1}{5.47}; \beta = \frac{0.9841\tilde{v}_3 - 3.49 + \tilde{v}_2}{2.759} \qquad (2.9)$$

This scheme has been tested by Edwards et. al. for studying the gelation of a set of L-lysine bis-urea gelators [20].

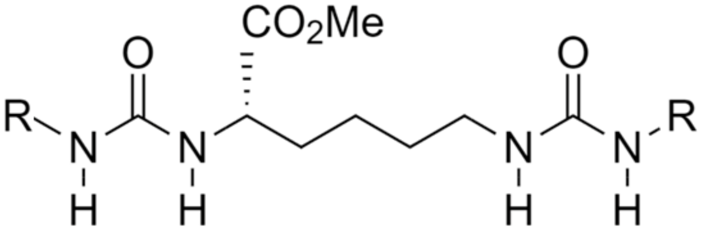

Figure 2.17: Chemical structure of the L-lysine bis-urea gelators, where R is an alkyl chain.

The authors concluded that, for this family of specific gelators: the α parameter determines whether a gelator forms a hydrogen bond network, the β parameter rules the thermal stability of the gel by gelator-gelator interactions, and the π parameter tunes the fiber-fiber and fiber-solvent interactions. Despite the specificity of this analysis, this break down shows the different competing interactions in gel formation: gelator-gelator (α and β), and fiber-solvent and fiber-fiber (π*).

2.2.5 Hansen solubility parameters

In 1967, Charles M. Hansen presented a three-dimensional solubility parameter when investigating polymer solubility [70], giving rise to the Hansen Solubility Parameters (HSP) description [71], [72]. This scheme extends the thermodynamic Hildebrand parameter approach (δ_t) by decomposing this parameter in three independent parameters to correlate dispersive (δ_d), polar (δ_p) and hydrogen bond (δ_h) interactions separately: $\delta_t^2 = \delta_d^2 + \delta_p^2 + \delta_h^2$.

$$\delta_t = \left(\frac{E_t}{V}\right)^{1/2} ;\ \delta_d = \left(\frac{E_d}{V}\right)^{1/2} ;\ \delta_p = \left(\frac{E_p}{V}\right)^{1/2} ;\ \delta_h = \left(\frac{E_h}{V}\right)^{1/2} \qquad (2.10)$$

where $\frac{E_d}{V}$, $\frac{E_p}{V}$ and $\frac{E_h}{V}$ are the dispersive, polar and hydrogen bond components of the total cohesive energy density $\left(\frac{E_t}{V}\right)$, respectively. Each contribution is assigned to a solvent using specific methods.

δ_d is obtained with the procedure of Blanks and Prausnitz which uses the evolution of the dispersion cohesive energy (E_d), or the dispersion cohesive energy density (c) as a function of the molar volume (V) for aliphatic, cycloaliphatic or aromatic compounds (see Figure 2.18) [73], [74].

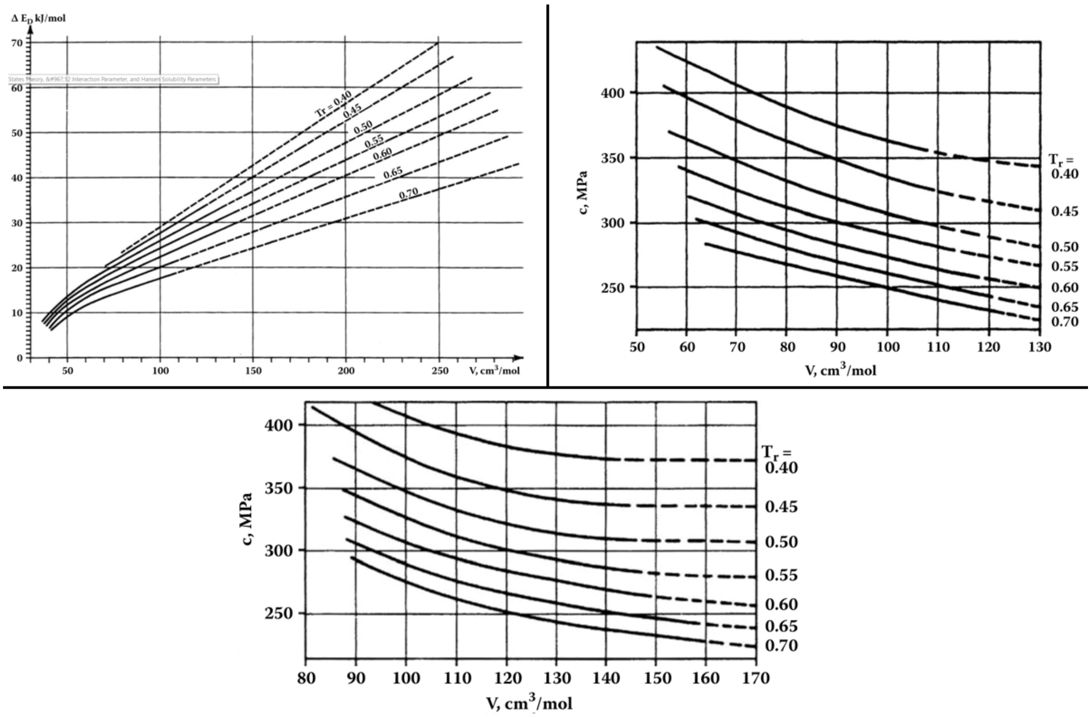

Figure 2.18: Experimental plots correlating the molar volume with, top-left: the energy of vaporization of aliphatic compounds, top-right: the cohesive energy density of cycloaliphatic compounds and bottom: the cohesive energy density of aromatic compounds at different reduced temperatures ($\mathbf{T_r = T/T_c}$), where T=298.15K and $\mathbf{T_c}$ is the critical temperature of the solvent **[74]**.

Let us mention that for polar solvents the group contribution method is recommended for determining δ_d, which uses preestablished reference tables where each functional group has an associated dispersion component ($\mathrm{F_d}$). δ_d is calculated as the sum of all the existing $\mathrm{F_d}$ averaged by the molar volume (V): $\delta_d = \frac{\sum \mathrm{F_d}}{\mathrm{V}}$ [74]–[78].

δ_p is calculated by the Hansen and Beerbower approach which is based on the dipole moment (μ) and the molar volume (V) of the compound [79]: $\delta_p = \frac{37.4\mu}{V^{1/2}}$.

δ_h is calculated as the difference between δ_t and its other components: $\delta_h = \sqrt{\delta_t^2 - \delta_d^2 - \delta_p^2}$.

With this solvent parametrization scheme, it is possible to make a 3D plot displaying each solvent as a point with its HSP terms as coordinates. For each point, it can be indicated whether the solute forms a solution, gel or precipitate in that solvent. This representation is the Hansen solubility space, where points with similar solubility tend to form regions. In the Hansen space, we can thus find: (i) a region where the solute is fully soluble, thus forming a solvated state, (ii) a partial solubility region, the domain of the gel, and (iii) an insoluble region where the solute forms a precipitate. The solubility and gelation regions are represented as spheres for the practicality of plotting and visualizing data. These spheres are named solubility and gelation spheres, respectively; the outer region is the insoluble space (see Figure 2.19).

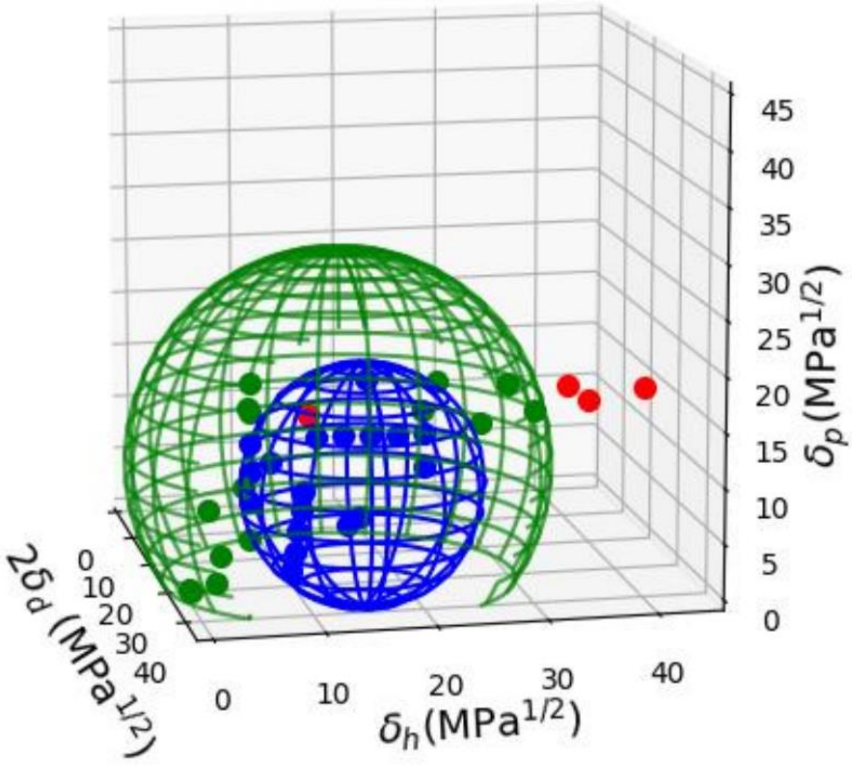

Figure 2.19: Illustrative example of the Hansen solubility space for one of the LMWG studied in this work. Blue, green and red dots represent solvents which form a solution, a gel and a precipitate with the solute, respectively. The blue and green spheres are the solubility and gelation spheres, respectively. Reference **[80]**.

Analogous to the relation of the Flory-Huggins parameter with the Hildebrand parameter [63]–[65], the Flory-Huggins parameter χ_{AB} is related to the HSP parameters by [71]:

$$\chi_{AB} = \frac{v_0}{kT}\left[4\left(\delta_{d,A} - \delta_{d,B}\right)^2 + \left(\delta_{p,A} - \delta_{p,B}\right)^2 + \left(\delta_{h,A} - \delta_{h,B}\right)^2\right] \qquad (2.11)$$

v_0 is the molecular volume of the solvent, k the Boltzmann constant, T is the temperature, $\delta_{d,A}$, $\delta_{p,A}$ and $\delta_{h,A}$ are the HSP parameters of the solute and $\delta_{d,B}$, $\delta_{p,B}$ and $\delta_{h,B}$ are the HSP parameters of the solvent. Therefore, when solute and solvent HSP parameters are very close, χ_{AB} is small, thus maximizing solubility. Hence, the solubility sphere represents the region of space where the Hansen parameters of the solute and solvent are similar, while the insoluble region corresponds to a region where the Hansen parameters of the solute and solvent are different. The gel sphere corresponds to the intermediate case.

In 2011, Bouteiller et. al. employed for the first time the HSP scheme for rationalizing organogelation, determining the solubility and gelation sphere for 8 LMWGs with solubility data available in the literature [12]. Based on the size and location of the solubility and gelation spheres in the Hansen space, the authors can now predict the aggregation state of LMWGs when dispersed in new solvents (see Figure 2.20).

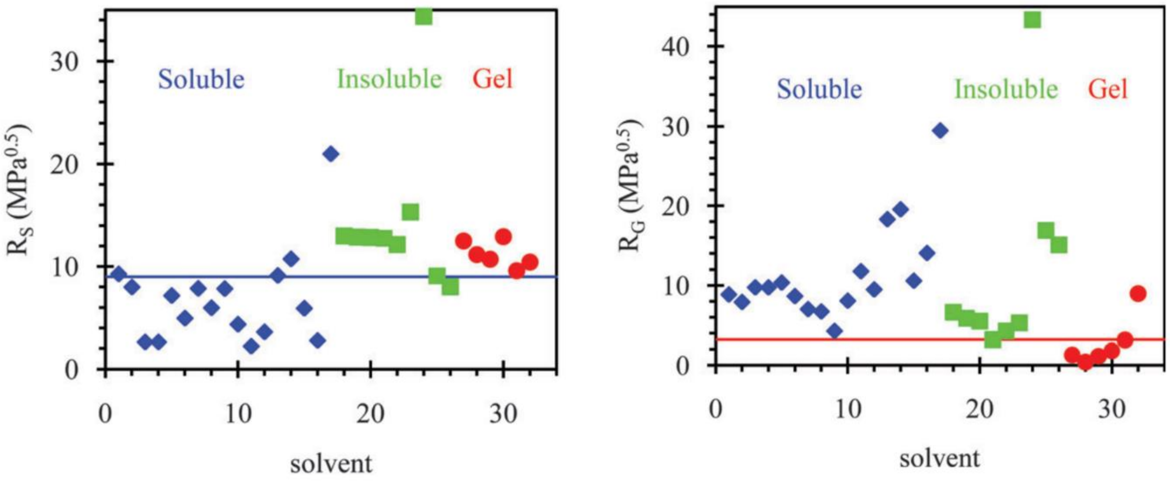

Figure 2.20: Distance between each solvent and the centre of the solubility sphere (left) or of the gelation sphere (right) in the Hansen space for a LMWG, a methyl 4,6-O-benzylidene monosaccharide derivative. The lines mark the radius of the corresponding sphere. Reference **[12]**.

Other studies have followed this parametrization scheme correlating organogelation and LMWG chemical structure [80]–[86]. For example, Ando et. al. [87] rationalized the gelation properties of a series of poly(aryl ether) dendron derivatives (Figure 2.21) employing the HSP scheme.

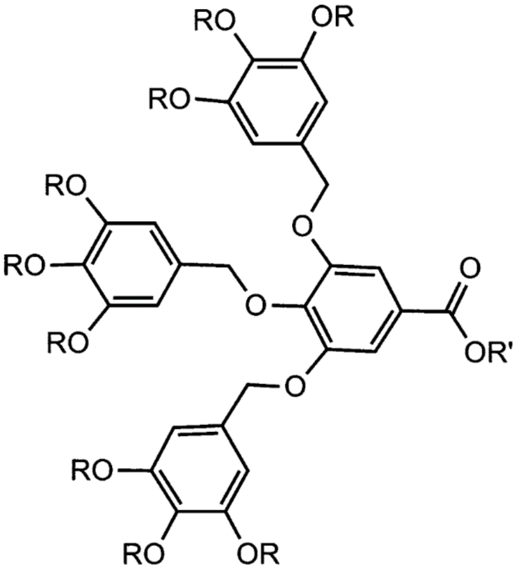

Figure 2.21: Chemical structure of the poly(aryl ether) dendron derivatives where R is an alkyl chain and R' is either a hydrogen atom or a methyl group. Reference **[87]**.

The authors simplified the interpretation of the gelation results by defining δ_a: $\delta_a^2 = \delta_p^2 + \delta_h^2$, and performing a 1-dimensional representation of δ_a showing the gel, soluble, and insoluble characterization of these dendron derivatives (Figure 2.22). Of course, the simplification leads to a coarsening of the description, compared to the use of the 3 HSP parameters.

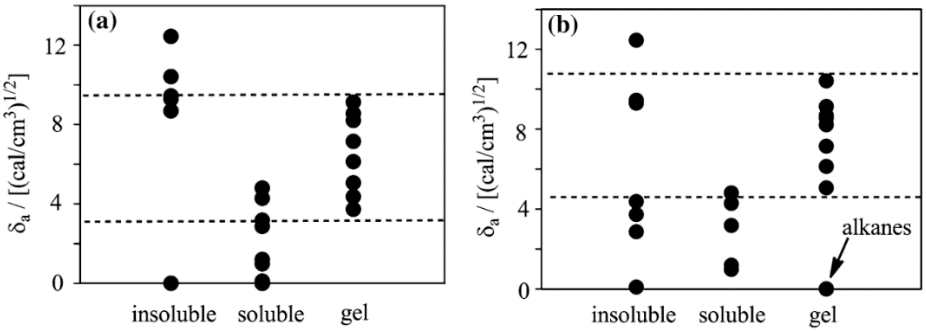

Figure 2.22: 1-dimensional representation of $\boldsymbol{\delta_a}$ displaying the gel, soluble and insoluble characterization of a dendron derivative (see **Figure 2.21**) with alkyl chains R of 12 carbon atoms and a (left) methyl group or (right) hydrogen atom R' attached to the carboxylic group. Gelation is favourable to occur in the $\boldsymbol{\delta_a}$ values comprised between the top and bottom dashed lines. Reference **[87]**.

2.2.6 Machine learning

We want to mention a recent work by Van Lommel et. al. [88] using a machine learning approach to rationalize the organogelation of urea-based gelators.

The machine learning field is spurring increasing attention every year and its wide application is a reality nowadays [89], [90]. Machine learning has also reached the field of physical chemistry and its application augurs a new big leap for computational chemistry [91]–[95]. In this case, Van Lommel et. al. [88] used what is called a "supervised learning" model.

The supervised learning model is based on training the machine with labeled examples which serve as the reference for predicting the output value for a new unknown case. In this case, they used a training set comprised of examples where it is known whether a certain LMWG forms a precipitate, gel or solution for a given solvent. Therefore, the machine can predict whether a LMWG will form a gel, precipitate or a solution when dispersed in a new solvent.

The authors labeled the LMWG-solvent pairs with features coming from previous molecular dynamics simulations:

- Relative solvent accessible surface area (rSASA). It is defined as the time-averaged total area of a molecule that is accessible to the solvent during the simulation time divided by its maximum value.
- Relative end-to-end distance (rH). It defines the shape of a single gelator molecule.
- Hydrogen bonding percentage (HB%). It quantifies the percentage of hydrogen bonds connecting the gelator molecules.
- Shape factor (F). It quantifies the shape of the aggregates.

The machine establishes a relation between these features and the expected output by optimizing a series of tunable parameters. Depending on how this procedure is done, there are different possible algorithms in literature [96]. The authors have chosen and validated the decision tree (DT) and the artificial neural network models (ANN). Figure 2.23 compares the prediction of the gelation ability for one of the urea-based LMWGs against the experimental observations for different solvents.

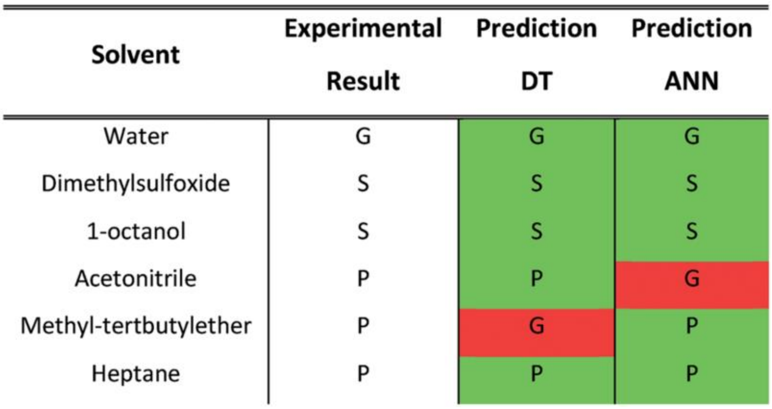

Solvent	Experimental Result	Prediction DT	Prediction ANN
Water	G	G	G
Dimethylsulfoxide	S	S	S
1-octanol	S	S	S
Acetonitrile	P	P	G
Methyl-tertbutylether	P	G	P
Heptane	P	P	P

Figure 2.23: Comparison of the gelation ability of one of the studied LMWGs in different solvents against the prediction with the decision tree (DT) or the artificial

neural network (ANN) models. G, S and P stands for gel, soluble and precipitate, respectively. Reference [88].

The success of this approach is reflected in the correct prediction of both models, except for one case. The main drawbacks of this approach comprise the high specificity of this analysis, which limits a broader application to other chemical systems and its high computational cost, arising from the time-consuming molecular dynamics simulations to obtain the labels.

In this thesis we study the correlation between the LMWG chemical structure and organogelation using a combined experimental and modelling approach. From the experimental part, the LMWGs are characterized structurally by powder X-ray diffraction and their gelation capability by Hansen Solubility Parameters. This information serves as the reference for the modelling where we deduce the crystal morphology of the LMWG gel fibers, characterizing their structure (i.e. molecular packing, surface chemical composition) and their gelation features by computing the surface energy parameters of the surfaces displayed on the fibers.

Chapter 3. **Methodology**

This chapter details the methodology developed for modelling the supramolecular structure within LMWG crystalline fibers and the interaction of the dominant facets with solvents. This approach is structured in three parts: (i) determining the crystal structure of the LMWG, (ii) deducing the microscopic morphology of the LMWG fibers and (iii) characterizing the dominant fiber facets by surface energy solubility criteria.

This procedure intertwines with the experimental efforts performed in parallel in the groups of Prof. Laurent Bouteiller (*Sorbonne Université*) and Prof. Pierre-Antoine Albouy (*Université Paris-Sud*) where gelation experiments were performed and gel fibers were synthesized and characterized by Hansen solubility parameters, Infrared spectroscopy (IR) and X-ray diffraction (XRD). Therefore, along this chapter, the methodology describes the modelling work jointly with experimental results.

First, we set the general framework for the molecular modelling of organic materials and the prediction of crystal structures. Then, we describe the technical details of the procedures at the end of this chapter, in the "Protocols" section, for the reader interested in reproducing this procedure with the Materials Studio software.

3.1 Framework

Molecular Mechanics (MM) and Molecular Dynamics (MD) are most useful approaches for performing potential energy calculations, geometry optimizations, and calculating dynamics properties of chemical systems [97]–[100]. In this work, the main modelling effort has been carried out within the Materials Studio software [101]. This software has several modules specialized for different tasks.

The MM and MD approaches are rooted in classical mechanics and consider that molecules are a collection of hard balls (atoms) connected by springs (atom bonds). This consideration leads to evaluate the potential energy of a molecular system as a sum of independent parametrizable bonded and non-bonded terms. Bonded terms account for energy changes of bonds, when e.g. stretching, bending or rotating around bonds. Non-bonded terms account for energy changes of long-range atom interactions that do not form a bond such as electrostatic, van-der-Waals or H-bonding interactions. A specific combination of terms and parameters, envisioned for a specific application, is called a forcefield.

Molecular Mechanics allows geometry optimization. It is based on minimizing the internal forces of the system and finding the potential energy minimum closest to the initial structure. The minimization process is exemplified in Figure 3.1 with a hypothetical potential energy curve of a formaldehyde molecule where initially, the carbon-oxygen bond distance is far from equilibrium (x_1) and, by a force minimization algorithm, the internal forces are minimized reaching the equilibrium configuration (x_5).

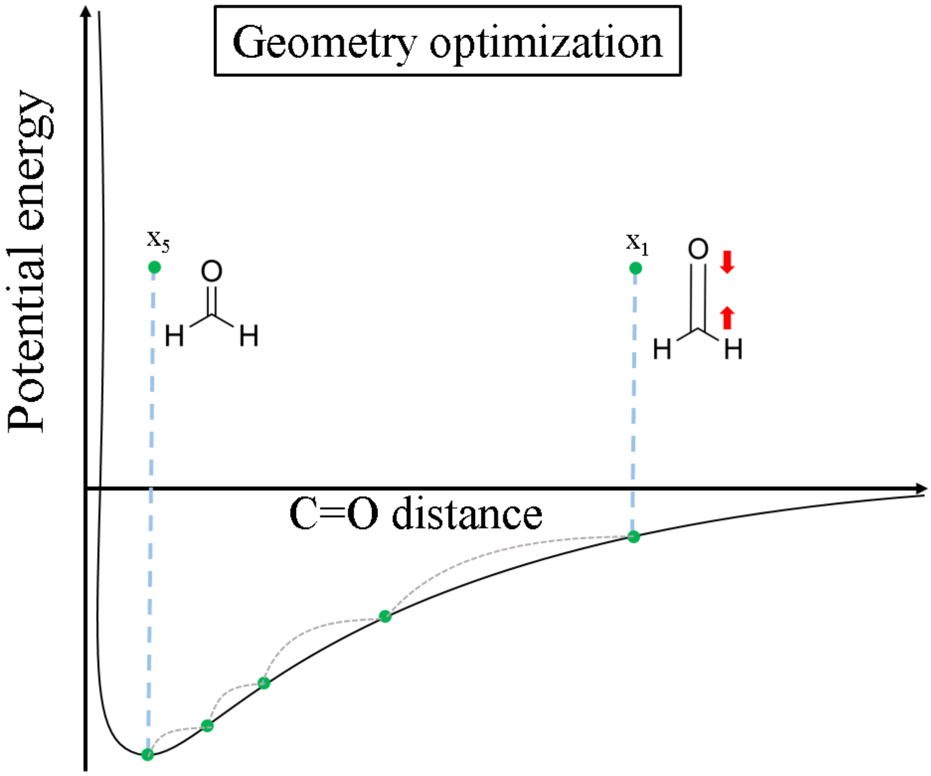

Figure 3.1: Example of the geometry optimization procedure: the forces of an initial chemical structure not in equilibrium (x_1) are reduced until reaching the equilibrium configuration (x_5), which corresponds to the structure of minimum potential energy.

A MM simulation generates only one structure, the local minimum located in the potential energy valley of the guess structure, while a MD simulation generates many structures when exploring the bottom and slopes of several potential energy valleys. A MD approach [100], [102], [103] is based on characterizing how the positions and velocities of the particles of a system change with time. This is achieved by integrating the second law of Newton (F=ma) for all the particles. For example, Equation (3.1) describes the motion of a particle with mass m_i along the coordinates x_i under the force $F(x_i)$ for a given time t:

$$x_i = \iint_t \frac{F(x_i)}{m_i} dt^2 \tag{3.1}$$

This integral is evaluated numerically by dividing the total time t in small time steps (δt) where, for each step, the total force is computed on each particle assuming that, in that step, the force is constant. Therefore, from the integration of the force, one obtains the positions and velocities of the particles for the next time step δ_t. Many algorithms have emerged over the years to perform the integration. The common grounds between them consider that the positions (r), velocities (v) and accelerations (a) can be approximated as Taylor series expansion:

$$r(t+\delta t) = r(t) + \delta t v(t) + \frac{1}{2}\delta t^2 a(t) + \frac{1}{6}\delta t^3 b(t) + \frac{1}{24}\delta t^4 c(t) + \cdots \tag{3.2}$$

$$v(t+\delta t) = v(t) + \delta t a(t) + \frac{1}{2}\delta t^2 b(t) + \frac{1}{6}\delta t^3 c(t) + \cdots \tag{3.3}$$

$$a(t+\delta t) = a(t) + \delta t b(t) + \frac{1}{2}\delta t^2 c(t) + \cdots \tag{3.4}$$

where b and c are the third and fourth derivative of r with respect to t, respectively. In order to simulate the chemical systems, some constraints must be used, e.g., keep the temperature (T), pressure (P) and number of particles (N) constant for modelling chemical substances at room temperature. Other physical quantities can also be fixed such as the volume (V) or the total energy (E). Therefore, from all different combinations of constraints, here we show the three most common sets of constrains, dubbed in statistical mechanics as ensembles:

- NVT. The number of particles (N), volume (V), and temperature (T) are constant. As the collisions between particles change the temperature of the system, T is regulated via a thermostat which controls the temperature variations. This ensemble is also known as the canonical ensemble.

- NVE. The number of particles (N), volume (V), and energy (E) are constant. The kinetic and potential energy (PE) is conserved without any control over T or P. This ensemble is also known as the microcanonical ensemble.

- NPT. The number of particles (N), pressure (P) and temperature (T) are constant. As the collisions between the particles change the temperature and pressure, these quantities are regulated by a thermostat and a barostat, respectively.

In this work we use the Dreiding forcefield. This forcefield has been conceived for "predicting structures and dynamics of organic, biological, and main-group inorganic molecules" [104]. The total potential energy of the system (E) is evaluated as follows:

$$\mathrm{E} = \mathrm{E}_{\mathrm{bond}} + \mathrm{E}_{\mathrm{non-bond}} \tag{3.5}$$

$$\mathrm{E}_{\mathrm{bond}} = \mathrm{E}_{\mathrm{B}} + \mathrm{E}_{\mathrm{A}} + \mathrm{E}_{\mathrm{T}} + \mathrm{E}_{\mathrm{I}} \tag{3.6}$$

$$\mathrm{E}_{non-bond} = \mathrm{E}_{\mathrm{vdw}} + \mathrm{E}_{\mathrm{Q}} + \mathrm{E}_{\mathrm{hb}} \tag{3.7}$$

where E_B, E_A, E_T and E_I are the bond stretch, bond angle-bend, dihedral angle torsion and inversion contributions to the bonded term. E_{vdw}, E_Q and E_{hb} are the van der Waals, electrostatic and hydrogen-bonding contributions to the non-bonded term.

When characterizing the dominant fiber facets by surface energy solubility criteria, we will refer to a key feature intrinsic of the Dreiding forcefield: it splits the potential energy in dispersive, polar and H-bonding contributions. This characteristic allows us to compare the theoretical and experimental dispersive, polar and H-bonding contributions of the dominant facets of the gel fibers. However, the Dreiding forcefield does not assign partial atomic charges to the chemical structure. Therefore, unless specified explicitly, we use the PCFF forcefield charges, which is a common procedure in this type of modelling [105]–[107].

The Dreiding forcefield has been widely used for modelling organic matter [108]–[114]. However, it is known to systematically underestimate the van der Waals interactions of hydrogen atoms. Therefore, we tuned the description of these interactions in the forcefield thanks to a collaboration with co-workers of our laboratory in University of Mons (Quentin Duez and Sébastien Hoyas). We tested this modification with 38 molecular crystals showing van der Waals and hydrogen bonding interactions (see Annex).

Figure 3.2 displays the experimental vs theoretical densities of the compounds treated with the 'classical' and modified versions of the Dreiding forcefield. Those two forcefields are compared after performing a geometry optimization of the compounds and after performing a 1ns NPT Molecular Dynamics at 298K. For each forcefield, we drew a linear regression line. The solid black line represents the ideal correlation between theory and experiment. The larger the regression line deviation, the poorer the description of the organic crystals. The data show that the modified version systematically outperforms the 'classical' Dreiding when performing Molecular Dynamics and geometry optimizations, as the slope of the linear regression gets closer to the unity value. Therefore, we used the modified version throughout all the modelling.

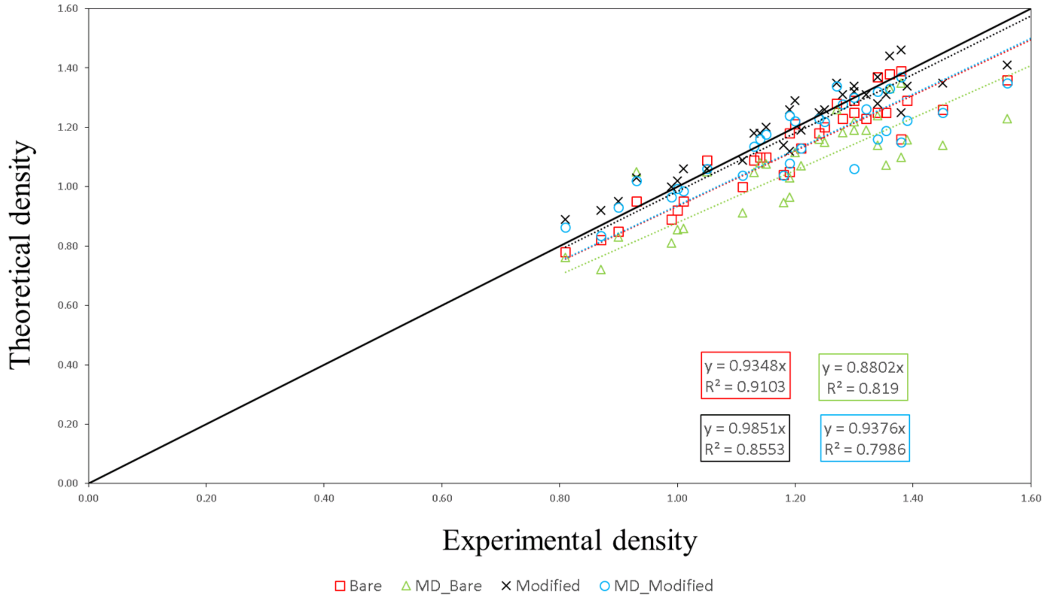

Figure 3.2: Theoretical densities compared to experimental densities for 38 compounds. Red squares and black crosses correspond to theoretical densities obtained by optimizing the crystal geometry by Dreiding and the modified Dreiding, respectively. Green triangles and blue circles correspond to the theoretical densities obtained by molecular dynamics simulations by Dreiding and the modified Dreiding, respectively.

3.2 Crystal structure determination

The experimental characterization by powder X-ray diffraction (XRD) of the gel fibers show that they have a crystalline character. Therefore, we decided to study the crystal structure and the molecular packing of the LMWG in the gel fibers. This procedure relies on the Polymorph and Reflex modules of Materials Studio and the indexation of the experimental powder XRD pattern.

From the modelling part, we used the Predictor function of the Polymorph module, which proposes potential stable polymorphs for a given compound. This function generates thousands of possible crystals, performs a geometry optimization, and suppresses the duplicates. In a general sense, this strategy follows the typical two-step crystal structure prediction (CSP): (i) generate possible stable polymorphs using a sampling algorithm that explores the conformational landscape of the organic crystal. Then, (ii) optimize the output crystals and rank them by an energy criterion [115]–[127].

The Predictor function, among the diverse set present in literature [128]–[135], uses the Simulated Annealing algorithm due to its effectiveness at "finding minima of large and rugged landscapes" [136], as is the case for organic crystals, which arises from the large number of degrees of freedom [137]–[140].

Given a trial space group and the chemical structure of the desired compound, the algorithm goes through the 'packing' stage, where it generates trial structures varying molecular orientations, positions and cell parameters randomly. This protocol aims to generate as many stable polymorphs as possible. However, due to the random search nature of the algorithm, several attempts may be necessary for finding all possible polymorphs, especially if the number of degrees of freedom is large and the landscape is rugged. After this Packing step, the geometry and cell parameters of the generated polymorphs are optimized. Finally, a clustering procedure is carried out to remove identical polymorphs using the radial distribution function which characterizes polymorphs by their atom distribution. The output is a collection of crystal structures ranked by potential energy.

As mentioned above, the Predictor function needs a trial space group, which is generally not known for the compound under consideration. The ten most common organic crystal space groups (in decreasing frequency) are: $P_{2_1/c}$, P_{-1} , $P_{2_12_12_1}$, $C_{2/c}$, P_{2_1}, P_{bca}, P_{nma}, P_{na2_1}, C_c, P_1 [141]. When there is no information about the space group, a blind guess can be done, starting from the most common space groups. However, this approach is very time-consuming. In this study, we could benefit from the experimental efforts of indexing the XRD pattern of the gel fibers, which provides a guess of the crystal cell parameters and space group.

After running the Predictor protocol, we have a collection of crystals that must be filtered to choose a candidate for the molecular packing in the gel fibers. In the CSP context, an energy criterion ranking is usually employed, where structures within less than 20kJ·mol^{-1} above the most stable structure are retained. Here, thanks to the indexing of the experimental powder XRD patterns, we further filtered the crystals based on cell parameters within 1Å from the guessed ones.

The cell parameters of the crystal candidates are then fitted to the guessed ones and the internal geometry of the unit cell (i.e., the position of the molecules and their internal geometry) is relaxed by MM while keeping the cell parameters fixed. Then, a Rietveld refinement coupled with an energy criterion is applied. The Rietveld refinement [142], [143] computes the intensity of diffraction peaks based on the atomic positions within the cell. Therefore, it tries to fit the crystal packing to an XRD pattern by varying structural quantities (unit cell, atom position, atomic occupancy) and the fitting profile (zero, scale, peak shape). This procedure alone would change significantly the molecular packing, bond lengths, etc. However, the inclusion of an energetic criterion prevents unrealistic and too large deformations. The balance between those constraints is achieved by minimizing the P_{comb} parameter, defined as:

$$R_{comb} = (1 - w)R_{wp} + wR_{energy} \qquad (3.8)$$

R_{wp} accounts for the difference between the experimental and simulated XRD patterns and R_{energy} accounts for the difference of potential energy between the current structure and its potential energy minimum, w is the weight assigned to each contribution. Therefore, the difference between the experimental and simulated XRD is minimized while keeping the structure within its potential energy well. A weight of 50% for both parameters has provided us successful results all over the work.

3.2.1 Validation of the crystal determination procedure

We validated the methodology described above by predicting the organization of a gelator for which: (i) the single-crystal structure is known and (ii) the molecular packing of the single-crystal is maintained in the gel fibers. The gelator is from the Bisamide family (Chapter 4) and named BiC4 from here on (Figure 3.3).

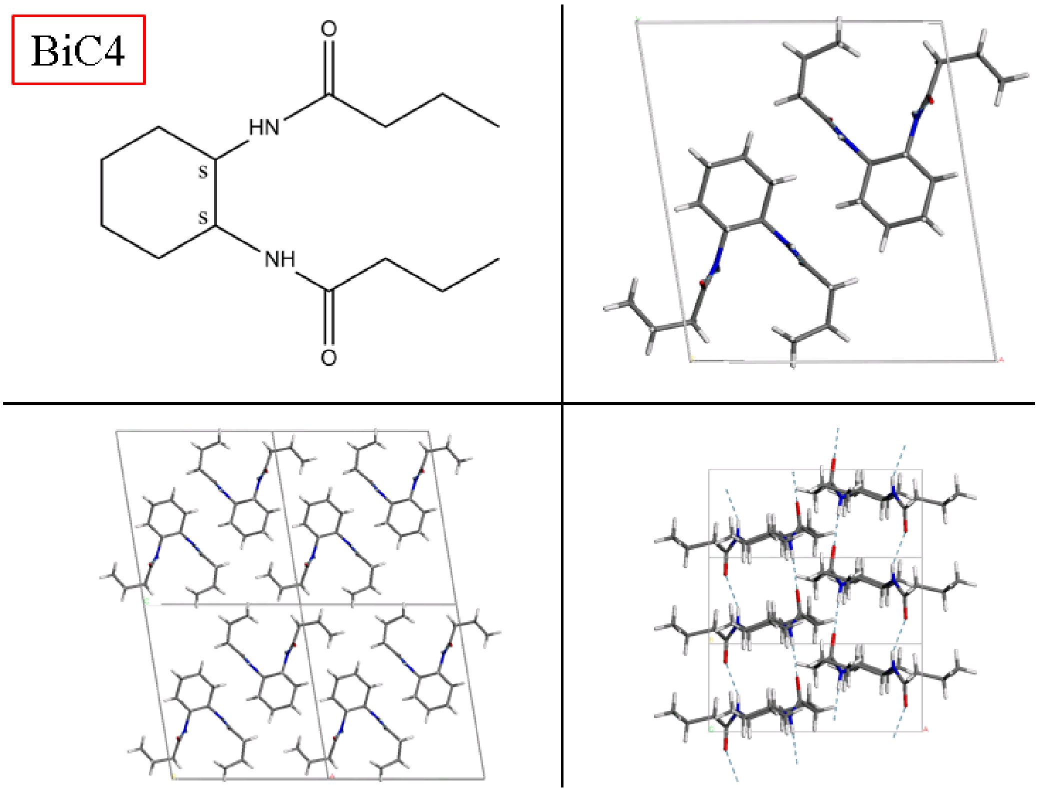

Figure 3.3: BiC4 single crystal. Top left panel: the chemical structure, top right panel: the unit cell, bottom left panel: the molecular packing and bottom right panel: a lateral view displaying the hydrogen bonding pattern (dashed lines).

The single crystal structure obtained experimentally [24] is characterized by a monoclinic unit cell with a $P2_1$ space group, where the BiC4 molecules are aligned in a row in an antiparallel fashion with both alkyl chains oriented towards the same side (e.g. the top molecule of the top right panel of Figure 3.3 has both alkyl chains oriented to the right. In the other molecule, both alkyl chains are oriented to the left). Cohesive interactions mainly comprise van der Waals interactions between alkyl chains and hydrogen-bonding between the amide groups, with distances of ~2.0Å between the oxygen atom of one molecule and the amide hydrogen atom of a neighboring molecule.

Figure 3.4 displays a comparison between the XRD powder pattern simulated from the experimental single crystal structure and the experimental pattern of the gel fibers. Both patterns match in the small angle region (5-12°), which corresponds to the cell parameters of the crystal, while there is a small constant shift of +0.3° from 12° on, which is related to the molecular packing.

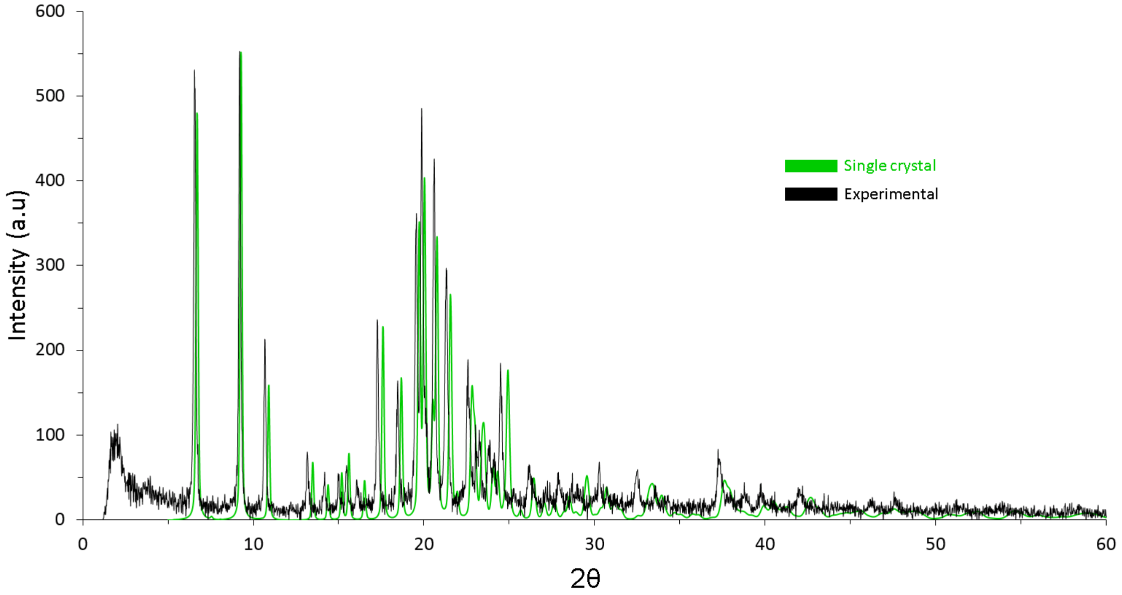

Figure 3.4: Simulated powder pattern from the single-crystal structure (green) vs experimental XRD pattern of the gel fibers (black). The experimental XRD has been measured by Danilo Nunes and colleagues in Paris.

This small shift is attributed to the slightly denser molecular packing (4.2%) of the single crystal with respect to the gel fibers. Table 3-1 compares the cell parameters and volume of the single crystal structure against the indexed cell parameters by our experimental partners in Paris. The slight difference in volume does not affect the molecular packing configuration, as the same diffraction peaks appear in both diffraction patterns, ensuring that the molecular packing is kept.

Table 3-1: Comparison of the cell parameters and volume of the BiC4 single crystal from literature **[24]** and the indexed values from the measurements in Paris.

BiC4	a (Å)	b (Å)	c (Å)	α (°)	β (°)	γ (°)	Volume ($Å^3$)
Single crystal	11.78	4.78	13.25	90	99.18	90	735.81
Indexed	11.91	4.81	13.55	90	98.33	90	768.41

With these experimental data as a basis for validation, we performed the prediction of the crystal structure of BiC4 using as only information its chemical structure and the $P2_1$ space group. Figure 3.5 displays the thousands of BiC4 polymorphs generated. Generally, the denser the crystal and the more negative the lattice energy, the more stable the polymorph.

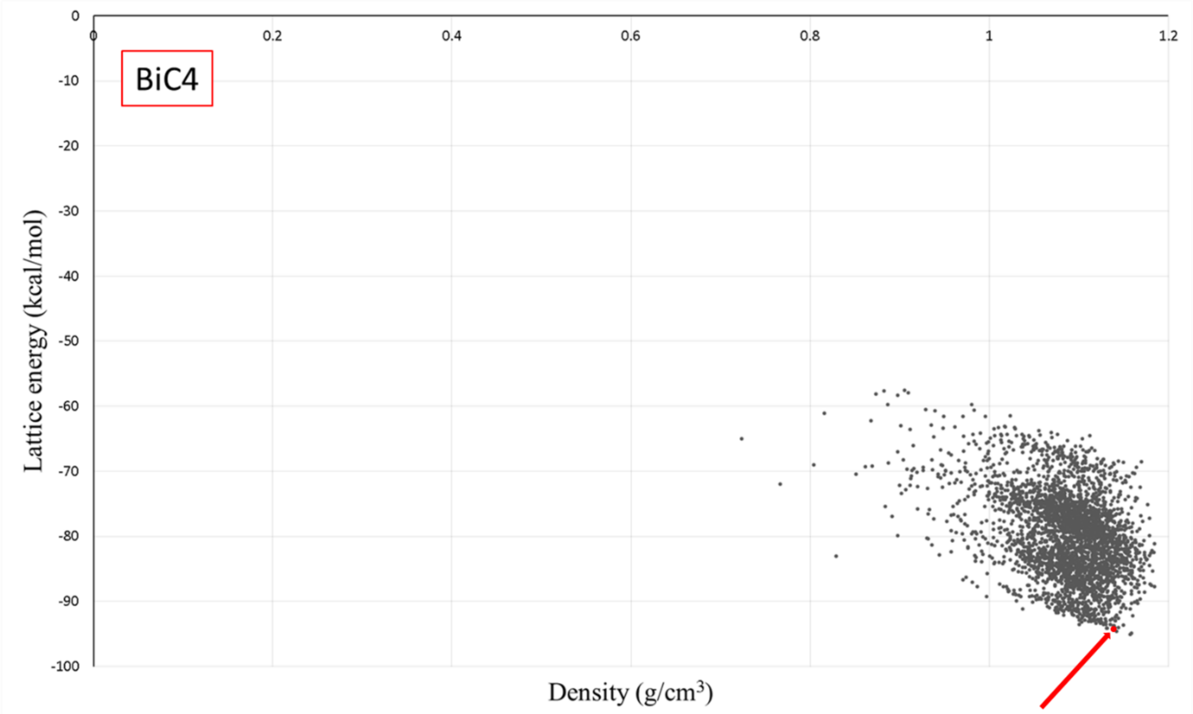

Figure 3.5: The generated BiC4 polymorphs. The density of the polymorphs is plotted against their lattice energies. The red arrow points to the red dot, which is the polymorph that we found matching the indexed cell parameters.

Within the outcome of this procedure, only one candidate is found with cell parameters within 1Å from the indexed ones. It has the fourth more negative lattice energy and its molecular packing is shown in Figure 3.6.

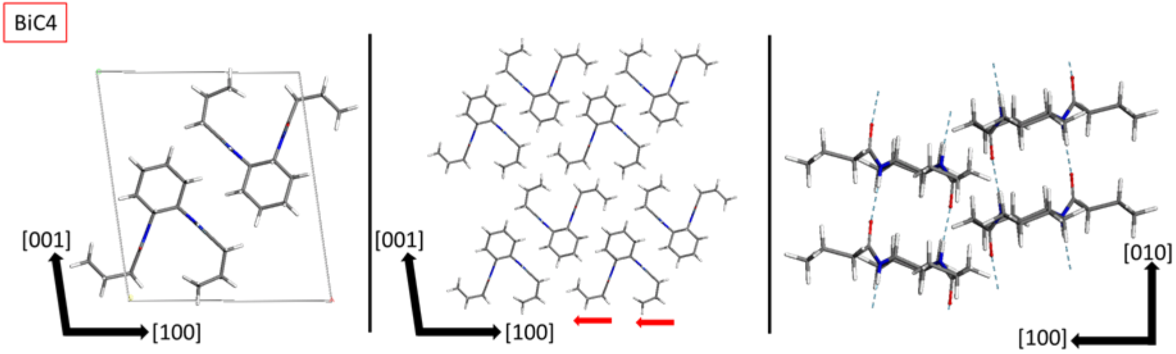

Figure 3.6: Predicted BiC4 molecular packing. Left panel: the unit cell, center panel: the molecular packing and right panel: a lateral view showing the hydrogen-bonding pattern.

This prediction shows a unidirectional hydrogen-bond pattern along the [010] direction through the two amide groups and both alkyl chains oriented to the same side, as in the single crystal molecular packing. In Figure 3.7, we superimpose the predicted and single crystal molecular packings, showing an excellent agreement.

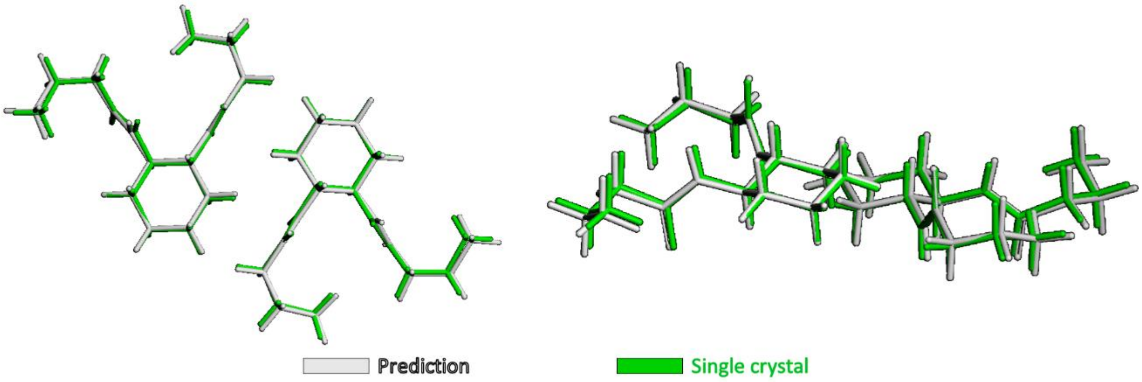

Figure 3.7: BiC4 Predicted (grey) vs single crystal molecular packing (green).

Consistently, the XRD powder pattern simulated for the predicted structure shows an excellent agreement with the experimental XRD pattern from the gel fibers (Figure 3.8), confirming the efficiency of the crystal prediction procedure. This procedure is further applied in Chapter 4 for other compounds.

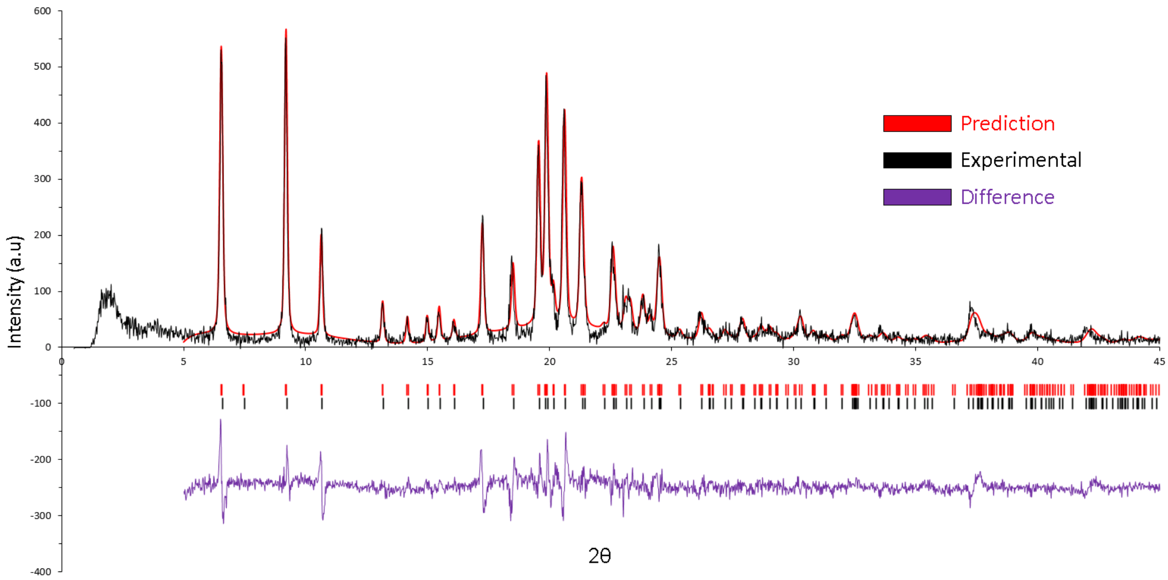

Figure 3.8: BiC4 experimental (black) vs predicted (red) XRD powder patterns.

3.3 Deducing the crystal morphology

After going from the molecular structure to the crystal structure, we move to the next step: from the crystal structure to the crystal morphology. To deduce the crystal morphology, we used the Morphology module in Materials Studio. This module employs growth kinetics principles to model crystal morphology.

The morphology of a crystal, or crystal habit, is a geometrical object that represents the morphology of a crystal and it is built using the Wulff construction principle [144] which: draws [hkl] vectors from a common origin point and defines a perpendicular (hkl) plane on the tip of each vector (Figure 3.9 top left and right panels). Then, the region of space enclosed by the intersection of the (hkl) planes forms a geometrical object known as the crystal habit (Figure 3.9 bottom panel). The (hkl) crystal planes displayed on the crystal habit are facets and their distance-to-center (D_{hkl}) depends on the growth kinetic principle considered. The facets that are equivalent by the symmetry of the lattice are further grouped in facet families (e.g. grouping (100) and (-100) in the {100} facet family).

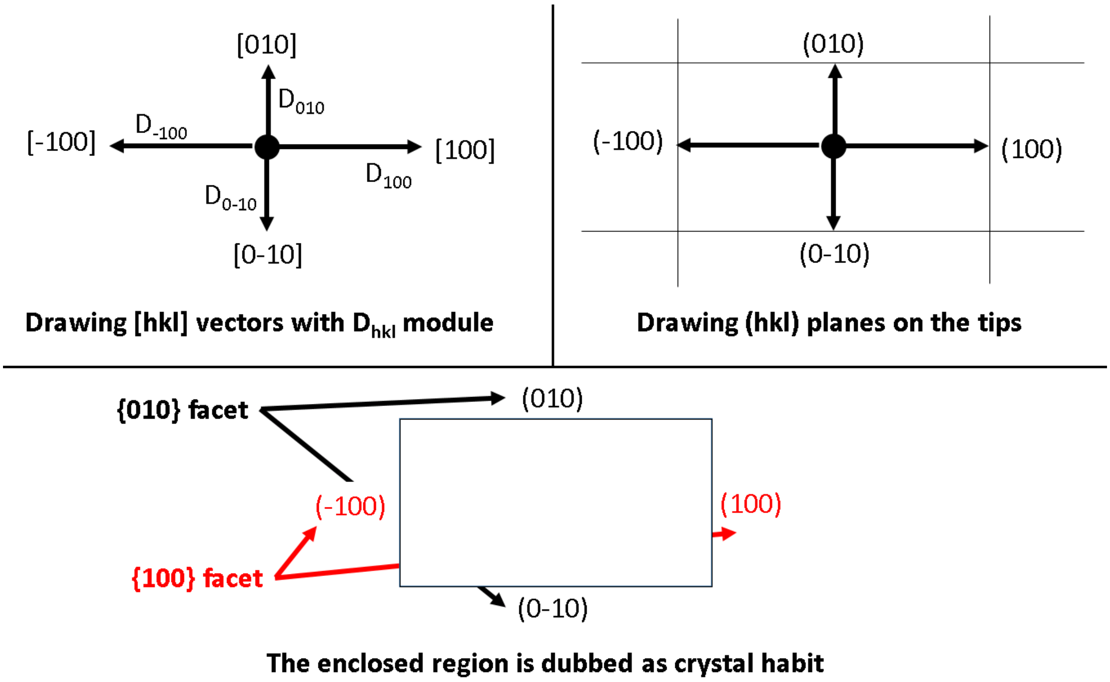

Figure 3.9: Sketch of the crystal habit generation following the Wulff's construction principle. Top left panel: the [hkl] vectors, top right panel: the (hkl) planes, bottom panel: the region of space enclosed by the (hkl) plane intersection, dubbed as crystal habit.

The facets are surfaces that can be characterized by the chemical nature of the growing (hkl) crystal plane. Therefore, depending on the position where the crystal plane is cleaved, a facet may expose different chemical compositions to the environment (terminations). Figure 3.10 shows the example of the two possible terminations of the (001) facet of the BiC4 crystal: on the left panel, the alkyl chains are exposed, on the right panel the cyclohexane rings are exposed.

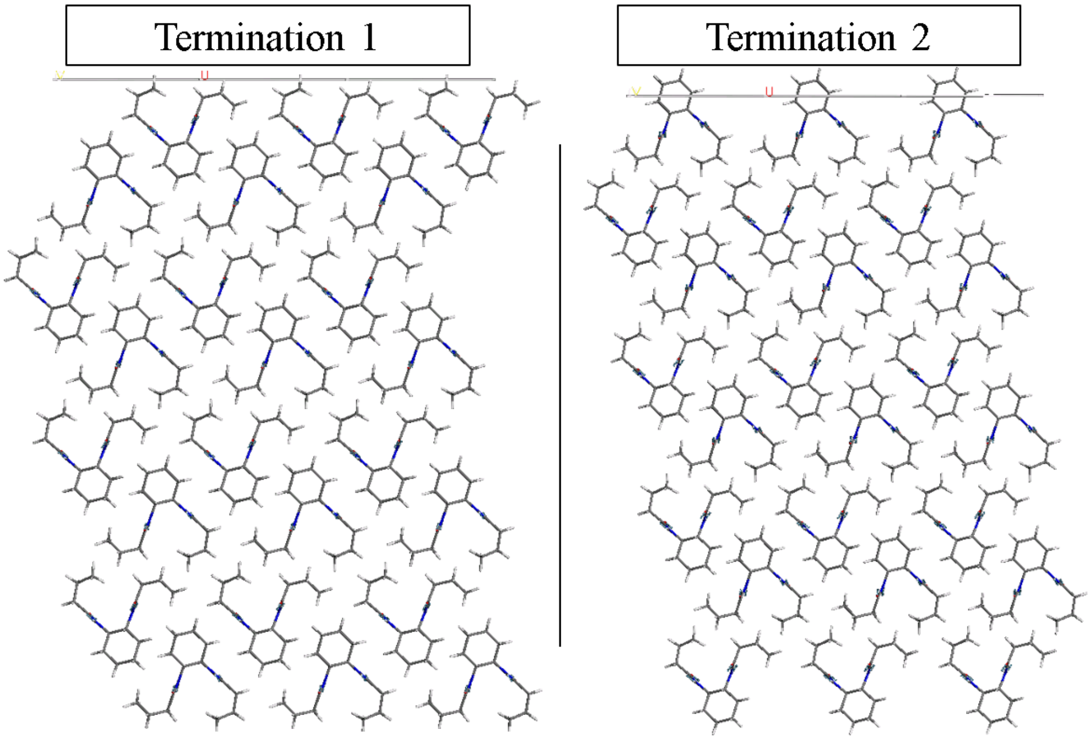

Figure 3.10: The two possible terminations of the BiC4 (001) facet: on the left panel the alkyl chains are exposed, on the right panel the cyclohexane ring is exposed. The line on top of the images represents the surface level, marking where the facet ends, and the vacuum starts.

The D_{hkl} value assigned to a facet changes depending on the growth kinetic principle considered and consequently the resulting crystal habit morphology. Below we introduce the three methods included in the Morphology module for assigning D_{hkl} values: the Bravais-Friedel Donnay-Harker (BFDH), Growth Morphology (GMM) and Equilibrium Morphology (EMM) methods. For each method, we give an example of how the crystal habit morphology is obtained for our reference compound, BiC4, and we compare them all at the end.

3.3.1 BFDH Method

The Bravais-Friedel Donnay-Harker (BFDH) method describes the crystal morphology using general rules derived from empirical observations of crystal morphologies [145]–[147]. Those observations indicate an inverse relationship between interplanar distances and morphological importance. This effect is rationalized from the precept that slow growth-rate crystal planes rule the crystal morphology. I.e., large interplanar distances correspond to slower growth rates than smaller ones, as the amount of matter necessary to grow one layer is larger. This assumption approximately holds during non-equilibrium growth conditions where the flux of matter is the limiting growth condition, and if there is no significant energetic criterion that affects asymmetrically the crystal growth (e.g. impurities, specific solvent-solute interactions, the presence of a substrate, etc.).

Therefore, this method assigns the module of the vectors D_{hkl} as the inverse of the interplanar distance (d_{hkl}) of the corresponding crystallographic plane:

$$D_{hkl} = \frac{1}{d_{hkl}} \tag{3.9}$$

This method provides an extremely fast (within seconds) rough approximation of the crystal morphology under non-equilibrium growth conditions. Figure 3.11 shows the example of computing the crystal habit of BiC4 with the BFDH method.

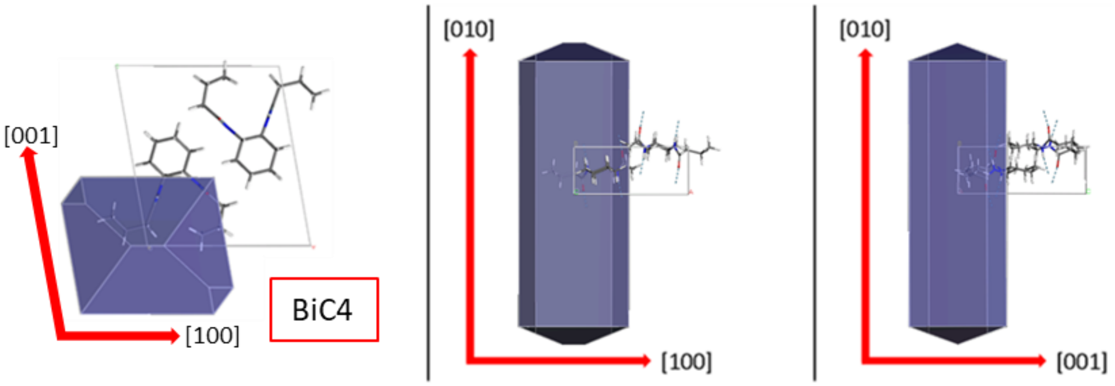

Figure 3.11: BiC4 crystal habit computed with the BFDH method. Left panel: the top view perpendicular to the [010] direction, center panel: the lateral view perpendicular to the [001] direction and right panel: lateral view perpendicular to the [100] direction.

The crystal habit computed with this method captures the one-dimensional growth preference of the BiC4 crystal. However, the description of the crystal morphology is much improved when including energetic factors. First, an energy-based D_{hkl} value provides a system-specific description capable of going from generic crystallographic foundations to concrete chemical information. Second, we gain insight on the terminations of the facets. This aspect is of vital importance for describing organogelation as the aggregation of the gel fibers may be directly mediated by the facet terminations of the fibers and consequently contributing to the physicochemical characteristics of organogelation.

Next, we describe the two energy-based methods for building the crystal habit: GMM, which is based on attachment energy and aims to describe crystal growth under non-equilibrium conditions (e.g. in solution) [148], and EMM, which is based on the surface energy definition and aims to represent crystal growth under equilibrium growth conditions (e.g. from a melt), formulated by Gibbs in 1928 [149].

3.3.2 Growth Morphology Method

The GMM method is rooted on the concept of the attachment energy (E_{att}) criterion, defined as "the energy released on attaching a growth slice to a growing crystal surface" [150], [151]. The attachment energy is specific for each facet termination. Therefore, for a given facet, there might be different attachment energy values. The lowest value is assigned as the D_{hkl} value for the facet, as it is the limiting growth rate step. Performing the same analysis for all considered facets, we build a crystal habit that is based on the attachment energy criteria, dubbed as the growth crystal shape. The attachment energy is evaluated as the difference between the lattice energy of the crystal (E_{latt}) and the energy of the growing slice of thickness d_{hkl} (E_{slice}) [151]:

$$E_{att} = E_{latt} - E_{slice} \tag{3.10}$$

E_{latt} is computed as the geometry-optimized bulk energy of the crystal employing the atom-based summation method, in order to be coherent with the energy calculation of the slice E_{slice}, which is modelled as a one-layer-thick slab of the corresponding termination. Figure 3.12 shows the example of computing the crystal habit of the BiC4 compound with the GMM method.

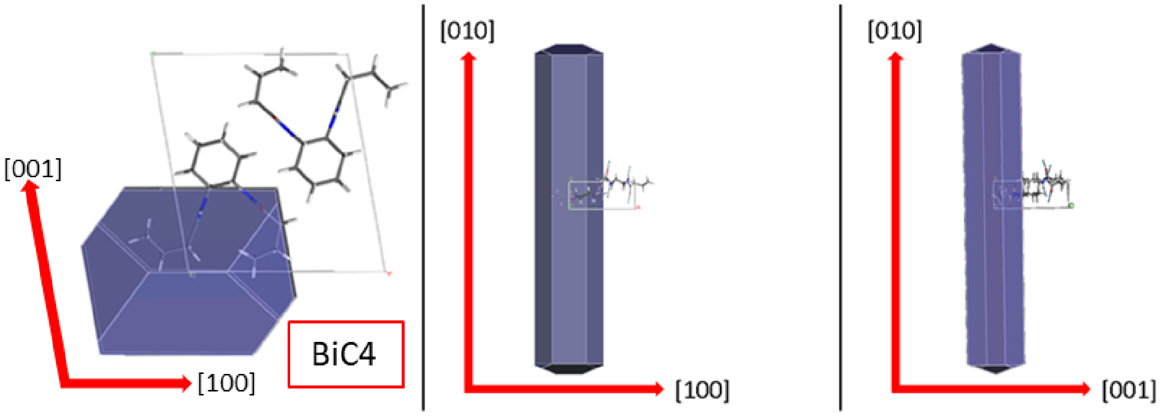

Figure 3.12: BiC4 crystal habit computed with the GMM method. Left panel: the top view perpendicular to the [010] direction, center panel: the lateral view perpendicular to the [001] direction and right panel: lateral view perpendicular to the [100] direction.

3.3.3 Equilibrium Morphology Method

The EMM method computes the morphology of a crystal using the surface energy (E_{surf}) criterion as the D_{hkl} value for each facet termination [149]. Surface energy is defined as the excess of energy when exposing a surface from a bulk material. Therefore, it is computed as the difference between the exposed surface (E_{slab}) and the bulk energy of the lattice (E_{bulk}) divided by the area of the slab (A), to evaluate it per unit area, and divided by 2, as two surfaces are exposed when cleaving the bulk. N is the number of layers of the slab.

$$E_{surf} = \frac{E_{slab} - N \cdot E_{bulk}}{2A} \qquad (3.11)$$

E_{bulk} is computed as the geometry-optimized bulk energy of the crystal and E_{slab} is modelled as a thick slab. For obtaining a reliable E_{slab} value, the slab must be thick enough so that potential energy does not change with the slab thickness. Purposely, there are two built-in criteria to evaluate how thick the slab must be: impose either a fix slab thickness or a potential energy error threshold. Fixing a slab thickness may not be suitable for all surfaces, as a specific crystallographic face may need a thicker slab for reaching convergence of the potential energy. Therefore, we used the second criterion, where the slab thickness is estimated to be large enough when the potential energy changes by less than 1% when increasing the slab thickness by one layer, thus indicating that convergence has been reached. This criterion is more robust than the first one and it is used for every E_{surf} calculation in this work. Additionally, E_{surf} is further improved including automatically the correction concerning the linear dependence of E_{surf} with the slab thickness, which arises from computing E_{bulk} and E_{slab} separately. It is corrected by calculating E_{bulk} from the slope of the linear regression of E_{slab} against the number of layers (N) as: $E_{slab} \approx 2E_{surf} + NE_{bulk}$ [152]–[154].

Each facet termination has an associated surface energy value. Analogously to the GMM method, there might be different surface energy values for a given facet. The lowest value is assigned as the D_{hkl} value for the facet, as it is the limiting growth rate step. Therefore, the resulting crystal habit is constructed with the lowest surface energy facets (see Figure 3.13). This resulting morphology is the Equilibrium Crystal Shape (ECS) formulated by Gibbs [149]. This method is employed for modelling crystal morphology under equilibrium growth conditions where heat transport is the limiting factor, e.g. long crystallization processes like single crystal growth or recrystallization.

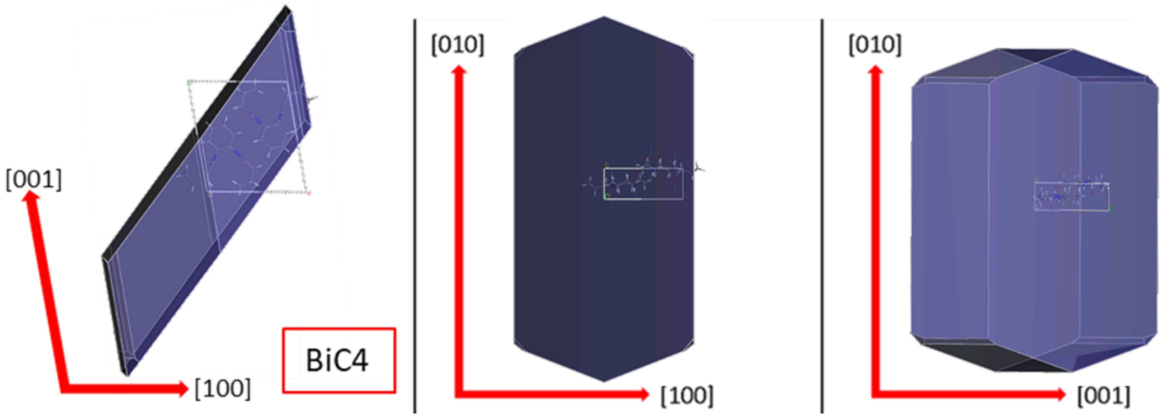

Figure 3.13: BiC4 crystal habit computed with the EMM method. Left panel: the top view perpendicular to the [010] direction, center panel: the lateral view perpendicular to the [001] direction and right panel: lateral view perpendicular to the [100] direction.

Figure 3.11-Figure 3.13 illustrate how, depending on the selected method, the computed crystal habit may change. As the BFDH and GMM methods represent non-equilibrium growth conditions, their crystal habits share more similarities than with the crystal habit found by the EMM method, in equilibrium growth conditions. From Table 3-2, we observe how the BFDH and GMM methods pinpoint the {001} and {100} lateral facets as predominant while the EMM method points to the {10-1}. From the BFDH to the GMM method, the inclusion of an energetic criterion, besides providing the chemical description of the facets, it also enhances the one-dimensional character by increasing the aspect ratio of the crystal habit. The percentage of facet area of the {10-1} facet increases too. In the case of the EMM method, the predominance of the {10-1} facet changes the crystal habit shape towards a two-dimensional preferential growth.

Table 3-2: Comparison of the aspect ratio and percentage of facet area of the lateral most relevant facets of the BiC4 crystal when computed with the BFDH, GMM and EMM methods.

	Aspect ratio	**Facets**		
		{001}	**{100}**	**{10-1}**
BFDH	3.1	39.2%	33.2%	9.8%
GMM	5.8	40.9%	30.0%	19.1%
EMM	6.5	-	21.2%	64.9%

In this work we chose the GMM method for comparing the computed crystal morphologies with respect to the experimental morphologies of the LMWG gel fibers, as observed in SEM images, as gel fibers are grown in solution under non-equilibrium growth conditions [148], [155]–[158], and the preferential termination of the facets is taken into account.

Therefore, once we have modelled the morphology of the crystal, we move to characterize its largest facets as they are expected to rule fiber-fiber interactions. We compute surface energy-related solubility parameters instead of cohesive energy-related solubility parameters because of: (i) practicality of time and resources and (ii) both concepts provide an equivalent solubility description [159]–[164]. Solubility description in surface energy terms has been already achieved in literature, with similar rationalization as "successful solvents tend to have surface energies very close to the surface energy of the solute" [22], [23].

3.4 Protocols

All the following protocols have been performed with the 2018 version of the Materials Studio software [101]. The protocols described here are the generic cases that are applied all over the work. When there is an exception, it is explicitly mentioned.

3.4.1 Forcite module

3.4.1.1 Potential energy calculations

The potential energy calculations are performed with the modified Dreiding forcefield where the only modification from the standard Dreiding forcefield are the H_ and H_{A} terms, for which the equilibrium distance R_0 is set to 2.83Å. The summation methods for electrostatic and van der Waals interactions are the Ewald summation method for crystals, which has a better accuracy for periodic systems than cutoff methods [165], [166], and atom-based cutoffs (cutoff distance of 14Å and 3Å of spline) for non-periodic structures. The charges are assigned by the PCFF forcefield.

The Dreiding version implemented in Materials Studio, and used in this work, uses [104]:

- The harmonic oscillator for the bond stretch term (E_B):

$$E_B = \frac{1}{2} k_e (R - R_e)^2, \qquad (3.12)$$

  where R_e is the equilibrium inter-atomic distance, k_e is the force constant and R is the inter-atomic distance.

- The harmonic cosine for the bond angle-bend term for two bonds IJ and JK sharing a common atom J ($E_{A,IJK}$):

$$E_{A,IJK} = \frac{1}{2} C_{IJK} \left[\cos\theta_{IJK} - \cos\theta_J^0\right]^2, \qquad (3.13)$$

  where θ_{IJK} is the angle between bonds IJ and JK, θ_J^0 is the equilibrium angle and C_{IJK} is a force constant.

- The cosine-Fourier expansion torsion term for the dihedral angle torsion for two bonds IJ and KL connected by a common bond JK ($E_{T,IJKL}$):

$$E_{T,IJKL} = \frac{1}{2}V_{JK}\left\{1 - \cos\left[n_{JK}\left(\phi - \phi_{JK}^{0}\right)\right]\right\}, \qquad (3.14)$$

  where ϕ is the dihedral angle between IJK and JKL, n_{JK} is the periodicity, V_{JK} is the rotation barrier and ϕ_{JK}^{0} is the equilibrium angle.
- The umbrella functional form for the inversion term ($E_{I,IJKL}$):

$$E_{I,IJKL} = \frac{1}{2}K_{I}\left(\frac{1}{\sin\Phi_{I}^{0}}\right)^{2}\left(\cos\Phi - \cos\Phi_{I}^{0}\right)^{2}, \qquad (3.15)$$

  where Φ is the angle between the IL bond and the JIK plane, Φ_{I}^{0} is the equilibrium angle that defines the planar geometry and K_{I} is the force constant.
- The Lennard-Jones 12-6 potential for the van der Waals term (E_{vdw}):

$$E_{vdw} = AR^{-12} - BR^{-6}, \qquad (3.16)$$

  where R is the inter-atomic distance and A, B are van der Waals parameters.
- The electrostatic interactions (E_{Q}):

$$E_{Q} = (322.0637)\frac{Q_{i}Q_{j}}{\epsilon R_{ij}}, \qquad (3.17)$$

  where Q_{i}, Q_{j} are the atomic charges in electron units, R_{ij} is the inter-atomic distance in angstrom, ϵ is the dielectric constant and 332.0637 is the unit conversion to express E_{Q} in kcal/mol.
- The Lennard-Jones 12-10 potential with angular dependency for the hydrogen-bonding term (E_{hb}):

$$E_{hb} = D_{hb}\left[5\left(\frac{R_{hb}}{R_{DA}}\right)^{12} - 6\left(\frac{R_{hb}}{R_{DA}}\right)^{10}\right]\cos^{4}(\theta_{DHA}), \qquad (3.18)$$

  where θ_{DHA} is the bond angle between the hydrogen donor (D), the hydrogen (H) and the hydrogen acceptor (A), R_{DA} is the inter-atomic distance between the donor and acceptor atoms expressed in angstroms, and D_{hb}, R_{hb} are hydrogen-bonding parameters.

3.4.1.2 Geometry optimizations

The geometry optimizations use the "Smart" algorithm with an Ultra-Fine quality and a maximum of 500 iterations. The cell parameters are optimized or not depending on the specific problem that it is treated. The energy settings follow the previous section.

3.4.2 Polymorph module

3.4.2.1 Predictor functionality

The molecular packing predictions are performed with the Predictor functionality. It is comprised of three parts. The first one, "packing", is used with the Ultra-Fine quality and the torsion degrees of freedom are only explored when some critical torsions are desired to be explored. The minimum temperature is 300K. If the space group of the target crystal is known the prediction is limited to that space group, otherwise a generic search of the most common space groups must be done. Several predictions must be done for predicting the crystal structure of a compound as the crystal generation algorithm is the Monte-Carlo Simulated annealing, i.e. the generation is random, thus a proper sampling is achieved by repeating several predictions. The more torsional degrees of freedom of the compound the more predictions are usually needed. The second part is "geometry optimization", where all the generated crystals are optimized following the geometry optimization settings described previously including the optimization of the cell parameters. The third part, "clustering", consists in removing duplicated structures. The quality is set to Ultra-Fine and all unique clusters are kept, without any limitation of number of clusters. The energy settings are the ones specified in the potential energy part.

3.4.3 Reflex module

3.4.3.1 Rietveld+Energies refinement

The Rietveld with Energies refinement is performed with the Powder Refinement option. This is specified on the type of calculation. The weight criteria, to balance XRD fitting and potential energy is set to half and half, i.e. 0.5. The energy window is kept to 40 kcal/mol to avoid leaving the potential energy well. The convergence quality is set to Ultra-Fine. For difficult converging fittings, the number of cycles can be increased if needed. The 2θ range to fit and the radiation is specific to the experimental setting that one wants to compare with. All possible degrees of freedom can vary. In order to simulate the thermal contribution to the XRD pattern, the atom occupancy and the U, V and W peak broadening parameters are optimized. The background coefficients and the zero-point are also optimized to match the zero point and the background of the experimental pattern. Mention that a more straightforward XRD fitting is usually achieved, without the peak broadening parameters to establish first the peak positions, and then a second XRD fitting is performed including the peak broadening parameters for the peak widths.

3.4.4 Reflex module

The summation method for electrostatics and van der Waals interactions change from Ewald to the atom-based approach (with a cutoff of 14Å and a spline of 3Å) due to the finite character in one dimension. For consistency, before using the methods below, the crystal is optimized (geometry and cell parameters) with this criterion. The number of Miller planes considered to build the crystal habit are up to the second order as it is usually enough for describing organic crystal morphology [145]–[147].

3.4.4.1 BFDH

The quality is customized to use the Miller planes up to the h, k, l values of 2.

3.4.4.2 Growth morphology method

The energy method is Forcite, i.e., the energy criteria is the same as in the potential energy section with the change of the summation method mentioned for this module. All surfaces are outputted, stable and non-stables. The quality is customized to use the Miller planes up to the h, k, l values of 2.

3.4.4.3 Equilibrium morphology method

The 1% fixed error bar option is used for calculating the surface energy. The energy criterion is the same as in the potential energy section with the change of the summation method mentioned for this module. All surfaces are outputted, stable and non-stables. The quality is customized to use the Miller planes up to the h, k, l values of 2.

Chapter 4. Modelling bisamide gel fibers using molecular packing and crystal morphology determination

In this chapter we study the bisamide family of organogelators using modelling techniques. We model the bisamide gel fibers as organogelation is triggered by fiber aggregation. For this purpose, first we determine the molecular organization of the bisamide molecules in the bulk of the fibers using the crystal structure prediction method. Then, we determine the crystal morphology of the gel fibers and the molecular organization of the bisamide molecules exposed outwards at the surface of the fiber using the crystal morphology method. Finally, we compare our theoretical findings with the parallel experimental efforts performed by our partners from the *Sorbonne Université* and *Université Paris-Sud*, who have characterized the organogels by their HSP parameters, combined with crystal structure studies with diffraction techniques.

4.1 Bisamide compounds as gelators

The bisamide-based compounds studied in this work (BiC3-6 in Figure 4.1) are formed by a cyclohexane ring decorated with two amide groups prolonged by an alkyl chain.

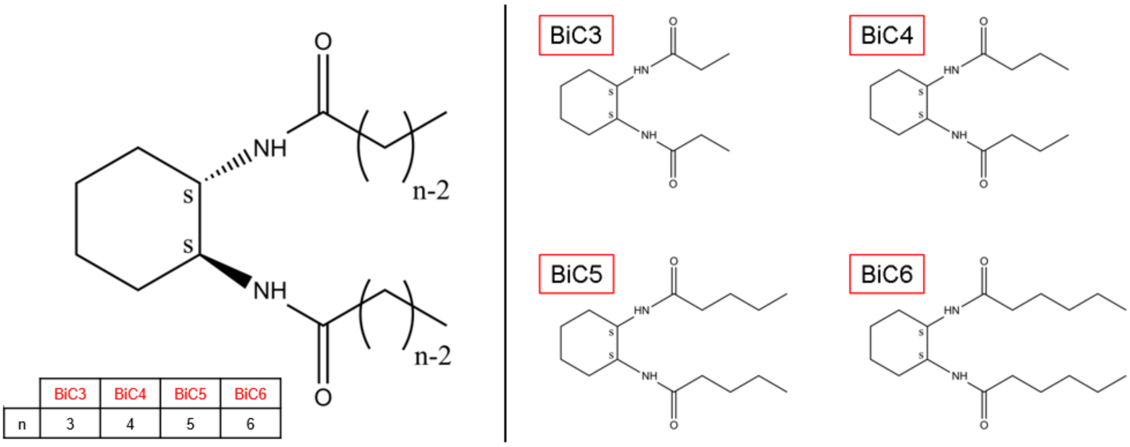

Figure 4.1: Compounds of the Bisamide family studied in this work. They only differ in the length of the alkyl chains.

The gelation ability of a bisamide with alkyl chains of 11 carbon atoms (BiC12) was first reported by Hanabusa et. al. [52]. The authors were interested in studying compounds capable of gelling organic liquids and they observed in previous works that molecules able to self-interact and form long supramolecular structures were essential for gelation [167]–[171]. It is the case for the BiC12 compound, as the amide groups of neighboring molecules could interact via hydrogen-bonding. In reference [52], the authors studied stereoisomeric variations of BiC12 that are shown in Figure 4.2. Note (i) the *cis/trans* notation, which corresponds to the relative orientation of the two arms with respect to the cyclohexane ring and (ii) the authors always considered the chair conformation of the cyclohexane rings as it is the most stable conformer.

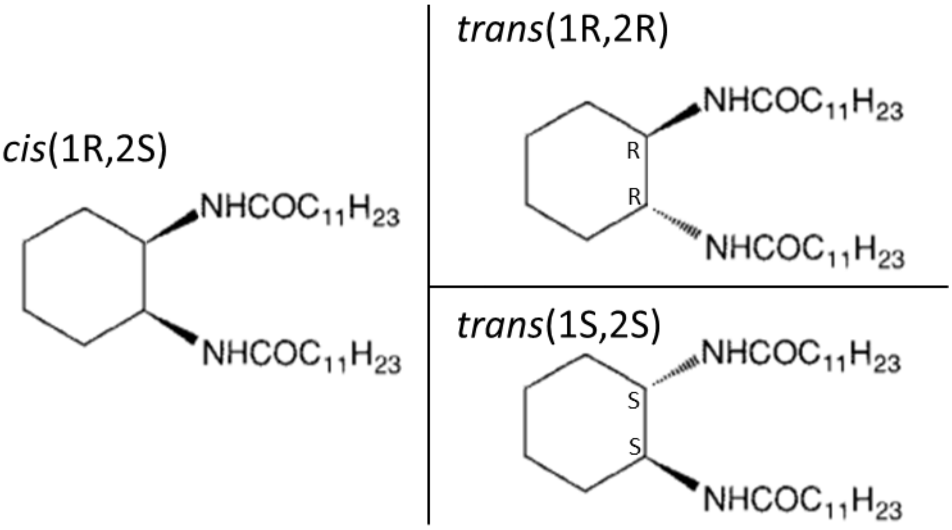

Figure 4.2: Enantiomeric variations of the BiC12 compound studied in reference **[52]**.

While the *trans*(1R,2R) compound forms gels, the *cis(1R,2S)* compound does not and to explain this difference of gelation ability, the authors compared the infrared spectra of the gels formed in cyclohexane. The *trans*(1R,2R) compound show broad bands associated to the stretching vibration modes of N-H and C=O of amides (3279 and 1637 cm^{-1}), shifted to a lower wavenumber with respect to the *cis* diastereoisomer (3300 and 1671 cm^{-1}). This means that the amides are hydrogen-bonded in the *trans* compound, and free in the *cis* compound. The authors attribute the lack of gelling ability of the *cis* isomers to a geometrical impossibility of forming hydrogen bonds. The resulting supramolecular structures of the *trans* compounds were characterized by circular dichroism, which characterizes their chirality, and by transmission electron microscopy, which characterizes their morphology. This combination of techniques allowed them to find right-handed helical structures for the *trans*(1R,2R) and left-handed for the *trans*(1S,2S). Thus, they proposed that hydrogen-bonded helical structures were responsible for triggering gelation (see Figure 4.3).

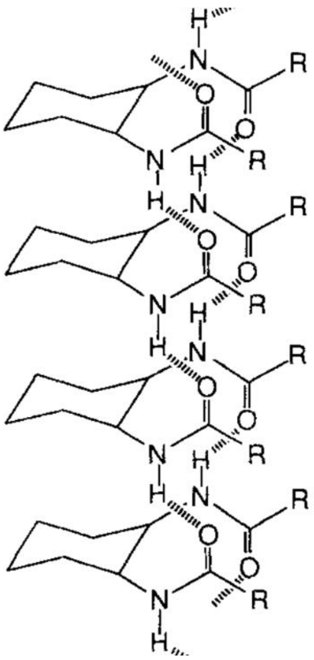

Figure 4.3: Sketch of a possible self-assembly configuration of the bisamide molecules forming a one-dimensional hydrogen-bonding pattern, as proposed by Hanabusa et. al. **[52]**.

A later work from Pi-Boleda et. al. [172] deepened on the *cis*/*trans* stereochemistry of bisamides, studying molecules with longer alkyl chains, BiC17, also correlating with their respective gelation behavior. In their work, the authors synthesized and characterized by circular dichroism both stereoisomers, observing gels of left-handed aggregates for the *trans*(1R,2R) isomer, and right-handed aggregates for the *cis* (1R,2S) compound; the *trans*(1R,2R) isomer gelled more solvents than its *cis* counterpart. This inversion may arise from the hydrogen bonding interactions ruling the aggregation of these compounds, which propagates the chirality of the molecule. The authors also modelled the helical aggregates to further understand their aggregation and they indeed observed the same helicity resulting from the aggregation geometry of the bisamide molecules (see Figure 4.4).

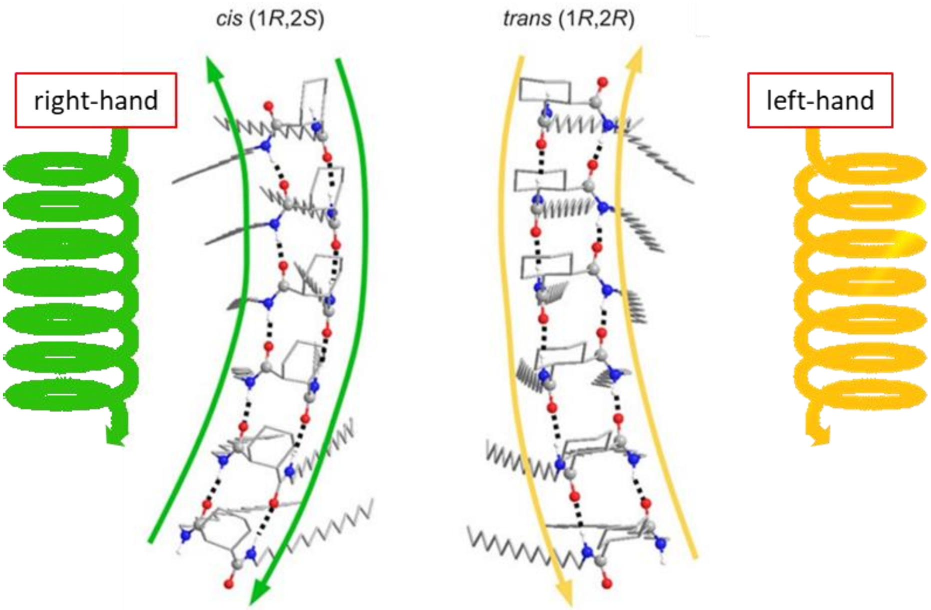

Figure 4.4: Modelled helical aggregates for the cis/trans stereoisomers. The drawn helices are a visual guide to the reader about the helicity of the aggregates. Adapted from reference **[172]**.

Zweep et. al. [24] expanded this bisamide gelation family to compounds with alkyl chains having from 2 to 17 carbons (BiC3 to BiC18). Their work aimed to understand the interactions involved in the formation of the gel fibers by evaluating the hydrogen-bond and the van-der-Waals contributions. For this purpose, they tested the gelation ability of BiC3-C18, and some bisurea compounds too, with polar and apolar solvents. When plotting the melting enthalpy of the gels with respect to the length of the alkyl chain, they found a linear correlation, allowing them to determine the individual contribution of adding a methylene unit to the gel stability, which is larger in polar than in apolar solvents (i.e., between 3.5 and 4.2 kJ/mol per methylene unit in polar solvents, and 2.2 kJ/mol in apolar solvents). Thus, the authors conclude that the forces contributing to the formation of the gel fibers are solvent-dependent and understanding their interplay is key for understanding gelation.

In this work, we study the *trans* (1S,2S) bisamide compounds as they were the ones studied by our experimental partners, based on the gelation studies of Zweep et.al. [24] (detailed onwards) and due to commercial availability. Our experimental partners have characterized the gelation, microscopic morphology, and crystallographic behavior of the BiC3 to BiC18 compounds by HSP parameters, Scanning Electron Microscopy (SEM), and powder X-ray diffraction. The BiC3 to BiC6 compounds show a crystalline XRD pattern, and we investigated them structurally and morphologically from a molecular modeling perspective.

The BiC8 to BiC18 compounds also form organogels but they have broad, unindexable diffraction features characteristic of an amorphous behavior, from which only partial structural and morphological information could be extracted. This work therefore mostly focuses on the BiC3-BiC6 series, as a maximum amount of gelation, structural and morphological data are available.

4.2 Crystal structure determination

The organogelator ability of the BiC4 compound is known in literature as well as its single crystal structure [24]. It has thus been used as a reference for validating the crystal structure prediction (CSP) procedure used to model the packing of organogelators in crystals. More information on the methodology and analyses can be obtained in the methodology chapter. Here, we extend the study to BiC3, BiC5 and BiC6 compounds.

We started performing the BiC3-6 CSP predictions based on the XRD patterns of the gel fibers formed in toluene. In order to confirm that the packing is conserved for all solvents, our experimental partners synthesized gel fibers in other solvents and characterized them by powder X-ray diffraction. The same diffraction peaks are present in all diffraction patterns of the BiC3 and BiC4 gel fibers, independent of the solvent. However, it is not the case for BiC5 and BiC6 (see Figure 4.5) where, depending on the solvent, additional diffraction peaks appear, indicating polymorphism. Therefore, we also aimed to characterize the second polymorph of BiC5 and BiC6. However, by the time of writing this manuscript, we have been only able to characterize the one of BiC6. For this purpose, we used the XRD pattern of BiC6 fibers formed in cyclohexane as a basis for our simulation, as this pattern only contains the new polymorph (named BiC6-2 from here on), instead of a mixture of polymorphs as in other solvents.

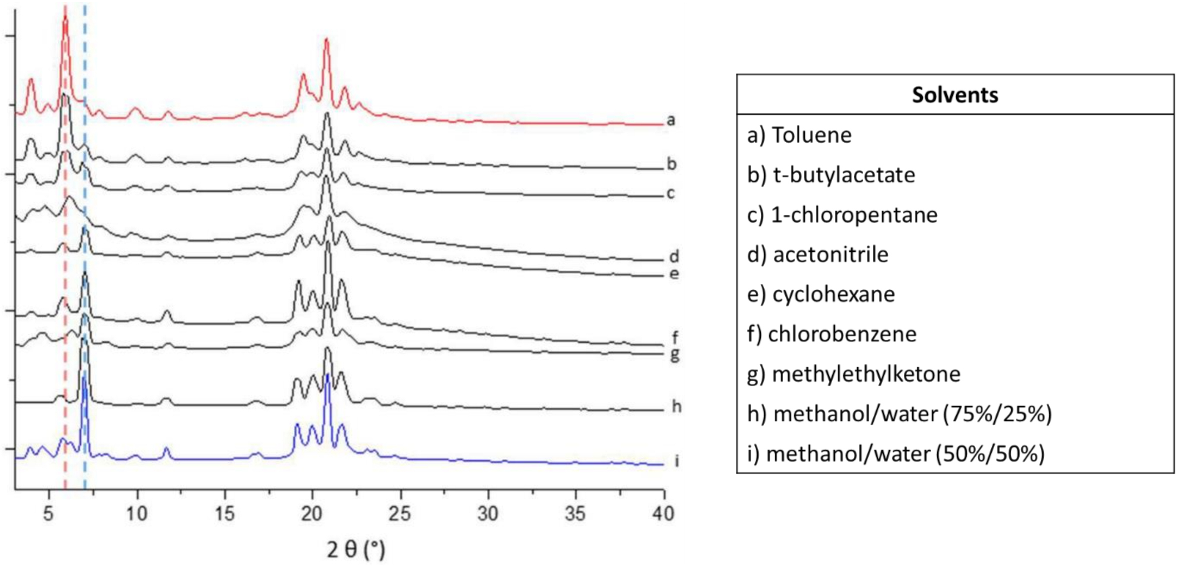

Figure 4.5: XRD patterns of BiC6 gel fibers synthesized in different solvents. The most intense signal for the commonly-observed polymorph ("BiC6-1" from here on) is represented in red, and for the new observed polymorph ("BiC6-2") is in blue. Reference **[80]**.

4.2.1 Understanding bisamide X-ray diffraction patterns

Table 4-1 shows the cell parameters proposed by our partners for the bisamide compounds.

Table 4-1: Cell parameters proposed by Danilo Nunes et. al. (Sorbonne Université).

	a (Å)	**b (Å)**	**c (Å)**	**α (º)**	**β (º)**	**γ (º)**
BiC6-2	13.02	4.86	18.05	90	119.56	90
BiC6-1	22.75	4.37	18.33	90	96.82	90
BiC5	12.10	4.87	15.74	90	107.22	90
BiC4	11.91	4.81	13.55	90	98.33	90
BiC3	12.28	4.80	12.01	90	108.15	90

Observing that the “c” axes are the largest ones for all bisamide compounds, except for BiC3, for consistency and for a better comparison, we take an equivalent unit cell for the BiC3 crystal, i.e. swapping the “a” and “c” axis. The crystal structure, morphology and properties are the exact same, just its “a” and “c” axes are swapped (see Table 4-2).

Table 4-2: Guessed cell parameters considering the equivalent BiC3 cell.

	a (Å)	**b (Å)**	**c (Å)**	**α (º)**	**β (º)**	**γ (º)**
BiC6-2	13.02	4.86	18.05	90	119.56	90
BiC6-1	22.75	4.37	18.33	90	96.82	90
BiC5	12.10	4.87	15.74	90	107.22	90
BiC4	11.91	4.81	13.55	90	98.33	90
BiC3	12.01	4.80	12.28	90	108.15	90

Figure 4.6 shows the experimental powder XRD patterns for the bisamide compounds, including the indexation of their diffraction peaks.

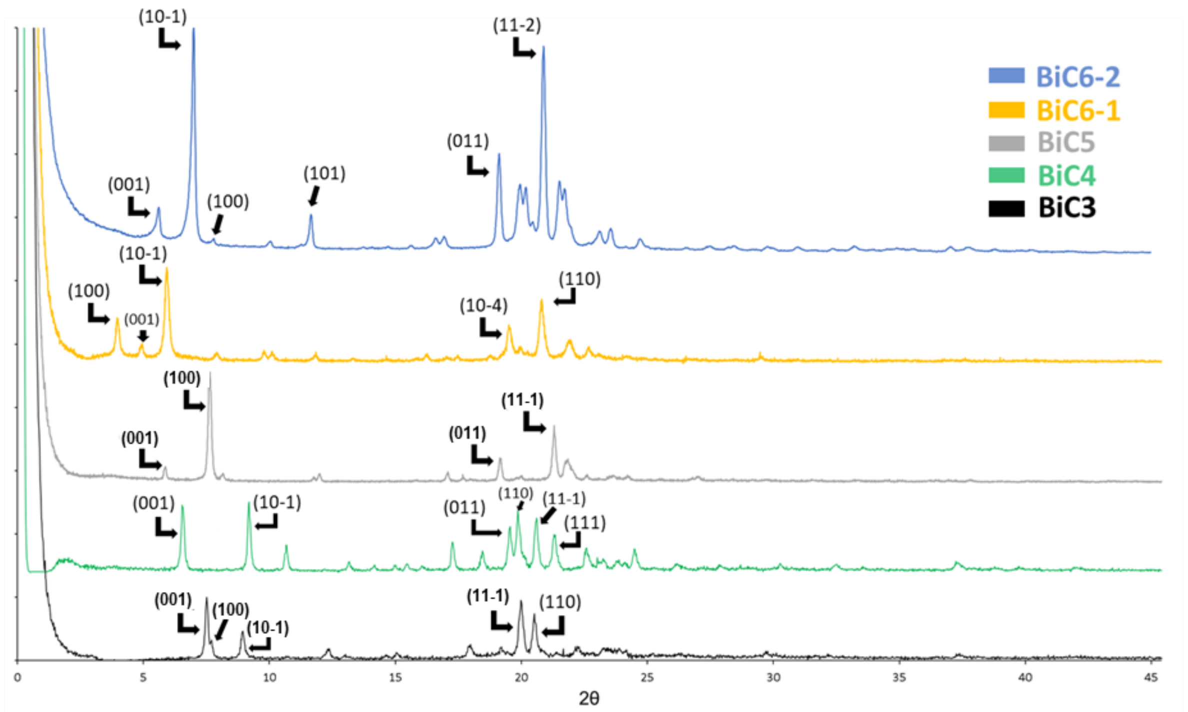

Figure 4.6: Experimental powder XRD patterns for the bisamide compounds. The XRD patterns are from the xerogels extracted from toluene and from cyclohexane in the case of BiC6-2.

The indexation of the XRD patterns, together with the cell parameter guesses, provides plenty of crystallographic information. Thus, we focus on two important regions of the XRD patterns: first, the 3-17º 2θ range of the XRD pattern comparing with the cell parameters, and second, the 17-25º 2θ range, giving information about the molecular packing. Following Bragg's diffraction law, the diffraction peaks furthest to the left correspond to crystallographic planes with the largest interplanar distances. It is in that region that the peaks corresponding to the largest cell parameters, here "a" and "c", can appear. Then, the following diffraction peaks, with smaller interplanar distances, usually correspond to diffraction planes arising from atomic dispositions inside the crystal cell, e.g. molecular packing conformations.

Starting with the guess of the "c" cell parameter, it appears that it increases continuously with the length of the alkyl chain. Continuing with Bragg's diffraction law, c*sinβ equals to the interplanar distance of the (001) crystal planes (d_{001}). Thus, the shift of the (001) diffraction peaks to lower 2θ values means that d_{001} increases, agreeing with the increase of the "c" guessed parameters. We can better compare the evolution of the cell parameters paying attention to the evolution of the corresponding interplanar distances (see Table 4-3).

Table 4-3: Evolution of the interplanar distances (Å) when elongating the alkyl chain.

	d_{100}	d_{010}	d_{001}
BiC3	11.41	4.80	11.67
BiC4	11.78	4.81	13.40
BiC5	11.56	4.87	15.03
BiC6-1	22.59	4.37	18.20
BiC6-2	11.32	4.86	15.70

Paying attention to the evolution of the d_{001} interplanar distances we indeed observe that it increases with the alkyl chain length. Note that, from the molecular weight of the BiC6 molecule, the volume derived from the cell parameters guess, and the typical density of organic compounds close to 1g/cm^3, we consider that the BiC6-1 must have 4 molecules per unit cell, differing from 2 molecules per unit cell for BiC3, BiC4, BiC5 and BiC6-2. As discussed below in this chapter, we confirm that it is indeed the case, and the molecular packing of BiC6-1 is not comparable to that of other compounds. Thus, we can now rationalize the abrupt change of d_{001} for BiC6-1.

With respect to the "a" and "b" cell parameters, the corresponding d_{100} and d_{010} remain constant with the elongation of the alkyl chain (considering the BiC6-1 as $d_{100}/2=11.30$Å), meaning that the increase of the alkyl chain length pushes the molecular centers apart in the "c" direction.

As for the "b" cell parameter, its value corresponds directly to the (010) interplanar distances, being BiC3→4.80Å, BiC4→4.81Å, BiC5→4.87Å, BiC6-1→4.34Å, BiC6-2→4.86Å. Following the previous intuition by Hanabusa [52], a periodicity of ~4.8Å perpendicular to the alkyl chains can be correlated to the stacked distance between two BiC4 bisamide molecules, likely dominated by cyclohexane stacking (4.81Å, see Figure 4.7). The invariancy of "b" from BiC3 to BiC6-2 suggests that they follow the BiC4 organization while the 10% deviation for BiC6-1 confirms the previously mentioned slightly different organization.

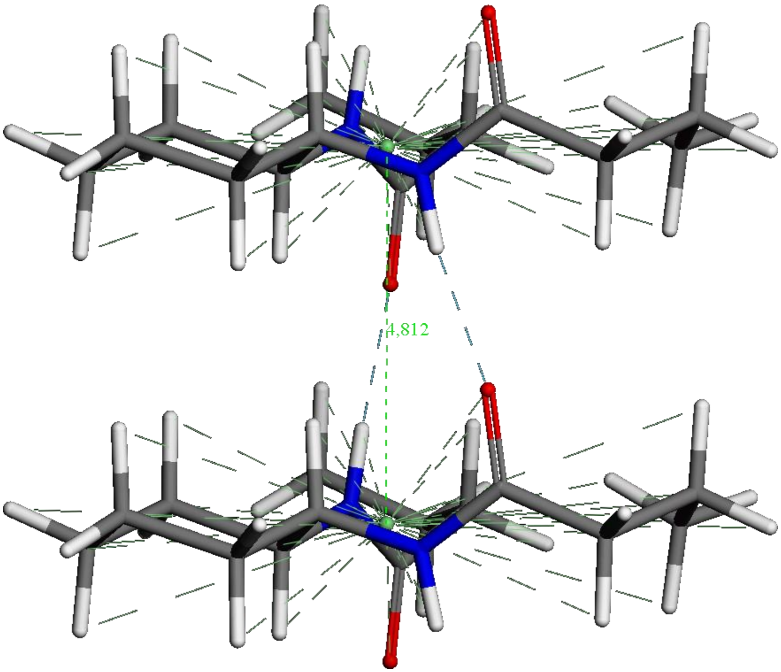

Figure 4.7: A stack of two BiC4 molecules separated by 4.81Å. The distance is measured between the centroid of the molecules (green dots). Reference **[24]**.

The β angle, i.e., the angle between the "a" and "c" cell parameters, shows an odd-even effect, where the value decreases from BiC3 to BiC4 and increases from BiC4 to BiC5. This effect will be explained below in the chapter, when discussing the simulation results.

Moving to the 17-25° 2θ range, the characteristic interplanar distances are between ~5.3-3.6Å. This range of values is usually related to short intermolecular distances. The main observation is that the observed diffraction peaks and their positions change for all compounds. Thus, we can think that the molecular packing is in principle different for each compound. It is common in molecular crystals to show many diffraction peaks in this region as many small interplanar distance periodicities could be defined, and sometimes diffraction peaks overlap, the low-order diffraction planes, such as the (110), (111), (011) and (11-1), being the most intense ones.

Extracting molecular packing information only from crystal interplanar distances is difficult, and additional information from other sources is welcome. Therefore, our theoretical effort is focused on predicting the molecular packing in the gel fibers for the bisamide compounds using the Crystal Structure Prediction (CSP) procedure described in the methodology chapter. We use the experimental powder XRD patterns of the gel fibers as references and their proposed cell parameters to help filter the possible crystals.

4.2.2 Crystal generation: exploring the polymorph landscape

Generally, it is conceived that the lower the potential energy of the lattice and the denser the crystal, the more likely is the crystal structure to be thermodynamically stable. The CSP method generated thousands of crystal structures with different molecular packings. It can be observed in Figure 4.10 that indeed the predicted crystals (red dots, pointed by red arrows) are on the bottom-right region of the stability-density plot and they could be apparently thermodynamically stable crystals.

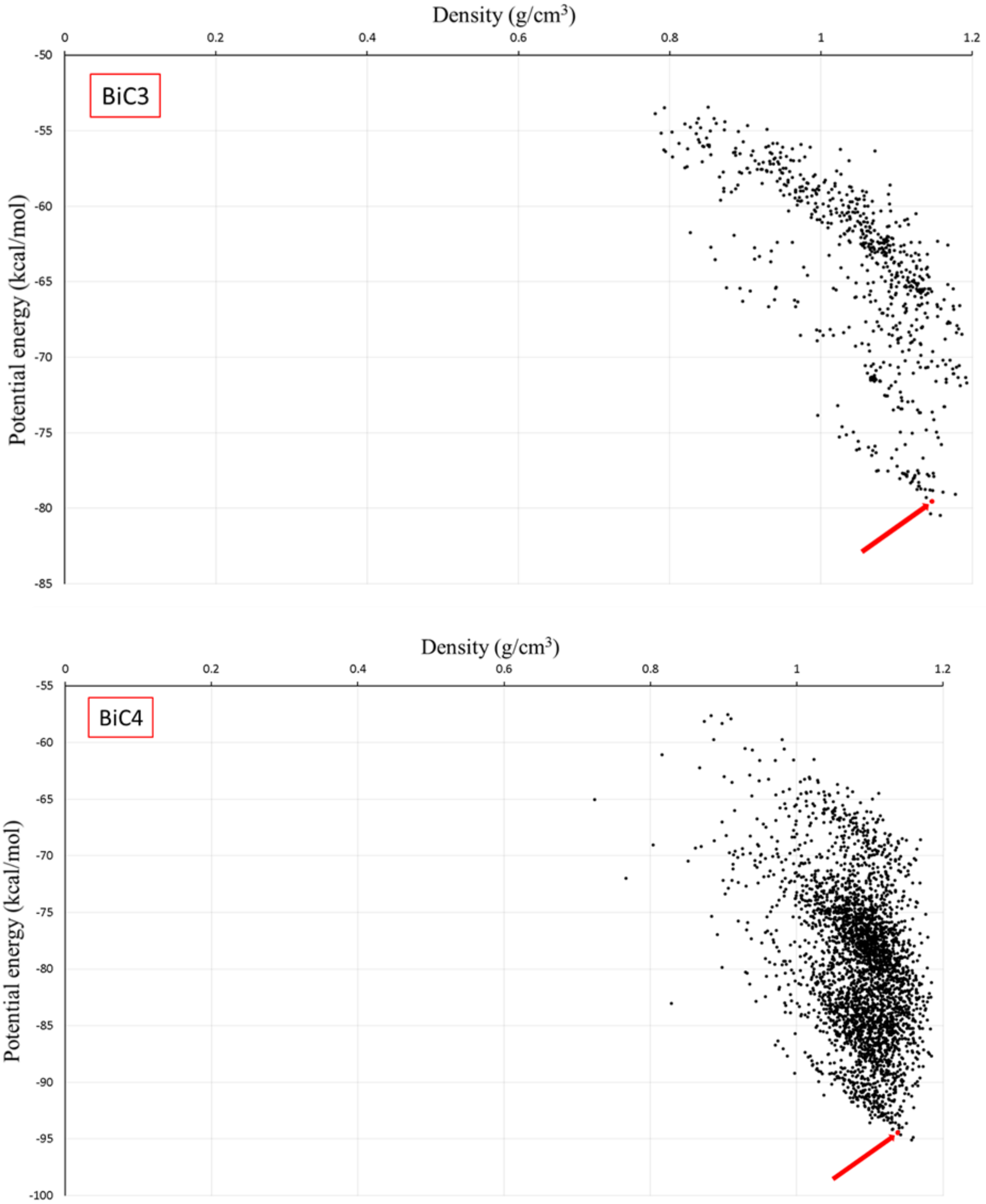

Figure 4.8: Potential energy against density for the predicted crystals for the BiC3-BiC6 structures.

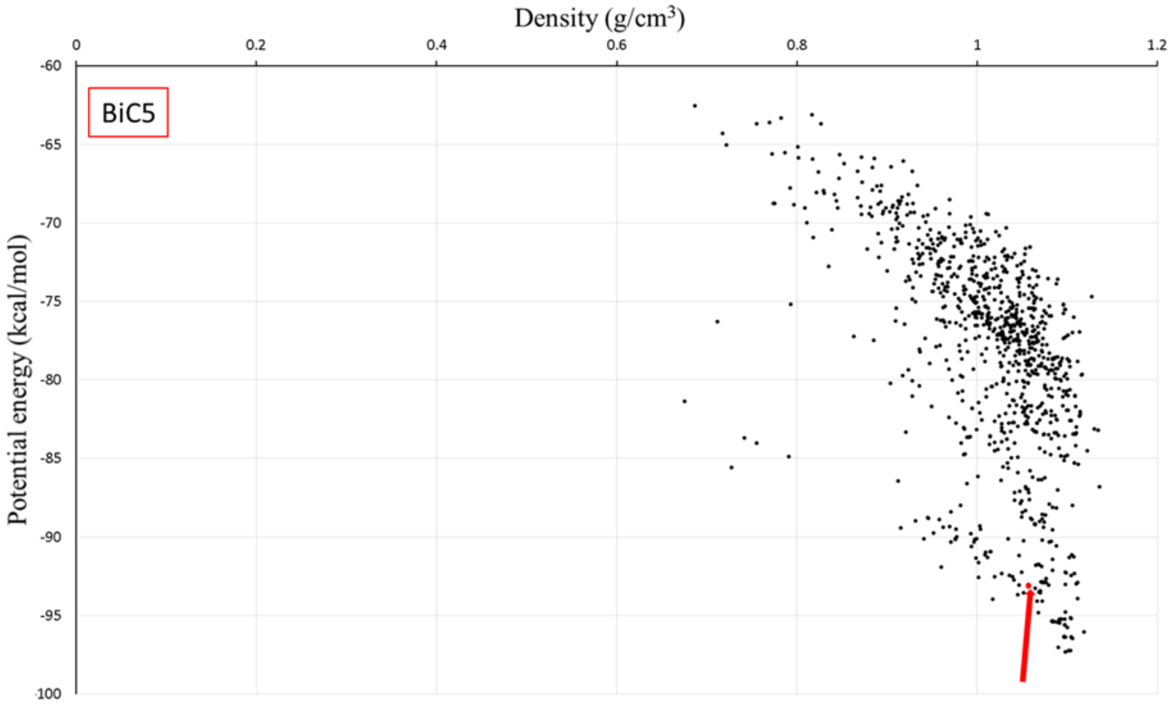

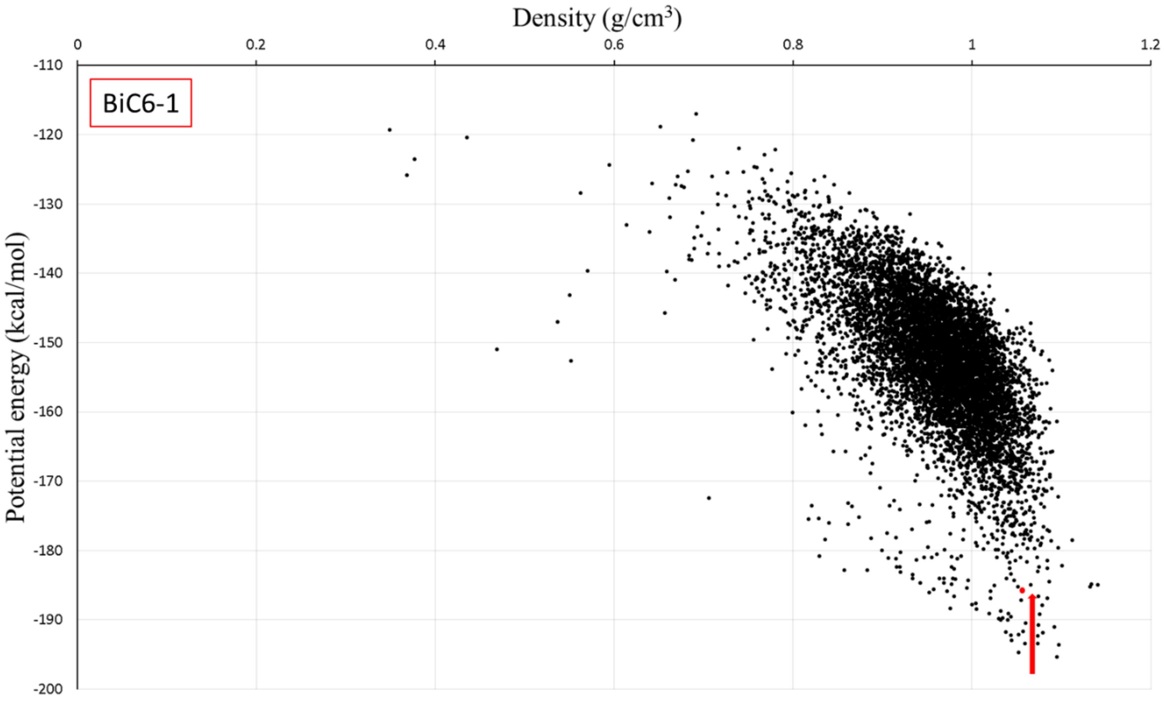

Figure 4.9 (continued): Potential energy against density for the predicted crystals for the BiC3-BiC6 structures.

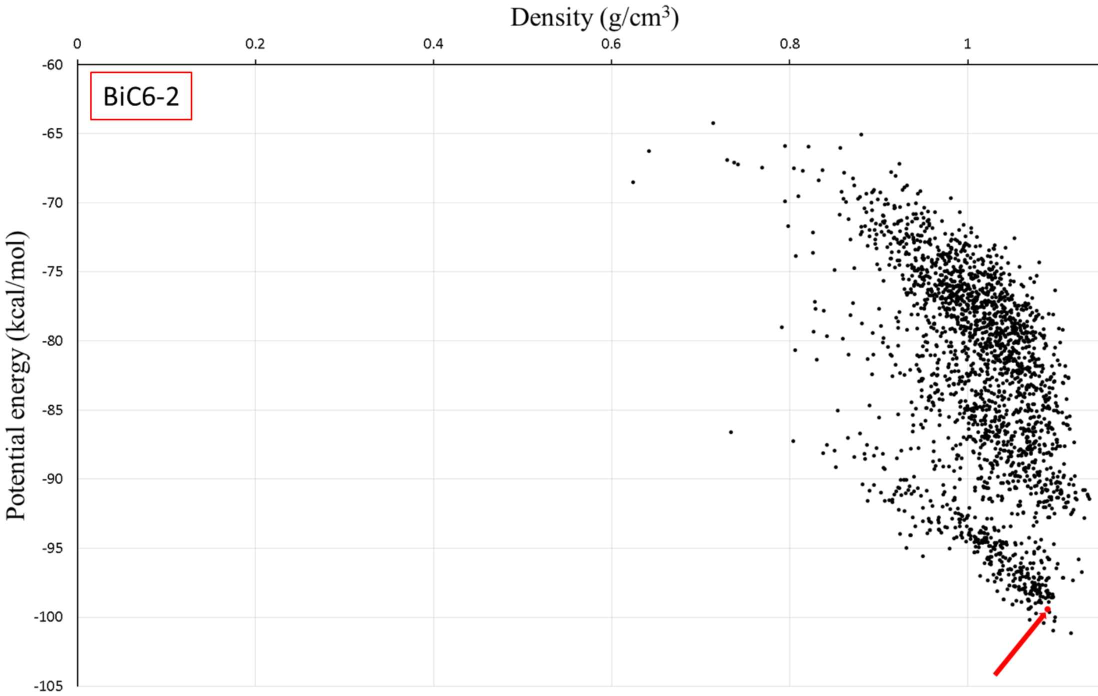

Figure 4.10 (continued): Potential energy against density for the predicted crystals for the BiC3-BiC6 structures.

The stability range of the predicted crystals lies within a window of ~30 kcal/mol for BiC3 and ~40kcal/mol for the other compounds (being ~80/2=40 kcal/mol for BiC6-1 to be comparable with the rest).

The plots of density against potential energy of lattices have two main limitations: (i) the evaluation of the potential energy and (ii) the crystal structure generation.

The evaluation of the lattice energy is a trade-off problem between accuracy and time- and resource-consumption. For instance, semi-empirical, molecular mechanics potentials or Density Functional Theory (DFT) can perform a fast routine evaluation of the lattice energy and rank adequately the possible crystals by energy. In this work we use our improved Dreiding potential, which is a molecular mechanics potential.

The crystal structures are generated employing a sampling algorithm that aims to explore the conformational landscape for a specific compound. How this landscape is explored is critical: it must search a region large enough to produce a variety of crystals while finding the low potential wells, which may correspond to a stable structure. The size of the landscape increases with the degrees of freedom and, for molecular crystals, the landscape is often very rugged with many potential wells separated by small energy barriers, where polymorphs generally differ in lattice energies by less than 4 kJ/mol [173]–[175]. This combination leads to a very hard task of finding out the stable crystals corresponding to the experimental reality. In this work, thanks to the space group determined by our experimental partners, we can restrict the size of the sampled landscape to a specific space group of symmetry (P_{2_1} for the bisamides), otherwise we would have had to explore at least the 10 most common molecular crystals space groups. We used a Monte Carlo Simulated Annealing algorithm, which, within the restriction of the chosen space group, samples that size of landscape randomly and finds the bottom of the potential wells by geometry optimization. This sampling algorithm has proven to be suitable for large and rugged landscapes, as in molecular crystals [136]. We run several times the simulation, and checked that in the low energy window (a few kcal/mol) no new dots appeared, meaning that the potential energy landscape has been appropriately explored.

4.2.3 Crystal structure refinement

After the crystal structure generation, we used the guessed cell parameters obtained by our experimental partners to select possible candidates. Table 4-4 shows the comparison of the cell parameters of the selected candidate crystals (from the CSP approach) together with the guessed ones (from the XRD patterns). It also reports the position of the candidate crystal in the ranking of energetic stability among the generated crystals (e.g. 4th means the 4th most energetically stable among the thousands of generated crystals).

Table 4-4: Comparison of the cell parameters of the candidate crystal versus the guessed ones.

		a	**b**	**c**	**α**	**β**	**γ**
BiC3	Guess	12.01	4.80	12.28	90	108.15	90
	Candidate (3rd)	11.72	4.79	12.27	90	107.90	90
BiC4	Guess	11.91	4.81	13.55	90	98.33	90
	Candidate (4th)	11.78	4.77	13.39	90	99.95	90
BiC5	Guess	12.10	4.87	15.74	90	107.22	90
	Candidate (41st)	12.18	4.77	16.01	90	108.60	90
BiC6-1	Guess	22.75	4.37	18.33	90	96.82	90
	Candidate (38th)	22.36	4.75	18.48	90	95.80	90
BiC6-2	Guess	13.02	4.86	18.05	90	119.56	90
	Candidate (10th)	12.82	4.77	17.89	90	120.25	90

The cell parameters of the selected candidates are very close to the guessed ones. The BiC3-6 candidates are found in the 3rd, 4th, 41st and 38th positions of most energetically stable polymorphs within the crystal predictions, respectively. We point that this ranking is the result of the evaluation of the potential energy and polymorph search, but we cannot further precise the reason of the candidate ranking. On the other side, we want to explicitly mention the two different polymorph search procedures that we have used for finding the bisamide candidates.

The first procedure concerns BiC3 and BiC4. For their case, we predicted crystals allowing their torsion degrees of freedom to vary, as their alkyl chains are short and the energy landscape is not as rugged as in BiC5. Thus, in one crystal generation run we could find the candidates.

The second procedure concerns the BiC5 and BiC6-1,2 candidates. In their case, as the energy landscape is more rugged, a single run allowing their torsion angles to vary is insufficient. Thus, we sampled the energy landscape with different runs where the initial molecular conformations were different for each run, and we did not allow the torsion angles of the alkyl chains to vary in the run. This approach produces similar crystals within one run but very variated structures when considering all runs together.

It is also mandatory for candidates that they match the experimental XRD pattern after refining them. The XRD patterns of crystals with the same cell parameters have peaks at the same positions, but with an intensity that differs depending on the molecular packing within the unit cell. Matching the experimental XRD pattern is thus a critical criterion to choose the final candidate. We applied the refinement procedure described in the methodology section to our candidates, using the experimental XRD patterns and guessed cell parameters. This procedure allows us to discern if the candidate is the polymorph that we are looking for or not. The resulting crystals have practically identical molecular packings to those of the candidates, but with cell parameters fit to the guessed ones. Figure 4.13 shows the excellent match between the experimental and simulated XRD patterns of the refined candidates, meaning that the predicted molecular packing of the BiC3-BiC6 refined candidates is representative of that of the gel fibers.

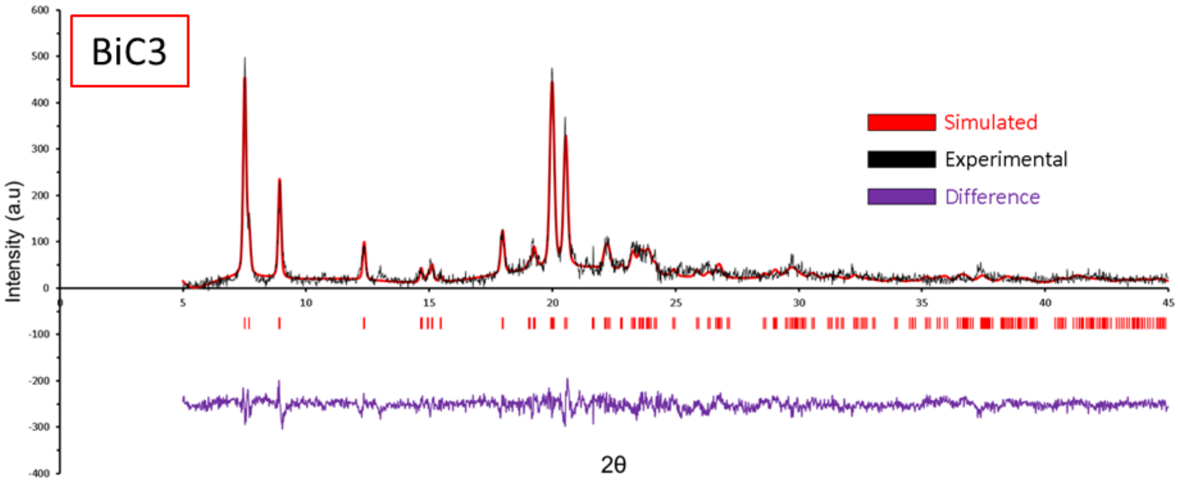

Figure 4.11: The BiC3-BiC6 simulated XRD patterns (red) against their experimental powder XRD pattern from our partners (black). The purple curve is the difference between them.

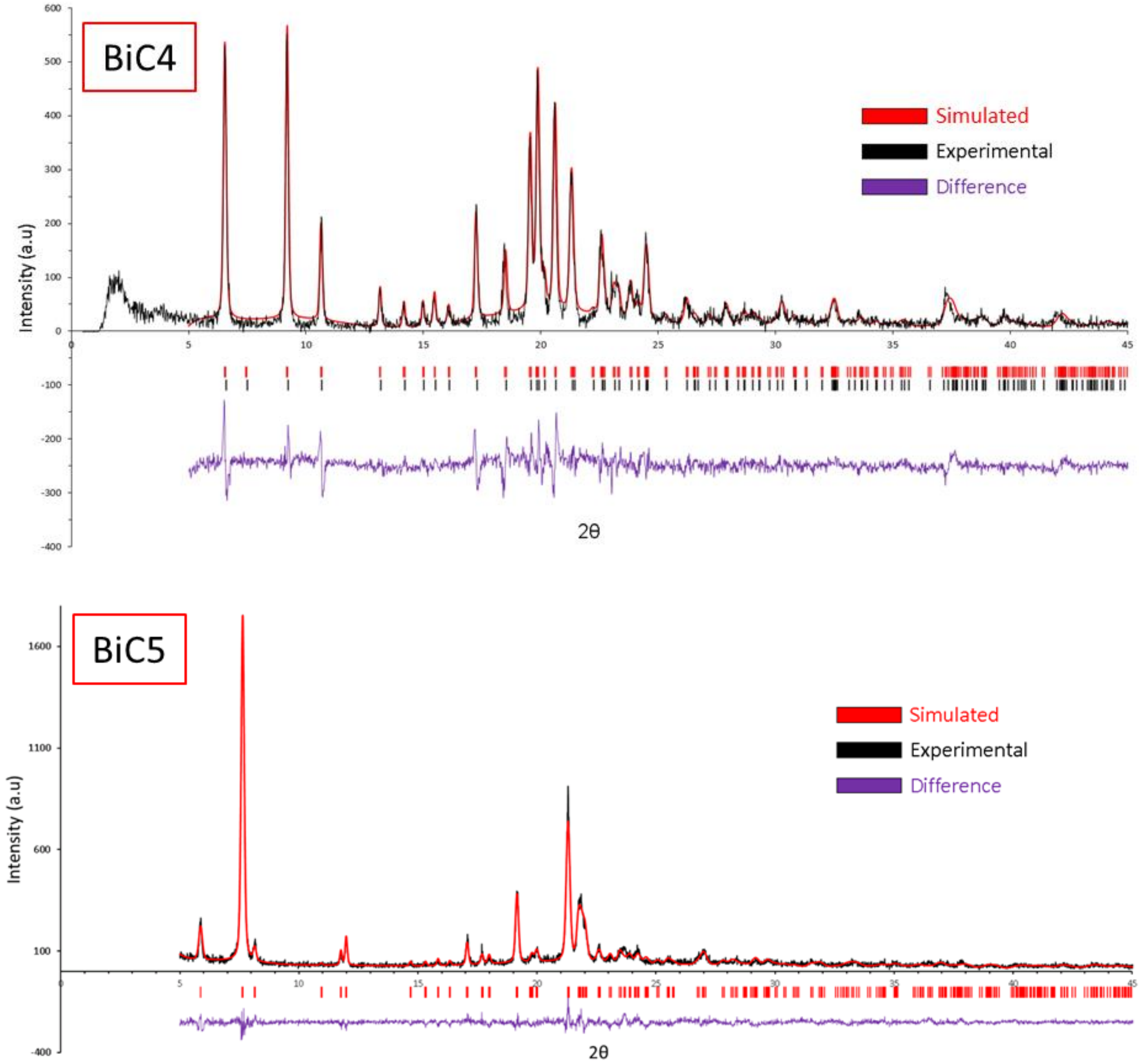

Figure 4.12 (continued): The BiC3-BiC6 simulated XRD patterns (red) against their experimental powder XRD pattern from our partners (black). The purple curve is the difference between them.

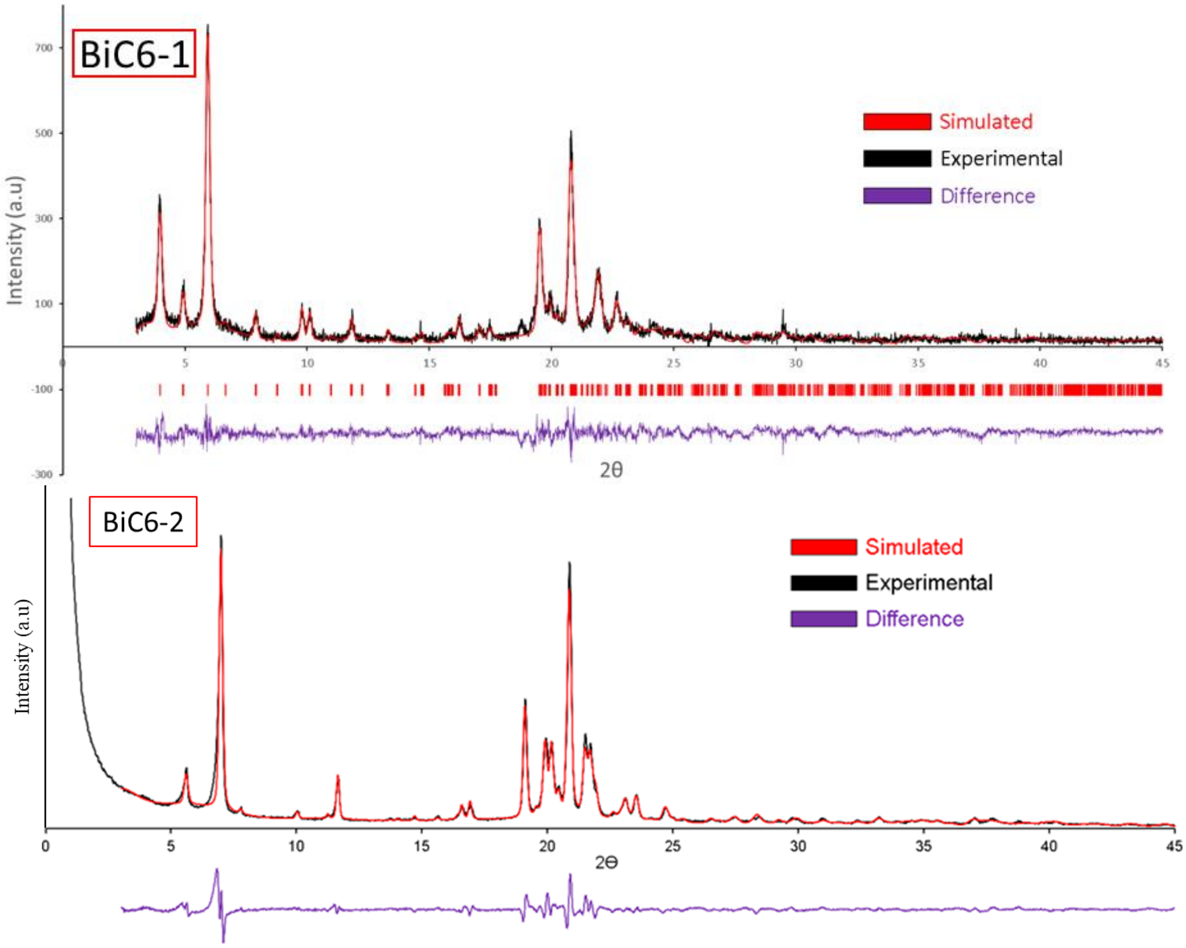

Figure 4.13 (continued): The BiC3-BiC6 simulated XRD patterns (red) against their experimental powder XRD pattern from our partners (black). The purple curve is the difference between them.

Next, we show in Figure 4.15 the predicted crystal structures for the BiC3-BiC6 compounds.

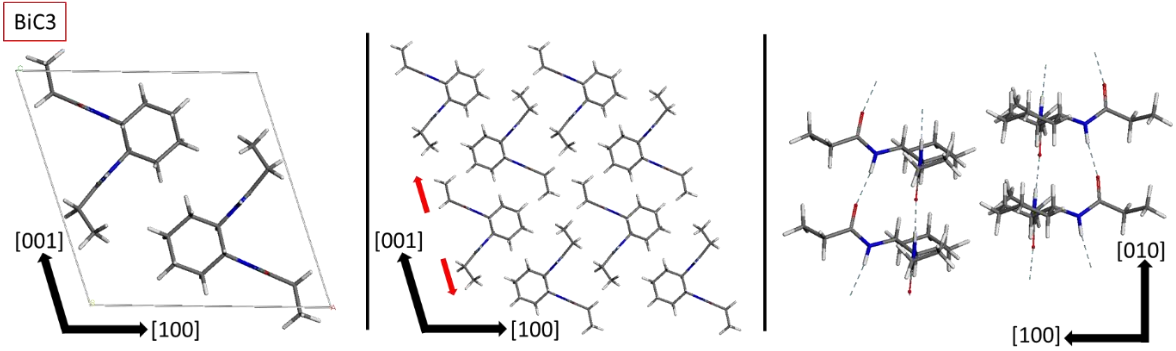

Figure 4.14: Predicted BiC3-BiC6 molecular packing. Left panel: the unit cell, center panel: the molecular packing and right panel: a lateral view showing the hydrogen-bonding pattern.

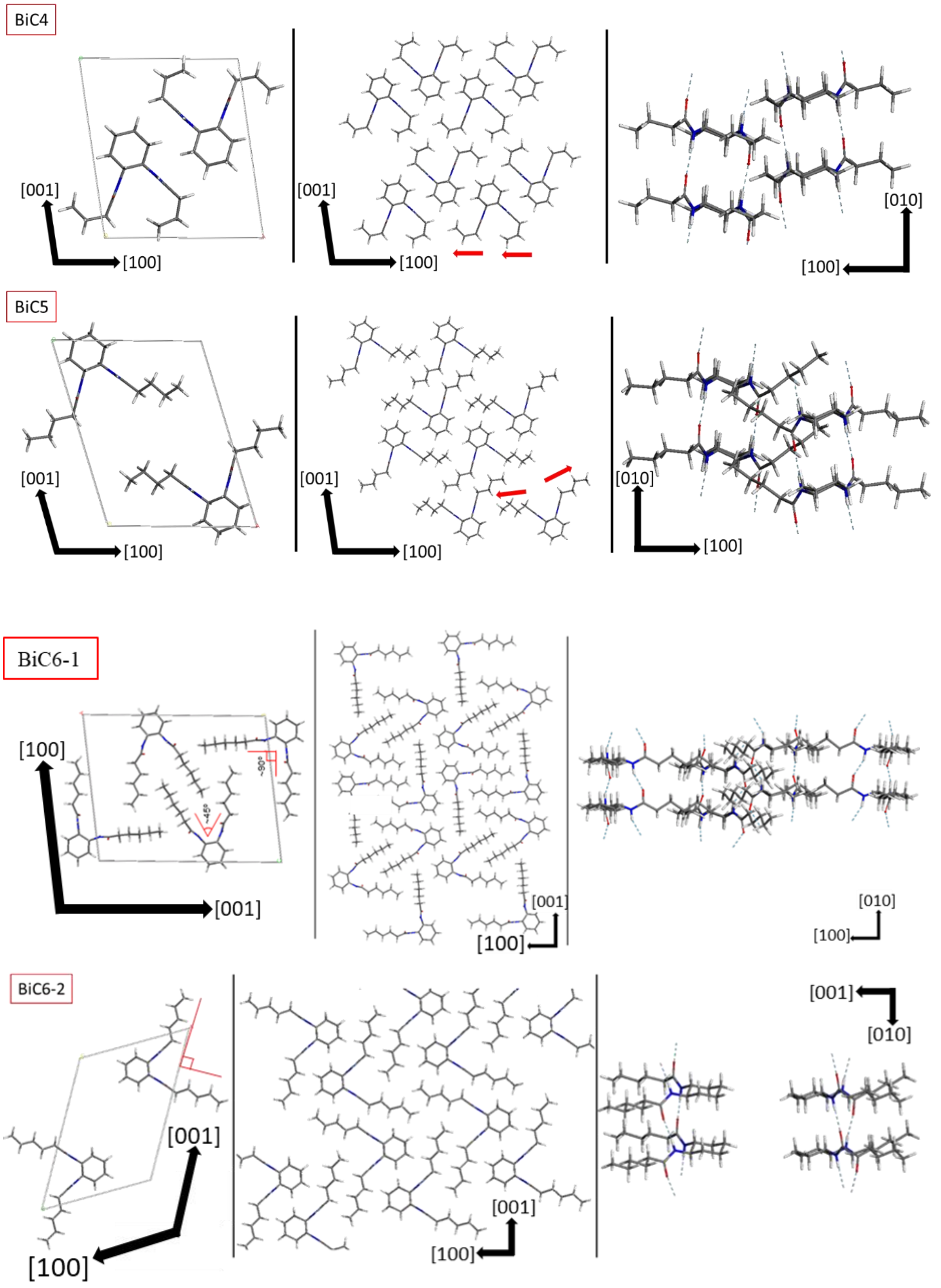

Figure 4.15 (continued): Predicted BiC3-BiC6 molecular packing. Left panel: the unit cell, center panel: the molecular packing and right panel: a lateral view showing the hydrogen-bonding pattern.

Figure 4.15 left panels show the unit cell composition for the BiC3-BiC6 structures. The BiC3-BiC5 and BiC6-2 structures have 2 molecules per unit cell while BiC6-1 has 4. All these crystals are of P_{2_1} space group, thus a rotation of 180º is followed by a translation of one half along b, the cell vector parallel to the rotation axis. Due to this symmetry element, there is only one conformation in BiC3-BiC5 and BiC6-2 while in BiC6-1 there are two: one with a ~45º angle between their alkyl chains and the other with an angle of ~90º. Figure 4.15 center panels show the molecular packing for the BiC3-BiC6 compounds and Figure 4.16 displays them all for a more straightforward comparison.

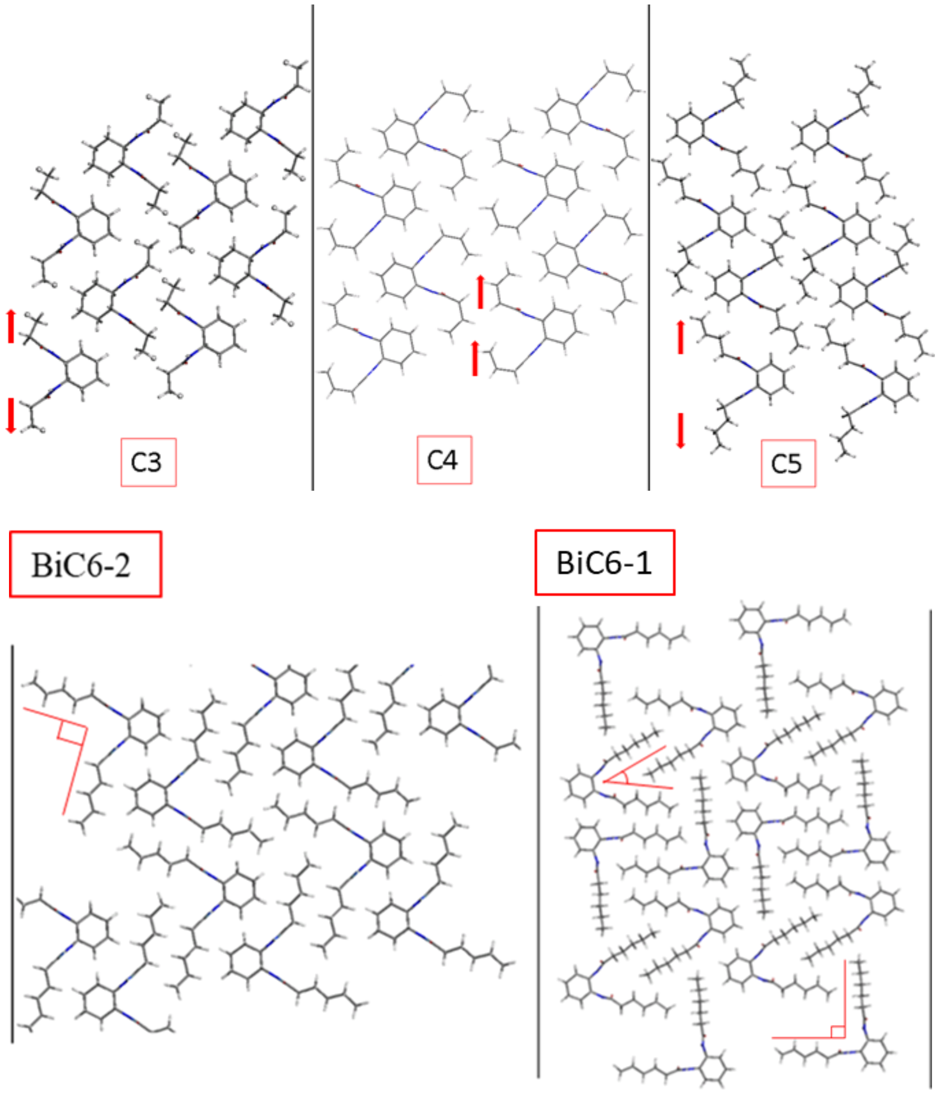

Figure 4.16: Molecular packing comparison for the BiC3-BiC6 compounds. For BiC3-BiC5, the red arrows show the orientation of the alkyl chains. In BiC6-1 and BiC6-2 the relative orientation of the alkyl chains is marked with red lines and angles.

The molecular packing diversity arises from the relative orientation of the alkyl chains. In the case of BiC3 and BiC5 the ends of the alkyl chains are oriented in opposite directions, while in BiC4 they are oriented towards the same side (see red arrows in Figure 4.16). In BiC6-1,2 the alkyl chains have a full trans conformation, maximizing the van-der-Waals interactions between them. BiC3 and BiC5 share the same molecular packing, which differs from that of BiC4 and BiC6-1,2. As the alkyl chains are mainly inscribed in the (010) crystal plane, more elongated or retracted alkyl chains affect directly the β angle. This effect could be the reason why the β shows an odd-even effect.

Figure 4.15 right panels show the hydrogen bonding network for the BiC3-BiC6 structures, characterized by a one-dimensionality in the [010] direction that may lead to the preferential growth of the fibers. This observation agrees with Hanabusa's hypothesis (see Figure 4.3) where bisamide molecules are stacked through a one-dimensional hydrogen-bond network. Table 4-5 shows the hydrogen-bond distances and N-H···O angles for the BiC3-BiC6 structures.

Table 4-5: Hydrogen-bond distance and angle for the BiC3-BiC6 structures.

	H-bonds	
	Distance (Å)	**Angle** (º)
BiC3	1.90	172.1
BiC4	1.92	167.5
BiC5	1.98	171.2
BiC6-1	1.88	148.0
BiC6-2	1.94	174.0

From BiC3 to BiC5 the hydrogen-bond distance increases while the evolution is less clear for the hydrogen-bond angle. In BiC6-1 hydrogen-bond distance is smaller but the angle is much more deviated from the ideal 180º than the previous ones. The larger is the distance and the more deviated is the angle from 180º, the weaker is the hydrogen bond strength. Here we have both effects combined and, in order to have a clear picture whether the hydrogen bonds are energetically stronger or weaker with the alkyl chain length, we look at the hydrogen bonding energy per hydrogen bond (see Table 4-6).

Table 4-6: Hydrogen bonding energy per hydrogen bond for the BiC3-BiC6 structures.

	BiC3	BiC4	BiC5	BiC6-1	BiC6-2
Energy per hydrogen bond (kcal/mol)	-3.7	-3.6	-3.5	-2.2	-3.4

The hydrogen-bonding energy decreases very slightly with the elongation of the alkyl chain from BiC3 to BiC5 and BiC6-2, while it is clearly much lower for BiC6-1. We mainly attribute this effect to the large angle deviation from the ideal 180º, as the hydrogen bonding energy is related to the angle (θ) by a $\cos^4(\theta)$ dependency (e.g. BiC3→$\cos^4(172.1) = 0.96$, BiC6-1→$\cos^4(148.0) = 0.52$, the energy being almost halved from BiC3 to BiC6-1 just with angle variations).

The BiC6-2 unit cell is characterized by two molecules with alkyl chains with ~90º of relative orientation between each other. As the BiC6-1 crystal also has molecules with this configuration, along with alkyl chains with ~45º relative orientation, these polymorphic molecular packings suggest that the relative orientation of the alkyl chains between them is critical. In order to determine their relative stability, we compare in Table 4-7 their density and cohesive energy ($E_{cohesive}$), defined as: $E_{cohesive} = -(E_{latt} - E_{monomers})/Z$, being E_{latt} the potential energy of the cell, $E_{monomers}$ the summed energy of the monomers isolated and optimized in vacuum and Z the number of molecules in the unit cell.

Table 4-7: Comparison of the BiC6-1 and BiC6-2 relative stability.

	Density (g/cm^3)	**$E_{cohesive}$** (kcal/mol)	**H-bonds**	
			Distance (Å)	**Angle** (º)
BiC6-1	1.06	77.83	1.88	148.0
BiC6-2	1.09	85.26	1.94	174.0

If we pay attention to density, the BiC6-2 crystal presents a denser packing than BiC6-1, and following the density rule [176], it should be more stable. Observing cohesive energy, the BiC6-2 is 7.43 kcal/mol more stable than BiC6-1, as the higher the cohesive energy, the more stable. In this case the density rule applies but from the 7.43 kcal/mol difference, we attribute two thirds of that difference to the hydrogen bond energy, i.e., the difference of hydrogen bond energy between BiC6-2 and BiC6-1 from Table 4-6 (3.4-2.2=1.2 kcal/mol per hydrogen bond)x4(H-bonds/unit cell)=4.8kcal/mol, while 7.43-4.80=2.63 kcal/mol may be attributed to the dispersive interactions. Thus, we point that the hydrogen bond geometries play a significant role in the BiC6 polymorphism, BiC6-1 being probably the kinetically stable crystal. In order to confirm this hypothesis, we combine the crystal structure generation results from BiC6-1 and BiC6-2 in one plot and spot the two polymorphs, dividing the BiC6-1 energies by 2 to be comparable (see Figure 4.17).

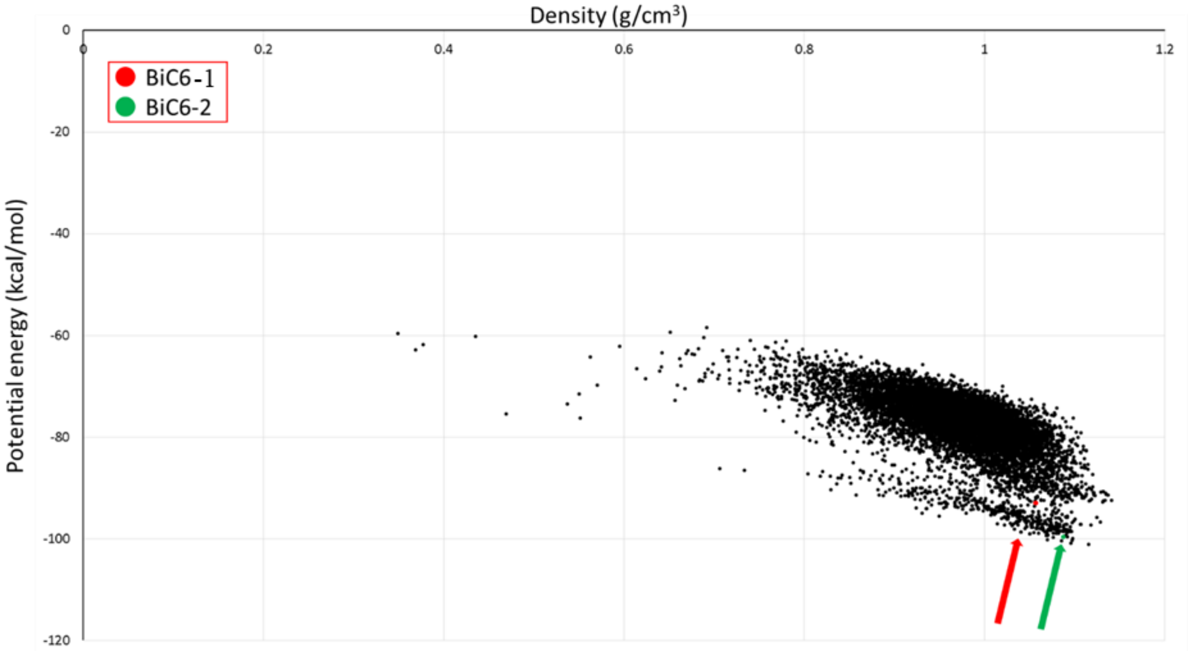

Figure 4.17: Combination of the BiC6-1 and BiC6-2 crystal structures generated with the CSP method. The (red) green dot and arrow corresponds to the (BiC6-1) BiC6-2 candidates.

For completion, we take the BiC3 and BiC5 crystals and we orient the alkyl chains towards the same direction (as in BiC4) and relax the molecular geometry without changing the cell parameters, to account only for molecular packing effects. We do the same for BiC4 but orienting their alkyl chains towards opposite sides (as in BiC3 and BiC5) and we also analyze the BiC3-BiC5 systems with fully trans alkyl chains. Table 4-8 compares their relative stability by computing their cohesive energy ($E_{cohesive}$).

Table 4-8: Comparison of the relative stability of the BiC3-BiC5 compounds with alkyl chains pointing towards the same directions, opposite directions or fully *trans*. We highlight in bold the structure found by the CSP method.

	$E_{cohesive}$ (kcal/mol)		
	BiC3	**BiC4**	**BiC5**
Fully trans	71.5	79.4	81.9
Same direction	70.6	**79.9**	81.4
Opposite direction	**72.0**	76.8	**81.8**

This comparison confirms that the observed conformation for BiC3 and BiC4 is indeed more stable than its conformational counterparts (1.4 and 0.5 kcal/mol for BiC3 and 3.1 and 0.5 kcal/mol for BiC4). For BiC5 the observed conformation is 0.4 kcal/mol more stable than its analog with the alkyl chains pointing in the same direction, and as stable as the fully trans conformation. As mentioned, the longer the alkyl chain the more favorable is the fully *trans* conformation, maximizing the van-der-Waals interactions between alkyl chains. Thus, this observation leads us to think that there could be a polymorph crystal of BiC5 with fully extended alkyl chains. In fact, the alkyl chains are fully extended in the BiC6 molecules, which suggests that this conformation could be highly relevant from BiC5 onwards. All the conformations commented above are shown in Figure 4.19.

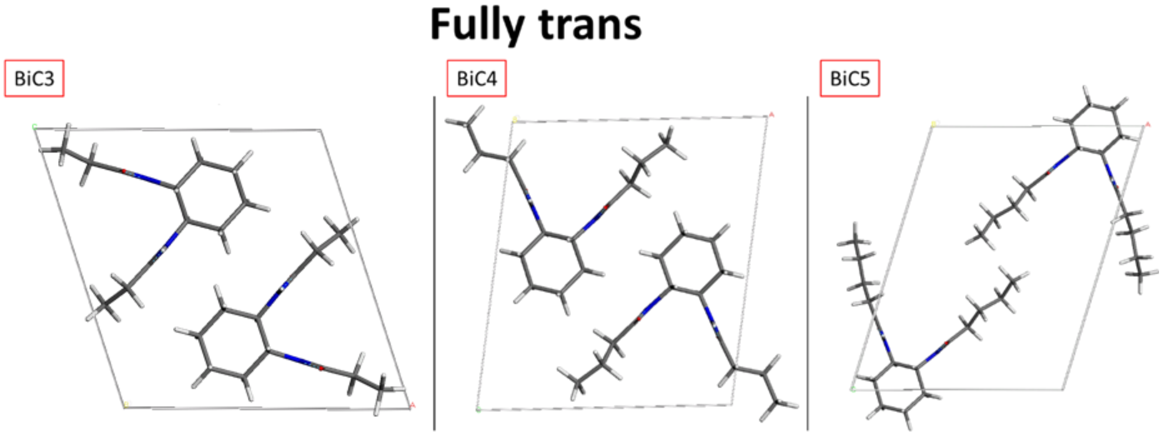

Figure 4.18: Packing configurations of BiC3-BiC5 with alkyl chains that are fully *trans*, in the same direction, and in opposite directions, respectively. The packings were optimized while freezing the cell parameters.

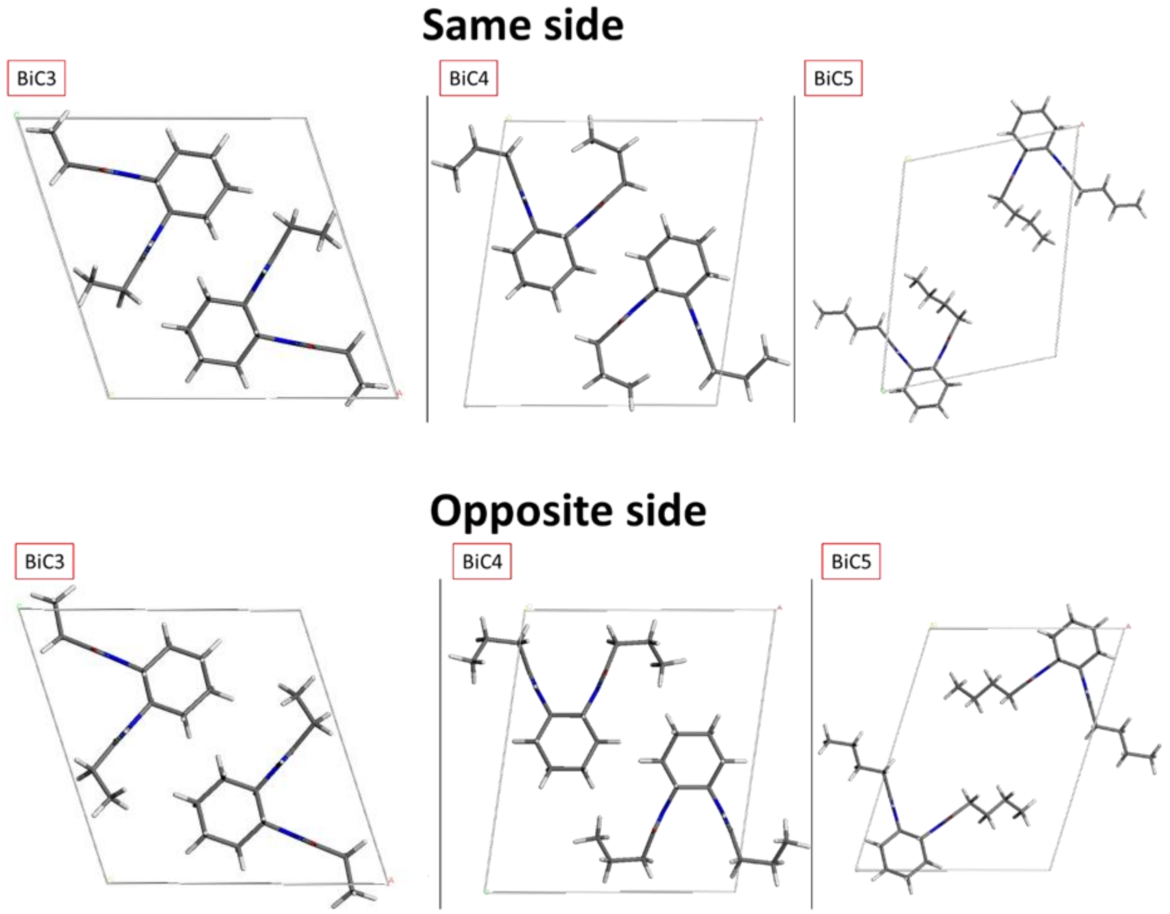

Figure 4.19 (continued): Packing configurations of BiC3-BiC5 with alkyl chains that are fully *trans*, in the same direction, and in opposite directions, respectively. The packings were optimized while freezing the cell parameters.

4.3 Crystal Morphology characterization

After determining the crystal structure of the bisamide compounds, we move to the study of their crystal morphology, first by employing the BFDH method, which uses only geometrical considerations (see Figure 4.21).

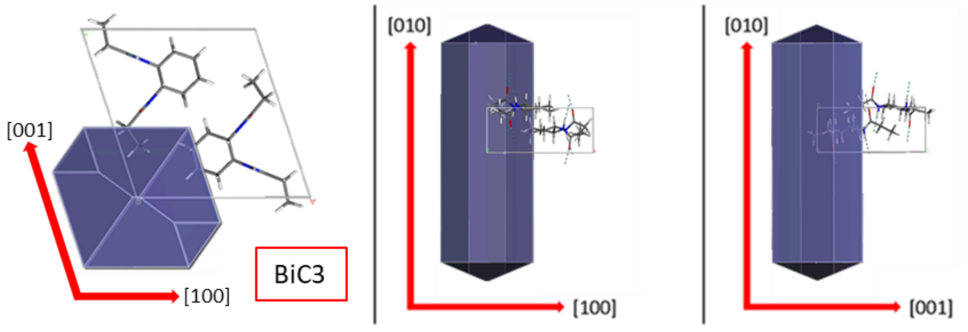

Figure 4.20: Computed crystal morphology for the BiC3-BiC6 structures with the BFDH method.

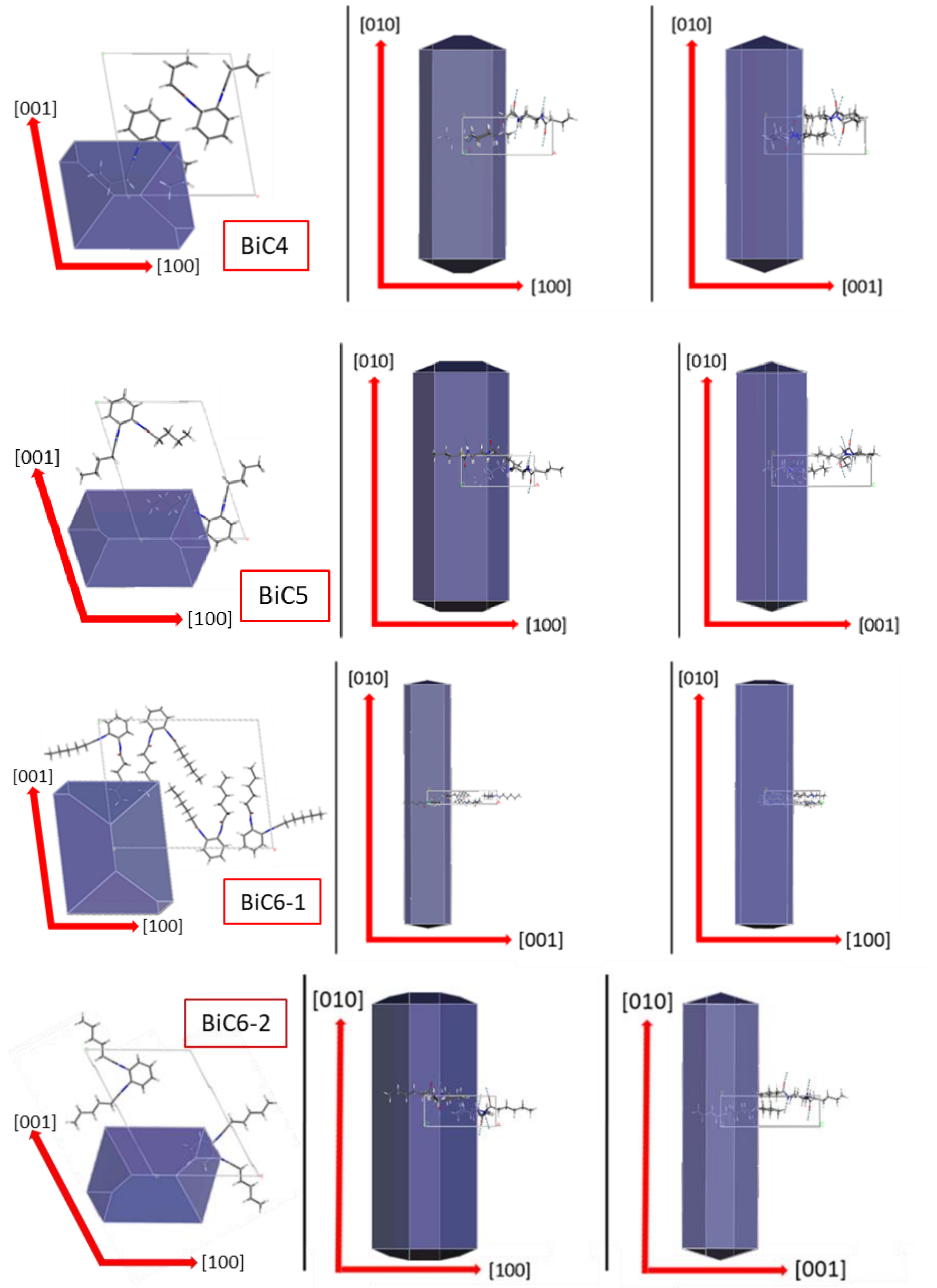

Figure 4.21 (continued): Computed crystal morphology for the BiC3-BiC6 structures with the BFDH method.

The BFDH method captures the one-dimensional preferentiality of the crystal, having a preferential growth direction along the [010] direction. However, this method does not provide any information about the energetics involved in the preferential growth of the fiber or the chemical composition of the facets displayed, which is essential for understanding their gelation behavior.

For this purpose, we then moved to the GMM method, which is based on the attachment energy, and therefore provides an energetic description of the crystal morphology. This method is appropriate as gel fibers are grown in solution, i.e. under non-equilibrium growth conditions. Figure 4.23 shows the computed crystal morphologies for the BiC3-BiC6 series. There is also a preferential crystal growth in the [010] direction, along the one-dimensional hydrogen-bonding pattern.

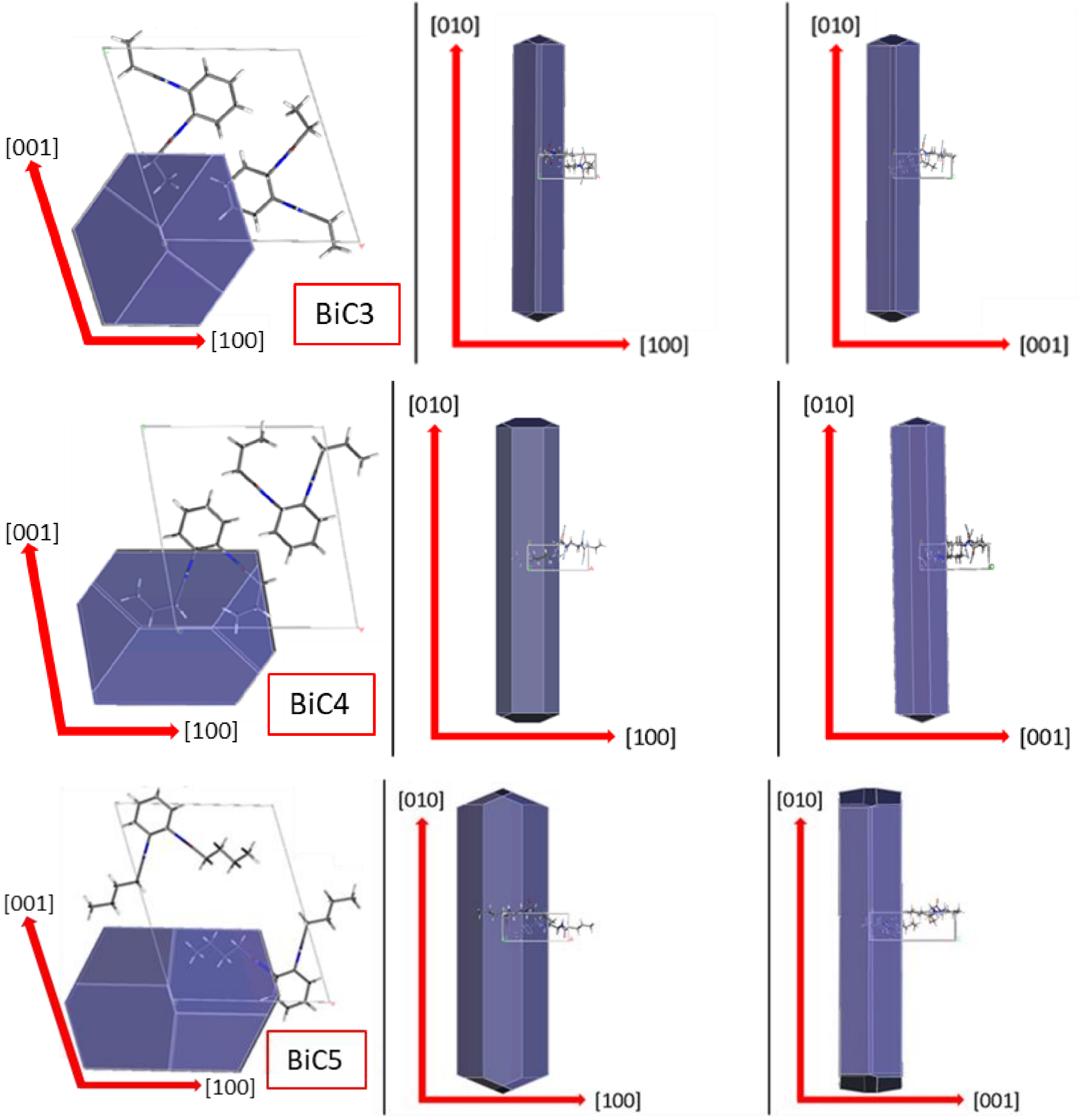

Figure 4.22: Computed crystal morphology for the BiC3-6 and BiC6-2 compounds with the GMM method.

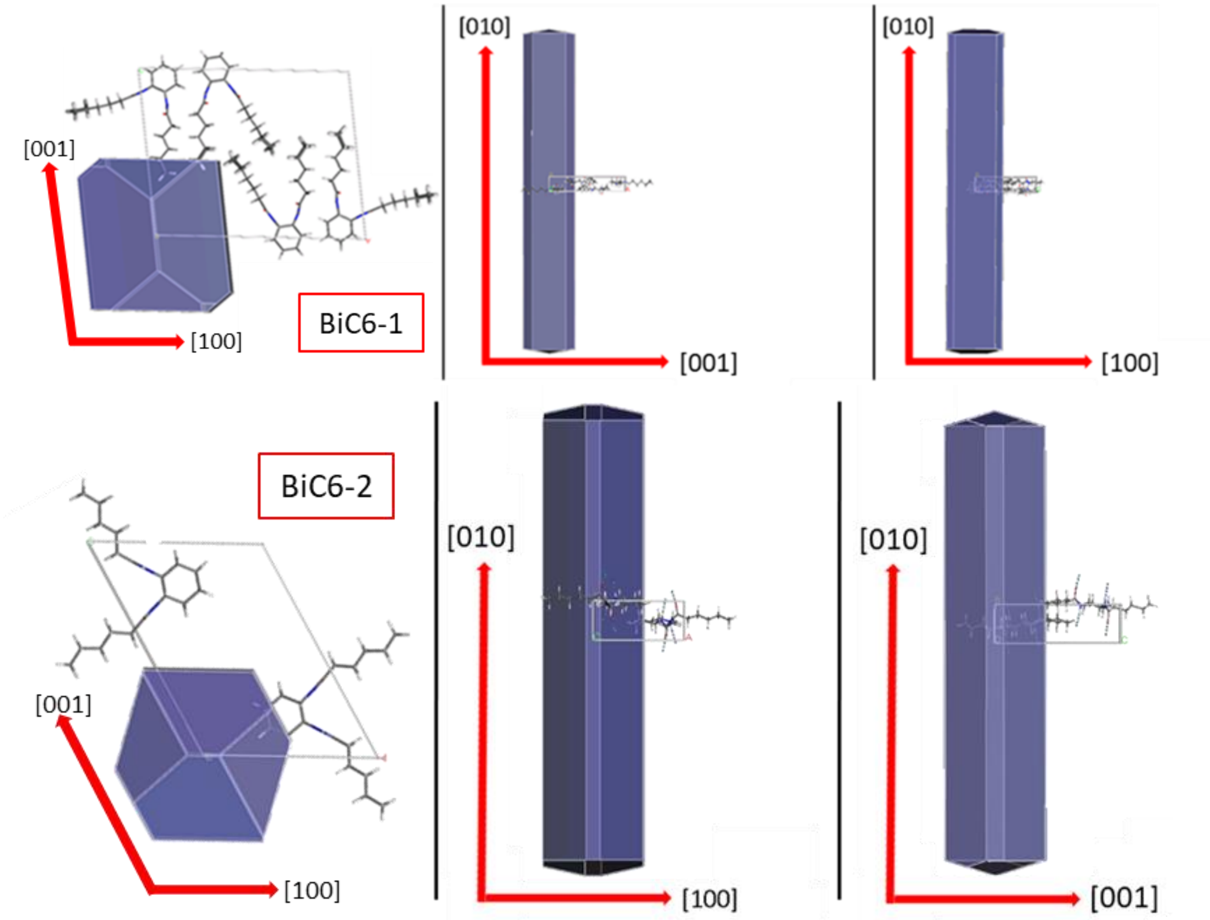

Figure 4.23 (continued): Computed crystal morphology for the BiC3-6 and BiC6-2 compounds with the GMM method.

The computed crystal morphology is characterized by its aspect ratio, its surface to volume ratio, and its facets (which crystal planes form these facets, which proportion of the total crystal surface they occupy, and which functional groups are exposed). We start analyzing the facets, showing the nature and coverage of the most relevant facets of the BiC3-6 compounds (see Table 4-9).

Table 4-9: Percentage of crystal area for the most relevant facets for BiC3-BiC6 obtained by GMM.

	{001}	**{100}**	**{10-1}**	**{110}**	**{1-10}**	**{011}**	**{0-11}**	**Total**
BiC3	30%	31%	29%	3%	3%	2%	2%	100%
BiC4	41%	30%	19%	1%	1%	4%	4%	100%
BiC5	43%	9%	38%	-	-	5%	5%	100%
BiC6-1	38%	44%	10%	3%	3%	1%	1%	100%
BiC6-2	33%	25%	32%	-	-	3%	3%	96%

The most relevant exposed facets of the bisamide family are the {001}, {100}, {10-1}, {110}, {1-10}, {011} and {0-11} facets. The notation {hkl} correspond to planes that are equivalent to the (hkl) planes by symmetry, for instance {100} comprises the (100) and (-100) facets. Mention that the {11-1} and {1-1-1} facets only appear for BiC6-2, accounting for a 2% of the total crystal area each. A straightforward comparison between the bisamide compounds is rather difficult as the molecular packing changes when elongating the alkyl chain.

However, we observe that the {h0l} facets are the largest ones through the family and they always sum up to more than 90% of the total facet area. The hydrogen-bonding network through the [010] direction is responsible for this ranking because the {h0l} facets only expose alkyl chains or cyclohexane rings to the environment, while facets with a non-zero $\vec{k}$ component also expose amide groups to the environment, increasing the instability of the facet, which thus grows faster. For instance, for BiC3, the attachment energy related to hydrogen-bonds and electrostatic interactions are 0 and less than 1 kcal/mol, respectively for {001}, {100} and {101} while it is ~15 and ~30 kcal/mol, respectively, for the {011} and {0-11} facets.

To evaluate which functional groups are exposed on the facets, a simulated crystal has been cut perpendicularly to the facets, thus revealing the organization of the molecules from the bulk of the crystal to the surface. Figure 4.25 represents the result for BiC3. We remind that a facet may expose different chemical compositions depending on the position where the crystal is cleaved. Each different chemical composition of a facet is called a termination. The facet terminations displayed in Figure 4.25 are the most stable ones, i.e., other molecular coverings of the facets are less stable. The different terminations of the facets are shown in the Annex for BiC3, as an illustrative case for the bisamide structures.

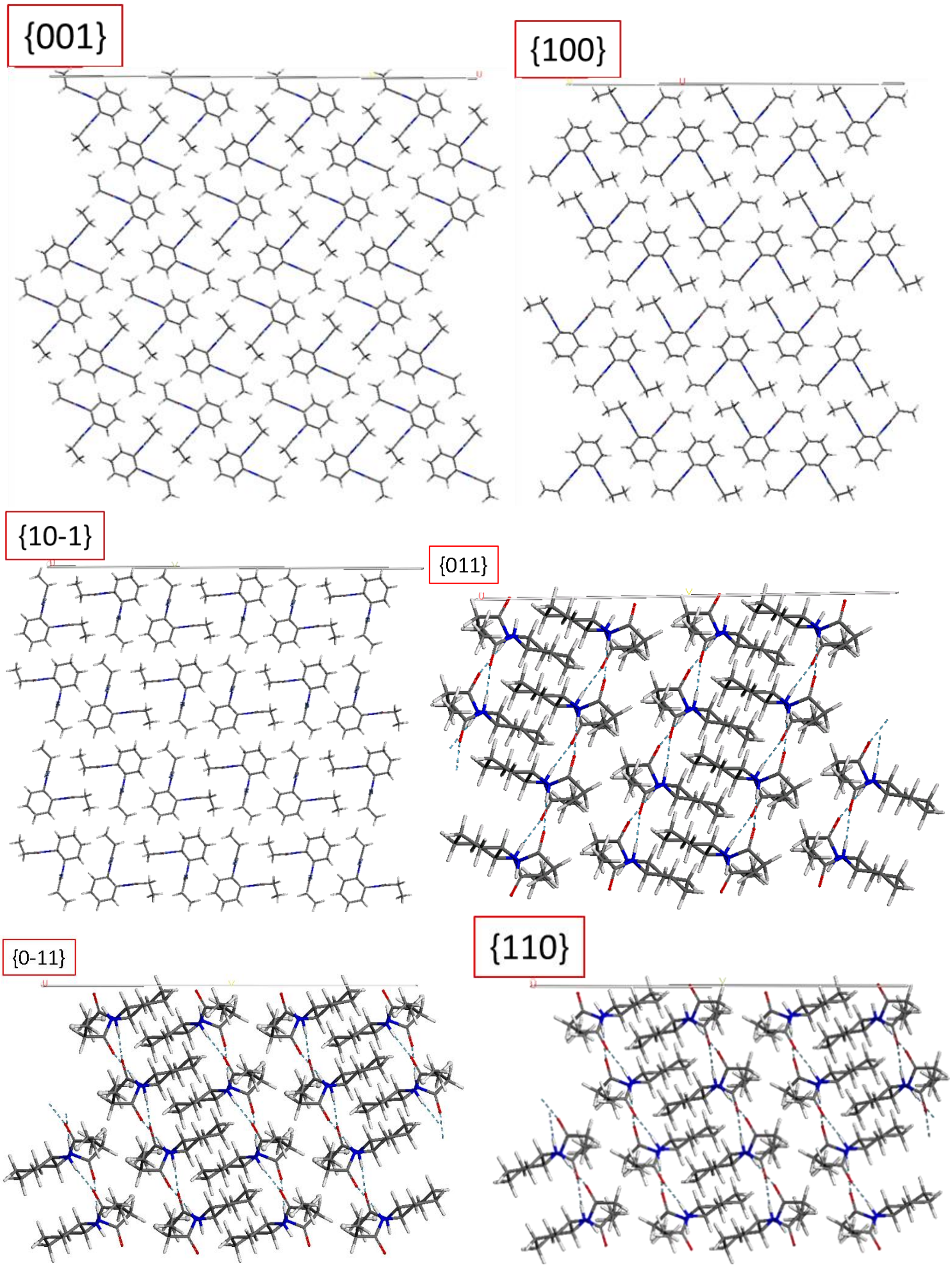

Figure 4.24: Organization of the molecules in the BiC3 crystal, from the bulk of the crystal to different facet surfaces; the surface is on top of the images, seen perpendicularly.

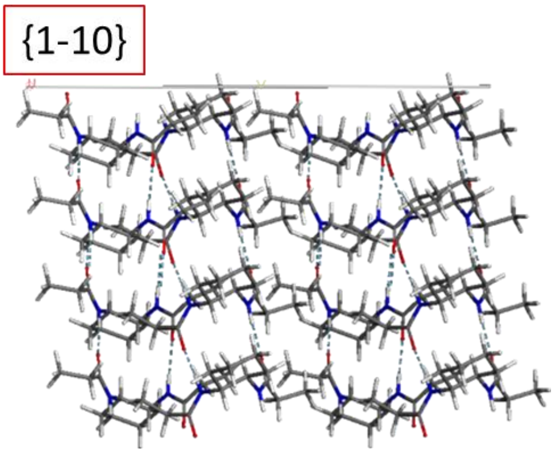

Figure 4.25 (continued): Organization of the molecules in the BiC3 crystal, from the bulk of the crystal to different facet surfaces; the surface is on top of the images, seen perpendicularly.

In the facet chemical composition, alkyl chains could be either protruding, forming sharp kinks on the surface, or lying flat, forming smooth terraces or steps. The kinks formed by protruding alkyl chains increase the roughness and surface area of the facet in comparison with the terraces or steps formed by alkyl chains lying flat. We calculate the Connolly surface area [177], [178] of the facets displayed in Figure 4.25 with a probe size of 1.4Å to provide a clearer picture of the roughness of the bisamide facets (see Figure 4.28).

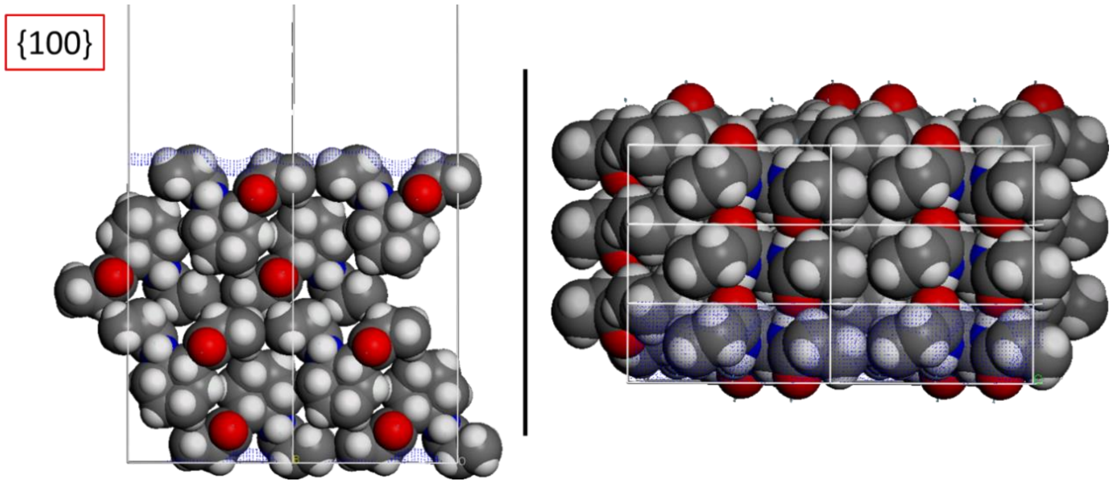

Figure 4.26: BiC3 facets seen parallel (left) and perpendicularly (right) to the surface. The Connolly isosurface is represented with blue dots.

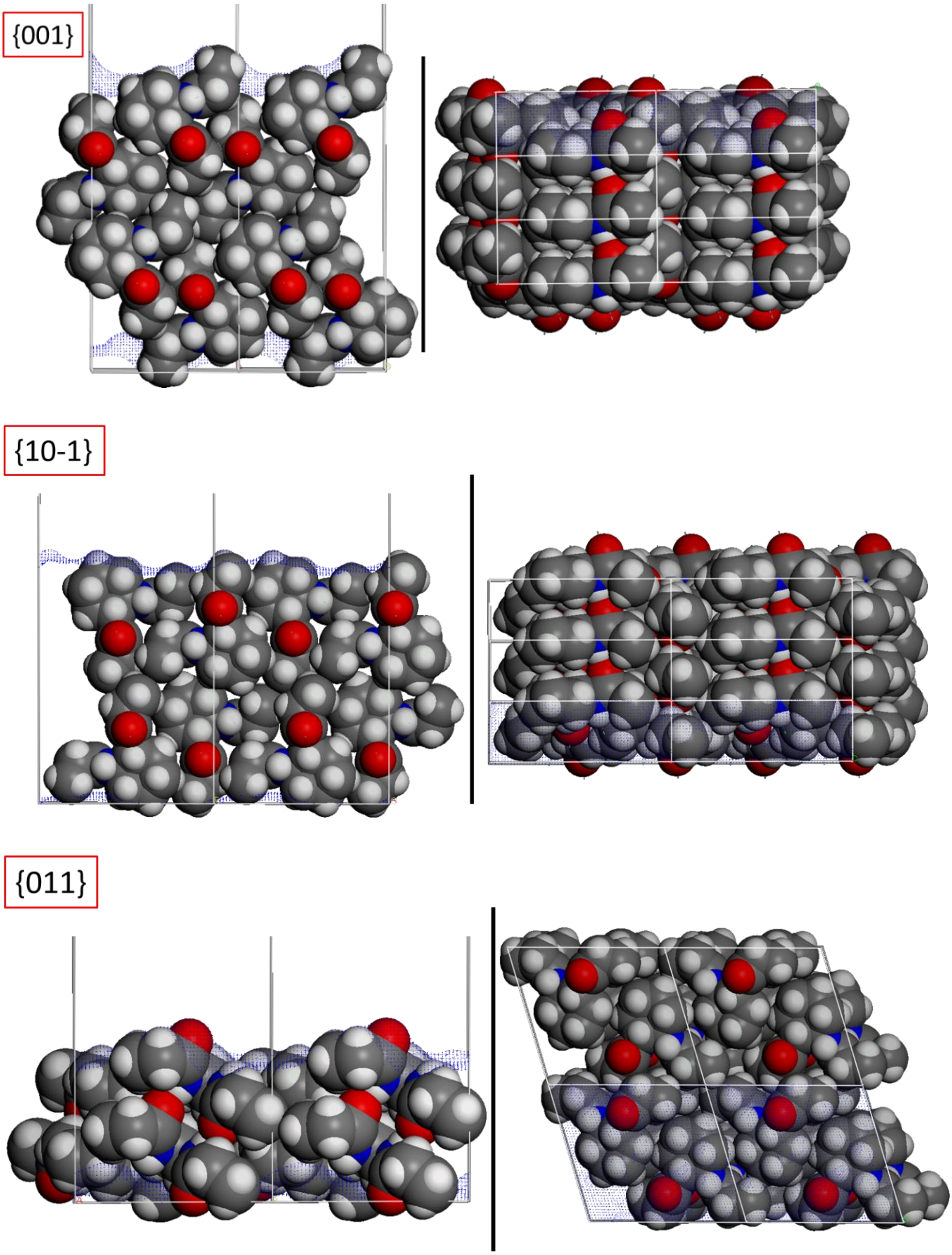
{001}

{10-1}

{011}

Figure 4.27 (continued): BiC3 facets seen parallel (left) and perpendicularly (right) to the surface. The Connolly isosurface is represented with blue dots.

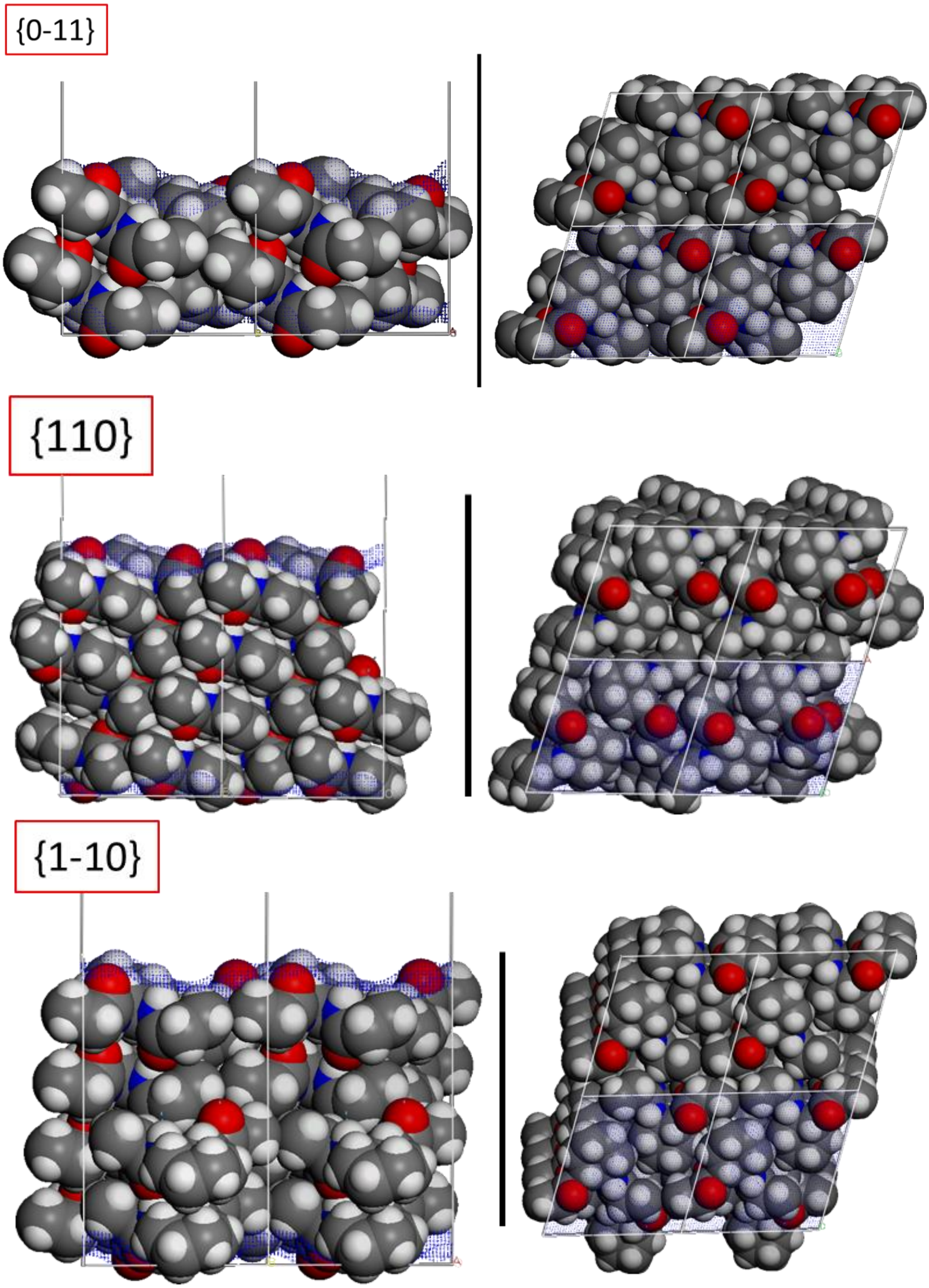

Figure 4.28 (continued): BiC3 facets seen parallel (left) and perpendicularly (right) to the surface. The Connolly isosurface is represented with blue dots.

The higher the roughness, the higher the surface area. Table 4-10 shows the roughness ratio of each facet, calculated as: Roughness ratio $= \frac{\text{Connolly area}}{\text{Flat area}}$. Note that the surface areas correspond to the areas of the planes contained in a unit cell.

Table 4-10: Roughness ratio of the BiC3 facets.

	Flat surface area (Å^2)	Connolly surface area (Å^2)	Roughness ratio
{100}	58.94	69.42	1.18
{001}	57.65	80.77	1.40
{10-1}	68.41	76.81	1.12
{011}	151.54	179.94	1.19
{0-11}	151.54	179.92	1.19
{110}	152.03	174.91	1.15
{1-10}	152.03	174.90	1.15

Generally, surfaces tend to minimize their area to increase their stability [27]. Thus, the bisamide family dominant facets are as smooth and apolar as possible. All the facets have a low roughness value, only the {001} deviates slightly. Among the {h0l} facets, the {001} facet slightly protrudes alkyl chains outwards, increasing the roughness with respect to the {100} facet where alkyl chains lie parallel, but this does not affect the facet area, as both facets have same surfaces. Finally, the {011} and {0-11} facets have a small percentage of facet area despite having a lower roughness value. We can rationalize this relation examining their attachment energies (E_{att}), which depend both on the surface defined by the plane contained in the unit cell (here almost three times the value that {100} and {001} have, see Table 4-10), and the nature of terminations. To better understand these effects, we separated the attachment energies into their dispersive, electrostatic and hydrogen-bonding components ($E_{att,D}$, $E_{att,P}$ and $E_{att,H}$, respectively) in Table 4-11.

Table 4-11: Attachment energies of the relevant BiC3 facets.

	E_{att} (kcal/mol)	$E_{att,D}$ (kcal/mol)	$E_{att,P}$ (kcal/mol)	$E_{att,H}$ (kcal/mol)
{100}	-13.3	-12.7	-0.6	0.0
{001}	-13.7	-13.6	-0.1	0.0
{10-1}	-12.7	-12.6	-0.1	0.0
{011}	-69.7	-24.5	-30.4	-14.8
{0-11}	-69.7	-24.5	-30.4	-14.8
{110}	-68.8	-23.7	-30.3	-14.8
{1-10}	-68.8	-23.7	-30.3	-14.8

The {100}, {001} and {10-1} facets have a similar attachment energy and facet area, strongly differing from the {011} and {0-11} facets. The attachment energy is much higher in the latter ones due to: (i) a surface per unit cell two to three times larger than that of the {h0l} facets, doubling the dispersive contribution, and (ii) the presence of amide groups, giving rise to electrostatic and hydrogen bonding contributions.

We now analyze the two geometrical features of the crystals: aspect ratio and surface to volume ratio (see Table 4-12). We also include the same parameters computed with the BFDH method as the BFDH method only includes geometrical effects. Thus, the differences between the BFDH and GMM methods allow us to analyze how much contribution is attributed to geometrical or energetic effects.

Table 4-12: Aspect ratio and surface to volume ratio computed with the GMM and BFDH methods for the BiC3-BiC6 crystals.

	Aspect ratio		**Surface to volume ratio**	
	GMM	**BFDH**	**GMM**	**BFDH**
BiC3	5.87	2.84	1.49	1.25
BiC4	5.80	3.10	1.48	1.28
BiC5	6.00	3.46	1.55	1.29
BiC6-1	6.37	5.39	1.57	1.49
BiC6-2	4.85	3.57	1.43	1.31

The first observation is that both quantities evolve similarly and are always larger when computed with the GMM than with the BFDH method. The larger values indicate that, for this family of compounds, the inclusion of the energetic contribution reinforces the unidirectional growth and a larger surface exposure. As in BFDH we do not explicitly calculate interactions, it is equivalent to say that interactions are homogeneous in the crystal. Thus, the increase of the aspect ratio obtained by GMM reflects the asymmetry of the energy interactions, as hydrogen bonds only occur along the [010] direction. The difference between the two sets of aspect ratio values decreases from BiC3 to BiC6, as the amide effect is likely diluted by the growth of alkyl chains.

The BFDH method shows an increasing aspect ratio with the elongation of the alkyl chain due to an increasingly larger difference between the (010) and (001) interplanar distances, which increases the asymmetry in the unit cell. We also observe this effect on the evolution of the {001} facet area percentages (see Table 4-13).

Table 4-13: Percentage of facet area of the exposed facets for the BiC3-BiC6 structures, as computed with the BFDH method.

	{001}	**{100}**	**{10-1}**	**{011}**	**{0-11}**	**{110}**	**{1-10}**	**Total**
BiC3	33%	31%	17%	4%	4%	4%	4%	97%
BiC4	39%	33%	10%	5%	5%	3%	3%	98%
BiC5	42%	24%	17%	6%	6%	2%	2%	99%
BiC6-1	47%	36%	7%	2%	2%	3%	3%	100%
BiC6-2	41%	15%	28%	5%	5%	1%	1%	96%

We would like to mention that the morphology calculations have been done without including the effect of the solvent while experimentally gel fibers are grown in solution. It is worth to mention that the organization of the molecules inside the crystal are unaffected by the solvent, except when it co-crystallizes with the molecules, which is not the case in the systems studied here. We are aware that solvents are key during gel formation and they could conform part of the fiber bundles [53]. However, including solvent in the simulations would highly increase the computational cost of the crystal morphology determination when this effect may just (de)stabilize some facets which would lead to different percentages of facet areas. For instance, a hydrogen-bond acceptor solvent could enhance the stability of the facets of a non-zero $\vec{k}$ component with respect to the {h0l} facets. We expect that this effect is small when the gelator-solvent interaction is non-specific, e.g., with van-der-Waals interactions, but it could be larger when there is specificity, e.g., with hydrogen-bonding. We should keep this effect in mind when making connections with experimental observations.

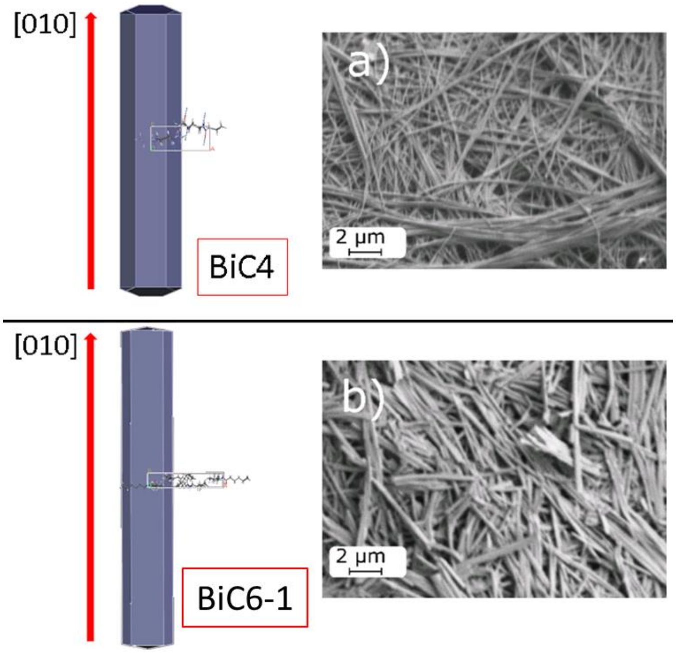

Figure 4.29: Comparison of the modelled crystal morphology for BiC4 (top) and BiC6-1 (bottom) against their respective experimental SEM images from our experimental partners. Top panel: BiC4, bottom panel: BiC6-1.

In Figure 4.29 we compared the computed crystal morphologies of BiC4 and BiC6-1 against their respective experimental SEM images. We observe fibrillar structures from both methodologies. The experimental gel fibers may be formed by agglomerated bundles of primitive, simpler fibrillar units [53]. We hypothesize that our computed crystal morphologies could be the primitive fibrillar unit that aggregates.

4.4 Rationalizing experiments from modelling

Next, we aim to connect our theoretical simulations with the HSP analysis of the gelation behavior by our partners (see Table 4-14).

Table 4-14: HSP values and radius of the center of the gelation sphere of the bisamide compounds. Reproduced from the thesis manuscript of Danilo Nunes Rosa (*Sorbonne Université*).

	δ_D (MPa$^{1/2}$)	δ_P (MPa$^{1/2}$)	δ_H (MPa$^{1/2}$)	Radius of gelation (MPa$^{1/2}$)
BiC3	-	-	-	-
BiC4	17.5±1.4	10.1±0.7	6.4±1.4	12.0±0.7
BiC5	14.8±0.4	12.1±0.6	16.8±0.4	21.1±0.4
BiC6	16.3±0.3	10.9±0.3	13.8±0.3	19.9±0.4
BiC8	16.3±0.3	11.4±0.3	12.7±0.2	20.1±1.8
BiC12	16.8±0.3	10.1±0.3	11.3±0.2	17.1±0.3
BiC14	16.8±0.3	10.2±0.3	11.3±0.3	16.9±0.3
BiC16	16.4±0.2	9.3±0.3	9.3±0.3	13.8±0.2
BiC18	16.4±0.2	9.3±0.3	9.3±0.3	13.8±0.2

No values are reported in the table for the BiC3 compound, as there is not enough gelation data to determine accurately the center of the gelation sphere (gels were only observed with 1-chloropentane and cyclohexane). The BiC4 values should also be taken carefully as the uncertainty is higher, as the center of the gelation sphere was determined with a limited amount of gelation dots. In order to have some familiarity with the experimental δ_i values, we provide first the HSP parameters of a few well-known solvents in Table 4-15 so the reader has a point of comparison.

Table 4-15: HSP parameters of a few well-known solvents.

	δ_D ($MPa^{1/2}$)	δ_P ($MPa^{1/2}$)	δ_H ($MPa^{1/2}$)
Toluene	18.0	1.4	2.0
Methanol	14.7	12.3	22.3
Water	15.5	16.0	42.3
N-methylformamide	17.4	18.8	15.9
Hexadecane	16.3	0	0

To explain the experimental evolution of the three HSP parameters when increasing the alkyl chain length, we used the EMM method to compute the surface energies of the facets, breaking down each facet in hydrogen-bonding, electrostatic, and dispersive contributions.

From BiC5, the experimental $\boldsymbol{\delta_H}$ values decrease constantly with the elongation of the alkyl chain. This decrease could mean that the contribution of the hydrogen bonds to the total surface energy decreases with the alkyl chain length. In Table 4-6 we analyze the energetics of one hydrogen bond from BiC3 to BiC6, and it indeed shows a decreasing trend. But more fundamentally, hydrogen bonding is diluted among other interactions (see
Table **4-16**).

Table 4-16: Hydrogen-bonding surface energy for the most relevant facets (kcal/mol).

	{001}	**{100}**	**{10-1}**	**{011}**	**{0-11}**	**{110}**	**{1-10}**
BiC3	0.0	0.0	0.0	33.9	33.9	33.9	33.9
BiC4	0.0	0.0	0.0	31.5	31.5	31.0	31.0
BiC5	0.0	0.0	0.0	27.2	27.2	26.2	26.2
BiC6-1	0.0	0.0	0.0	16.0	16.0	16.1	16.1
BiC6-2	0.0	0.0	0.0	22.8	22.8	21.9	21.9

The hydrogen-bonding network extends through the [010] direction, and is thus absent from the {h0l} facets, which thus do not participate in potential hydrogen bonds with the solvent. Concerning the {011}, {0-11}, {110} and {1-10} facets, as they have a non-zero $\vec{k}$ component, there are amide bonds pointing outwards and consequently they do have a hydrogen-bonding contribution, which decreases monotonously from BiC3 to BiC6, mainly due to the dilution by alkyl chains and the increasing area of the plane inside the unit cell. This trend matches with the experimental one, pointing that the decrease of the δ_H values is attributed to a subsequently weaker role of the hydrogen-bonds.

Initially, we though that the lateral facets of the fiber, the {h0l} facets, were mainly responsible of the fiber aggregation that finally leads to the fibrillar network. However, the experimental δ_H values are far from being zero. Thus, we think that due to the specific hydrogen-bonding interaction between the gelator and the solvent, when the solvent is able to form hydrogen bonds, the non-zero $\vec{k}$ component facets, which are present on the tips of the fibers, may be stabilized enough to play a role too. The contribution of the tips of the fibers to organogelation has also been considered previously in literature [179]–[183]. For example, in Reference [179], the authors discuss about how the 3D fibrillar network is formed during organogelation. The popular idea is that the gelator molecules self-assemble forming fibers which then entangle and form the 3D network. In Reference [179] the authors propose that the 3D network is formed by a branching process at the tips of the growing fibers. This proposed mechanism is based on the hypothesis that a solvent molecule, or an additive in their case, adsorbs on the tip of the growing fiber causing a mismatch for the daughter growing fibers. This mismatch results in a divergence of the new growing fibers that produces a branching that finally leads to the formation of the 3D network. The authors named this mechanism the Crystallographic Mismatch Branching (CMB) mechanism (see Figure 4.30).

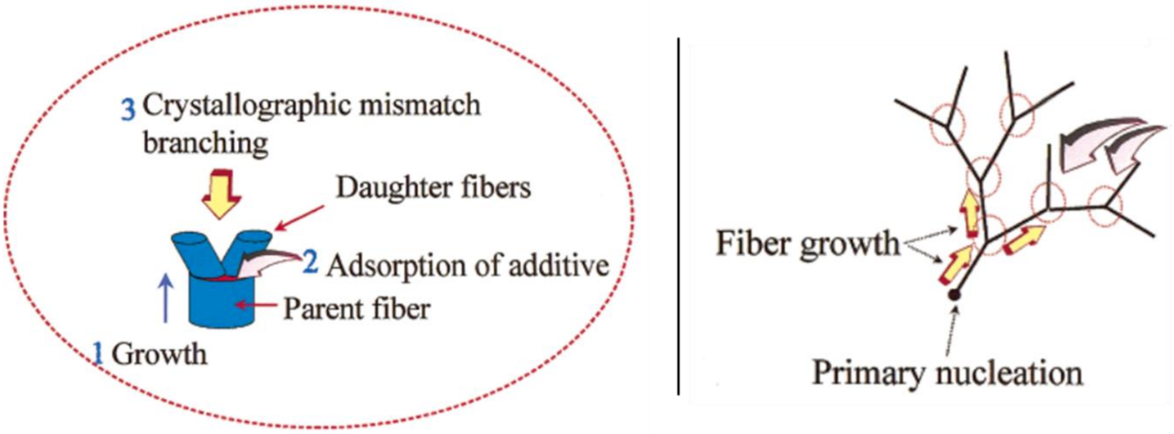

Figure 4.30: (left) sketch of the Crystallographic Mismatch Branching Mechanism (CMB) steps. (right) 3D network result of this mechanism. Adapted from reference **[179]**.

We think that this mechanism is plausible when there are strong, stabilizing interactions between the gelator molecules and the solvent. In the case of the bisamide compounds, having the ability of forming hydrogen bonds, this mechanism may explain why we observe experimentally a strong hydrogen bond component despite the fact that there is no hydrogen bond exposure on the lateral facets of the fibers.

Experimentally, δ_P also decreases with the elongation of the alkyl chain. Intuitively one could hypothesize that polarity should decrease when adding extra CH_2 units.

In Table 4-17 we compare the electrostatic contribution to the surface energy of the most relevant facets.

Table 4-17: Electrostatic surface energy for the most relevant facets (kcal/mol).

	{001}	**{100}**	**{10-1}**	**{011}**	**{0-11}**	**{110}**	**{1-10}**
BiC3	0.2	3.5	0.4	72.3	72.3	72.2	72.2
BiC4	1.1	-0.1	1.2	68.4	68.4	67.7	67.7
BiC5	0.9	0.6	0.8	56.6	56.6	55.0	55.0
BiC6-1	4.7	0.6	1.2	53.7	53.7	53.6	53.6
BiC6-2	2.5	0.5	1.0	52.4	52.4	50.0	50.0

The {h0l} facets have a small electrostatic contribution as they mainly have alkyl chains pointing outwards, and consequently establishing a trend is rather difficult. However, the non-zero $\vec{k}$ component facets have a much higher electrostatic contribution because they show, besides alkyl chains, amide groups outwards. In this case there is a clear decreasing trend, attributed to the addition of CH_2 units, which may dilute and affect the electrostatic contribution of the facet (see for instance the {011} facets in Figure 4.31).

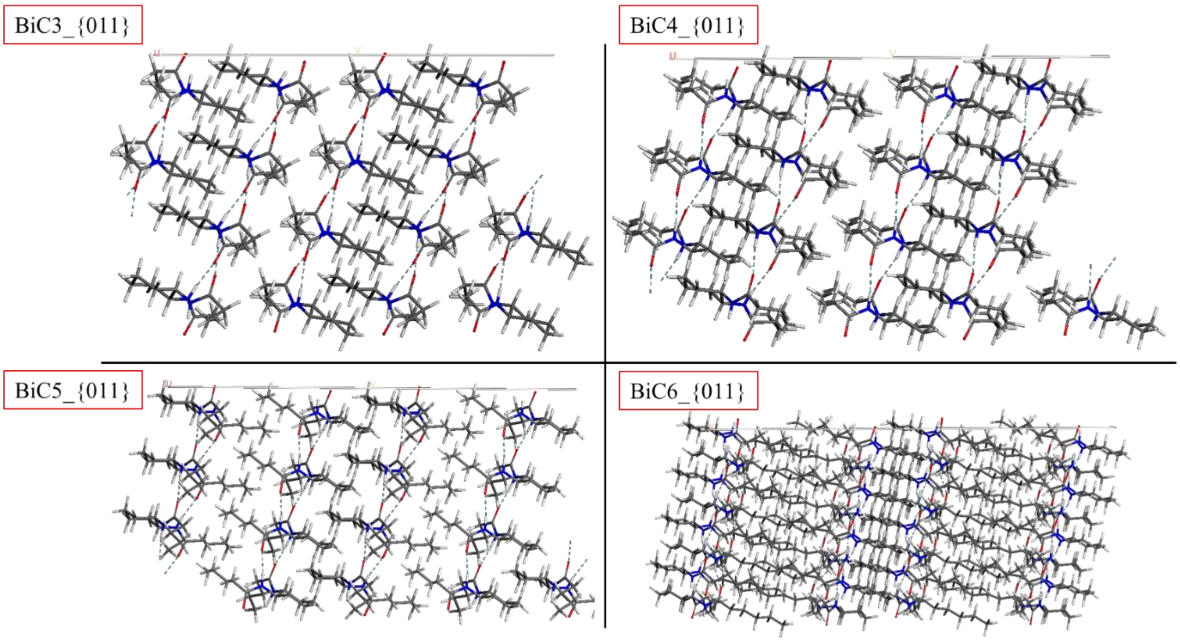

Figure 4.31: {011} facet comparison for the BiC3-BiC6 compounds.

Experimentally, the third HSP parameter, δ_D, fluctuates and then plateaus from BiC6 on. Intuitively, we propose that the longer the alkyl chain length the more CH_2 units exposed outwards. Table 4-18 shows the dispersive surface energy for the most relevant facets.

Table 4-18: Dispersive surface energy for the most relevant facets (kcal/mol).

	{001}	**{100}**	**{10-1}**	**{011}**	**{0-11}**	**{110}**	**{1-10}**
BiC3	76.4	69.2	59.5	55.9	55.9	55.8	55.8
BiC4	76.3	84.8	69.2	63.1	63.1	65.2	65.2
BiC5	73.1	87.7	54.7	55.7	55.7	63.5	63.5
BiC6-1	87.1	76.9	79.5	54.2	54.2	54.2	54.2
BiC6-2	93.0	67.8	71.8	63.6	63.6	66.6	66.6

There is no clear trend for dispersive surface energy, neither within a facet family nor between facet families, but its value is high for all facets, especially for lateral facets. This lack of clear trend could be responsible of the plateau in δ_D with the alkyl chain length. We hypothesize that it could arise from a saturation value of van-der-Waals interactions per unit area of the predominant facets, which is expected for flat surfaces composed of alkyl moieties, as the nature of interactions does not change with the size of the alkyl chains. It is more surprising for facets with amide groups.

Concerning the radius of the gelation sphere, gelation is mainly triggered due to the surface tension of the fiber facets which limits the flow of the liquid in which the fibers are embedded [54]. Thus, we think that the surface-to-volume ratio of the modelled crystal morphologies could be a semi-quantitative parameter that we could use as the larger surface area of the fibers are exposed with respect to their volume, the better should be the gelation capability on average. Table 4-12 show an increasing surface-to-volume ratio trend (GMM method) which could agree with the radius of the gelation sphere of the bisamide compounds. This aspect could be one effect to consider but other factors may also affect the final experimental observations.

4.5 The BiC8-BiC18 compounds

Regarding the BiC8-BiC18 compounds, even though we cannot determine precisely their molecular packing, we can get some information from the insights drawn from the molecular packing of BiC3-BiC6, and comparing their X-ray patterns (see Figure 4.32).

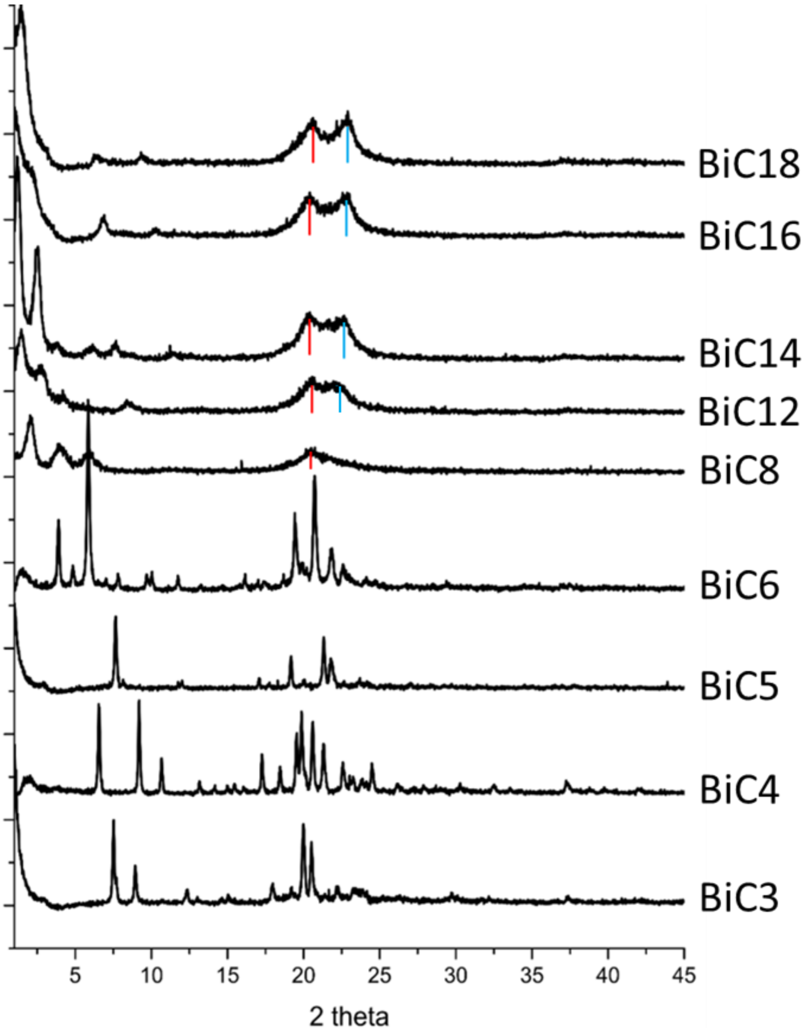

Figure 4.32: XRD patterns of the BiC3-BiC18 compounds obtained in toluene. The blue and red bars mark two invariant peaks. Adapted from the thesis manuscript of Danilo Nunes Rosa (*Sorbonne Université*).

We expect diffraction peaks corresponding to large cell parameters distances in the small angle region (approximately 2θ=0º to 5º, >18Å) and those corresponding to short molecular packing from 2θ=5º on (<18Å) for BiC8-BiC18. In the small angle region, the high intensity peaks appear at very low values (e.g. 2θ=2.04º, 1.46º, 1.20º or 1.44º for BiC8-BiC14, BiC18), even reaching the instrumental limit; this means that periodicity appears at very long range (converting the above values: 43Å, 60Å, 73Å or 61Å). We observe two peaks in the molecular packing region close to 20.5º and 22.5º with corresponding distances of ~4.3Å and 3.9Å, respectively (marked with red and blue bars in Figure 4.32). Long alkyl chains are expected to have a full trans conformation, packing in the typical interdigitated fashion [184]–[189]. Thus, we guess that the 20.5º and 22.5º peak could correspond to an alkyl chain-alkyl chain packing distance. To examine the characteristic distances between alkyl chains, we created an array of n-octane molecules in vacuum and optimized them. We observe an in-plane distance between centroids of ~4.3Å

(Figure 4.33, left) and ~4.1Å out-of-plane (Figure 4.33, right), which roughly agree with the experimental ~4.3Å and 3.9Å distances.

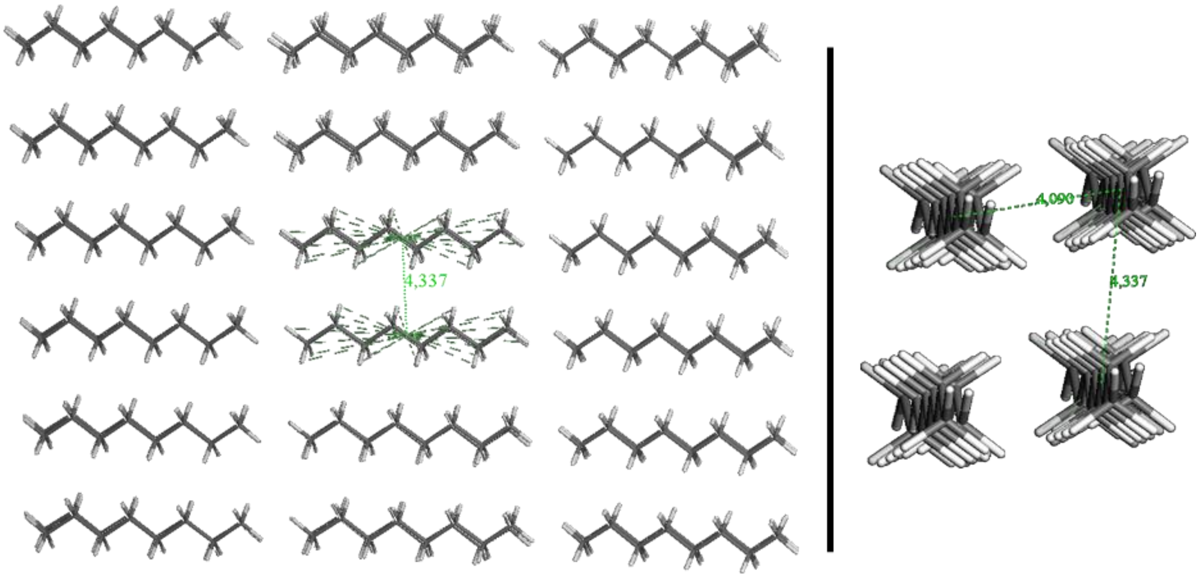

Figure 4.33: Distances between centroids of packed n-octane molecules: (left) 4.3Å in-plane and (right) 4.1Å out-of-plane.

The combination of analyzing the BiC8-BiC18 XRD patterns, the previous experimental results and simulation data on the BiC3-BiC6 molecules, and the simulation of the packing of long alkyl chains leads to the conclusion that the BiC8-18 gelators most probably organize similarly to BiC6 (polymorph 1 or 2), with bisamide molecules hydrogen-bonded in one preferential direction and forming an interdigitated alkyl chain pattern. Thus, their gelation behavior is expected to be similar to that of the BiC3-BiC6 gelators.

4.6 Conclusions

In conclusion we have modelled the gel fibers of the bisamide gelators and have correlated our modelling with the parallel experimental observations from our partners. For this purpose, we have predicted the crystal structure and crystal morphology of four bisamide gelators. In this process, we have understood how the bisamide molecules are arranged both in the core and at the surface of the gel fibers. From the internal characterization of the fibers, we have determined their molecular organization, characterizing the forces that interplay in the fiber growth, pointing especially to the one-dimensional hydrogen-bonding pattern along the [010] direction, which provides directionality to the fiber growth. Our modelling studies have also revealed that the relative orientation of the alkyl chains is key for the molecular packing in this family of gelators. From the fiber surface composition, we have determined which crystal planes are exposed outwards, which are key for the fiber aggregation that finally leads to the 3D fiber network that triggers gelation. We have also determined the chemical composition of the facets, considering different facet terminations, characterizing the gelation casuistic by surface energies, and providing plausible explanation to the experimental gelation trends of the bisamide gelators. We found that the chemical composition and gelation ability of the bisamide fibers are highly anisotropic: governed by dispersive interactions on the lateral facets while polar with a high hydrogen bond contribution on the direction of growth. Based on the experimental and modelling data we also point to the relevance of the tip of the fibers when specific interactions are taking place, such as hydrogen-bonds. Finally, we make some suggestions about the BiC8-BiC18 molecular organization in the fibers.

Chapter 5. Crystal structure, morphology, and solubility modelling of thiazole organogelators

In this chapter we introduce a set of thiazole-based organogelators. First, we determine their crystal structure to reveal their supramolecular organization, focusing on breaking down the inter- and intra-molecular interactions. Then, we model their crystal morphology, which shows a needle shape, and we analyze it to understand the growth anisotropy. We also determine the chemical composition of the facets exposed by the fiber and characterize their gelation ability by surface energy parameters. We compare our theoretical findings throughout the chapter with experimental data obtained by our partners, the group of L. Bouteiller.

5.1 The structure of thiazole organogelators

The thiazole-based compounds studied in this work are formed by a thiazole ring decorated with a methyl group in the 5 position and an amide group in the 2-position. The amide is extended by an alkyl moiety, the whole chain having between 12 and 18 carbons atoms (Th12-18 in Figure 5.1).

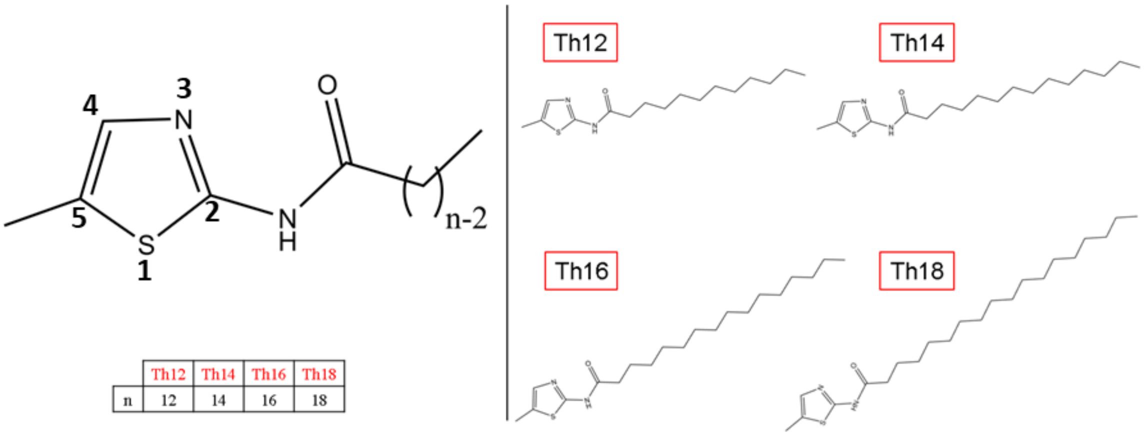

Figure 5.1: The thiazole compounds studied in this work: they only differ in the length of the attached alkyl chain.

This family of compounds is attractive to study the influence of a systematic chemical modification (increase of the alkyl chain) on the gelation properties. To illustrate such influence, in reference [25], there is no gelation when the methyl group is on position 4 of the thiazole ring, and gelation does occur when the methyl is on position 5 or is replaced by a hydrogen atom. The correlation between gelation ability and chemical modification of attaching a methyl or hydrogen moiety on the position 4 or 5 led the authors to propose that the strength and nature of the interactions ruling the supramolecular assemblies affecting fiber formation may vary between: unique strong cyclic N-H···N interactions, a combination of N-H···N and N-H···O interactions or a (methyl)C-H···N, C-H··O and van der Waals interactions.

In this work, we aim to understand the gelation properties of the thiazole molecules bearing a methyl group on position 5, and decorated with an increasingly longer alkyl chain.

Two members of the family, Th12 and Th14, have been reported in the literature to have an organogelation ability, and their single crystal structures have been determined too [25], [26]. Our experimental partners later found that Th16 and Th18 are also capable of forming organogels. As the experimental powder XRD patterns of the gel fibers show a crystalline behavior, our theoretical approach is based on determining the crystal structure of the gel fibers of the four compounds, deducing their morphology, and predicting their surface energy parameters. The theoretical morphology is compared to experimental SEM images of the gel fibers and the predicted surface energy parameters are compared to the experimental ones.

5.2 Crystal structure determination

From our partners we have the experimental XRD patterns of the gel fibers and a guess of the space group and cell parameters of the unit cell for Th12-18 (See Figure 5.2).

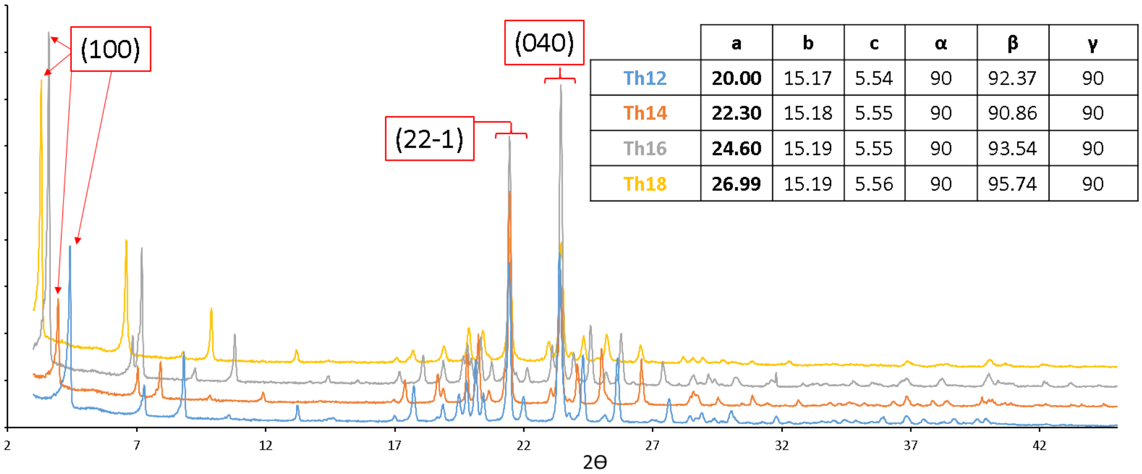

	a	b	c	α	β	γ
Th12	**20.00**	15.17	5.54	90	92.37	90
Th14	**22.30**	15.18	5.55	90	90.86	90
Th16	**24.60**	15.19	5.55	90	93.54	90
Th18	**26.99**	15.19	5.56	90	95.74	90

Figure 5.2: Comparison of the experimental XRD patterns of Th12-18. The cell parameters are an initial guess (data from the thesis of Danilo Nunes Rosa, *Sorbonne Université*).

First, we remark the shift of the (100) peak from Th12 to Th18, which is related to a progressively larger "a" cell parameter. The incremental increase of ~2.3Å of the interplanar distance from Th12 to Th18 is ~8% shorter than the increase of the alkyl chain length when adding two CH_2 groups (~2.5Å, considering the connection of two sp^3 carbon covalent bonds of ~1.54Å by an angle of ~109.5°). In contrast, the “b” and “c” cell parameters, however, remain practically constant with the alkyl chain length. Thus, the alkyl chains have a strong component aligned in the [100] direction, i.e, they are slightly tilted with respect to that direction, and increasing their length practically does not affect the molecular packing in the [010] and [001] directions. Note that the (010) and (001) crystal planes do not appear in the diffractions patterns as they have a zero value of intensity.

The intense peaks corresponding to the (22-1) and (040) crystal planes are at the same position from Th12 to Th18, with thus constant interplanar distances of ~4.1Å and ~3.8Å, respectively. They may correspond to the characteristic interplanar distances of stacks of alkyl chains. We hypothesize this could be the case as we observed the same invariant distances previously when we discussed in Chapter 4 about the molecular packing of the BiC8-BiC18 molecules (~4.3Å and ~3.9Å), which also have long alkyl chains.

Considering all the previous reasoning, we apply our crystal prediction method to Th12 and then we build the Th14, Th16 and Th18 crystals from the Th12 crystal by adding additional CH_2 units, imposing cell parameters identical to those suggested from the XRD experiment on gel fibers, and finally optimizing the internal geometry of the crystal. We used this procedure to take advantage of the crystallographic information drawn from the XRD characterization and because it is much more time efficient. For this case, as we will see in the following figures, this procedure leads to the correct molecular packing structures.

Figure 5.3 shows that for all thiazole systems the theoretical XRD pattern of the simulated crystals agrees excellently with the experimental XRD pattern obtained on the gel fibers.

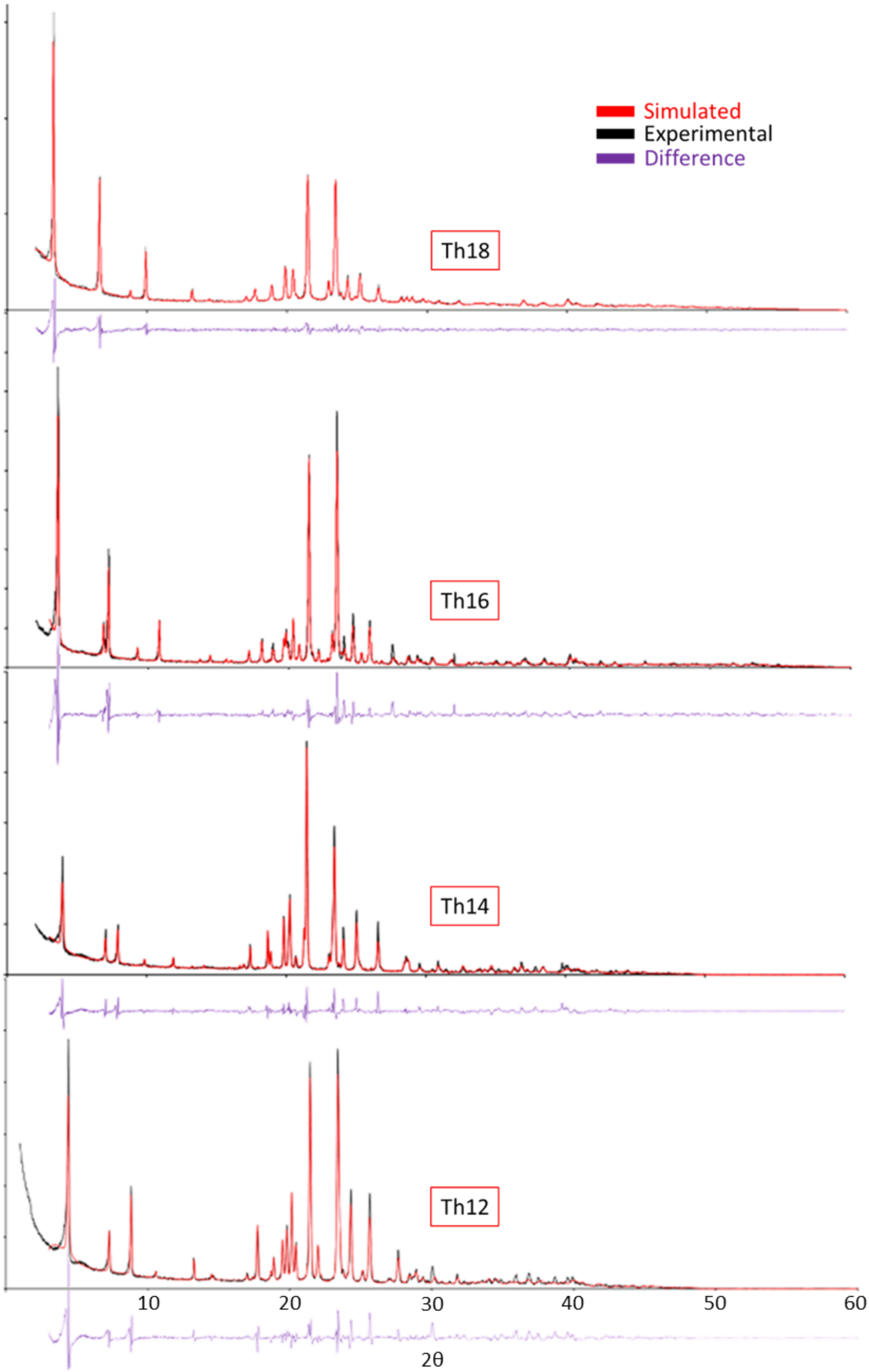

Figure 5.3: Comparison of the simulated XRD pattern for Th12 to Th18 (red) to the experimental powder XRD pattern obtained by our partners (black). The purple curve is the difference between them.

The match between the simulated and experimental XRD patterns means that the simulated molecular packing of the thiazole compounds represents that of the experimental gel fibers, thus confirming our hypothesis that the same type of molecular packing is conserved for all the thiazole compounds. We detail in Figure 5.4 the predicted molecular packing for Th12.

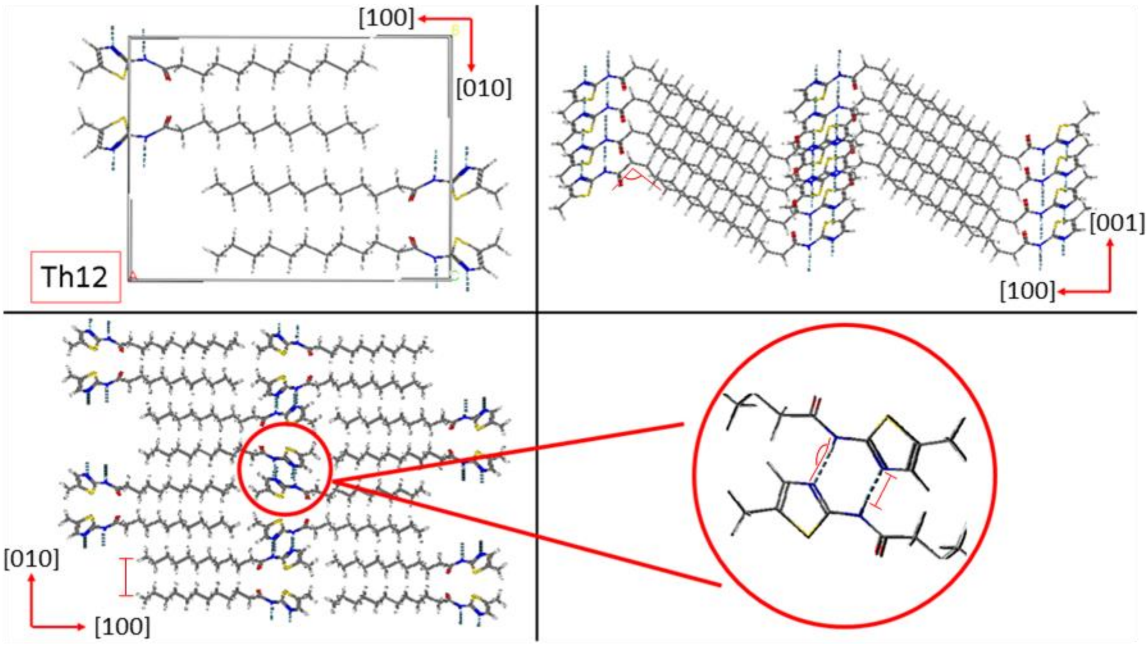

Figure 5.4: Predicted molecular packing for Th12. Top left panel: unit cell, top right panel: view through the [010] direction, bottom left panel: view through the [001] direction, bottom right panel: zoom of the cyclic hydrogen-bonding pattern.

The unit cell has a $P_{2_1/c}$ space group symmetry and it is characterized by four thiazole molecules paired in dimers connected by two hydrogen bonds between the nitrogen atom of the heterocycle and the hydrogen atom of the amide of its neighboring molecule in a cyclic manner (Figure 5.4: bottom right panel). Hydrogen bonds have a distance of 2.04Å and an N-H··· N angle of 165.48°. Alkyl chains are connected to the amide groups by a torsion angle of 116.01° (Figure 5.4: top right panel) and display a 2+2 interdigitated scheme where alkyl chains are in (040) planes spaced by 3.8Å, i.e., by one fourth the (010) interplanar distance (Figure 5.4: red bar in the bottom left panel). We also observe an intramolecular S···O distance of 2.95Å, similar to that of 2.80Å for several compounds in literature [190], [191], which may lock this thiazole molecular configuration (see Figure 5.5). We also highlight the small deviation of 13.8° from planarity between the thiazole ring and the amide group (Figure 5.5: right panel).

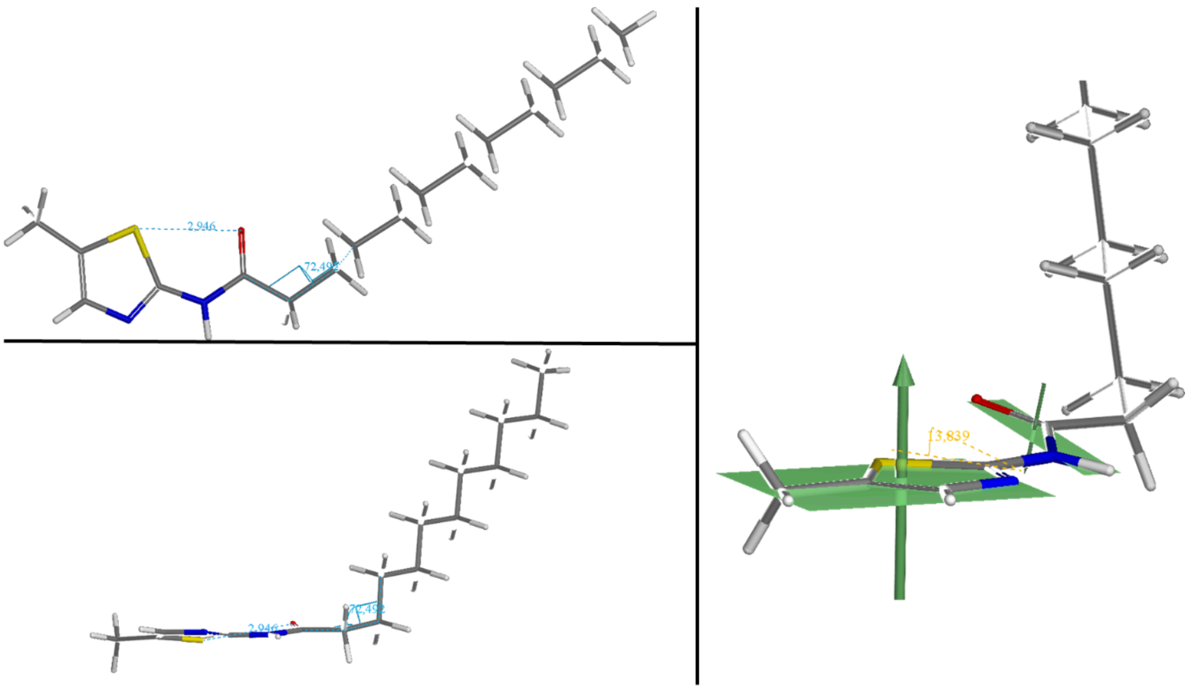

Figure 5.5: Internal conformation of the Th12 molecule in the crystal. Left panel: highlighting the S···O interaction and torsion angle between the alkyl chain and amide group, right panel: the deviation of the amide moiety from the thiazole plane.

The cyclic hydrogen bonding topology leads to a 0-dimensional hydrogen-bond network, from which it is not intuitive to understand how the 1-dimensional fiber structure may emerge, in contrast to, e.g., the continuous 1-dimensional hydrogen bonding network in the bisamide case. However, having a closer look at the molecular packing, we observe a slipped π-stacking configuration along the [001] direction with a distance of 3.37 Å between thiazole rings. Thus, hydrogen bonds and π-stacking may alternatingly 'paste' the thiazole molecules along the [001] direction (see Figure 5.6).

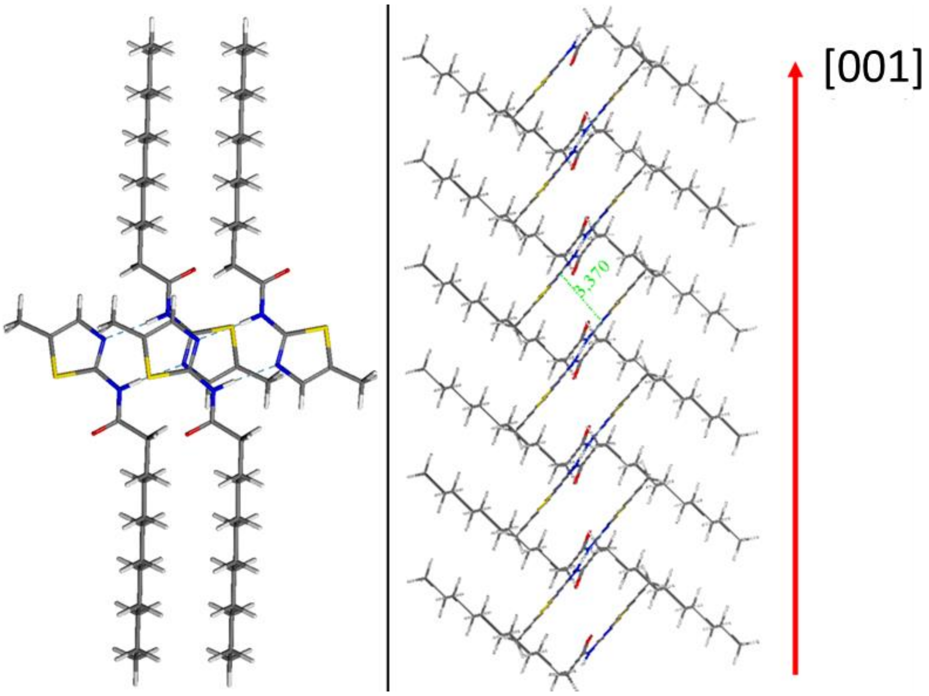

Figure 5.6: (left) Close-up of the slipped π-stacking configuration that propagates. (right) Extracted stacks of thiazole molecules to illustrate the preferential growth along the [001] direction.

We pinpoint several interactions involved in this crystal structure. As mentioned in reference [25], the presence (or absence) and position of the methyl group affected the gelation behavior of the thiazole molecules. Here, we observe a C-H-π interaction in Th12 between the methyl group and the heterocycle, with a distance of 2.69Å (see Figure 5.7), which is relevant in the molecular packing of organic crystals [192]–[196]. For instance, a hydrogen atom-toluene interaction is observed to have an hydrogen-centroid distance of 2.73-3.05Å [197]

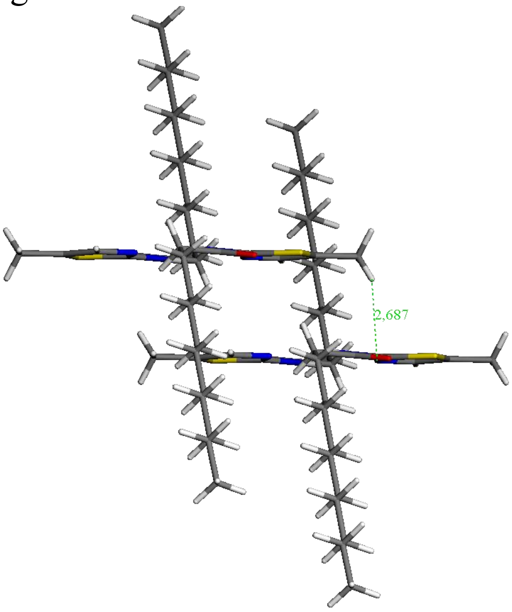

Figure 5.7: Extracted Th12 molecules illustrating the C-H-π interaction.

In literature the C-H-π interactions have a strength between 0.5 and 2kcal/mol [194]. Thus, we think that this type of interaction can contribute to the stabilization of the stacks. Returning to reference [25], where the gelation ability of the thiazole-based compound changed depending on whether the methyl group is on the 4 or 5 position, we hypothesize that this modification can affect the supramolecular organization of the thiazole molecules, thus favoring or disrupting the formation of elongated 1-dimensional fibers. If the methyl group was on position 4 in Th12, it would be located above the amide group of another thiazole molecule, being too far from the thiazole ring to trigger CH-π interactions.

We also observe a close 3.63Å distance between the sulfur and nitrogen atoms, maybe forming two extra noncovalent interactions per stack, with a distance similar to that of 3.35Å in literature [190], [191] (see Figure 5.8). We also mention that sulfur-sulfur repulsion may play a role, favoring the slipping of the stacks [191].

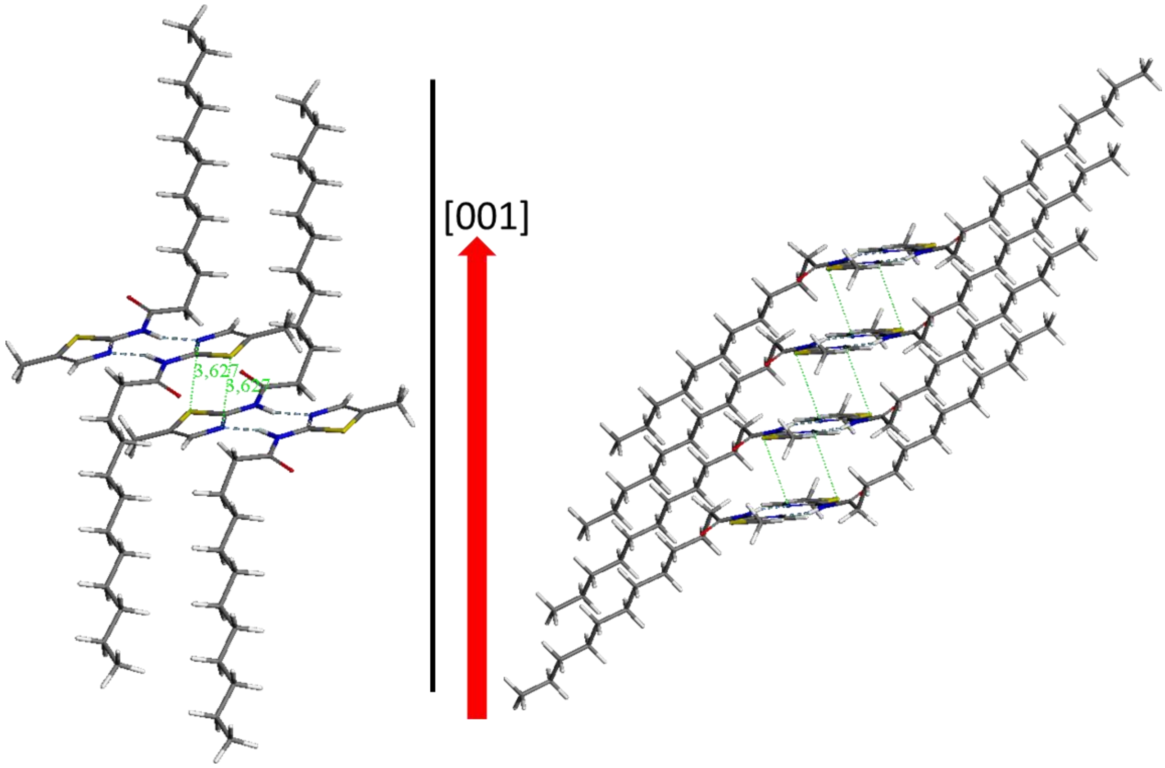

Figure 5.8: Illustration of the sulfur nitrogen contacts (green). Left panel: close-up of the contacts, right panel: its propagation through the [001] direction.

The analysis made for Th12 also applies for Th14 to Th18 as the molecular packing does not change; only the "a" cell parameter is elongated (see Figure 5.9).

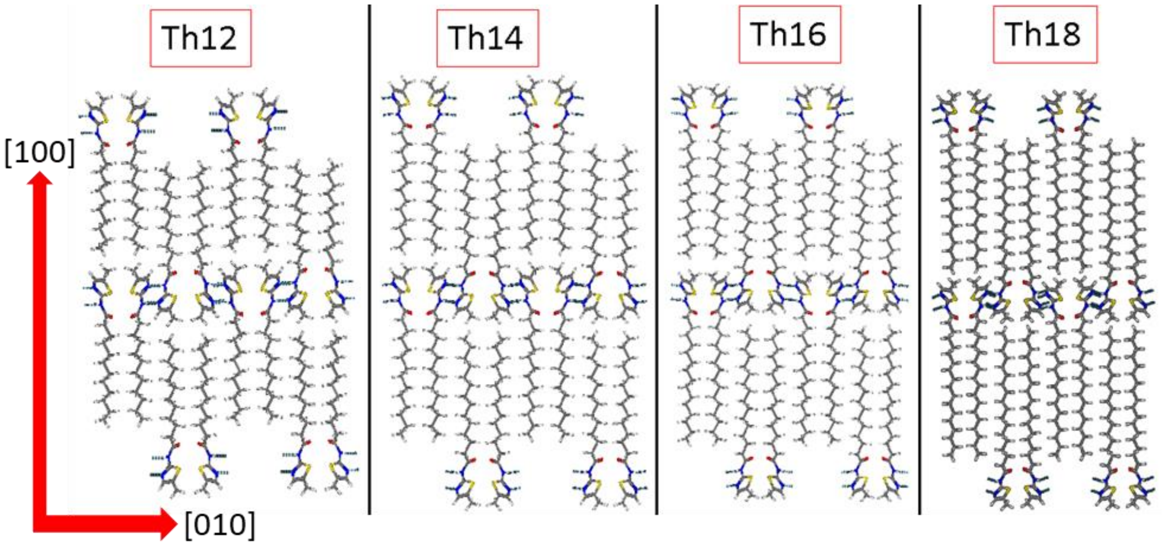

Figure 5.9: Molecular packing comparison for the Th12-18 compounds.

Additionally, we also evaluated for Th12 and Th14 whether the packing in the gel fibers is similar to that found in single crystals reported in the literature [25], [26]. Figure 5.10 shows a superposition of molecules extracted from the simulated crystals and from the single crystal reported in the literature. Their agreement confirms that it is indeed the case.

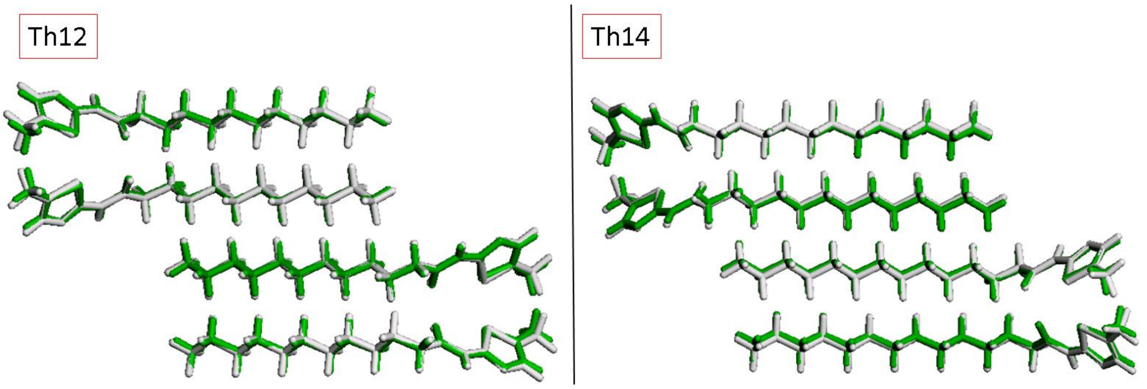

		a (Å)	b (Å)	c (Å)	α (º)	β (º)	γ (º)	Volume (Å^3)
Th12	**Single crystal**	20.05	15.18	5.55	90.00	92.41	90.00	1687.70
	This work	20.00	15.17	5.54	90.00	92.37	90.00	1679.40
Th14	**Single crystal**	22.30	14.61	5.54	90.00	91.68	90.00	1804.17
	This work	22.30	15.18	5.55	90.00	90.86	90.00	1881.91

Figure 5.10: Predicted molecular packing (grey) superimposed to the single crystal molecular packing from literature (green) for Th12(left) and Th14 (right). Comparison between the cell parameters of the gel fibers studied in this work and the single crystal structures reported in the literature **[25], [26]**.

5.3 Morphology of the thiazole crystals

The gel fibers are grown in solution under non-equilibrium growth conditions. Therefore, we used the GMM method to model the crystal morphology. We introduce first the computed crystal morphology of the Th12 crystal to illustrate the crystal morphology of this family of compounds (see Figure 5.11).

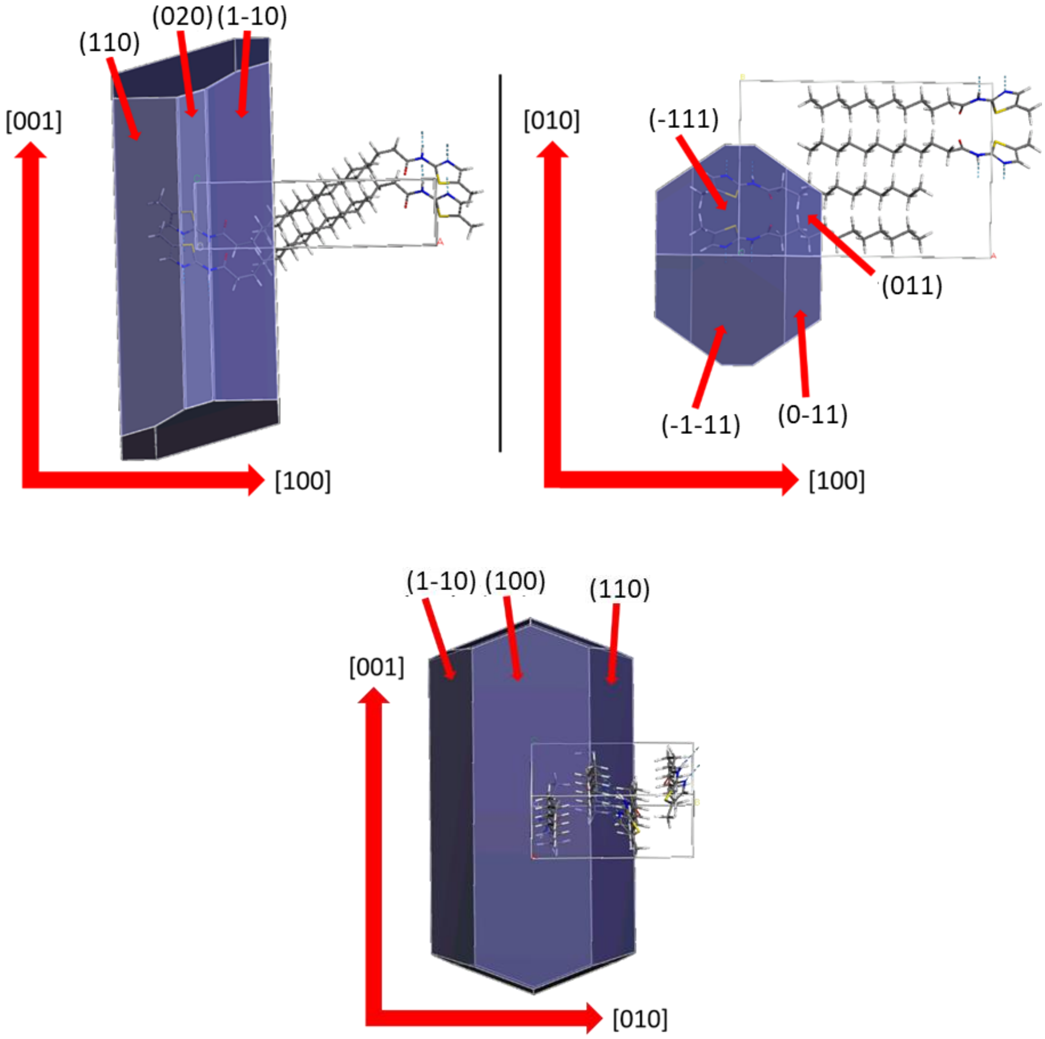

Figure 5.11: Computed Th12 crystal morphology along the three axes. The dominant facets are indicated.

The crystal is a needle elongated in the [001] direction and the dominant facets are the {110}, {100}, {11-1}, {011} and {020}. These features are observed for the Th12-18 compounds. The notation {hkl} correspond to planes that are equivalent by symmetry, for instance {110} comprises the (110), (1-10), (-110) and (-1-10) planes.

In Figure 5.12 the modelled crystal habits for Th12-18 are compared with the corresponding SEM images. The modelled crystal morphologies computed with the

GMM method qualitatively agree with the fibrillar structures shown in the experimental SEM images, Th18 looking more aggregated.

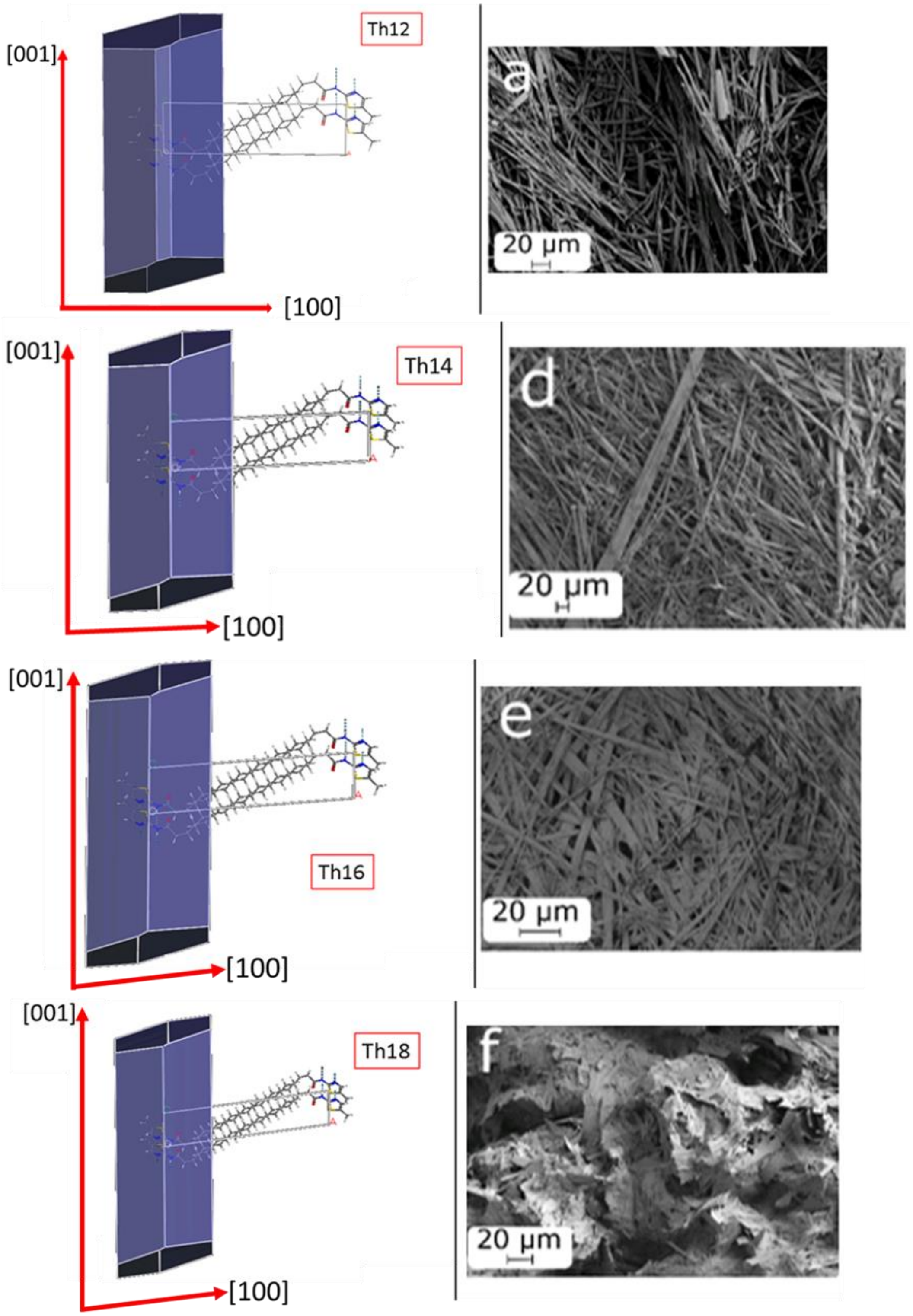

Figure 5.12: Comparison between the modelled crystal morphology for Th12-18 using the GMM method and their respective experimental SEM images.

The preferential growth along the [001] direction was further confirmed when our experimental partners compared the XRD patterns of Th12 gel fibers preferentially oriented (I) to that of fibers that are randomly oriented (II) (see Figure 5.13).

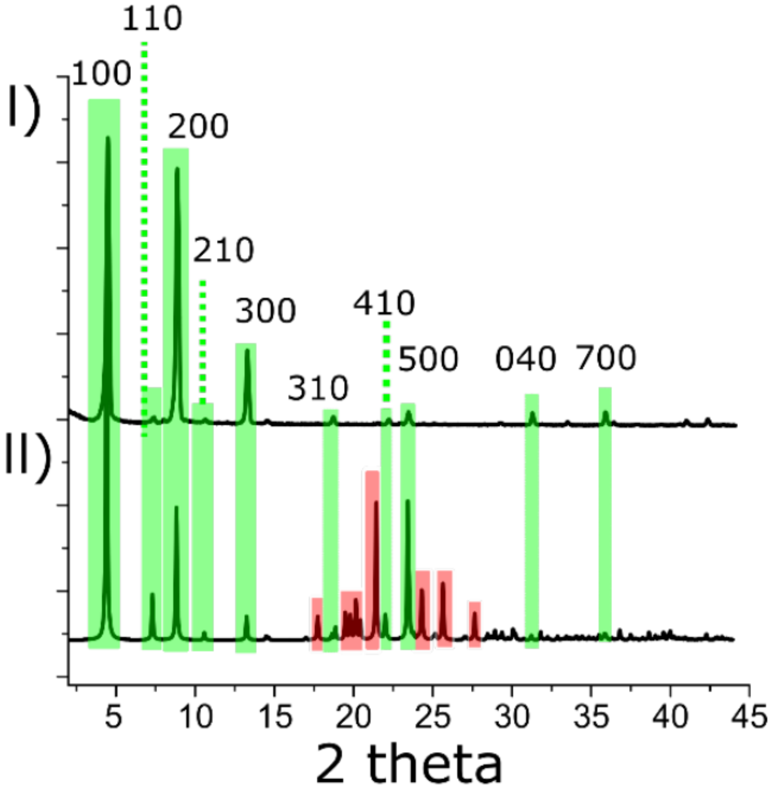

Figure 5.13: Experimental XRD pattern of Th12 gel fibers that were preferentially oriented (I) and randomly oriented (II) (data from the thesis of Danilo Nunes Rosa, Sorbonne Université). The green-highlighted diffraction peaks appear in both X-ray patterns, while the red-highlighted diffraction peaks only appear in the randomly oriented fibers.

In the randomly oriented sample, the gel fibers are grinded, leading to short, randomized fibers. The transmission of X-rays through the sample allows all diffraction peaks to possibly appear in the X-ray pattern. In the preferentially oriented sample, the gel fibers are not grinded, and they are compacted as a film on a flat surface. In this case, gel fibers are parallel to the surface where they are deposited and only reflections from planes parallel to the fiber axis appear in the diffraction pattern (see Figure 5.14).

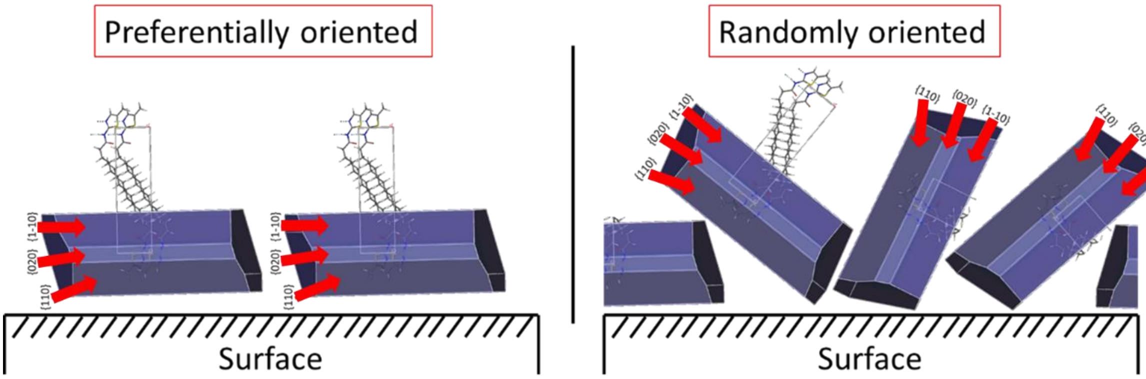

Figure 5.14: Sketch of the disposition of the fibers on the surface when (left) preferentially or (right) randomly arranged.

Thus, the diffraction peaks that appear for both the randomly oriented sample and the preferentially oriented sample, indicate which is the elongated fiber axis. The (hk0) planes appear in both diffraction patterns (green highlight) while the other planes, i.e., with a l index different from 0, are visible only for the randomly oriented fibers (red highlight). Therefore, the fiber is elongated along the [001] direction, thus confirming the [001] direction as the preferential growth direction of the fiber.

Regarding what is the driving force triggering the one-directional growth character, we must distinguish if it is a geometrical or an energetic effect. We can isolate the geometrical contribution comparing the crystal morphologies computed with the GMM and BFDH methods, as the BFDH method only considers the d_{hkl} interplanar distances of facets for building the crystal habit while the GMM method uses the attachment energy criteria.

We remind that in the BFDH method, energy has a role via the thickness of the layers, but the chemical nature and packing are not evaluated, thus the interactions are supposed homogeneous throughout the volume. In the GMM method, in addition to the effect due to the layer thickness, the interactions differ from place to place, depending on the chemical nature and packing, which are here reproduced. This can be important because molecules with no preferential interactions could have very similar habits in BFDH and GMM, while a small molecular moiety but with strong preferential interactions could affect selected planes of the habit, therefore producing important differences between the BFDH and GMM habits. Note the difference of the crystal habits computed with the GMM method in Figure 5.12 with respect to those computed with the BFDH method in Figure 5.15.

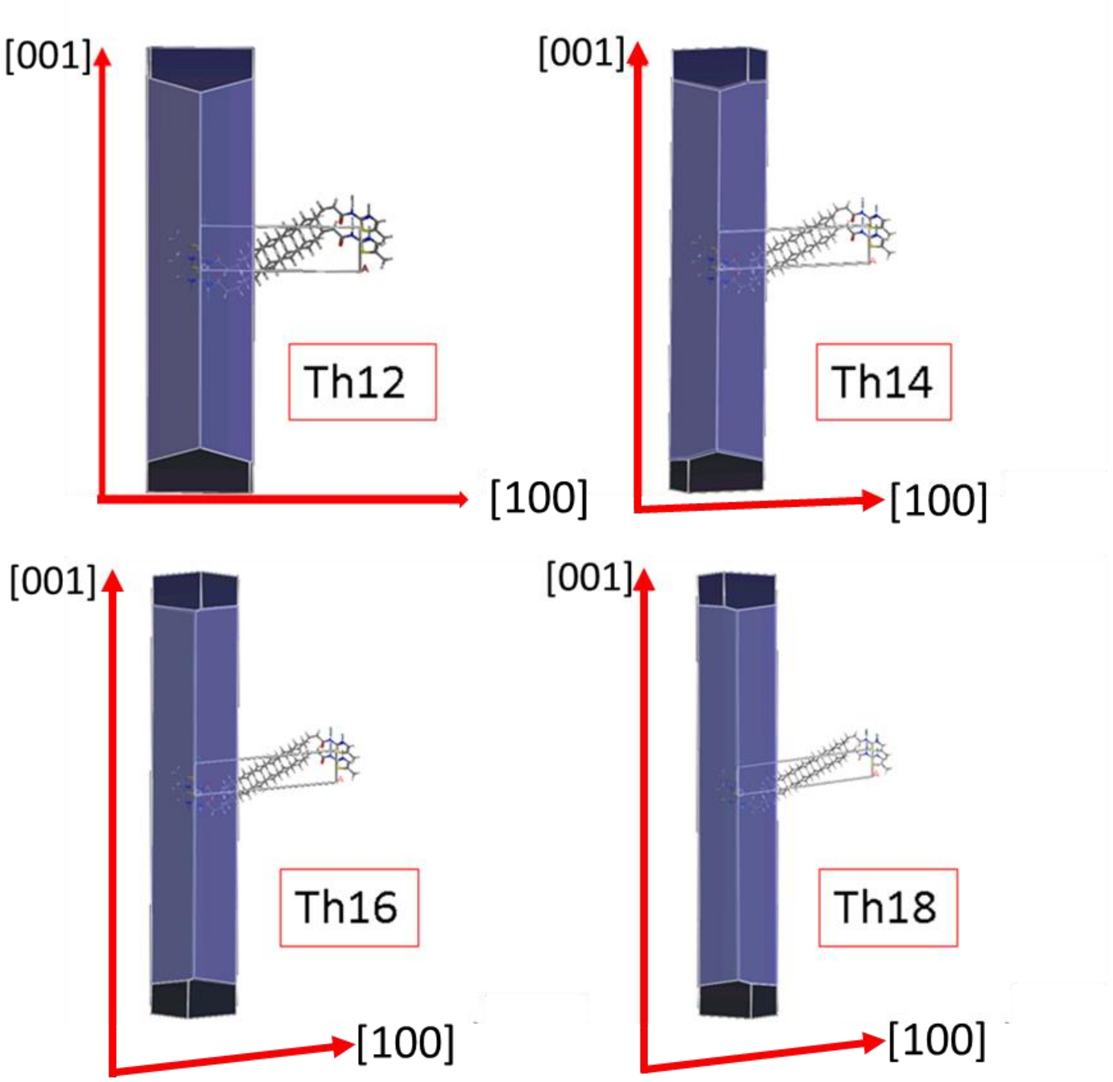

Figure 5.15: Computed crystal morphology with the BFDH method for the Th12-18 compounds.

The BFDH method, with only geometrical assumptions, can reproduce the one-dimensional preferential growth. This observation is consistent with the fact that GMM and BFDH methods are meant to reproduce the crystal habit under non-equilibrium growth conditions. As mentioned, energy has a role in the BFDH method via the thickness of the layers and its proximity to the GMM results is due to the layer thickness and attachment energy agreeing, for the thiazole compounds, on assigning a larger facet area percentage to the largest interplanar distances facets.

In Table 5-1, we compare the aspect ratio of the crystal morphologies computed with both methods. The aspect ratio is the ratio between the longest and the shortest distances between the center of the crystal to its surface. We also indicate the relative distance measured perpendicularly from a facet to the crystal center (D values) of the {002}, {020}, {100} and {110} facets to have a clearer picture of the observed trends, normalizing these values to that of the {002} facet. We only use the {002} facet in the following discussion about the aspect ratio of the crystal habit to have a geometrical reference for the [001] direction of the fiber, i.e., the {002} facet is not displayed in the crystal habit, we only use it to rationalize the geometry of the crystal habits and their aspect ratios. The D value of a facet in the GMM method is calculated as its attachment energy, while in the BFDH it is calculated as the inverse of the interplanar distance (d_{hkl}) of the facet. Also notice that the {002} and {020} facets appear instead of the {001} and {010} facets, as the symmetry operations allow these facets to grow by half a layer at a time.

Table 5-1: Comparison of the aspect ratio of the crystal morphology for the Th12-18 compounds. The D values used for constructing the crystal habit are also shown, normalized to that of the {002} facet.

	GMM					**BFDH**				
	Aspect ratio	**D=Eatt**				**Aspect ratio**	**D=1/d_{hkl}**			
		{100}	**{020}**	**{110}**	**{002}**		**{100}**	**{020}**	**{110}**	**{002}**
Th12	2.83	0.33	0.44	0.39	1	4.32	0.14	0.39	0.24	1
Th14	2.76	0.35	0.45	0.38	1	4.76	0.12	0.39	0.23	1
Th16	2.71	0.36	0.45	0.37	1	5.22	0.11	0.39	0.23	1
Th18	2.73	0.36	0.46	0.36	1	5.70	0.10	0.39	0.22	1

From Th12 to Th18, the aspect ratio trends differ depending on the method: increasing for BFDH and decreasing for GMM. Both trends are well explained by paying attention to the evolution of the D values of the facets. The crystal is elongated along the [001] direction, forming a needle. Therefore, an increase of the D values of the {100}, {110} or {020} facets would result in a widening of the needle, decreasing the aspect ratio, i.e., towards a flake shape.

In BFDH, the D value of a facet is calculated as the inverse of its interplanar distance d_{hkl}. As only the “a” cell parameter increases from Th12 to Th18, d_{hkl} with “h” different from 0 also increases, and consequently the D value of the lateral {100} and {110} facets decrease, while {020} is remaining constant. As a result, there is a monotonous increase of the aspect ratio.

In the GMM method, the constant increase of the D values of the {100} and {020} facets result in a constant decrease of the aspect ratio, overshadowing the decreasing trend of {110}. As D is the attachment energy of the facet, the increase of the contribution of the {020} and {100} facets are either coming from a stabilization of these facets or a destabilization of the {002} facet. We characterize this casuistic with the absolute value of attachment energies of the facets, see Table 5-2.

Table 5-2: Attachment energy (kcal/mol) of the {100}, {020}, {110}, {002}, {11-1} and {011} facets for Th12-18.

	{100}	{020}	{110}	{002}	{11-1}	{011}
Th12	-50.18	-66.93	-60.21	-152.49	-113.32	-124.02
Th14	-57.91	-74.58	-64.20	-167.32	-124.84	-135.55
Th16	-65.64	-82.25	-68.20	-182.17	-136.36	-147.09
Th18	-71.50	-89.93	-72.24	-197.04	-147.88	-158.64

We remind that the more negative the attachment energy, the more unstable the facet. The {002} facet is consistently destabilized by ~15 kcal/mol per $(CH_2)_2$ unit from Th12 to Th18, while the destabilization is ~8 kcal/mol for {100} and {020} and ~4 kcal/mol for {110}. But when expressing these energy variations in percentage of the attachment energy, the {002} facet is less destabilized than the {100} and {020} lateral facets when elongating the alkyl chain, thus lowering the aspect ratio values. The effect is however small, as from Th12 to Th18 the aspect ratio drops by only 4% with GMM, compared to an increase of 30% with BFDH. Below we show in Table 5-3 that the sum of the percentage of total facet area of the lateral facets barely increases from Th12 to 18 (77% to 78%), while the percentage for the tips barely decreases (23% to 22%), leading to barely shorter aspect ratios.

The aspect ratio found by GMM is also smaller than that found by BFDH, indicating that the cyclic hydrogen bonds, instead of reinforcing the growth directionality along the [001] direction, undermine it. This analysis contrasts with that in the bisamide family, where hydrogen-bonding reinforced the fiber anisotropy. Thus, the GMM versus BFDH analysis is useful to understand which interactions affect preferential growth, and thus envision designing rules for future systems. The GMM analysis also reveals the surface area of the facets (see Table 5-3).

Table 5-3: Percentages of the total crystal surface area covered by the facets for the Th12-18 compounds.

%Facet area	{110}	{100}	{11-1}	{011}	{020}	Total
Th12	38%	32%	19%	4%	7%	100%
Th14	47%	30%	17%	5%	1%	100%
Th16	49%	29%	16%	6%	-	100%
Th18	49%	29%	16%	6%	-	100%

The percentage of surface area covered by the {110} and {011} facets increases with the length of the alkyl chain while for the other facets it decreases, even disappearing in the case of the {020} facet. In order to understand this behavior, we now present the molecular organization at those facets (see Figure 5.17).

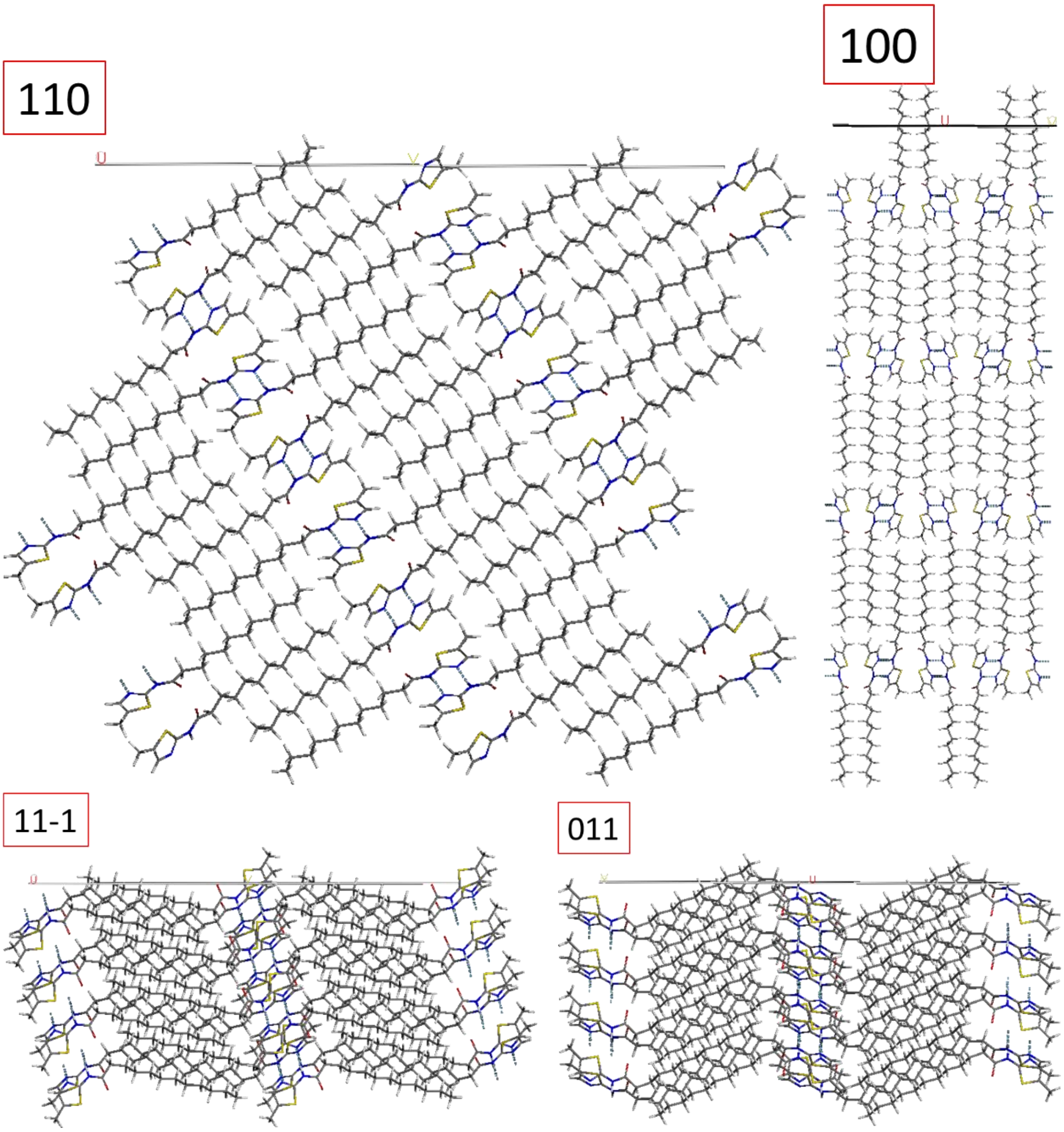

Figure 5.16: Organization of the molecules at the surface of the {110}, {100}, {11-1}, {011} and {020} facets for the Th12 compound. The facets are perpendicular to the plane of the document.

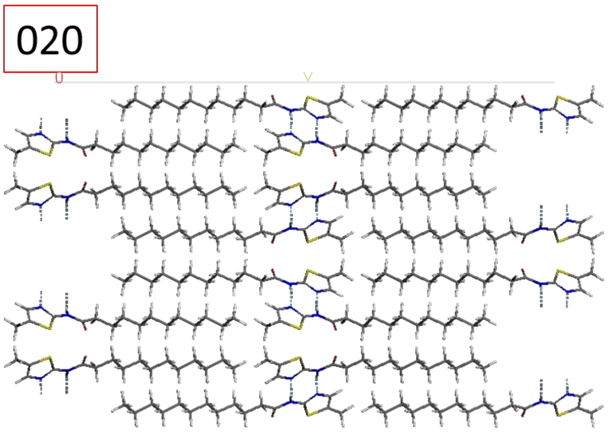

Figure 5.17 (continued): Organization of the molecules at the surface of the {110}, {100}, {11-1}, {011} and {020} facets for the Th12 compound. The facets are perpendicular to the plane of the document.

The percentage of facet area of the {110} and {011} facets increases with the elongation of the alkyl chain, oppositely to the other facets. We spot that the {110} and {011} facets have non hydrogen-bonded thiazole dimers exposed to the environment (which would increase the surface dipole), while thiazole rings are always involved in forming hydrogen-bonding dimers for the rest of the facets. Thus, we think that the increase of the alkyl chain could reduce the penalty of exposing non hydrogen-bonded thiazole dimers.

In general trends, in order to minimize the surface area, the surfaces with a terrace configuration are more stable than the stepped ones, and these ones are more stable than the kinked ones. Thus, the {020} facet with a terrace configuration should be more stable than the {110}, {11-1} and {011} stepped ones, and these ones should be more favorable than the {100} kinked one. Nevertheless, the area of the crystal plane (the attachment energy is calculated for the part of the plane delimited by the crystal cell) and the chemical composition exposed by the facet must also be considered.

We remind that a facet may expose different chemical compositions depending on the position where the crystal is cleaved. Each different chemical composition of a facet is called a termination. The molecular coverings of all possible terminations are shown in the Annex for Th12, representative for all thiazole compounds. We mention below the specific case of the {100} facet of Th18 where “Termination 2” is more stable than “Termination 1”. Therefore, we use the attachment energy of the facets to compare with our specific case. The facet terminations displayed in Figure 5.17 are the most stable ones, i.e., other molecular coverings of the facets are less stable (see Table 5-4, where the terminations shown in Figure 5.17 corresponds to “Termination 1”).

Table 5-4: Attachment energies of all possible terminations for all the exposed facets (see the Annex for the representation of the different terminations).

Attachment energy (kcal/mol)		**Th12**	**Th14**	**Th16**	**Th18**
{110}	Termination 1	-60	-64	-68	-72
	Termination 2	-94	-98	-102	-106
	Termination 3	-94	-98	-102	-106
	Termination 4	-106	-116	-126	-136
{100}	Termination 1	-50	-58	-66	-73
	Termination 2	-71	-71	-71	-71
{11-1}	Termination 1	-113	-125	-136	-148
	Termination 2	-120	-132	-143	-155
	Termination 3	-120	-132	-143	-155
	Termination 4	-127	-139	-151	-163
{011}	Termination 1	-124	-135	-147	-159
	Termination 2	-134	-146	-157	-169
	Termination 3	-134	-146	-157	-169
	Termination 4	-135	-148	-161	-174
{020}	Termination 1	-67	-75	-82	-90
	Termination 2	-93	-101	-109	-116

The attachment energy increases from Th12 to Th18 because the attachment energy is an extensive magnitude, and more interactions are included when elongating the alkyl chain as the area of all crystal planes delimited by the cell walls, except {100}, increase.

The {hk0} facets ({100}, {110} and {020}) have a lower attachment energy value than {11-1} and {011} mainly because they have a lower dispersive component. For instance, for Th12, the dispersive component of {100}, {110} and {020} is ~50, ~45 and ~67 kcal/mol, respectively, while it is ~105 and ~89 kcal/mol for {11-1} and {011}, respectively. The larger the surface area of the facet, the larger the attachment energy due to a larger exposure of molecules, considering the same chemical morphology at the surface. Thus, we reevaluate the attachment energies of the previously mentioned facets dividing by their surface areas (see Table 5-5).

Table 5-5: Components of the attachment energies in kcal/mol and kcal/mol·Å^2 for Th12.

		{100}	{110}	{020}	{11-1}	{011}
Attachment energy (kcal/mol)	Dispersive	-50	-45	-67	-105	-89
	Polar	0	-8	0	-8	-22
	Hydrogen-bonding	0	-7	0	0	-13
Surface area (Å^2)		76	134	110	308	298
Attachment energy (kcal/mol·Å^2)	Dispersive	-0.66	-0.33	-0.61	-0.34	-0.30
	Polar	0	-0.06	0	-0.03	-0.07
	Hydrogen-bonding	0	-0.05	0	0	-0.04

The largest dispersive attachment energy values of the {11-1} and {011} facets match with the fact that the related cell planes have the largest surface areas. We observe that the values of the {110}, {11-1} and {011} facets double that of the {100} and {020} facets when we express the attachment energies per unit area. This correlation is attributed to the fact that the attachment energy is expressed for a motif of four molecules (as the four molecules per unit cell). It is the case for the {110}, {11-1} and {011} facets, but the motif is of two molecules for the {100} and {020} facets, thus doubling the energy to express it per four molecules. The same correlation happens with the polar and hydrogen-bonding contributions.

In Table 5-4, Termination 1 is always the most stable termination except for the case of the {100} facet in the Th18 compound, where Termination 2 (thiazole ring termination) is ~2kcal/mol more stable than Termination 1 (alkyl chain termination), see Figure 5.18.

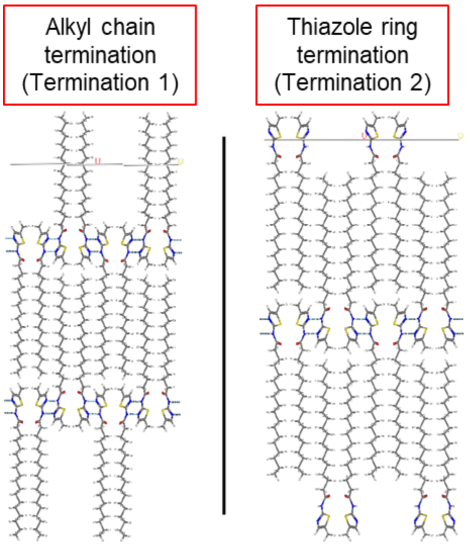

Figure 5.18: The two possible {100} facet terminations of Th18: (left) Termination 1, protruding alkyl chains outwards, (right) Termination 2, protruding thiazole rings outwards.

Exposing alkyl chains is generally more favorable than exposing thiazole rings to avoid breaking hydrogen-bonds. However, as alkyl chains are protruding outwards in Termination 1, this termination is subsequently more unstable when increasing the alkyl chain length. In the case of Termination 2, its attachment energy is constant because it always exposes the same thiazole rings, the alkyl chains remaining inside the facet. Thus, in the {100} facet of Th18, the protrusion of the alkyl chains is large enough to destabilize Termination 1 beyond the situation of Termination 2, which becomes more favorable.

Thiazole facets are more stable when minimizing protrusion (Figure 5.19, top) or unbalanced interactions (hydrogen-bonds, in Figure 5.19, bottom). This conclusion contrasts with the bisamide family where hydrogen bonds were much relevant. Therefore, the chemistry of facets is clearly connected with the chemical nature of the molecules.

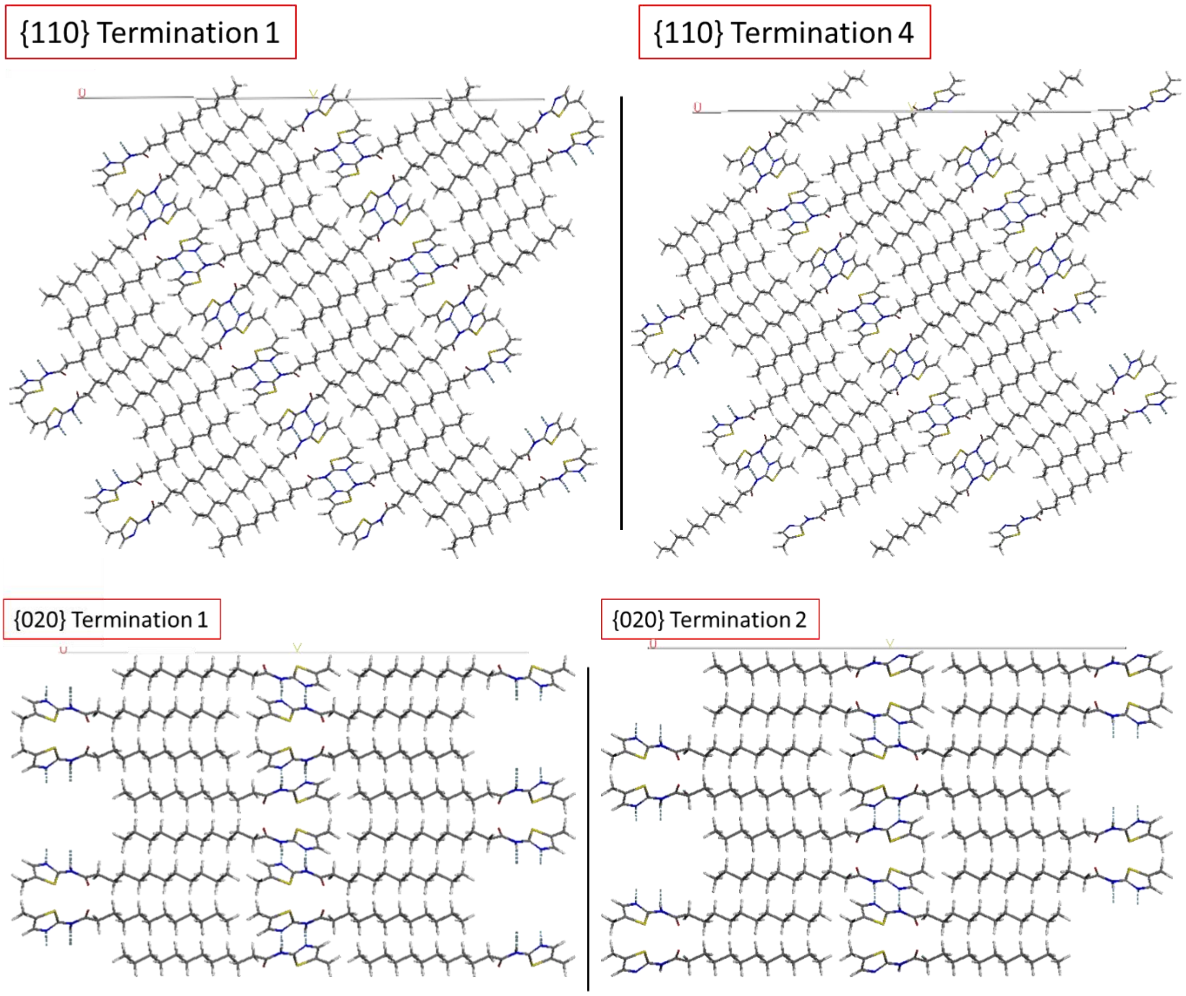

Figure 5.19: Illustrative examples for minimizing: (top) protrusion, (bottom) unbalanced interactions, using different terminations of the {110} and {020} facets, respectively.

Concerning organogelation, we think that the facets parallel to the fiber axis ({110}, {100} and {020}) are highly relevant for fiber-fiber aggregation when forming the entangled network that triggers gelation. In fact, reference [198] points that the individual facets are directly responsible of the observed gelation properties. The authors reached this conclusion after characterizing experimentally the gelation behavior of nanocrystals of cellulose using HSP parameters to explain their amphiphilic character. They determined two gelation spheres very differentiated in Hansen space, assigning one to a polar facet and the other one to an apolar facet (see Figure 5.20).

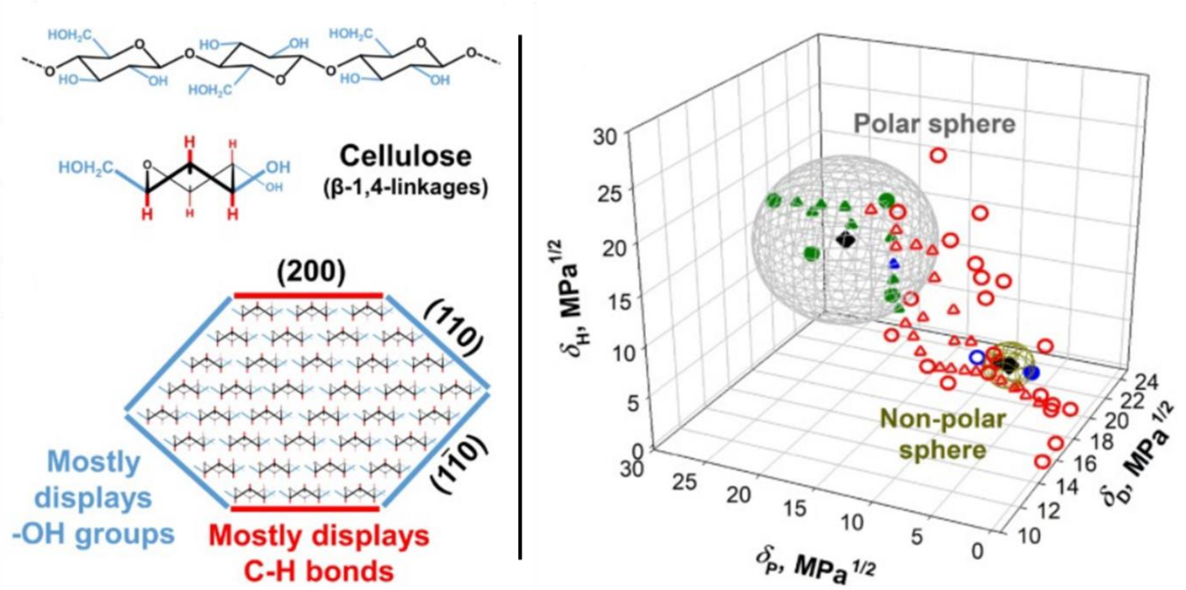

Figure 5.20: The amphiphilic character of nanocrystals of cellulose. (left) on top the cellulose polymer, in the middle its monomeric unit, and bottom its crystallite: in (red) blue the (a)polar contributions, being (200) the apolar surface and (110) and (1-10) the polar surfaces. (right) The Hansen solubility space for the cellulose nanocrystal: pure solvents are represented by circles, binary mixtures by triangles, gelation sphere centers by black diamonds; the symbols located inside a gelation sphere are full and the symbols outside are empty. Adapted from reference **[198]**.

Thus, we proceed to characterize the thiazole facets by surface energy parameters.

5.4 Solubility characterization

Many solubility schemes have been described in Chapter 2 to characterize solvents experimentally, based on thermodynamical, solvatochromic or other magnitudes, and correlating their properties to the chemical structure of gelators and their gelation behavior. On the *in silico* side, organogelation studies are more scarce [13], [14], [199]–[203] and we commented in Chapter 3 a very recent machine-learning approach as a pioneering strategy [88]. Based on the idea that the facets of the fibers may play a crucial role on the gelation phenomenon, we selected the surface energy parameters scheme (∂_i's), which characterizes the solubility as the square root of the surface energy ($\mathrm{E}_{\mathrm{s},i}$): $\partial_i = \sqrt{\mathrm{E}_{\mathrm{s,i}}}$. As the surface energy can be split in dispersive, polar and hydrogen-bonding contributions ($\mathrm{E}_{\mathrm{s,D}}$, $\mathrm{E}_{\mathrm{s,P}}$ and $\mathrm{E}_{\mathrm{s,H}}$, respectively), the dispersive, polar and hydrogen-bonding surface energy parameters are also defined as: $\partial_D = \sqrt{\mathrm{E}_{\mathrm{s,D}}}$, $\partial_P = \sqrt{\mathrm{E}_{\mathrm{s,P}}}$ and $\partial_H = \sqrt{\mathrm{E}_{\mathrm{s,H}}}$, respectively).

We selected this solubility scheme inspired by the experimental work performed by Bergin et. al. [23] where the authors apply this scheme to study the dispersibility of carbon nanotubes in different solvents. They use this scheme because “carbon nanotubes have well-defined surfaces which are the ones interacting with the solvent”, i.e., that the surfaces of carbon nanotubes are responsible of their solubility behavior. Thus, instead of using a cohesive energy definition for the solubility of carbon nanotubes (as in the HSP parameters), the authors argue that a surface energy definition would be more suitable. The general solubility rule is redefined as: the closer are the surface energies of solute and solvent, the better will be the solubility.

They validate this argument by plotting the dispersibility of the nanotubes as a function of the surface energy parameters of the solvents and calculating the weighted average to evaluate the surface energy parameters of the nanotubes (see Figure 5.21).

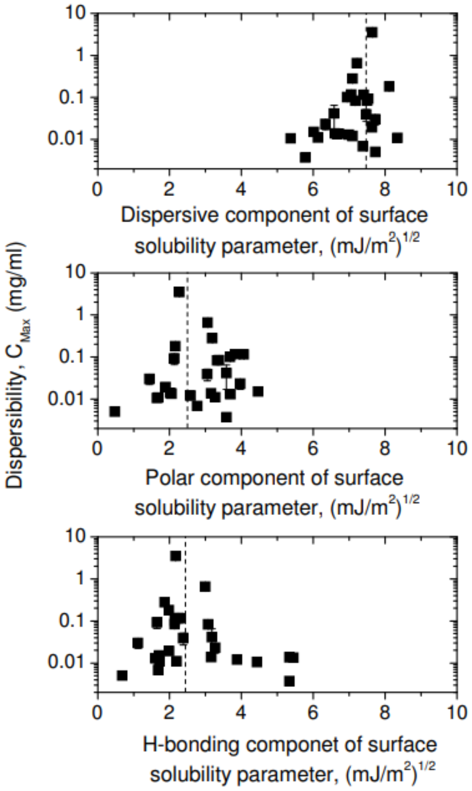

Figure 5.21: Dispersibility of nanotubes versus dispersive (∂_D), polar (∂_P) and H-bonding (∂_H) surface energy solubility parameters of the solvents. Reference [23].

The surface energy parameters of the nanotubes found by this method are ∂_D=7.5 $(mJ/m^2)^{1/2}$, ∂_P=2.6 $(mJ/m^2)^{1/2}$ and ∂_H=2.3 $(mJ/m^2)^{1/2}$, accounting for a total surface energy $E_{S,T}=7.5^2+2.6^2+2.3^2=68.3 mJ/m^2$, which is in agreement with their previous estimation of 65-70mJ/m^2 [22].

We have translated this new perspective about solubility to the characterization of the gel fibers where we think that the facets parallel to the [001] fiber axis are mainly responsible of the interactions with the solvent that finally leads to the fibrillar network ({110}, {100} and {020}). We computed the surface energy and its components for these facets using the EMM method with the 1% error threshold for the Th12-18 compounds (see Table 5-6).

Table 5-6: Theoretical surface energy $\mathbf{E_s}$ and its dispersive, polar and hydrogen-bonding components ($\mathbf{E_{s,D}}$, $\mathbf{E_{s,P}}$ and $\mathbf{E_{s,H}}$, respectively) for the exposed facets parallel to the [001] fiber axis for the Th12-18 compounds. The percentages in parenthesis indicate the contribution of each component to the total surface energy of the facet.

		$\mathrm{E_s}$ (mJ/m^2)	$\mathrm{E_{s,D}}$ (mJ/m^2)	$\mathrm{E_{s,P}}$ (mJ/m^2)	$\mathrm{E_{s,H}}$ (mJ/m^2)
Th12	{110}	**144.58**(100%)	**110.12**(76.16%)	**17.16**(11.87%)	**17.30**(11.97%)
	{100}	**214.38**(100%)	**214.37**(99.99%)	**0.01**(0.01%)	**0**(0%)
	{020}	**102.00**(100%)	**102.30**(100.29%)	**-0.30**(-0.29%)	**0**(0%)
Th14	{110}	**146.53**(100%)	**111.63**(76.18%)	**18.75**(12.80%)	**15.10**(11.02%)
	{100}	**248.83**(100%)	**248.82**(99.99%)	**0.01**(0.01%)	**0**(0%)
	{020}	**102.61**(100%)	**102.98**(100.36%)	**-0.37**(-0.36%)	**0**(0%)
Th16	{110}	**145.90**(100%)	**112.75**(77.28%)	**17.99**(12.33%)	**15.10**(10.39%)
	{100}	**283.43**(100%)	**283.38**(99.98%)	**0.05**(0.02%)	**0**(0%)
Th18	{110}	**144.51**(100%)	**113.60**(78.61%)	**16.81**(11.63%)	**14.17**(9.80%)
	{100}	**318.12**(100%)	**318.00**(99.96%)	**0.12**(0.04%)	**0**(0%)

This characterization confirms that the chemical nature of the facets is ruled by dispersive interactions; it indicates that the (100) facet is the most unstable one, followed by the (110), and then the (020) facet, following the general rule of surface stability: kinked surfaces (100) are more unstable than stepped surfaces (110), and more unstable than terraced surfaces (020). Note that the polar and hydrogen bonding contributions only appear for the {110} facet with similar energy contribution, since amide groups are not forming hydrogen bonds.

In order to compare our theoretical findings with the experimental results, we first considered to use the ∂_i parameters as a common reference because the experimental HSP values of solvents can be converted to ∂_i [204], and obtain the center of the gelation sphere in the ∂_i space. From our theoretical results, in order to have a single dispersive, polar and hydrogen-bonding ∂_i value for each thiazole fiber, we calculated the average of the $\mathrm{E}_{\mathrm{s},i}$ facet values weighted by their corresponding percentage of the crystal area and then calculated its square root to obtain the $\bar{\partial}_D$, $\bar{\partial}_P$ and $\bar{\partial}_H$ values.

$$\bar{\partial}_i = \sqrt{\frac{\sum_i \mathrm{E}_{s,i} \cdot \%\text{Facet Area}}{\sum_i \%\text{Facet Area}}} \tag{5.1}$$

Table 5-7 shows the comparison between theoretical and experimental $\bar{\partial}_i$ values.

Table 5-7: Theoretical against experimental $\boldsymbol{\bar{\partial}_i}$ values.

	Experiment				**Theory**			
	Th12	**Th14**	**Th16**	**Th18**	**Th12**	**Th14**	**Th16**	**Th18**
$\bar{\partial}_{\mathrm{D}}$	6.75	6.31	5.88	5.86	12.36	12.82	13.27	13.77
$\bar{\partial}_{\mathrm{P}}$	1.36	0.00	0.94	0.92	2.91	3.36	3.36	3.26
$\bar{\partial}_{\mathrm{H}}$	4.42	2.92	0.94	0.86	2.92	3.02	3.08	2.98

The trends are opposed for the three contributions, and the magnitude of the dispersive contribution is much higher in theory than in experiment. We point that the 0.00 experimental value of $\bar{\partial}_{\mathrm{P}}$ for Th14 may arise either from a miscalculation of the center of the gelation sphere or a too small amount of data.

Faced with those discrepancies, our first effort was to improve the theoretical values by considering that some surfaces have a high roughness, meaning that the solvent is in contact with a larger surface than when considering a totally smooth facet. We thus recalculated the surface area of every facet. For that purpose, we used the Connolly approach which characterizes the van-der-Waals surface of a molecule by rolling a spherical solvent molecule with a user-defined probe radius and atomic van-der Waals radii, thus creating a contour of the surface [177], [178]. Figure 5.22 shows a comparison of the surface area computed for the {100} facet of Th12 using the Connolly method or the flat area.

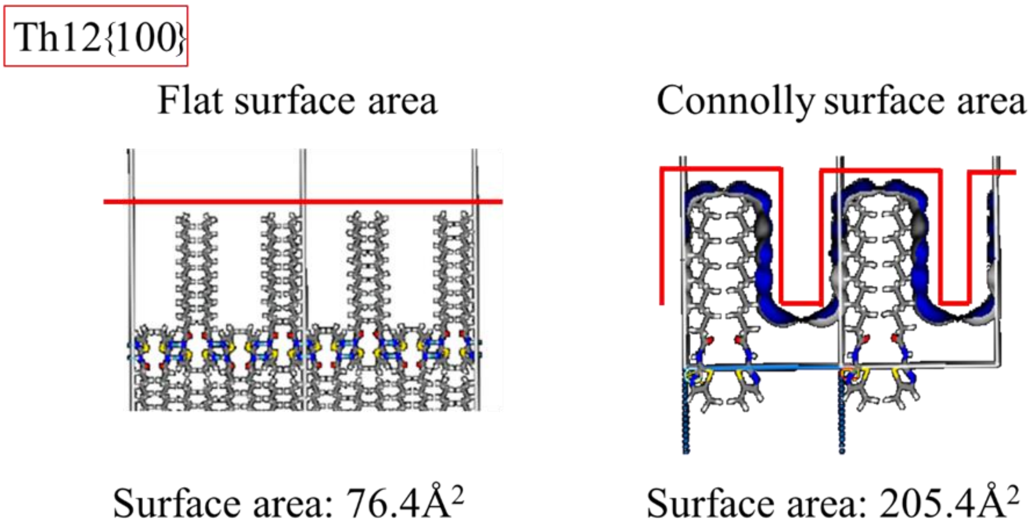

Figure 5.22: Comparison of the surface area computed (left) as a flat area or (right) by the Connolly method.

The Connolly method leads to new surface areas for the Th12-18 compounds (see Table 5-8).

Table 5-8: Connolly versus flat surface areas for the {110}, {100} and {020} facets for the Th12-18 compounds.

	Flat surface area (Å^2)			**Connolly surface area (Å^2)**		
	{110}	**{100}**	**{020}**	**{110}**	**{100}**	**{020}**
Th12	133.9	76.4	110.0	186.6	205.4	123.1
Th14	143.6	76.2	121.8	199.5	232.0	136.3
Th16	153.7	75.9	133.6	212.5	258.4	149.5
Th18	164.0	75.7	145.4	225.5	285.0	162.7

As expected, the Connolly surface areas are larger than the flat ones as the roughness of the molecules is considered. We observe that the largest difference is for the kinked {100} facet surface area, due to the long kinks formed by the alkyl chains protruding outwards. For flat areas, the surface increases with the alkyl chain length in all cases except for the {100} facets, which have a constant surface area that is small compared to that of the other facets. After the Connolly correction, the surface area of the {100} facet is larger than that of other facets and increases with the alkyl chain length, thus better reflecting the increase of the interactions between the solvent and the facet terminations. Thus, the Connolly correction, in addition to providing a more precise surface area value, also corrects the trends. These Connolly values, however, also include implicitly a smaller effect of the atomic roughness, i.e., that the atoms are not flat, but rather spherical, which could overestimate the surface area correction that we have applied. Thus, to account for that subtle effect, we calculated the roughness ratio, as the coefficient of the Connolly surface area divided by the flat area, and defined the “corrected areas” as the Connolly surface divided by the smallest roughness value (1.12), which corresponds to the {020} facet. This facet has a terrace surface morphology with no molecular moieties protruding, and can thus be considered as flat. By applying this factor to all facets, we remove the overcorrection due to atomic roughness (see Table 5-9).

Table 5-9: Roughness ratio and corrected areas for the {110}, {100} and {020} facets for the Th12-18 compounds.

	$\textbf{Roughness ratio} = \frac{\text{Connolly surface area}}{\text{Flat area}}$			$\textbf{Corrected area} = \frac{\text{Connolly surface area}}{1.12}$		
	{110}	**{100}**	**{020}**	**{110}**	**{100}**	**{020}**
Th12	1.39	2.69	1.12	166.6	183.4	110.0
Th14	1.39	3.04	1.12	178.1	207.1	121.8
Th16	1.38	3.40	1.12	189.7	230.7	133.6
Th18	1.38	3.76	1.12	201.3	254.5	145.4

Thus, we recompute the surface energies as: $\mathrm{E}_{\mathrm{s},i} = \left(\text{Previous } \mathrm{E}_{\mathrm{s,i}}\right) * \frac{\text{Flat area}}{\text{Corrected area}}$, see Table 5-10.

Table 5-10: Recalculated $\mathbf{E}_{\mathbf{s},\boldsymbol{i}}$'s using the corrected areas.

		$\mathrm{E_s}$ (mJ/m^2)	$\mathrm{E_{s,D}}$ (mJ/m^2)	$\mathrm{E_{s,P}}$ (mJ/m^2)	$\mathrm{E_{s,H}}$ (mJ/m^2)
Th12	(110)	**116.19** (100%)	**88.50** (76.17%)	**13.79** (11.87%)	**13.90** (11.96%)
	(100)	**89.31** (100%)	**89.30** (99.99%)	**0.01** (0.01%)	**0.00** (0%)
	(020)	**102.08** (100%)	**102.08** (100%)	**0.00** (0%)	**0.00** (0%)
Th14	(110)	**117.28** (100%)	**89.99** (76.73%)	**15.12** (12.89%)	**12.17** (10.38%)
	(100)	**91.54** (100%)	**91.53** (99.99%)	**0.01** (0.01%)	**0.00** (0%)
	(020)	**102.70** (100%)	**102.70** (100%)	**0.00** (0%)	**0.00** (0%)
Th16	(110)	**118.14** (100%)	**91.34** (77.32%)	**14.57** (12.33%)	**12.23** (10.35%)
	(100)	**93.24** (100%)	**93.23** (99.99%)	**0.01** (0.01%)	**0.00** (0%)
Th18	(110)	**117.76** (100%)	**92.53** (78.58%)	**13.69** (11.62%)	**11.54** (9.80%)
	(100)	**94.64** (100%)	**94.60** (99.96%)	**0.04** (0.04%)	**0.00** (0%)

Considering the corrected areas, we recalculate the percentage of facet area shared by the lateral facets in the crystal habit. For this purpose, we deduce the proportion of the corrugated facet area (C$_i$) as the previous percentage of facet area (F$_i$), scaled by the roughness ratio (r$_i$), and averaged for all lateral facets: $\mathrm{C}_i(\%) = \frac{F_i * r_i}{\sum_i F_i * r_i} * 100$, (see Table 5-11).

Table 5-11: Recalculated percentage of facet area considering the lateral facets of the crystal habit.

%Facet area	**{110}**	**{100}**	**{020}**	**Total**
Th12	36%	59%	5%	100%
Th14	41%	58%	1%	100%
Th16	41%	59%	0	100%
Th18	38%	62%	0	100%

The recalculation of the percentage of facet area for the lateral facets leads to a decrease of the {110} facet and an increase of the {100} when elongating the alkyl chain length. These findings contrast to that of Table 5-3, where the trends are inverted. Thus, the effect of considering the corrugation of the facets appears to be of great importance to characterize the facets. Using these reevaluated percentages, we compare again the theoretical and experimental $\bar{\partial}_i$ values (see Table 5-12).

Table 5-12: Recalculated theoretical against experimental $\bar{\partial}_i$ values.

	Experiment				Theory			
	Th12	**Th14**	**Th16**	**Th18**	**Th12**	**Th14**	**Th16**	**Th18**
$\bar{\partial}_{\mathrm{D}}$	6.75	6.31	5.88	5.86	9.47	9.54	9.61	9.68
$\bar{\partial}_{\mathrm{P}}$	1.36	0.00	0.94	0.92	2.23	2.49	2.44	2.29
$\bar{\partial}_{\mathrm{H}}$	4.42	2.92	0.94	0.86	2.24	2.23	2.24	2.09

The theoretical values have improved considerably: their magnitude is much closer to the experimental ones. The theoretical $\bar{\partial}_{\mathrm{P}}$ and $\bar{\partial}_{\mathrm{H}}$ values remain almost constant from Th12 to Th18, versus the experimental ones which are decreasing. The main difference is still the opposed trends for $\bar{\partial}_{\mathrm{D}}$.

Several reasons can explain this discrepancy, such as: (i) the relaxation of the surface, which could for instance restore hydrogen bonds between neighboring thiazoles and allow the surfaces to adapt their morphology depending on the solvent. (ii) The software used for obtaining the center of the gelation sphere in the ∂_i space is not prepared for this space, i.e., the HSP parameters form spheres in the Hansen space, but the ∂_i values do not form spheres in the ∂_i space but ellipsoids. (iii) The influence of the tips, which have polar and hydrogen-bonding contributions, were not included in the analysis.

5.5 Conclusions

In conclusion, we successfully modelled the molecular packing and morphology of the thiazole gelators, first inside the gel fibers, observing that thiazole molecules interact through a combination of hydrogen-bonding, π-stacking and sulfur-related interactions. Since the aspect ratio value is lower for the GMM method, which takes into account the specificity of the interactions, than for the BFDH method, which is based on geometric factors instead, we identify the crystal cell geometry as the main driver for the anisotropy of the gel fibers, indicating that thiazole interactions play a minor role in fiber elongation. We determined and characterized the chemical composition of the facets exposed by the fibers, correlating that the chemical composition of the fiber facets, and thus the solubility behavior of gel fibers, is closely related to the chemical structure of the gelator molecules. We characterized the gelation ability of the thiazole fibers by the surface energy solubility parameters of their lateral facets. We improved our modelling strategy by accounting for the rugosity of the facets and reevaluating these parameters. We reached a closer agreement but there are still some discrepancies, indicating that other factors should also be considered to have a better representation of the phenomena.

Chapter 6. **Conclusions and perspectives**

6.1 Conclusions

The understanding of the supramolecular organogelation phenomena is partial and this thesis aimed to correlate the chemical structure of sets of chemically diverse gelators and their gelation behavior using modelling. The formation of gel fibers is key for organogelation; we therefore focused on the structure of those fibers and we successfully modelled the bulk and surface composition of gel fibers for four bisamide (BiC3-6) and four thiazole (Th12-18) gelators of increasingly longer alkyl chain, always comparing with experimental observations obtained in the groups of Prof. Laurent Bouteiller (Sorbonne Université) and Prof. Pierre-Antoine Albouy (Université Paris-Sud). We also draw some insights for five additional bisamide gelators (BiC8-18) with longer alkyl chains, which give rise to amorphous assemblies.

First, we characterized ***the organization of gelator molecules inside the gel fibers*** by developing a Crystal Structure Prediction strategy based on combining crystal cell generation and powder X-ray diffraction simulations.

The molecular packing of bisamide gelators is characterized by stacked cyclohexane rings where the amide groups are connected by hydrogen bonds that propagate along one specific direction and directs fiber growth preferentiality. Despite similar stacking, the orientation of alkyl chains varies from one compound to the next: the alkyl chains are either oriented in opposite directions (BiC3 and BiC5), or in the same direction (BiC4), or in a fully trans conformation (BiC6). Thus, one cannot assume in principle any predefined orientation of alkyl chains in molecular crystals with 5 or less aliphatic carbons, due to the flexibility of alkyl chains to adopt different molecular orientations. Nevertheless, we expect for BiC8 to BiC18 that their molecular packing is kept, showing a hydrogen bonding pattern similar to that for the BiC3-6 compounds and alkyl chains having a fully *trans* conformation, likely showing an interdigitated arrangement.

Experimentally, polymorphism was observed for the BiC5 and BiC6 gelators. We characterized the two polymorphs of BiC6. They differ in the number of molecules in the unit cell, the angle between the alkyl chains and the geometry of hydrogen bonds. The potential energy of the polymorphs differs by 7.4 kcal/mol, with 4.8 kcal/mol related to hydrogen bond geometries. Thus, hydrogen bond geometries are also relevant for the polymorphism of the bisamide gelators. As one of the polymorphs is probably the kinetically-stable form of the BiC6 gelator, we also think that gel fibers can be formed by kinetically or thermodynamically stable conformations of the gelators.

The molecular packing in the second family of compounds, i.e., the thiazole gelators, is characterized by thiazole molecules forming dimers connected by hydrogen bonds in a cyclic manner. We find that the intramolecular sulfur-oxygen non-covalent interaction may generate a specific molecular conformation that favors this cyclic hydrogen bonding scheme. The alkyl chains have a fully *trans* configuration, showing a 2+2 interdigitation scheme. This molecular packing is conserved from Th12 to Th18. In contrast to the bisamide family, there is no clear interaction that favors the preferential growth of the fibers.

We then modeled ***the crystal morphology of gel fibers*** with the BFDH, GMM and EMM morphology methods, which provide the aspect ratio of the gel fibers, the direction of growth, the chemical composition displayed on the facets and the surface energy of the facets. When we compared the aspect ratio of the modelled fibers generated by the different approaches for the thiazole compounds, we identify the crystal cell geometry as the main driver for the anisotropy of the gel fibers, since the aspect ratio value is lower for the GMM method, which takes into account the specificity of the interactions, than for the BFDH method, which is based on geometric factors instead, indicating that thiazole interactions play a minor role in fiber elongation. In contrast, for the bisamide gelators, the aspect ratio values are higher with the GMM method than with the BFDH method, indicating that the interactions along the direction of growth reinforce anisotropy. This contrast can be correlated with the fact that hydrogen bonds are aligned and fully connected in the direction of growth for bisamides, while for thiazoles they are neither aligned nor fully connected. Thus, hydrogen bonds are not always the main driver for anisotropic growth.

The determination of the crystal morphology also revealed the chemical moieties exposed on the fiber facets. There are two types of thiazole facets, governed by dispersive interactions from the alkyl chain parts. In the first type, dispersive interactions account for two thirds of the total attachment energy of the facet, the last third being assigned to the polar and hydrogen-bonding contributions, which are related to the amide and thiazole ring groups. In the second type, dispersive interactions almost totally dominate the attachment energy of the facet. These two types of facets are observed both for the lateral facets and the tips of the fibers. Such isotropy is not present for the bisamide fibers, where the lateral facets are governed only by dispersive interactions, from the alkyl chains and cyclohexane rings, while for the tips interactions are highly polar and with a strong hydrogen-bonding character. This anisotropy is due to the alignment of hydrogen bonds in the elongated direction of the fiber. We initially thought that the gelation behavior of fibers was mainly characterized by the chemical composition of the lateral facets; in other terms, we had hypothesized that the network formation was driven by the lateral aggregation of fibers. However, the high hydrogen bond contribution from the experimental Hansen Solubility Parameters for the bisamide gels indicates that hydrogen bonding, and thus the tips of the fibers, plays a significant role in the gelation process of bisamides.

In this work, we used surface energy parameters as a common reference point to compare the modelling and experimental solubility characterization of the thiazole set of gelators. We characterized the lateral facets of the gel fibers by surface energy with the EMM method and we compared these values with the surface energy parameters derived from the experimental Hansen Solubility Parameters, observing major differences both in the amplitude and evolution with the length of the alkyl chain. We improved this comparison by computing a more accurate surface area with the Connolly method, accounting for the roughness of the facets and reevaluating these parameters. This procedure is especially advisable for facets with high roughness, like kinked facets. We reached a closer agreement but there are still some discrepancies, indicating that other factors should also be considered to have a better representation of the phenomena.

6.2 Perspectives

Thanks to the combination of modelling and experimental efforts, we have several established procedures that can be applied for studying future gelators. Thus, one first perspective of this work could be to apply the molecular packing, crystal morphology and solubility characterization procedures to other families of gelators with systematic chemical variations. For example, it could be highly interesting to study the influence of the methyl moiety variations on the thiazole rings, as experimental data are available, showing which compounds are gelators and which ones are not. One could correlate the chemical structure of the gelator and the gelation ability to the supramolecular interactions that propagate through the elongated direction of growth. With these possible correlations, we could propose some new guidelines for rationally designing new gelators.

Also, some strategies could be envisioned to improve the solubility characterization. The first and more straightforward approach would be to include the tips of the fibers, as their relevance has been highlighted for the bisamide gelators. This strategy would allow reevaluating the solubility parameters of the gel fibers and likely provide a more realistic evaluation of the gelation behavior. Also, deriving an expression to convert surface energy-related values to the Hansen Solubility Parameters scheme could directly compare theory and modelling, eliminating the error of determining the center of the sphere in the surface energy parameter space.

As our calculations are performed at the temperature of 0K, we do not include temperature effects. Thus, an additional strategy could be to include them, which would allow to address the reorganization of the molecules, which can affect the surface energy values. This effect could be implemented e.g., by Molecular Dynamics simulations.

Another factor that we do not include explicitly in our simulations is the solvent. We discussed that the effect of the solvent would likely only modify the percentage area of the facets that we have already characterized in this work. However, we think it could be more interesting to study the specific gelator-solvent interaction, as the Crystal Mismatch Branching (CMB) mechanism hypothesizes that a solvent molecule, or an additive, can adsorb on the tip of the growing fiber and change the process of gel formation from fiber aggregation to the CMB process. This study may lead to new insights on the formation of gel fibers and obtain new designing rules for gelators.

For the BiC8 to BiC18 gelators, as we cannot get the structural information about their molecular packing from the powder X-ray diffraction patterns, our experimental partners determined the Pair Distribution Function (PDF) of these gelators using a synchrotron. We generated different possible molecular packings by modelling, but without further refinement, we remain cautious about the generated molecular packings. Softwares for PDF refinement exist, but they are mostly used for inorganic materials. In this work, we tested the XINTERPDF software, which is more suitable for molecular crystals, and some preliminary results indicated a possible viability for determining the molecular packing for these bisamide gelators. Thus, a methodology based on molecular packing generation and PDF refinement could be explored in the future.

We also tried to predict from scratch the crystal structure of BiC4, as a test, combining crystal cell generation and energy ranking, observing the structures ranked among the most stable ones. We then compared the energy ranking obtained by Molecular Mechanics with those obtained by state-of-the-art tight-binding potentials for molecular crystals where, depending on the selected method for evaluating the relative energy of the generated cells, the ranking changed due to the different approximations used. It could be highly interesting to develop a strategy to identify potential crystal cells for a given gelator when no structural information is available. This strategy should aim to compute relative energies accurately while keeping a moderate computational cost, as thousands of possible cells must be evaluated. For example, one state-of-the-art approach uses a force field tuned for crystal structure prediction [205], [206]. If this step is achieved, automatic *in-silico* evaluations of crystal morphology and solubility parameters could be done for new potential gelators, saving large time and resources for designing new gelators.

In the literature [53], it was found that different stages of the organogelation process have been characterized experimentally using transient AFM images. From that characterization, one of the early stages consisted in the formation of gelator stacks that later evolve into gel fibers. We humbly hypothesize that there might be some energy threshold between the gelator molecules that favors the stacking of the gelator molecules which may later act as the nuclei to the formation of the gel fibers. Thus, we think that this energy threshold could be related to the nucleation energy barrier of the formation of the gel fibers. A study of the energetics between the gelator stacks that propagate through the elongated direction of growth, for gelators with different functional groups and moieties, could establish potential rules for designing new gelators. For example, this approach could be implemented with gelators whose molecular packing is already known, as those in this work.

Finally, the tools that have been developed for the Machine Learning (ML) field could also be potentially applied to characterize the organogelation phenomena and design new gelators *in-silico*. In order to incorporate these tools, one must keep in mind two factors that are key to make successful predictions. The first one is the amount of reference samples for the machine to learn. For example, a reduced amount of reference samples would lead to highly inaccurate predictions for cases where the machine has to perform a large extrapolation. The second factor is the description of the system to treat. For example, a poor choice of the variables to describe the problem would make it highly difficult or impossible for the machine to learn. Another additional consideration is that there are different predictive models, and thus the prediction also depends on the selection of the model to train the machine. In the case of organogelation, there are many solubility tests available, and one could think of predicting whether gelation is likely to be triggered with descriptors based on the chemical structure of the gelator and the solvent. This approach may result interesting as we commented in this work that the chemical composition of the fiber facets, and thus the solubility behavior of gel fibers, is closely related to the chemical structure of the gelator molecules. Thus, for example, a promising future work would be to find the proper predictive model and set of descriptors that correlate best for different sets of chemically diverse gelators.

A. Appendices

A1. Chapter 3

The 38 molecular crystals used for tuning the van der Waals interactions of hydrogen atoms in the Dreiding forcefield are the following:

Piperazine

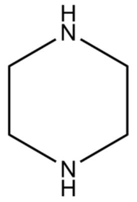

1

Cyclohexane-1,4-dione

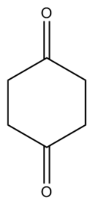

2

cis,cis-cyclohexane-1,3,5-tricarboxamide

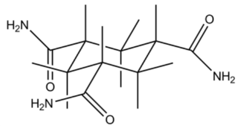

3

cis(1R,2S)-2-hydroxy-1-cyclopentanecarboxamide

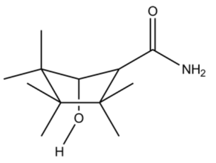

4

1-Aminocyclopentanecarboxamide

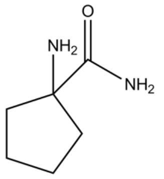

5

2-Cyano-N-cyclohexylacetamide

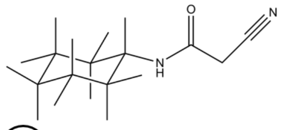

6

N-Phenylcyclohexanecarboxamide

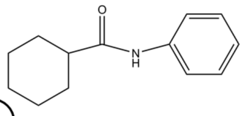

7

2-Amino-2,3-dimethylbutanamide

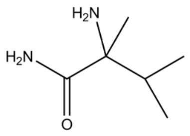

8

3-Diazo-N-[(2S)-1-hydroxypropan-2-yl]-2-oxopropanamide

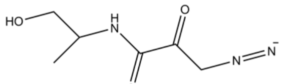

9

N-tert-Butyl-2-methyl-propanamide

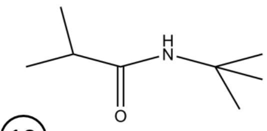

10

Cyclohexane

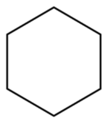

11

Cyclopentane

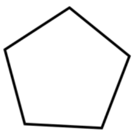

12

n-hexane

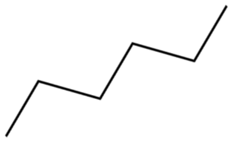

⑬

n-pentane

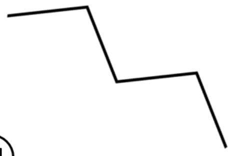

⑭

n-butane

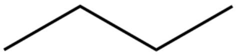

⑮

butyramide

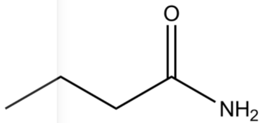

⑯

Acetic acid

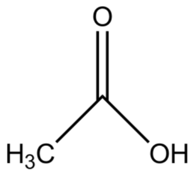

⑰

Adamantane

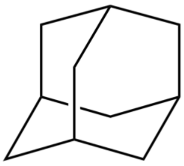

⑱

Ammonia

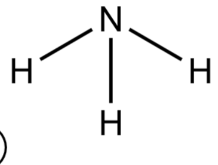

⑲

Anthracene

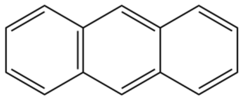

⑳

Benzene

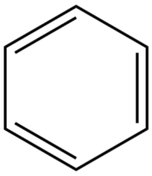

㉑

CO_2

㉒

Cyanamide

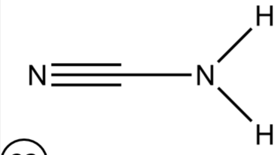

㉓

Cytosine

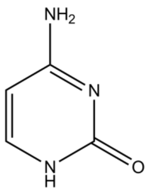

㉔

Ethyl carbamate

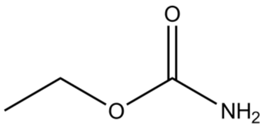

㉕

Formamide

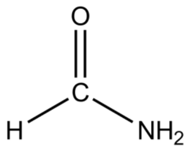

㉖

Imidazole

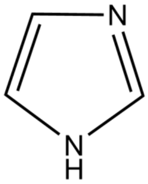

㉗

Hexamine

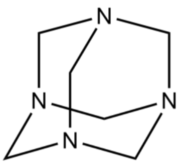

㉘

Napthalene

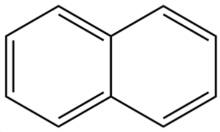

㉙

Oxalic acid α

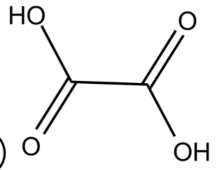

㉚

Oxalic acid β

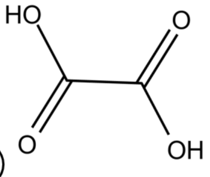

㉛

Pyrazine

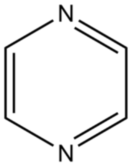

㉜

Pyrazole

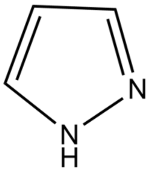

㉝

Succinic acid

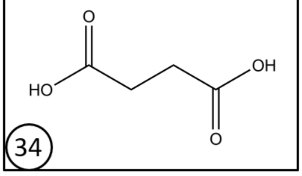

㉞

Triazine

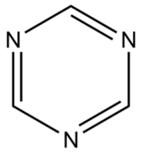

㉟

Trioxane

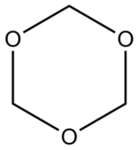

㊱

Uracil

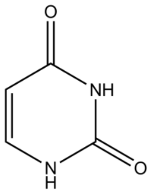

㊲

Urea

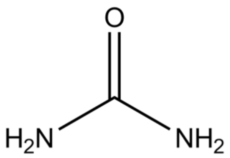

㊳

A2. **Chapter 4**

The different terminations of the facets exposed by the bisamide structures are illustrated here with the example of the BiC3 compound. Note that the terminations dubbed as T1 (Termination 1) are the most stable ones for each facet.

{100} facet

T1

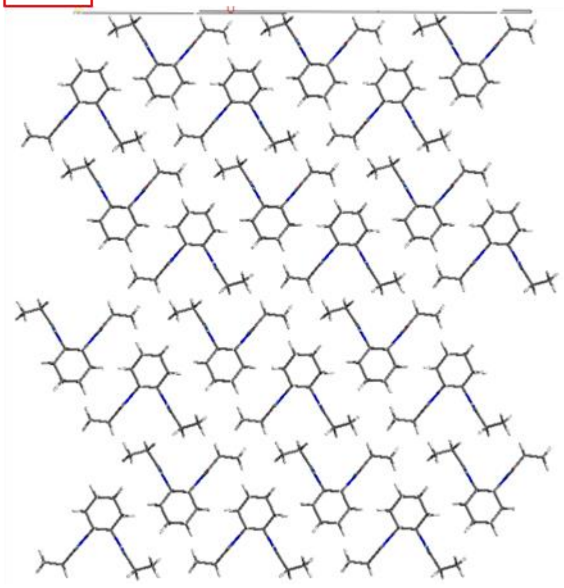

T2

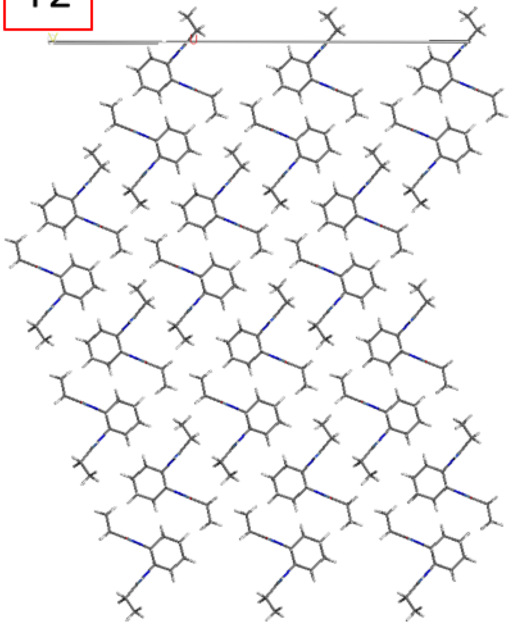

{001} facet

T1

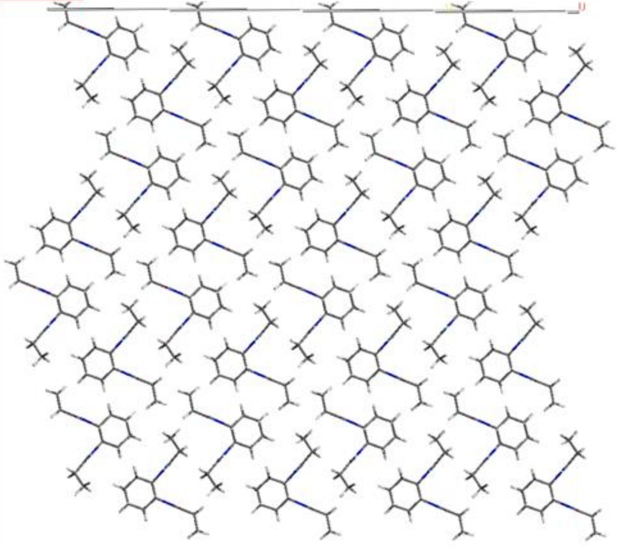

T2

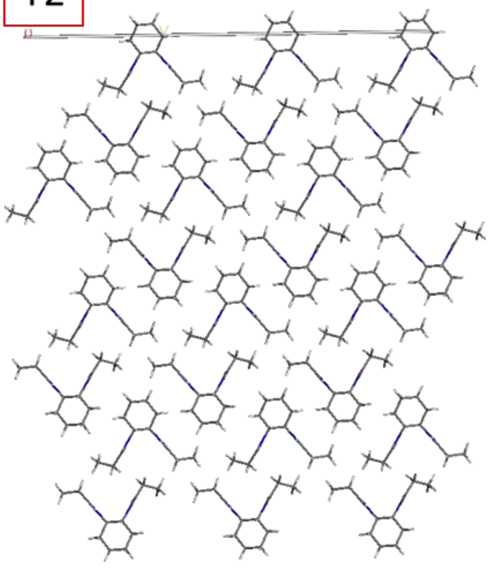

{10-1} facet

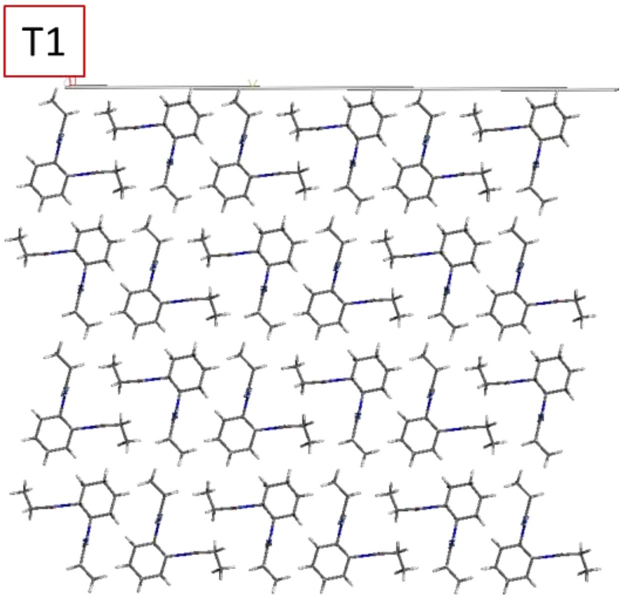

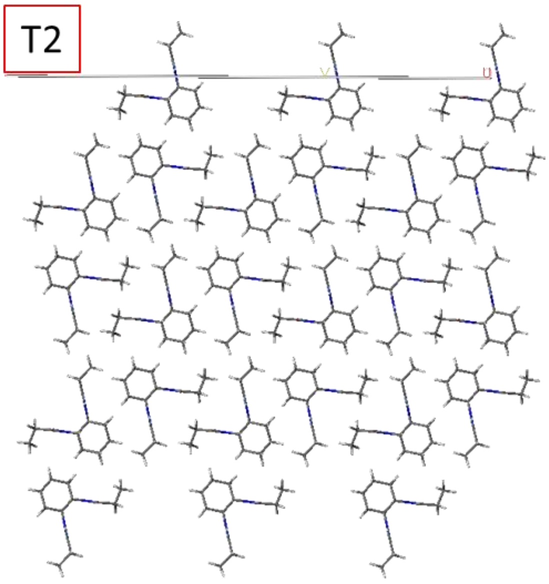

{011} facet

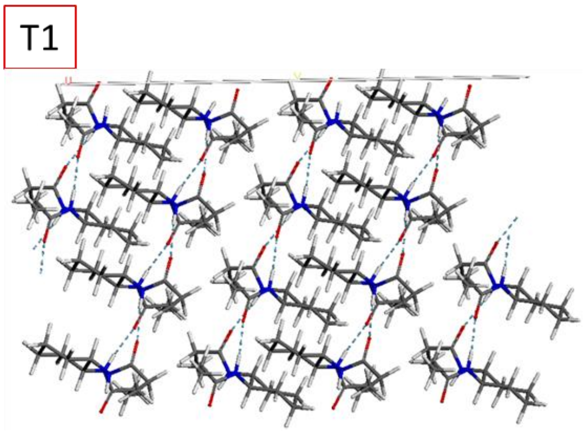

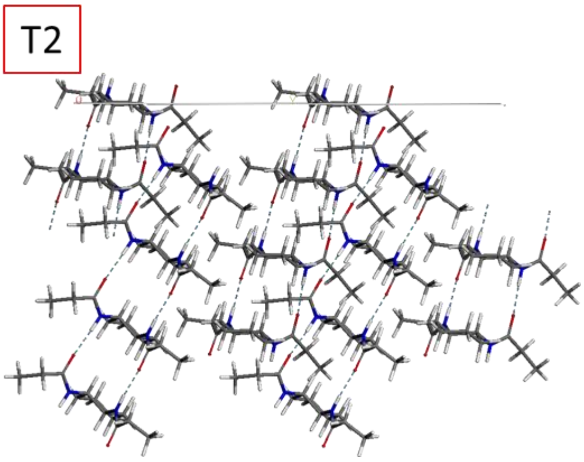

{0-11} facet

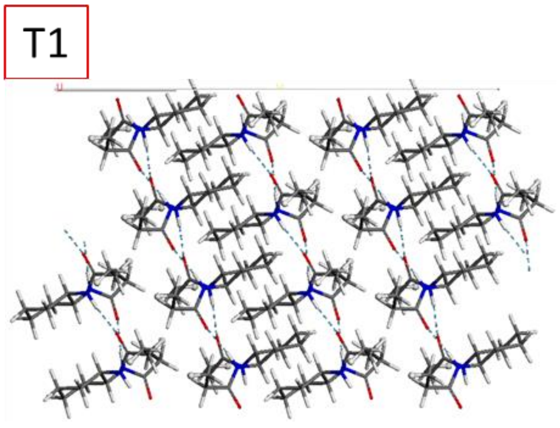

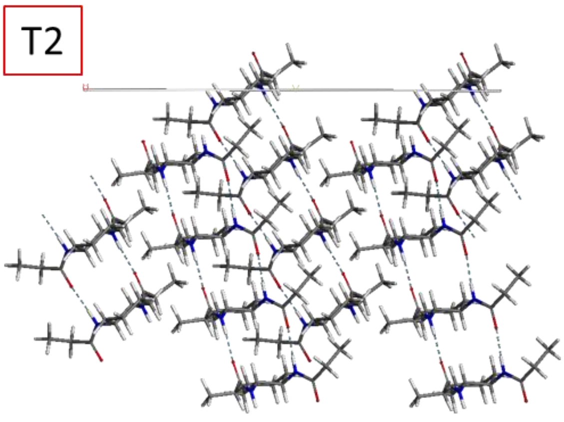

{110} facet

T1

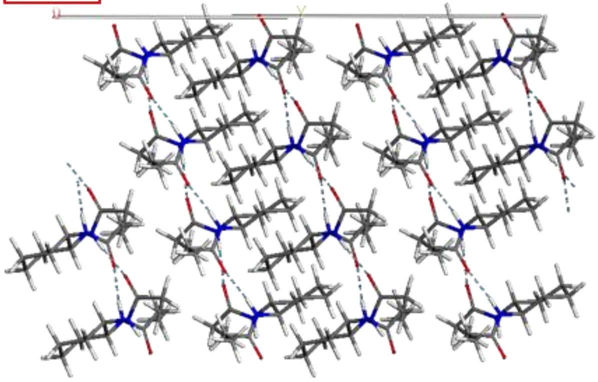

T2

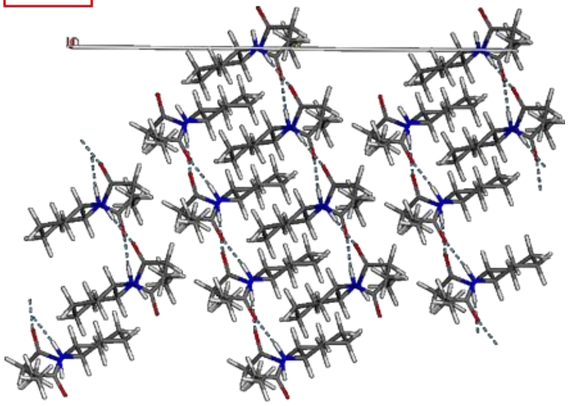

{1-10} facet

T1

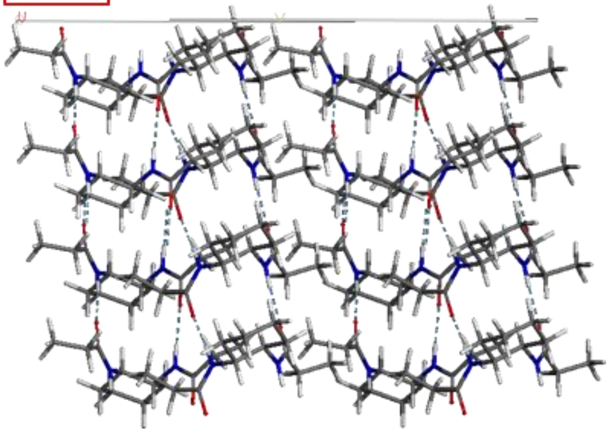

T2

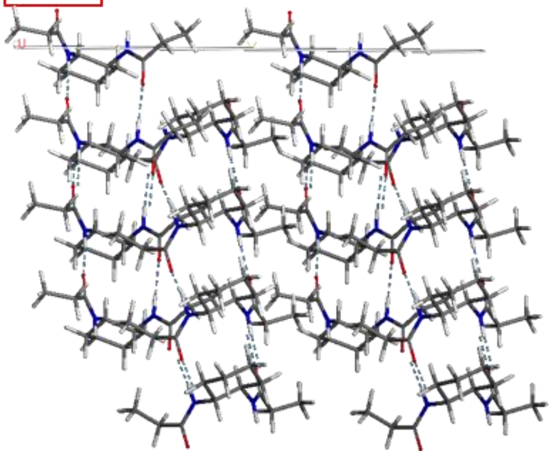

A3. Chapter 5

Molecular coverings

The different terminations of the facets exposed by the thiazole structures are illustrated here with the example of the Th12 compound. Note that the terminations dubbed as T1 (Termination 1) are the most stable ones of each facet for Th12.

{110} facet

T1

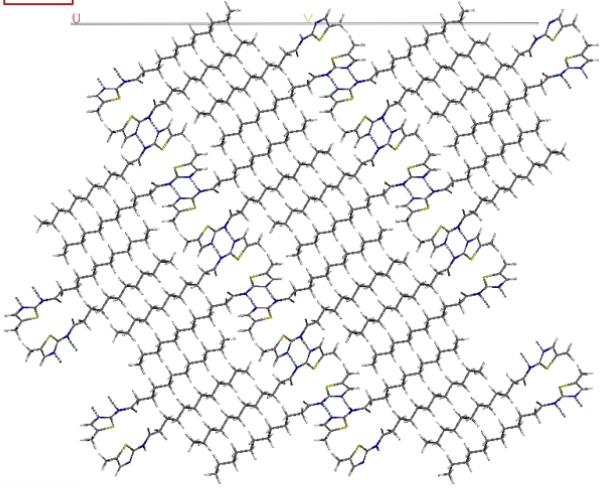

T2

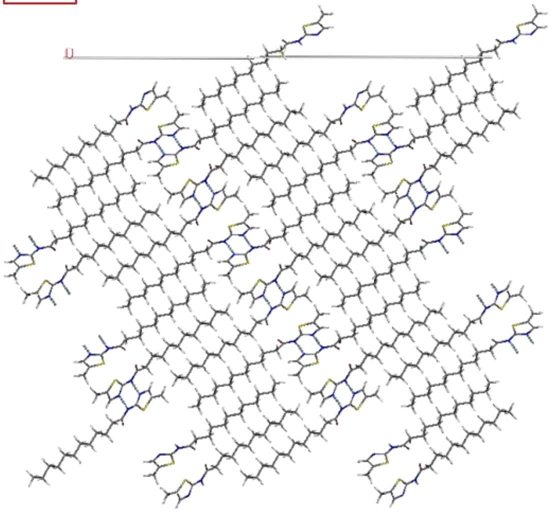

T3

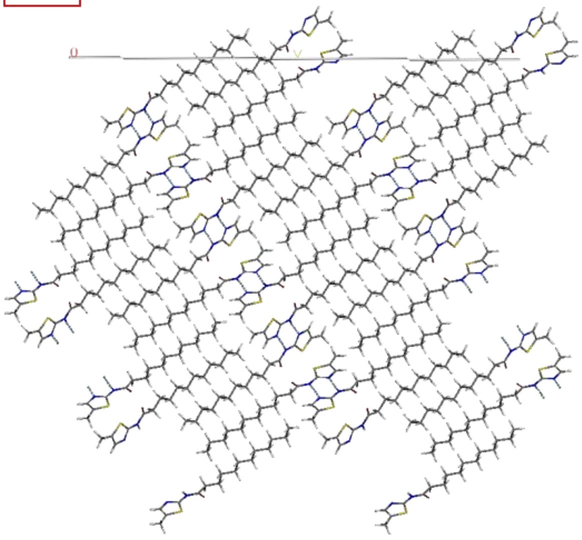

T4

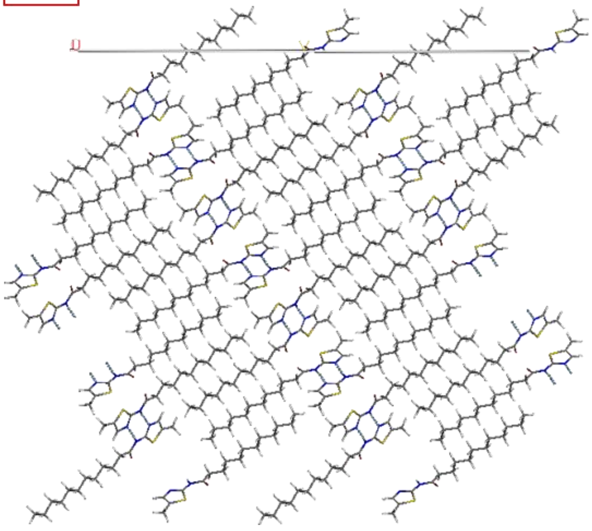

{100} facet

T1

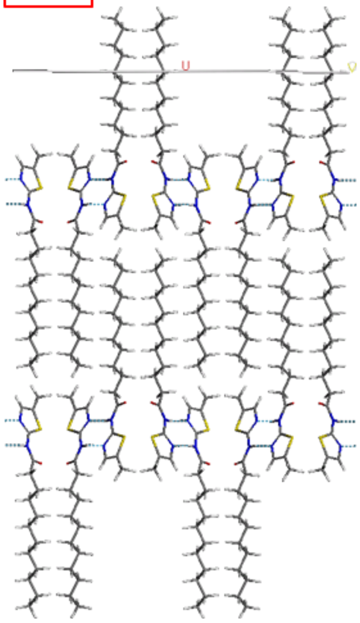

T2

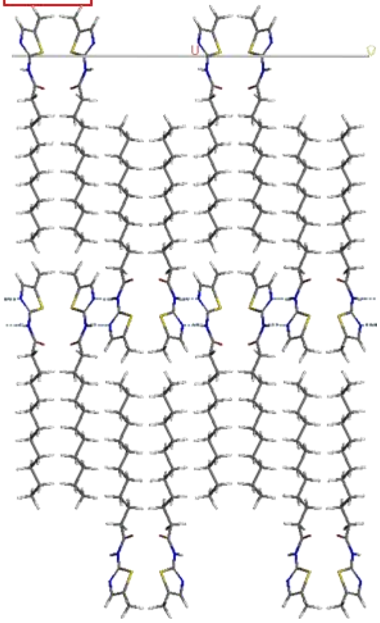

{11-1} facet

T1

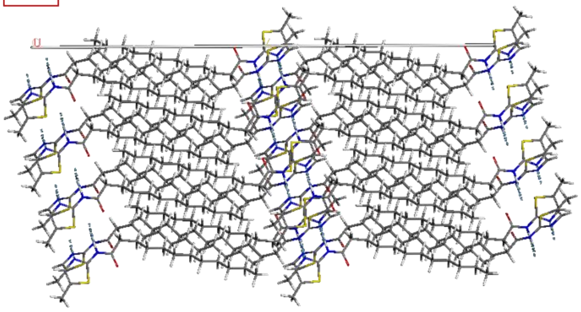

T2

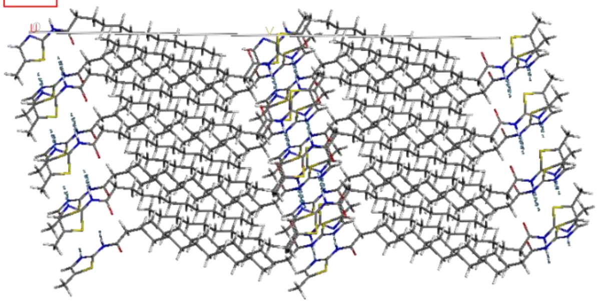

T3

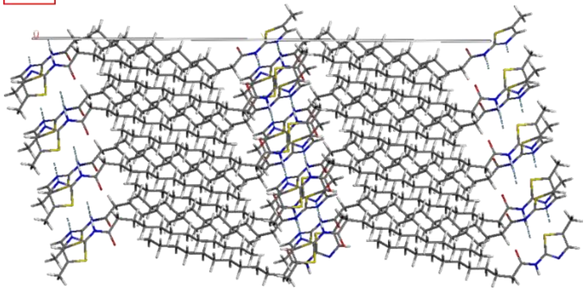

T4

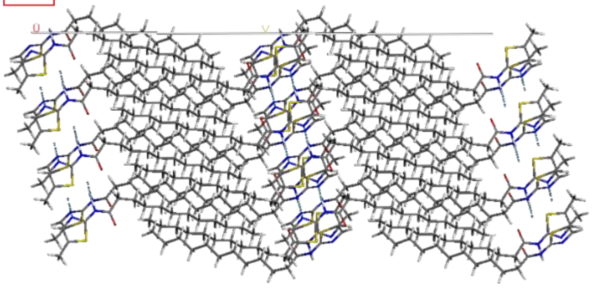

{011} facet

T1

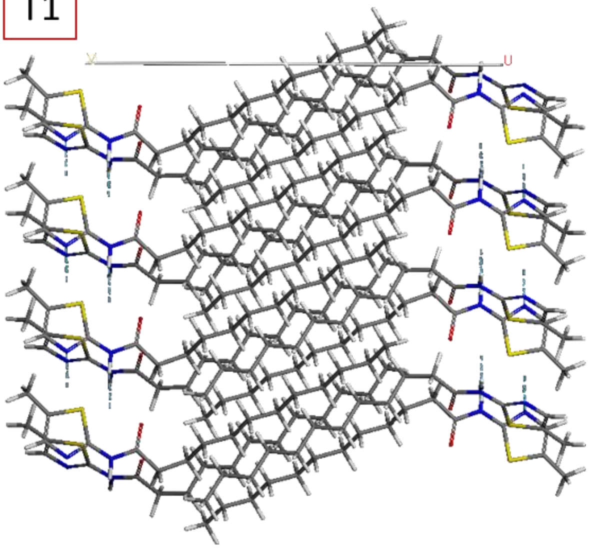

T2

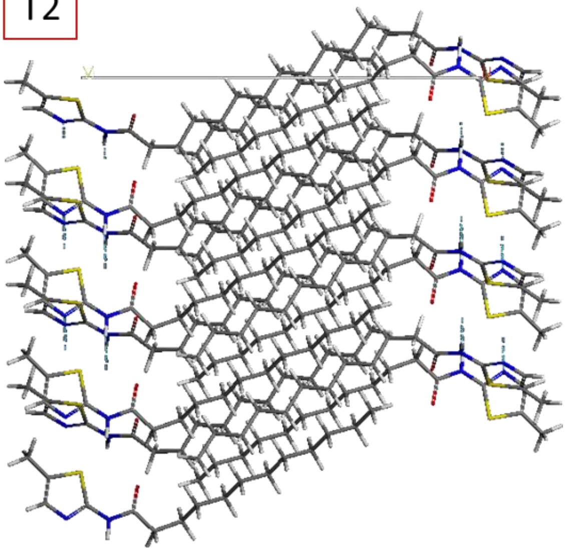

T3

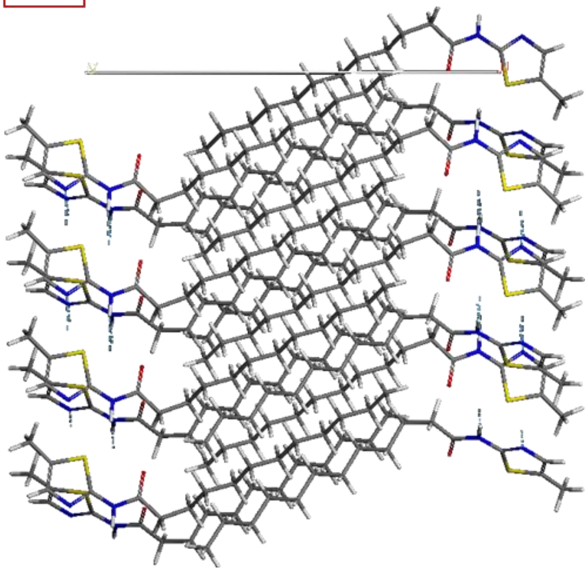

T4

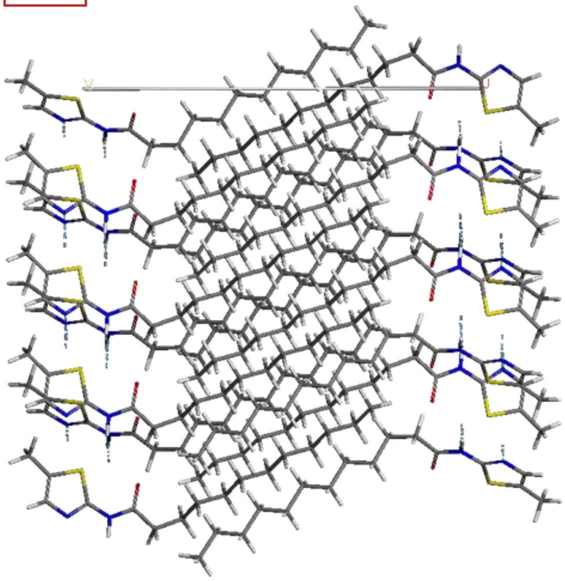

{020} facet

T1

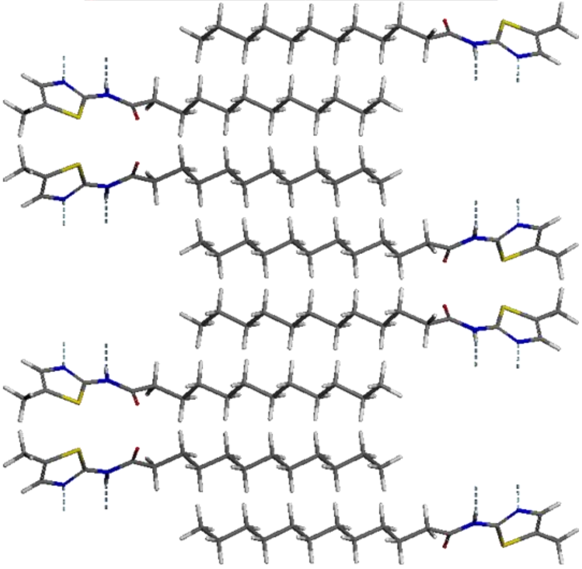

T2

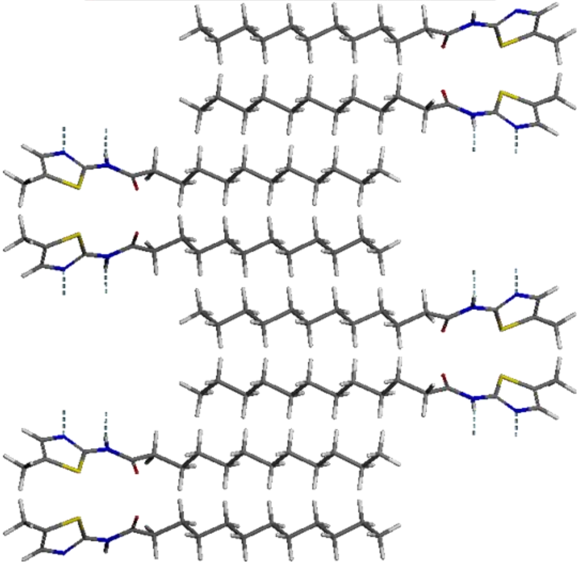

Bibliography

[1] T. Graham, 'X. Liquid diffusion applied to analysis', *Philosophical transactions of the Royal Society of London*, no. 151, pp. 183–224, 1861.

[2] R. B. Dean and others, 'Modern colloids', 1948.

[3] P. Hermans, 'Gels', *Colloid science*, vol. 2, pp. 483–651, 1949.

[4] J. D. Ferry, *Viscoelastic properties of polymers*. John Wiley & Sons, 1980.

[5] J. Alemán *et al.*, 'Definitions of terms relating to the structure and processing of sols, gels, networks, and inorganic-organic hybrid materials (IUPAC Recommendations 2007)', *Pure and Applied Chemistry*, vol. 79, no. 10, pp. 1801–1829, 2007.

[6] P. Flory, 'Introductory lecture', *Faraday Discussions of the Chemical Society*, vol. 57, pp. 7–18, 1974.

[7] Y. Lan, M. Corradini, aR G. Weiss, S. Raghavan, and M. Rogers, 'To gel or not to gel: correlating molecular gelation with solvent parameters', *Chemical Society Reviews*, vol. 44, no. 17, pp. 6035–6058, 2015.

[8] C. D. Jones and J. W. Steed, 'Gels with sense: supramolecular materials that respond to heat, light and sound', *Chemical Society Reviews*, vol. 45, no. 23, pp. 6546–6596, 2016.

[9] S. Ghosh, V. K. Praveen, and A. Ajayaghosh, 'The chemistry and applications of π-gels', *Annual Review of Materials Research*, vol. 46, pp. 235–262, 2016.

[10] J. Wang, K. Liu, R. Xing, and X. Yan, 'Peptide self-assembly: thermodynamics and kinetics', *Chemical Society Reviews*, vol. 45, no. 20, pp. 5589–5604, 2016.

[11] P. Cintas, G. Cravotto, A. Barge, and K. Martina, 'Interplay between mechanochemistry and sonochemistry', in *Polymer Mechanochemistry*, Springer, 2014, pp. 239–284.

[12] M. Raynal and L. Bouteiller, 'Organogel formation rationalized by Hansen solubility parameters', *Chemical communications*, vol. 47, no. 29, pp. 8271–8273, 2011.

[13] J. K. Gupta, D. J. Adams, and N. G. Berry, 'Will it gel? Successful computational prediction of peptide gelators using physicochemical properties and molecular fingerprints', *Chemical science*, vol. 7, no. 7, pp. 4713–4719, 2016.

[14] P. W. Frederix *et al.*, 'Exploring the sequence space for (tri-) peptide self-assembly to design and discover new hydrogels', *Nature chemistry*, vol. 7, no. 1, p. 30, 2015.

[15] J. H. van Esch, 'We can design molecular gelators, but do we understand them?', *Langmuir*, vol. 25, no. 15, pp. 8392–8394, 2009.

[16] K. Murata *et al.*, 'Thermal and light control of the sol-gel phase transition in cholesterol-based organic gels. Novel helical aggregation modes as detected by circular dichroism and electron microscopic observation', *Journal of the American Chemical Society*, vol. 116, no. 15, pp. 6664–6676, 1994.

[17] D. J. Abdallah and R. G. Weiss, 'Organogels and low molecular mass organic gelators', *Advanced Materials*, vol. 12, no. 17, pp. 1237–1247, 2000.

[18] A. R. Hirst and D. K. Smith, 'Solvent effects on supramolecular gel-phase materials: Two-component dendritic gel', *Langmuir*, vol. 20, no. 25, pp. 10851–10857, 2004.

[19] W. Fräßdorf, M. Fahrländer, K. Fuchs, and C. Friedrich, 'Thermorheological properties of self-assembled dibenzylidene sorbitol structures in various polymer matrices: Determination and prediction of characteristic temperatures', *Journal of Rheology*, vol. 47, no. 6, pp. 1445–1454, 2003.

[20] W. Edwards, C. A. Lagadec, and D. K. Smith, 'Solvent–gelator interactions—using empirical solvent parameters to better understand the self-assembly of gel-phase materials', *Soft Matter*, vol. 7, no. 1, pp. 110–117, 2011.

[21] K. Hanabusa, M. Matsumoto, M. Kimura, A. Kakehi, and H. Shirai, 'Low molecular weight gelators for organic fluids: gelation using a family of cyclo (dipeptide) s', *Journal of colloid and interface science*, vol. 224, no. 2, pp. 231–244, 2000.

[22] S. D. Bergin *et al.*, 'Towards solutions of single-walled carbon nanotubes in common solvents', *Advanced Materials*, vol. 20, no. 10, pp. 1876–1881, 2008.

[23] S. D. Bergin, Z. Sun, D. Rickard, P. V. Streich, J. P. Hamilton, and J. N. Coleman, 'Multicomponent solubility parameters for single-walled carbon nanotube- solvent mixtures', *ACS nano*, vol. 3, no. 8, pp. 2340–2350, 2009.

[24] N. Zweep, A. Hopkinson, A. Meetsma, W. R. Browne, B. L. Feringa, and J. H. van Esch, 'Balancing hydrogen bonding and van der Waals interactions in cyclohexane-based bisamide and bisurea organogelators', *Langmuir*, vol. 25, no. 15, pp. 8802–8809, 2009.

[25] P. Yadav and A. Ballabh, ‘Odd–even effect in a thiazole based organogelator: understanding the interplay of non-covalent interactions on property and applications’, *New Journal of Chemistry*, vol. 39, no. 1, pp. 721–730, 2015.

[26] P. Yadav, D. Kaur, and V. Gupta, ‘Rajnikant and A. Ballabh’, *RSC Adv*, vol. 3, pp. 8417–8421, 2013.

[27] J. N. Israelachvili, *Intermolecular and surface forces*. Academic press, 2011.

[28] H. von Helmholtz, ‘Ueber einige Gesetze der Vertheilung elektrischer Ströme in körperlichen Leitern, mit Anwendung auf die thierisch-elektrischen Versuche (Schluss.)’, *Annalen der Physik*, vol. 165, no. 7, pp. 353–377, 1853.

[29] M. Gouy, ‘Sur la constitution de la charge électrique à la surface d’un électrolyte’, 1910.

[30] D. L. Chapman, ‘LI. A contribution to the theory of electrocapillarity’, *The London, Edinburgh, and Dublin philosophical magazine and journal of science*, vol. 25, no. 148, pp. 475–481, 1913.

[31] O. Stern, ‘Zur theorie der elektrolytischen doppelschicht’, *Zeitschrift für Elektrochemie und angewandte physikalische Chemie*, vol. 30, no. 21–22, pp. 508–516, 1924.

[32] E. J. W. Verwey, ‘Theory of the stability of lyophobic colloids.’, *The Journal of Physical Chemistry*, vol. 51, no. 3, pp. 631–636, 1947.

[33] E. J. W. Verwey, J. T. G. Overbeek, and J. T. G. Overbeek, *Theory of the Stability of Lyophobic Colloids*. Dover Publications, 1999. [Online]. Available: https://books.google.be/books?id=B285yQEACAAJ

[34] C. J. Brinker and G. W. Scherer, *Sol-gel science: the physics and chemistry of sol-gel processing*. Academic press, 2013.

[35] B. Gauthier-Manuel, E. Guyon, S. Roux, S. Gits, and F. Lefaucheux, ‘Critical viscoelastic study of the gelation of silica particles’, *Journal de Physique*, vol. 48, no. 5, pp. 869–875, 1987.

[36] P. J. Flory, *Principles of polymer chemistry*. Cornell University Press, 1953.

[37] B. H. Zimm and W. H. Stockmayer, ‘The dimensions of chain molecules containing branches and rings’, *The Journal of Chemical Physics*, vol. 17, no. 12, pp. 1301–1314, 1949.

[38] P.-G. de Gennes, ‘Statistics of branching and hairpin helices for the dAT copolymer’, *Biopolymers: Original Research on Biomolecules*, vol. 6, no. 5, pp. 715–729, 1968.

[39] R. Zallen, *The physics of amorphous solids*. John Wiley & Sons, 2008.

[40] R. Zallen, ‘The formation of amorphous solids’, *The physics of amorphous solids. New York: Wiley*, pp. 1–22, 1983.

[41] D. Stauffer, A. Coniglio, and M. Adam, ‘Gelation and critical phenomena’, in *Polymer networks*, Springer, 1982, pp. 103–158.

[42] S. Chandrasekhar, ‘Stochastic problems in physics and astronomy’, *Reviews of modern physics*, vol. 15, no. 1, p. 1, 1943.

[43] M. Ernst, ‘Kinetics of clustering in irreversible aggregation’, in *Fractals in Physics*, Elsevier, 1986, pp. 289–302.

[44] L. Pietronero and E. Tosatti, *Fractals in physics*. Elsevier, 2012.

[45] P. Van Dongen and M. Ernst, ‘Dynamic scaling in the kinetics of clustering’, *Physical review letters*, vol. 54, no. 13, p. 1396, 1985.

[46] D. Tyrer, ‘The theory of solubility’, *Journal of physical chemistry*, vol. 16, no. 1, pp. 69–85, 1912.

[47] M. L. Huggins, ‘Some properties of solutions of long-chain compounds.’, *The Journal of Physical Chemistry*, vol. 46, no. 1, pp. 151–158, 1942.

[48] P. J. Flory, ‘Thermodynamics of high polymer solutions’, *The Journal of chemical physics*, vol. 9, no. 8, pp. 660–660, 1941.

[49] P. J. Flory, ‘Thermodynamics of high polymer solutions’, *The Journal of chemical physics*, vol. 10, no. 1, pp. 51–61, 1942.

[50] Y. Meng and X. Zhang, ‘Nanostructure Formation in Thermoset/Block Copolymer and Thermoset/Hyperbranched Polymer Blends’, in *Nanostructured Polymer Blends*, Elsevier, 2014, pp. 161–194.

[51] M. De Loos, J. van Esch, I. Stokroos, R. M. Kellogg, and B. L. Feringa, ‘Remarkable stabilization of self-assembled organogels by polymerization’, *Journal of the American Chemical Society*, vol. 119, no. 51, pp. 12675–12676, 1997.

[52] K. Hanabusa, M. Yamada, M. Kimura, and H. Shirai, ‘Prominent gelation and chiral aggregation of alkylamides derived from trans-1, 2-diaminocyclohexane’, *Angewandte Chemie International Edition in English*, vol. 35, no. 17, pp. 1949–1951, 1996.

[53] R. Wang, C. Geiger, L. Chen, B. Swanson, and D. G. Whitten, ‘Direct observation of sol- gel conversion: the role of the solvent in organogel formation’, *Journal of the American Chemical Society*, vol. 122, no. 10, pp. 2399–2400, 2000.

[54] P. Terech and R. G. Weiss, ‘Low molecular mass gelators of organic liquids and the properties of their gels’, *Chemical reviews*, vol. 97, no. 8, pp. 3133–3160, 1997.

[55] L. A. Estroff and A. D. Hamilton, ‘Water gelation by small organic molecules’, *Chemical reviews*, vol. 104, no. 3, pp. 1201–1218, 2004.

[56] M. George and R. G. Weiss, ‘Molecular organogels. Soft matter comprised of low-molecular-mass organic gelators and organic liquids’, *Accounts of chemical research*, vol. 39, no. 8, pp. 489–497, 2006.

[57] J. Makarević, M. Jokić, B. Perić, V. Tomišić, B. Kojić-Prodić, and M. Žinić, ‘Bis (amino acid) oxalyl amides as ambidextrous gelators of water and organic solvents: supramolecular gels with temperature dependent assembly/dissolution equilibrium’, *Chemistry–A European Journal*, vol. 7, no. 15, pp. 3328–3341, 2001.

[58] V. G. Machado and C. Machado, ‘An easy and versatile experiment to demonstrate solvent polarity using solvatochromic dyes’, *Journal of Chemical Education*, vol. 78, no. 5, p. 649, 2001.

[59] C. Reichardt, ‘Polarity of ionic liquids determined empirically by means of solvatochromic pyridinium N-phenolate betaine dyes’, *Green Chemistry*, vol. 7, no. 5, pp. 339–351, 2005.

[60] Y. Lan *et al.*, ‘Comparing and correlating solubility parameters governing the self-assembly of molecular gels using 1, 3: 2, 4-dibenzylidene sorbitol as the gelator’, *Langmuir*, vol. 30, no. 47, pp. 14128–14142, 2014.

[61] J. Kaszyńska, A. \Lapiński, M. Bielejewski, R. Luboradzki, and J. Tritt-Goc, ‘On the relation between the solvent parameters and the physical properties of methyl-4, 6-O-benzylidene-α-d-glucopyranoside organogels’, *Tetrahedron*, vol. 68, no. 20, pp. 3803–3810, 2012.

[62] J. Burke, ‘Solubility parameters: theory and application’, 1984.

[63] J. H. Hildebrand, *Solubility of Non-electrolytes*. Reinhold Publishing Corporation, 1936. [Online]. Available: https://books.google.be/books?id=59AgAAAAMAAJ

[64] D. Patterson, ‘Role of free volume changes in polymer solution thermodynamics’, in *Journal of Polymer Science Part C: Polymer Symposia*, 1967, vol. 16, no. 6, pp. 3379–3389.

[65] J. Biroa, L. Zeman, and D. Patterson, ‘Prediction of the x parameter by the solubility parameter and corresponding states theories’, *Macromolecules*, vol. 4, no. 1, pp. 30–35, 1971.

[66] V. T. Wyatt, D. Bush, J. Lu, J. P. Hallett, C. L. Liotta, and C. A. Eckert, ‘Determination of solvatochromic solvent parameters for the characterization of gas-expanded liquids’, *The Journal of supercritical fluids*, vol. 36, no. 1, pp. 16–22, 2005.

[67] A. F. Lagalante, C. Wood, A. M. Clarke, and T. J. Bruno, ‘Kamlet–Taft solvatochromic parameters for 25 glycol ether solvents and glycol ether aqueous solutions’, *Journal of solution chemistry*, vol. 27, no. 10, pp. 887–900, 1998.

[68] R. Taft, J.-L. M. Abboud, and M. J. Kamlet, ‘Solvatochromic comparison method. 20. Linear solvation energy relationships. 12. The d. delta. term in the solvatochromic equations’, *Journal of the American Chemical Society*, vol. 103, no. 5, pp. 1080–1086, 1981.

[69] P. Muller, ‘Glossary of terms used in physical organic chemistry (IUPAC Recommendations 1994)’, *Pure and Applied Chemistry*, vol. 66, no. 5, pp. 1077–1184, 1994.

[70] C. M. Hansen, *The three dimensional solubility parameter and solvent diffusion coefficient: Their importance in surface coating formulation*. 1967.

[71] C. M. Hansen, *Hansen solubility parameters: a user’s handbook*. CRC press, 2007.

[72] S. Abbott and C. M. Hansen, *Hansen solubility parameters in practice*. Hansen-Solubility, 2008.

[73] R. F. Blanks and J. Prausnitz, ‘Thermodynamics of polymer solubility in polar and nonpolar systems’, *Industrial & Engineering Chemistry Fundamentals*, vol. 3, no. 1, pp. 1–8, 1964.

[74] J. V. Koleske, *Paint and coating testing manual: of the Gardner-Sward handbook; Paint testing manual*. 1995.

[75] P. Hoftyzer and D. Van Krevelen, ‘Properties of polymers’, *Elsevier, New York*, 1976.

[76] A. F. Barton, *CRC handbook of solubility parameters and other cohesion parameters*. CRC press, 1991.

[77] A. Beerbower, ‘Environmental capability of liquid lubricants’, *Interdisciplinary approach to liquid lubricant technology*, pp. 365–431, 1973.

[78] D. W. Van Krevelen and K. Te Nijenhuis, *Properties of polymers: their correlation with chemical structure; their numerical estimation and prediction from additive group contributions*. Elsevier, 2009.

[79] C. M. Hansen and A. Beerbower, ‘Solubility parameters’, *Kirk-Othmer Encyclopedia of Chemical Technology*, vol. 2, no. 2, pp. 889–910, 1971.

[80] D. R. Nunes, M. Raynal, B. Isare, P.-A. Albouy, and L. Bouteiller, ‘Organogel formation rationalized by Hansen solubility parameters: improved methodology’, *Soft matter*, vol. 14, no. 23, pp. 4805–4809, 2018.

[81] J. Bonnet, G. Suissa, M. Raynal, and L. Bouteiller, ‘Organogel formation rationalized by Hansen solubility parameters: dos and don’ts’, *Soft Matter*, vol. 10, no. 18, pp. 3154–3160, 2014.

[82] J. Bonnet, G. Suissa, M. Raynal, and L. Bouteiller, ‘Organogel formation rationalized by Hansen solubility parameters: influence of gelator structure’, *Soft matter*, vol. 11, no. 11, pp. 2308–2312, 2015.

[83] E. Ressouche, S. Pensec, B. Isare, G. Ducouret, and L. Bouteiller, ‘Rational design of urea-based two-component organogelators’, *ACS Macro Letters*, vol. 5, no. 2, pp. 244–247, 2016.

[84] Y. Huang, Y. Yuan, W. Tu, Y. Zhang, M. Zhang, and H. Qu, ‘Preparation of efficient organogelators based on pyrazine-2, 5-dicarboxylic acid showing room temperature mesophase’, *Tetrahedron*, vol. 71, no. 21, pp. 3221–3230, 2015.

[85] L. He, X. Ran, J. Li, Q. Gao, Y. Kuang, and L. Guo, ‘A highly transparent and autonomic self-healing organogel from solvent regulation based on hydrazide derivatives’, *Journal of Materials Chemistry A*, vol. 6, no. 34, pp. 16600–16609, 2018.

[86] T. Wang, X. Yu, Y. Li, J. Ren, and X. Zhen, ‘Robust, self-healing, and multistimuli-responsive supergelator for the visual recognition and separation of short-chain cycloalkanes and alkanes’, *ACS applied materials & interfaces*, vol. 9, no. 15, pp. 13666–13675, 2017.

[87] T. Ando and K. Ito, ‘Gelation properties of poly (aryl ether) dendrons bearing long alkyl chains’, *Journal of Inclusion Phenomena and Macrocyclic Chemistry*, vol. 80, no. 3–4, pp. 285–294, 2014.

[88] R. Van Lommel, J. Zhao, W. M. De Borggraeve, F. De Proft, and M. Alonso, ‘Molecular dynamics based descriptors for predicting supramolecular gelation’, *Chemical Science*, vol. 11, no. 16, pp. 4226–4238, 2020.

[89] K. Hao, *We analyzed 16,625 papers to figure out where AI is headed next*. 2020. [Online]. Available: https://www.technologyreview.com/2019/01/25/1436/we-analyzed-16625-papers-to-figure-out-where-ai-is-headed-next/

[90] P. P. Shinde and S. Shah, ‘A Review of Machine Learning and Deep Learning Applications’, in *2018 Fourth International Conference on Computing Communication Control and Automation (ICCUBEA)*, 2018, pp. 1–6.

[91] P. O. Dral, ‘Quantum chemistry in the age of machine learning’, *The Journal of Physical Chemistry Letters*, vol. 11, no. 6, pp. 2336–2347, 2020.

[92] O. V. Prezhdo, *Advancing Physical Chemistry with Machine Learning*. ACS Publications, 2020.

[93] A. L. Ferguson, J. Hachmann, T. F. Miller, and J. Pfaendtner, *The Journal of Physical Chemistry A/B/C Virtual Special Issue on Machine Learning in Physical Chemistry*. ACS Publications, 2020.

[94] G. R. Schleder, A. C. Padilha, C. M. Acosta, M. Costa, and A. Fazzio, ‘From DFT to machine learning: recent approaches to materials science–a review’, *Journal of Physics: Materials*, vol. 2, no. 3, p. 032001, 2019.

[95] J. Zhang *et al.*, ‘A Perspective on Deep Learning for Molecular Modeling and Simulations’, *arXiv preprint arXiv:2004.13011*, 2020.

[96] J. Brownlee, *Master Machine Learning Algorithms: discover how they work and implement them from scratch*. Machine Learning Mastery, 2016.

[97] N. Allinger and U. Burkert, *Molecular Mechanics’, ACS Monograph 177*. American Chemical Society: Washington, DC, 1982.

[98] N. Allinger, ‘Calculation of molecular structure and energy by force-field methods’, in *Advances in physical organic chemistry*, vol. 13, Elsevier, 1976, pp. 1–82.

[99] B. P. Hay, ‘Methods for molecular mechanics modeling of coordination compounds’, *Coordination chemistry reviews*, vol. 126, no. 1–2, pp. 177–236, 1993.

[100] A. R. Leach and A. R. Leach, *Molecular modelling: principles and applications*. Pearson education, 2001.

[101] D. S. Biovia, ‘Materials Studio’, *R2 (Dassault Systèmes BIOVIA, San Diego*, 2017.

[102] M. P. Allen and D. J. Tildesley, *Computer simulation of liquids*. Oxford university press, 2017.

[103] D. Frenkel and B. Smit, *Understanding molecular simulation: from algorithms to applications*, vol. 1. Elsevier, 2001.

[104] S. L. Mayo, B. D. Olafson, and W. A. Goddard, ‘DREIDING: a generic force field for molecular simulations’, *Journal of Physical chemistry*, vol. 94, no. 26, pp. 8897–8909, 1990.

[105] H. Sun, ‘Force field for computation of conformational energies, structures, and vibrational frequencies of aromatic polyesters’, *Journal of Computational Chemistry*, vol. 15, no. 7, pp. 752–768, 1994.

[106] H. Sun, S. J. Mumby, J. R. Maple, and A. T. Hagler, ‘An ab initio CFF93 all-atom force field for polycarbonates’, *Journal of the American Chemical Society*, vol. 116, no. 7, pp. 2978–2987, 1994.

[107] H. Sun, ‘Ab initio calculations and force field development for computer simulation of polysilanes’, *Macromolecules*, vol. 28, no. 3, pp. 701–712, 1995.

[108] M. Svard and \AAke C Rasmuson, ‘Force fields and point charges for crystal structure modeling’, *Industrial & engineering chemistry research*, vol. 48, no. 6, pp. 2899–2912, 2009.

[109] S. Brodersen, S. Wilke, F. Leusen, and G. Engel, ‘A study of different approaches to the electrostatic interaction in force field methods for organic crystals’, *Physical Chemistry Chemical Physics*, vol. 5, no. 21, pp. 4923–4931, 2003.

[110] N. Panina *et al.*, ‘Crystal structure prediction of organic pigments: quinacridone as an example’, *Journal of applied crystallography*, vol. 40, no. 1, pp. 105–114, 2007.

[111] V. Bisker-Leib and M. F. Doherty, ‘Modeling crystal shape of polar organic materials: applications to amino acids’, *Crystal growth & design*, vol. 3, no. 2, pp. 221–237, 2003.

[112] Y. Quo, N. Karasawa, and W. A. Goddard, ‘Prediction of fullerene packing in C 60 and C 70 crystals’, *Nature*, vol. 351, no. 6326, pp. 464–467, 1991.

[113] R. E. Tuzun, D. W. Noid, B. G. Sumpter, and R. C. Merkle, ‘Dynamics of fluid flow inside carbon nanotubes’, *Nanotechnology*, vol. 7, no. 3, p. 241, 1996.

[114] R. E. Tuzun, D. W. Noid, B. G. Sumpter, and R. C. Merkle, ‘Dynamics of flow inside carbon nanotubes’, *Nanotechnology*, vol. 8, no. 3, p. 112, 1997.

[115] J. P. Lommerse *et al.*, ‘A test of crystal structure prediction of small organic molecules’, *Acta Crystallographica Section B: Structural Science*, vol. 56, no. 4, pp. 697–714, 2000.

[116] G. R. Desiraju, ‘Crystal engineering: from molecule to crystal’, *Journal of the American Chemical Society*, vol. 135, no. 27, pp. 9952–9967, 2013.

[117] M. A. Neumann, F. J. Leusen, and J. Kendrick, ‘A major advance in crystal structure prediction’, *Angewandte Chemie International Edition*, vol. 47, no. 13, pp. 2427–2430, 2008.

[118] C. Krishnamohan Sharma, ‘Crystal engineering- where do we go from here?’, *Crystal growth & design*, vol. 2, no. 6, pp. 465–474, 2002.

[119] P. G. Karamertzanis *et al.*, ‘Can the formation of pharmaceutical cocrystals be computationally predicted? 2. Crystal structure prediction’, *Journal of Chemical Theory and Computation*, vol. 5, no. 5, pp. 1432–1448, 2009.

[120] N. Issa, P. G. Karamertzanis, G. W. Welch, and S. L. Price, ‘Can the formation of pharmaceutical cocrystals be computationally predicted? I. Comparison of lattice energies’, *Crystal Growth and Design*, vol. 9, no. 1, pp. 442–453, 2009.

[121] S. (Sally) L. Price, ‘Computed crystal energy landscapes for understanding and predicting organic crystal structures and polymorphism’, *Accounts of chemical research*, vol. 42, no. 1, pp. 117–126, 2009.

[122] G. R. Desiraju, ‘Crystal engineering: A brief overview’, *Journal of chemical sciences*, vol. 122, no. 5, pp. 667–675, 2010.

[123] W. S. Motherwell *et al.*, ‘Crystal structure prediction of small organic molecules: a second blind test’, *Acta Crystallographica Section B: Structural Science*, vol. 58, no. 4, pp. 647–661, 2002.

[124] G. Day *et al.*, ‘A third blind test of crystal structure prediction’, *Acta Crystallographica Section B: Structural Science*, vol. 61, no. 5, pp. 511–527, 2005.

[125] G. M. Day *et al.*, ‘Significant progress in predicting the crystal structures of small organic molecules–a report on the fourth blind test’, *Acta Crystallographica Section B: Structural Science*, vol. 65, no. 2, pp. 107–125, 2009.

[126] D. A. Bardwell *et al.*, ‘Towards crystal structure prediction of complex organic compounds–a report on the fifth blind test’, *Acta Crystallographica Section B: Structural Science*, vol. 67, no. 6, pp. 535–551, 2011.

[127] A. M. Reilly *et al.*, ‘Report on the sixth blind test of organic crystal structure prediction methods’, *Acta Crystallographica Section B: Structural Science, Crystal Engineering and Materials*, vol. 72, no. 4, pp. 439–459, 2016.

[128] U. H. Hansmann, ‘Parallel tempering algorithm for conformational studies of biological molecules’, *Chemical Physics Letters*, vol. 281, no. 1–3, pp. 140–150, 1997.

[129] D. J. Earl and M. W. Deem, ‘Parallel tempering: Theory, applications, and new perspectives’, *Physical Chemistry Chemical Physics*, vol. 7, no. 23, pp. 3910–3916, 2005.

[130] D. J. Wales and J. P. Doye, ‘Global optimization by basin-hopping and the lowest energy structures of Lennard-Jones clusters containing up to 110 atoms’, *The Journal of Physical Chemistry A*, vol. 101, no. 28, pp. 5111–5116, 1997.

[131] E. Zitzler and L. Thiele, ‘An evolutionary algorithm for multiobjective optimization: The strength pareto approach’, *TIK-report*, vol. 43, 1998.

[132] C. W. Glass, A. R. Oganov, and N. Hansen, ‘USPEX—Evolutionary crystal structure prediction’, *Computer physics communications*, vol. 175, no. 11–12, pp. 713–720, 2006.

[133] A. O. Lyakhov, A. R. Oganov, H. T. Stokes, and Q. Zhu, ‘New developments in evolutionary structure prediction algorithm USPEX’, *Computer Physics Communications*, vol. 184, no. 4, pp. 1172–1182, 2013.

[134] A. Barducci, M. Bonomi, and M. Parrinello, ‘Metadynamics’, *Wiley Interdisciplinary Reviews: Computational Molecular Science*, vol. 1, no. 5, pp. 826–843, 2011.

[135] A. Laio, A. Rodriguez-Fortea, F. L. Gervasio, M. Ceccarelli, and M. Parrinello, ‘Assessing the accuracy of metadynamics’, *The journal of physical chemistry B*, vol. 109, no. 14, pp. 6714–6721, 2005.

[136] R. L. Akkermans, N. A. Spenley, and S. H. Robertson, ‘Monte Carlo methods in materials studio’, *Molecular Simulation*, vol. 39, no. 14–15, pp. 1153–1164, 2013.

[137] S. L. Price, ‘From crystal structure prediction to polymorph prediction: interpreting the crystal energy landscape’, *Physical Chemistry Chemical Physics*, vol. 10, no. 15, pp. 1996–2009, 2008.

[138] S. Price, ‘Computational prediction of organic crystal structures and polymorphism’, *International Reviews in Physical Chemistry*, vol. 27, no. 3, pp. 541–568, 2008.

[139] P. Pisani *et al.*, ‘Describing the conformational landscape of small organic molecules through gaussian mixtures in dihedral space’, *Journal of chemical theory and computation*, vol. 10, no. 6, pp. 2557–2568, 2014.

[140] J. Yang, S. De, J. E. Campbell, S. Li, M. Ceriotti, and G. M. Day, ‘Large-Scale Computational Screening of Molecular Organic Semiconductors Using Crystal Structure Prediction’, *Chemistry of Materials*, vol. 30, no. 13, pp. 4361–4371, 2018.

[141] D. Braga, F. Grepioni, and G. R. Desiraju, ‘Crystal engineering and organometallic architecture’, *Chemical reviews*, vol. 98, no. 4, pp. 1375–1406, 1998.

[142] H. Rietveld, ‘A profile refinement method for nuclear and magnetic structures’, *Journal of applied Crystallography*, vol. 2, no. 2, pp. 65–71, 1969.

[143] H. Rietveld, ‘Line profiles of neutron powder-diffraction peaks for structure refinement’, *Acta Crystallographica*, vol. 22, no. 1, pp. 151–152, 1967.

[144] G. Wulff, ‘Zeitschriftfür Kristallographie’, *Cryst Mater*, vol. 34, no. 1–6, pp. 449–530, 1901.

[145] A. Bravais, ‘Etudes Crystallographiques; Academie des Sciences: Paris, 1913’.

[146] G. Friedel, ‘Etudes sur la loi de Bravais’, *Bulletin de Minéralogie*, vol. 30, no. 9, pp. 326–455, 1907.

[147] J. H. Donnay and D. Harker, ‘A new law of crystal morphology extending the law of Bravais’, *American Mineralogist: Journal of Earth and Planetary Materials*, vol. 22, no. 5, pp. 446–467, 1937.

[148] K. Tsukamoto, ‘In situ observation of Crystal growth and flows by optical techniques’, in *Handbook of Crystal Growth*, Elsevier, 2015, pp. 1031–1060.

[149] J. W. Gibbs, ‘Collected Works Longmans’, *Green and Co., New York*, 1928.

[150] R. Docherty, G. Clydesdale, K. Roberts, and P. Bennema, ‘Application of Bravais-Friedel-Donnay-Harker, attachment energy and Ising models to predicting and understanding the morphology of molecular crystals’, *Journal of Physics D: Applied Physics*, vol. 24, no. 2, p. 89, 1991.

[151] Z. Berkovitch-Yellin, ‘Toward an ab initio derivation of crystal morphology’, *Journal of the American Chemical Society*, vol. 107, no. 26, pp. 8239–8253, 1985.

[152] V. Fiorentini and M. Methfessel, ‘Extracting convergent surface energies from slab calculations’, *Journal of Physics: Condensed Matter*, vol. 8, no. 36, p. 6525, 1996.

[153] J. Boettger, ‘Nonconvergence of surface energies obtained from thin-film calculations’, *Physical Review B*, vol. 49, no. 23, p. 16798, 1994.

[154] W. Liu, J. Li, W. Zheng, and Q. Jiang, ‘Ni Al (110)/ Cr (110) interface: A density functional theory study’, *Physical Review B*, vol. 73, no. 20, p. 205421, 2006.

[155] T. Nishinaga, *Handbook of Crystal Growth: Fundamentals*. Elsevier, 2014.

[156] B. Vainshtein, A. Chernov, and L. Shuvalov, *Modern Crystallography III. Crystal Growth*. Springer-Verlag, Berlin, 1984.

[157] A. Chernov, ‘Crystal growth and crystallography’, *Acta Crystallographica Section A: Foundations of Crystallography*, vol. 54, no. 6, pp. 859–872, 1998.

[158] P. Bennema, ‘Analysis of crystal growth models for slightly supersaturated solutions’, *Journal of Crystal Growth*, vol. 1, no. 5, pp. 278–286, 1967.

[159] H. Schonhorn, ‘Theoretical relationship between surface tension and cohesive energy density’, *The Journal of Chemical Physics*, vol. 43, no. 6, pp. 2041–2043, 1965.

[160] P. Becher, ‘The calculation of cohesive energy density from the surface tension of liquids’, *Journal of Colloid and Interface Science*, vol. 38, no. 2, pp. 291–293, 1972.

[161] J. Gardon, ‘Relationship between cohesive energy densities of polymers and Zisman’s critical surface tensions’, *The Journal of Physical Chemistry*, vol. 67, no. 9, pp. 1935–1936, 1963.

[162] K. Lissant, ‘Geometry of emulsions’, *Journal of the Society of Cosmetic Chemists*, vol. 21, no. 3, p. 141, 1970.

[163] K. Lissant, ‘The geometry of high-internal-phase-ratio emulsions’, *Journal of colloid and interface science*, vol. 22, no. 5, pp. 462–468, 1966.

[164] J. Hildebrand and R. Scott, ‘Solutions of nonelectrolytes’, *Annual Review of Physical Chemistry*, vol. 1, no. 1, pp. 75–92, 1950.

[165] M. P. Tosi, ‘Cohesion of ionic solids in the Born model’, in *Solid state physics*, vol. 16, Elsevier, 1964, pp. 1–120.

[166] B. optischer und elektrostatischer Gitterpotentiale, ‘Ewald, PP’, *Die Ann. Phys*, vol. 64, pp. 253–287, 1921.

[167] J.-M. Lehn, M. Mascal, A. Decian, and J. Fischer, ‘Molecular recognition directed self-assembly of ordered supramolecular strands by cocrystallization of complementary molecular components’, *Journal of the Chemical Society, Chemical Communications*, no. 6, pp. 479–481, 1990.

[168] C. Margaret and others, ‘The use of cocrystallization as a method of studying hydrogen bond preferences of 2-aminopyrimidine’, *Journal of the Chemical Society, Chemical Communications*, no. 8, pp. 589–591, 1990.

[169] C. KrishnamohanáSharma and others, ‘Molecular recognition via C–H··· O hydrogen bonding. Crystal structure of the 1: 1 complex 4-nitrobenzoic acid–4-(N, N-dimethylamino) benzoic acid’, *Journal of the Chemical Society, Chemical Communications*, no. 11, pp. 832–833, 1992.

[170] J. A. Zerkowski, C. T. Seto, D. A. Wierda, and G. M. Whitesides, ‘The design of organic structures in the solid state: hydrogen-bonded molecular" tapes"’, *Journal of the American Chemical Society*, vol. 112, no. 24, pp. 9025–9026, 1990.

[171] J. A. Zerkowski, C. T. Seto, and G. M. Whitesides, ‘Solid-state structures of rosette and crinkled tape motifs derived from the cyanuric acid melamine lattice’, *Journal of the American Chemical Society*, vol. 114, no. 13, pp. 5473–5475, 1992.

[172] B. Pi-Boleda *et al.*, ‘Studies on Cycloalkane-Based Bisamide Organogelators: A New Example of Stochastic Chiral Symmetry-Breaking Induced by Sonication’, *Chemistry–A European Journal*, vol. 23, no. 14, pp. 3357–3365, 2017.

[173] A. J. Cruz-Cabeza and J. Bernstein, ‘Conformational polymorphism’, *Chemical reviews*, vol. 114, no. 4, pp. 2170–2191, 2014.

[174] A. J. Cruz-Cabeza, S. M. Reutzel-Edens, and J. Bernstein, ‘Facts and fictions about polymorphism’, *Chemical Society Reviews*, vol. 44, no. 23, pp. 8619–8635, 2015.

[175] J. Bernstein, R. J. Davey, and J.-O. Henck, ‘Concomitant polymorphs’, *Angewandte Chemie International Edition*, vol. 38, no. 23, pp. 3440–3461, 1999.

[176] A. Burger and R. Ramberger, ‘On the polymorphism of pharmaceuticals and other molecular crystals. I’, *Microchimica Acta*, vol. 72, no. 3–4, pp. 259–271, 1979.

[177] M. L. Connolly, ‘Analytical molecular surface calculation’, *Journal of applied crystallography*, vol. 16, no. 5, pp. 548–558, 1983.

[178] M. L. Connolly, ‘Computation of molecular volume’, *Journal of the American Chemical society*, vol. 107, no. 5, pp. 1118–1124, 1985.

[179] X. Y. Liu, P. D. Sawant, W. B. Tan, I. Noor, C. Pramesti, and B.-H. Chen, ‘Creating new supramolecular materials by architecture of three-dimensional nanocrystal fiber networks’, *Journal of the American Chemical Society*, vol. 124, no. 50, pp. 15055–15063, 2002.

[180] J. L. Li, X. Y. Liu, C. S. Strom, and J. Y. Xiong, ‘Engineering of small molecule organogels by design of the nanometer structure of fiber networks’, *Advanced materials*, vol. 18, no. 19, pp. 2574–2578, 2006.

[181] R.-Y. Wang, X.-Y. Liu, J. Narayanan, J.-Y. Xiong, and J.-L. Li, ‘Architecture of fiber network: from understanding to engineering of molecular gels’, *The Journal of Physical Chemistry B*, vol. 110, no. 51, pp. 25797–25802, 2006.

[182] J.-Y. Xiong, X.-Y. Liu, J.-L. Li, and M. W. Vallon, ‘Architecture of macromolecular network of soft functional materials: from structure to function’, *The Journal of Physical Chemistry B*, vol. 111, no. 20, pp. 5558–5563, 2007.

[183] R. Wang, X.-Y. Liu, J. Xiong, and J. Li, ‘Real-time observation of fiber network formation in molecular organogel: supersaturation-dependent microstructure and its related rheological property’, *The journal of physical chemistry b*, vol. 110, no. 14, pp. 7275–7280, 2006.

[184] T. Prosa, M. Winokur, J. Moulton, P. Smith, and A. Heeger, ‘X-ray structural studies of poly (3-alkylthiophenes): an example of an inverse comb’, *Macromolecules*, vol. 25, no. 17, pp. 4364–4372, 1992.

[185] T. Prosa, M. Winokur, and R. McCullough, ‘Evidence of a novel side chain structure in regioregular poly (3-alkylthiophenes)’, *Macromolecules*, vol. 29, no. 10, pp. 3654–3656, 1996.

[186] K. S. Ahn, H. Jo, J. B. Kim, I. Seo, H. H. Lee, and D. R. Lee, ‘Structural Transition and Interdigitation of Alkyl Side Chains in the Conjugated Polymer Poly (3-hexylthiophene) and Their Effects on the Device Performance of the Associated Organic Field-Effect Transistor’, *ACS Applied Materials & Interfaces*, vol. 12, no. 1, pp. 1142–1150, 2019.

[187] T. Marszalek, M. Li, and W. Pisula, ‘Design directed self-assembly of donor–acceptor polymers’, *Chemical Communications*, vol. 52, no. 73, pp. 10938–10947, 2016.

[188] B. E. Hirsch, K. P. McDonald, A. H. Flood, and S. L. Tait, ‘Living on the edge: Tuning supramolecular interactions to design two-dimensional organic crystals near the boundary of two stable structural phases’, *The Journal of chemical physics*, vol. 142, no. 10, p. 101914, 2015.

[189] Y. Hu, K. Miao, L. Xu, B. Zha, X. Miao, and W. Deng, ‘Effects of alkyl chain number and position on 2D self-assemblies’, *RSC advances*, vol. 7, no. 51, pp. 32391–32398, 2017.

[190] B. R. Beno, K.-S. Yeung, M. D. Bartberger, L. D. Pennington, and N. A. Meanwell, ‘A survey of the role of noncovalent sulfur interactions in drug design’, *Journal of medicinal chemistry*, vol. 58, no. 11, pp. 4383–4438, 2015.

[191] G. Conboy *et al.*, ‘To bend or not to bend–are heteroatom interactions within conjugated molecules effective in dictating conformation and planarity?’, *Materials Horizons*, vol. 3, no. 4, pp. 333–339, 2016.

[192] K. Kobayashi, Y. Asakawa, Y. Kikuchi, H. Toi, and Y. Aoyama, ‘CH-. pi. interaction as an important driving force of host-guest complexation in apolar organic media. Binding of monools and acetylated compounds to resorcinol cyclic tetramer as studied by proton NMR and circular dichroism spectroscopy’, *Journal of the American Chemical Society*, vol. 115, no. 7, pp. 2648–2654, 1993.

[193] M.-F. Fan, Z. Lin, J. E. McGrady, and D. M. P. Mingos, ‘Novel intermolecular CH pi interactions: An ab initio and density functional theory study’, *Journal OF The Chemical society-perkin TRANSACTIONS 2*, vol. 4, no. 4, 1996.

[194] M. Nishio, ‘CH/π hydrogen bonds in crystals’, *CrystEngComm*, vol. 6, no. 27, pp. 130–158, 2004.

[195] M. Nishio, ‘The CH/π hydrogen bond in chemistry. Conformation, supramolecules, optical resolution and interactions involving carbohydrates’, *Physical Chemistry Chemical Physics*, vol. 13, no. 31, pp. 13873–13900, 2011.

[196] A. Guijarro, J. A. Vergés Brotons, E. San-Fabián, G. Chiappe, E. Louis, and others, ‘Herringbone Pattern and CH–π Bonding in the Crystal Architecture of Linear Polycyclic Aromatic Hydrocarbons’, 2016.

[197] N. L. Madhavi, G. R. Desiraju, A. K. Katz, H. Carrell, and A. Nangia, ‘Evidence for the characterisation of the C–H··· π interaction as a weak hydrogen bond: toluene and chlorobenzene solvates of 2, 3, 7, 8-tetraphenyl-1, 9, 10-anthyridine’, *Chemical Communications*, no. 20, pp. 1953–1954, 1997.

[198] C. Bruel, J. R. Tavares, P. J. Carreau, and M.-C. Heuzey, ‘The structural amphiphilicity of cellulose nanocrystals characterized from their cohesion parameters’, *Carbohydrate polymers*, vol. 205, pp. 184–191, 2019.

[199] S. Meng, W. Li, X. Yin, and J. Xie, ‘A comprehensive theoretical study of the hydrogen bonding interactions and microscopic solvation structures of a pyridyl-urea-based hydrogelator in aqueous solution’, *Computational and Theoretical Chemistry*, vol. 1006, pp. 76–84, 2013.

[200] S. Meng, Y. Tang, Y. Yin, X. Yin, and J. Xie, ‘A theoretical study of molecular conformations and gelation ability of N, N′-dipyridyl urea compounds in ethanol solution: DFT calculations and MD simulations’, *RSC advances*, vol. 3, no. 39, pp. 18115–18127, 2013.

[201] C. D. Jones, H. T. Simmons, K. E. Horner, K. Liu, R. L. Thompson, and J. W. Steed, ‘Braiding, branching and chiral amplification of nanofibres in supramolecular gels’, *Nature chemistry*, vol. 11, no. 4, pp. 375–381, 2019.

[202] M. G. Angelerou *et al.*, ‘Supramolecular nucleoside-based gel: molecular dynamics simulation and characterization of its nanoarchitecture and self-assembly mechanism’, *Langmuir*, vol. 34, no. 23, pp. 6912–6921, 2018.

[203] R. Van Lommel, L. A. Rutgeerts, W. M. De Borggraeve, F. De Proft, and M. Alonso, ‘Rationalising Supramolecular Hydrogelation of Bis-Urea-Based Gelators through a Multiscale Approach’, *ChemPlusChem*, vol. 85, no. 2, pp. 267–276, 2020.

[204] A. Beerbower, ‘Surface free energy: a new relationship to bulk energies’, *Journal of Colloid and Interface Science*, vol. 35, no. 1, pp. 126–132, 1971.

[205] M. A. Neumann, ‘Tailor-made force fields for crystal-structure prediction’, *The Journal of Physical Chemistry B*, vol. 112, no. 32, pp. 9810–9829, 2008.

[206] G. M. Day, ‘Current approaches to predicting molecular organic crystal structures’, *Crystallography Reviews*, vol. 17, no. 1, pp. 3–52, 2011.